On the Correlation between Cosmic Ray Arrival Directions and the Sources of Galactic Cosmic Rays.

zur Erlangung des akademischen Grades eines
Doktors der Naturwissenschaften

von der Fakultät Physik des Karlsruher Instituts für Technologie (KIT)

genehmigte Dissertation
von

Dipl.-Phys. Matthias Albert Maria Weinreuter

Institut für Experimentelle Kernphysik (EKP)

Erstgutachter: Prof. Dr. Wim de Boer
Zweitgutachter: Prof. Dr. Thomas Müller
Betreuender Mitarbeiter: Dr. Iris Gebauer

Tag der mündlichen Prüfung:
28. Oktober 2016

Ich versichere wahrheitsgemäß, die Arbeit selbstständig angefertigt, alle benutzten Hilfsmittel vollständig und genau angegeben und alles kenntlich gemacht zu haben, was aus Arbeiten anderer unverändert oder mit Änderungen entnommen wurde.

Karlsruhe, 11. Oktober 2016

. . . .

(Dipl-Phys. Matthias Albert Maria Weinreuter)

Contents

List of Figures

List of Tables

List of abbreviations

B/C .... Boron over Carbon ratio

$^{10}Be/^9Be$ .... Beryllium ratio

$\bar{p}/p$ .... Antiproton over proton ratio

BR .... Bremsstrahlung

CL .... Confidence Level

CMB .... Cosmic Microwave Background

CNM .... Cold Neutral Medium

CR .... Cosmic Ray

DM .... Dark Matter

DRAGON .... (proper name)

DSA .... Diffusive Shock Acceleration

FFA .... Force-Field Modulation

GAC .... Galactic Anti-Center (opposing GC)

GALPROP .... (proper name)

GC .... Galactic Center

GCR .... Galactic Cosmic Ray

GMF .... Galactic Magnetic Field

GNP .... Galactic North Pole

GSP .... Galactic South Pole

HEALpix .... Hierarchical Equal Area iso-Latitude Pixelization

HI .... neutral atomic hydrogen

HII .... ionized atomic hydrogen

$H2$ .... molecular hydrogen

HIM .... Hot Ionized Medium

HMF .... Heliospheric Magnetic Field

IC .... Inverse Compton

ISM .... Interstellar Medium

ISRF .... Interstellar Radiation Field

LB .... Local Bubble

LOS .... Line Of Sight

MC .... Molecular Cloud

MF .... Magnetic Field

PDE .... Partial Differential Equation

PWN .... Pulsar Wind Nebula

QED .... Quantum Electrodynamics

QLT .... Quasi-Linear Theory

SA .... Shock Acceleration

Sync .... Synchrotron radiation

SN . . . . Supernova
SNR . . . . Supernova Remnant
TE . . . . Transport Equation
WIM . . . . Warm Ionized Medium
WIMP . . . . Weakly-Interacting Massive Particle
WNM . . . . Warm Neutral Medium
UHECR . . . . Ultra-High-Energy Cosmic Ray
UL (95%) . . . . Upper Limit (95% Confidence Level)
UV . . . . Ultra-Violet

Names of Experiments / Telescopes

ACE . . . . Advanced Composition Explorer
ACE-CRIS . . . . Advanced Composition Explorer (Cosmic Ray Isotope Spectrometer)
ACE-SIS . . . . Advanced Composition Explorer (Solar Isotope Spectrometer)
AMS / AMS-02 . . . Alpha Magnetic Spectrometer (02)
Chandra HRC . . . Chandra High Resolution Camera
CREAM . . . . Cosmic Ray Energetics And Mass
EGRET . . . . Energetic Gamma Ray Experiment Telescope
Fermi-LAT . . . . Fermi Large Area Telescope
HEAO-3 . . . . High-Energy Astrophysics Observatory (3)
HST . . . . Hubble Space Telescope
ISOMAX . . . . Isotopce Magnetic Experiment
PAMELA . . . . Payload for Antimatter Exploration and Light-nuclei Astrophysics

0.Introduction and Motivation

The field of cosmic ray physics is currently undergoing a fundamental revolution. With the launch of the AMS-02 detector in May 2011, a milestone in observing galactic cosmic rays has been reached: Never before had particle fluxes been measured at a few-percent accuracy. With analysis of AMS-02 data incoming, the world of cosmic ray transport models is shaken, as decade-old simplifications and accepted assumptions seem to come into conflict.

Indeed, the installation of AMS-02 on the International Space Station in 2011 came to pass nearly one century after this mysterious stream of high-energy particles was first discovered. When in 1911, an Austrian named Victor Hess decided to mount some electroscopes on a balloon, and an Italian named Domenico Pacini had the idea of plunge some undersea, it was a common idea in physics that radioactive decays in the Earth crust are responsible for ionizing radiation in the atmosphere. It then occurred to them that this radiation increased with altitude - hence, it was not terrestrial, it was of cosmic origin (or in Austrian terminology, *Höhenstrahlung*). It was confirmed by a German called Werner Kolhörster, who in 1928 could provide, that cosmic rays are indeed not actually radiation, but particles.

Then, an incredible avalanche of physical progress was fueled by the further observation of cosmic rays. Years before quantum field theory was established and man could dream of giant particle accelerators he would later build himself, cosmic objects had been speeding up particles already to inconceivable energies, providing a wealth of discoveries that had not been experimentally observable before. It lead to the discovery of the positron in 1932 (the first known representative of antimatter), the muon in 1937 (showing there was more than one leptonic family), the pion in 1947 (backing Yukawa's theory of strong interaction), plus the Kaon (the first known baryon containing a strange quark) in the same year. Without overstatement, the ideas produced by Hess, Pacini, Kolhörster and others did finally bring the dawn of our understanding of elementary particle physics, as the establishing of the Standard Model that is hold in high esteem today.

And yet, today it is not entirely known what these objects are - the *sources of cosmic rays*. For the twentieth century, simple models were sufficient to explain observational data with 30% uncertainty or more. A standard picture of cosmic rays has emerged, but with rising precision, many questions have been raised. Ultimately, explaining cosmic ray measurements is a very intricate enterprise, as not only the nature of galactic cosmic ray sources, but also *the nature of their transport* has to be understood, and these two are tightly linked.

One leading frontier in our current understanding of the universe is the question of what Dark Matter is made of. This elusive component permeates all of space, is known to amount to 84.5% of the total mass in the universe and has been shown responsible for rotary dynamics, velocity dispersion and the large-scale structure formation of galaxies.

Proposed by Fritz Zwicky in 1932 and established by Vera Rubin by over two hundred galaxy measurements in the 1970's, this hypothesis still has no comprehensive alternative to describe most of its attributed properties, yet no plausible correspondent in the established Standard Model has been proven. Considering the role of Dark Matter in galactic and cosmological phenomena, it is currently investigated for a potential signature in the local cosmic ray fluxes.

Thus, the advent of high-precision measurement as with AMS-02 currently or, hopefully, ISS-CREAM in the close future, brings an exciting time. As historically universal throughout Physics, rising accuracy of measurements inevitably leads to the abandonment, reappraisal or reinvention of held beliefs. For the last 50 years, crude approximations of the Milky Way could be applied to describe local cosmic ray measurements, but ultimately, the boundaries of this approach are reached.

Foremost example is the mystery of the energetic positron population, at an energy above 10 GeV. In 2009, the PAMELA mission first observed that the positron fraction of the cosmic ray leptons, $e^+/e^\pm$, shows a distinct rise towards higher energies - while prevalent models predict a steady decrease. As AMS-02 confirmed this measurement with unprecedented statistics in 2014, it now has become clear that previous state-of-the-art models can not account for the whole picture of cosmic ray propagation.

With modern space detectors, also a new observable of galactic cosmic rays has finally become determinable: Their *arrival direction*. Latest analysis of AMS-02 data reveals the anisotropic component of electron and positron fluxes in the energy range $[16, 350]$ GeV to be below 2%. This is generally taken to be a valuable discriminator between explanation approaches of the origin of energetic positron population: While the hypothesis of a *point source*, like pulsars, is expected to show an observable anisotropy, the hypothesis of a *distributed source* hypothesis, like Dark Matter annihilation within its smooth halo, do not carry this expectation.

The correlation between the arrival directions of cosmic rays and their galactic sources is a highly topical question because a single cosmic ray particle is an imperfect carrier of information: Details of its origin are washed out during its chaotic random walk throughout the Milky Way, and a statistical approach is required to understand their directions of arrival. Positrons experience strong energy losses as they travel through magnetic and radiation fields, which places close constraints on the distance of their source regions. This implicates that our models have to account for the *solar neighborhood*, which hosts a few hundred parsec wide structure called the the Local Bubble, to which very limited attention has been spent in the cosmic ray literature before. But *without understanding the local transport processes in the solar neighborhood, we can not understand the sources of the high-energy positron component.*

The hereby presented thesis is, to our knowledge, the first of its kind to examine the impact of the Local Bubble on cosmic ray transport models. We consistently study the combined effect on model predictions on electrons, positrons, protons, antiprotons, the

ratio of boron over carbon flux and the ratio of beryllium-10 over beryllium-9 isotopes, for which observational data exist. We give the model predictions of dipole anisotropy in leptonic fluxes, for which upper limits have been given by the Fermi-LAT collaboration, and of positrons relative to protons, for which we have current AMS-02 upper limits.

My thesis is structured as follows:

- Chapter 1 gives a comprehensive review of the Milky Way and the phenomena that are currently forming our understanding of cosmic ray transport. This especially reviews the understanding of cosmic ray acceleration mechanisms and the interactions during cosmic ray transport. We review current observations of the Local Bubble.

- Chapter 2 lays the theoretical groundwork for cosmic ray propagation. The cosmic ray transport equation is derived from first principles and the connection to dipole anisotropy is made. We present the numerical algorithm to solve the transport equation by the publicly available DRAGON code and discuss the analytical solution of a point-like source scenario.

- Chapter 3 introduces the reference transport model we further base our study on and shows that a non-uniform grid has to be implemented in DRAGON to allow for local transport models. For this reason, we modified this code and resubmitted the implementation to the scientific community as accepted from the original DRAGON authors. We discuss several astrophysical processes which are likely to play a role in local transport models and suggest 34 different scenarios of local diffusion and gas properties. The impact on the aforementioned cosmic ray observables is discussed.

- Chapter 4 investigates the pulsar hypothesis of the energetic positron component. Using an analytical approach, we build a number of five source scenarios of close-by pulsars, in agreement with the observational constraints of positron flux and dipole anisotropy. We implement local transport models and discuss the potential impact in light of the dipole anisotropy limits.

We summarize our findings and discuss the implications for the future of galactic cosmic ray model building in the chapter "Conclusion and Outlook".

1. Our Galactic Environment

"There are more things in heaven and earth, Horatio,
than are dreamt of in your philosophy."
– Shakespeare, Hamlet

This chapter is the summary of our phenomenological understanding of cosmic rays. In here, we will define the galactic stage on which our cosmic actors perform their nebulous play. This is a play that has been started over a hundred years ago, and yet many details - where cosmic ray particles are accelerated to close the speed of light, how the scenery in the Milky Way shapes their energy spectra, and how they finally arrive at Earth - still leave a multitude of questions about what happens. And in a figurative sense it is true that this is some giant piece of theater as we, as the observers, are ultimately bound to our terrestrial seat (or in very proximate space) in our attempt to figure everything out.

1.1. Observing Galactic Cosmic Rays

As we are limited to do measurements in close vicinity of the Earth and a single cosmic ray particle bears no memory of how it got there, the amount of information is mainly of statistical nature. So the physical quantities that can be measured (and are open then for interpretation, as described later on), are:

1. *Local spectrum of particle flux.* As many of the processes are energy-dependent, the overall *spectral shape* carries information of a particle species' history. In this regard it is remarkable that most particle species are described by a power law behavior $\sim E^{-\gamma}$ with spectral index γ over a wide range of energy. Some observables show a change in γ at a certain *break energy*, pointing to a fundamental change in what processes define the shape above and below the break. The low-energy range of any observation, $E \lesssim 1\,\text{GeV}$ (per nucleon) is usually hard to interpret because at that energies, the heliosphere[1] dominates particle propagation. The rising precision measurements in latest years gave us a rising ability to constrain *transport models*, that is, the entirety of assumptions that are made to predict cosmic ray phenomena.

2. *Chemical composition* measurements are useful to interpret the amount of particle interactions during the propagation of one cosmic ray population. This especially holds when one species is mainly of *primary* origin (present in the source accelerator) and the other one *secondary*, i.e. a product of a nuclear reaction or isotopic decay. Commonly studied are the ratios of B/C, $^{10}Be/^{9}Be$, $\bar{p}/p$ and $e^{+}/(e^{+}+e^{-})$. For isotopic ratios like $^{10}Be/^{9}Be$, precise measurement is more difficult, however, as a detector has to resolve the particle mass accurately, not only its charge.

---

[1]The heliosphere is the range of influence of the solar wind and magnetic field, and its effect on the flux of cosmic rays is explained below.

3. *Arrival directions* can, to a certain extent, hint to the distribution of the cosmic ray accelerator regions, or the large-scale distribution of cosmic rays. Cosmic ray arrival directions have been known to be remarkable isotropic up to the tera-electron volt (TeV) range, with the level of anisotropy at most at percent level. This is currently a field of precise investigation, because it is commonly held that from the arrival directions, implications about the cosmic ray sources can be inferred. As the galactic cosmic ray propagation is a mainly diffusive transport, however, this correlation is imperfect. In this thesis, we will further challenge this point.

4. The points above holds for charged cosmic rays. γ-rays (high-energy photons) on the other hands are not deflected on galactic scales, so one measures *line-of-sight integrals (LOS)* when observing the γ-rays coming from a certain direction - any direction of sight will contain the sum of everything produced somewhere in that direction. This can be used as a tracer of point-like source regions. Also, so-called *diffuse* γ-rays are the products of the interaction of cosmic rays with their environment during propagation, which, in turn, links the interpretation of γ-rays to the propagation model of the charged species.

1.2. The Milky Way: State of knowledge

"The study of origins is the art of drawing sufficient conclusions from insufficient evidence." - Allan Sandage

The Milky Way is a (barred) spiral Galaxy, consisting of an inhomogeneous rotating disc of about $15 - 30$ kpc in radius [1] that carries most of its visible material. This disc is home to about 10^{11} stars and in between, the *interstellar medium* (ISM), described below. For the ordinary human view, the Milky Way obscures most of its features – due to multiple reasons: the majority of interstellar phenomena is very faint; the structure is incomprehensibly vast and empty; most of its radiation is not easily accessible by the human eye; and, of course, we are an observer *inside*, living at about 8.3 kpc distance from its center and rotating around it with a cosmically tiny pace of ca. $230\frac{\text{km}}{\text{s}}$. Cosmic ray observation therefore enables yet another approach towards understanding the structure of the Galaxy, and especially towards our more local environment. In the following explications, we move from the grandest picture (the Universe) to the smallest (the Solar System) structures in which we live.

First, we review the current understanding of what our Galaxy is made. In short terms, next to the visible stars and the mysterious Dark matter component, these are the interstellar gas, dust, photonic radiation, magnetic fields and cosmic rays. Those components are described below and in section 1.3, we will illuminate how these environmental components differently affect cosmic ray propagation. A theoretical description of the mathematical framework behind cosmic ray transport will finally be given in chapter 2.

1.2.1. Formation of the Galaxy

As most of the matter that currently exists in the universe, the origin of the Milky Way lies in the very first second of the Big Bang. From a soup of quarks and leptons, antiquarks and antileptons, the temperature dropped below $T \lesssim 10^{12}$ K. Matter became to dominate the antimatter, known as baryon asymmetry, for reasons not yet understood. It was then cool enough for quarks to form protons and, by fusion with electrons, neutrons. After three minutes, the temperature reached $T \lesssim 10^9$ K, allowing protons and neutrons to undergo nucleosynthesis, producing the cores of Hydrogen and Helium (and only traces of Lithium and Beryllium). Nuclear fusion of heavier elements was impossible, then, as a higher density and temperature would have been required. Both quantities, however, were decreasing to about 17 minutes later, element production was disrupted altogether. In the time between 0.24 Myr and 300 Myr, then, little changed in the chemical composition of the universe - with $T \lesssim 3000$ K and matter density low enough, the nuclei were able to capture free-floating electrons (thus coined "recombination phase"), and subsequently the neutral gas was in a nearly homogeneous state, with small inhomogeneities remaining – as the product of inflation from these tiny quantum fluctuations in the earliest second.

Enduring gravitational pull, then, allowed agglomerations of matter (*protogalaxies* to gain concentration even with the universe expanding further, and at an age of about 150 Myr, the first objects formed that, by radiating strongly, reionized the gas again. The first stars are assumed to have formed at an age of about 300 Myr, consisting of hydrogen and helium, that, upon gravitational compression heated up until thermonuclear fusion became possible. This, for the first time, produced heavier nuclei (called *metals* by astronomers). When all the fuel for any fusion process is finally used up, further collapse is inevitable and the star is torn apart in a thermonuclear runaway *supernova* explosion, feeding back all heavier elements into the cloud[2], heating up and enriching the protogalactic cloud with metals. By further aggregation of many of these clouds, galactic progenitors could form that, over time, were able to dissipate energy in the contraction by electromagnetic friction so that under conservation of angular momentum, the gaseous material was cast into the rather thin disc. Galaxy formation is, to this day, an ongoing process even in the Milky Way, that continues to swallow dwarf galaxies. The famous galactic spiral arm patterns arose during this process through the percussions of smaller galaxies into the existing agglomeration, sparking up-and-down oscillations of the disc leading to density waves similar to giant curvilinear sound waves.

1.2.2. The interstellar medium (ISM)

In a full-grown galaxy like the Milky Way, the chemical composition seems to have settled into an steady state. From enriched gas clouds, new stars are born containing already heavier elements in their core, that are now able to produce even more heavy nuclei until

---

[2]these special kinds of SNe are called "pair-instability supernova". These come from low-metallicity stars with lighter cores than in the SNe common today, and release radiation pressure by efficient creation of electron-positron pairs. This has the effect of rapidly burning *all* of the star up, leaving no remnant and feeding back all heavy elements into the environment

nuclear fusion stops at ^{56}Ni, which decays to ^{56}Fe as the heaviest stable isotope[3]. When these stars reach their supernova state, its particle content becomes accelerated by the powerful shocks (see Fermi acceleration, below) together with the surrounding material, finally giving rise to a relativistic particle population: *these are then cosmic rays.*

The non-accelerated, thermal matter in the ISM is present in a broad range of phases, which are in thermal pressure equilibrium [2]. A short synopsis of these states is given now. For an overview of typical physical parameters, see Tab. 1.1 below, however, the level of detail given therein is not important for this brief outline.

- **Molecular Clouds (MC)**, which are the very coldest regions in the galaxy. Only at these very low temperatures, in the inner regions that are shielded from damaging UV radiation by the outer layers, the formation of molecules from interstellar atoms can take place. This detection was made first by radio spectroscopy, as radio waves travel through the surrounding regions quite unobstructed [2]. The far most abundant molecule naturally is H_2 which, however, is not visible in radio frequencies as there are no permitted transitions in this energy range. It is therefore mainly inferred from measurement of the second most abundant molecule, CO, which emits a $J = 1 \rightarrow 0$ rotational transition at 2.6 mm radio wavelength [3]. In the context of cosmic ray propagation, MCs are mostly relevant because these H_2-distributions provide dense material for interactions: They are thought to make up only $\leq 2\%$ of the total ISM volume, but about 40% of its mass [4].

- **Cold Neutral Medium (CNM)**, often called **HI clouds** for denoting atomic hydrogen in the unionized "I" state. It is mostly detected via the well-probed "21cm line", emerging from the hydrogen hyperfine structure: When the electron undergoes a spin flip from antiparallel to parallel with respect to the proton, the corresponding low-energy radio emission of 21 cm wavelength happens[4].
  Since 1974 [5] it is known that in the intermediate vicinity of the solar system there is a *HI cavity*, an underdensity of the CNM. This is accounted for by the *Local Bubble* [6], a local structure in the Milky Way (details given below) in which the expansion of hot gas pushed the surrounding neutral gas outwards, that is now residing in the overdense *Bubble Wall* regions.
  Similar to the colder MCs, HI clouds only contribute to the bottom $\leq 2\%$ of the total ISM volume. In mass, they are believed to make up another share of 40% [4].

- **Warm Neutral Medium (WNM)** also is mostly neutral hydrogen that exists in pressure equilibrium with the cold neutral phase. By that, their densities and temperature are inversely linked: $(n \cdot T)_{\mathrm{WNM}} \approx (n \cdot T)_{\mathrm{CNM}}$, see Tab. 1.1. This medium therefore takes up about 50% of the ISM volume and the remaining 20% of its mass. The majority of neutral hydrogen is in this phase. In our local neighborhood, there seem to be several warm clouds, and while the solar system currently might lie inside

---

[3]The one nucleus carrying a slightly higher binding energy is ^{62}Ne, but there is no efficient fusion chain available to produce this isotope.

[4]This is indeed a highly forbidden process, happening only once in about 11 Myr, but has the advantage that the 21-cm-photons can travel large distances mainly undisturbed.

one (the "Local Fluff"), we do not consider them relevant for cosmic ray transport due to their small size.

- **Warm Ionized Medium (WIM)** or **HII regions**, at about the same temperature as the WNM or slightly higher.
  Described according to the Saha-Langmuir equation[7], the degree of ionization in hydrogen in equilibrium is below 10% at these temperatures, so for these regions to be ionized, they need a strong source of UV radiation. These are found in the most massive of stars (classified as "O" or "B" star, or "early-type"), which are also the hottest (with an effective temperature of over 10^4 K). The UV radiation from those stars gets absorbed quickly in the surrounding hydrogen, but these ions constantly need to be re-ionized, as chance of recombination with a stray electron is large. By this balance, the HII region around such a star is very confined.
  While these formations pose regions in which the scattering of cosmic rays might be highly amplified (see [8] and references therein), the HII distribution generally enters numerical propagation models only in their increase in CR energy loss (see below).

- **Hot Ionized Medium (HIM)** forms the high-energy end of interstellar material. This phase is also called **coronal gas** as it was originally proposed [9] to exist in giant "galactic corona" around the galactic Disc, similar in physical properties to the Sun corona.
  Originally introduced to account for the stability of high-latitude HI clouds and galactic spiral arms – which would naturally expand at the speed of sound, but seem to be in pressure equilibrium – subsequent observations by OAO-3/Copernicus (1972) found this phase to be present in most parts of the galactic Disc, as well. It was the suggestion [6, 10] that this gas is heated in the blast waves of supernovae. Nowadays it is believed that $\sim 30 - 80\%$ of the ISM volume is filled by this phase, which is only to be sustained against radiative cooling by the high occurrence of supernova explosions. Coronal gas is detectable mainly through highly ionized oxygen and nitrogen and their subsequent UV emissions (OVI and NV lines), as these excitations are only common in the hottest environments. Another important tracer is the 0.25 keV soft X-ray radiation, which is the thermal radiation emitted at these temperatures. A general uncertainty about the detection of these lines, however, is given by the fact that UV and X-ray lines are blocked by the Earth atmosphere, which requires measurements to be done in space (e.g. sounding rockets), generally being detrimental in spatial resolution.
  By interpreting a Soft X-Ray component seemingly coming from every direction, it was discovered that the Sun lies inside the Local Bubble, a vast region further to be described below.

Furthermore, there is a solid phase – **interstellar dust** – composed of grains (few μm) mostly of carbon- and silicate-rich molecules, but complex molecules as polycyclic aromatic hydrocarbons have also been found. The dust distribution is found to follow the HI distribution. The formation of dust grains is currently not well understood. Dust layers play a role in shielding molecular clouds from radiation, thus supporting the formation of stars. However, in the context of cosmic ray propagation the presence of the dust is only relevant because of its contribution to the interstellar radiation field: Optical radiation is absorbed and heats up the dust (to about 10–100 K), which then gives rise to infrared photon emissions as the thermal blackbody radiation. This is more efficient for shorter wavelengths, thus leading to *reddening* of the starlight. From this effect ("dust extinction"), the column density in neutral hydrogen can thus be inferred, a tool which was recently used to study the gas distribution in the solar neighborhood (see Figs. 1.23, 1.22)

Figure 1.1. The Pillars of Creation, a Molecular Cloud with a high star birth rate, inside the Eagle Nebula, a glowing HII nebula. [11]

It is a remarkable fact of the galactic dynamics that the gaseous phases are in a constant state of metamorphosis, as the following cycle demonstrates: Molecular clouds can only form when matter accumulates that is sufficiently dense to shield the molecules from radiation of UV energy and above, as they would get dissociated otherwise. Again, these are *star birth* regions (see Fig. 1.1) because only there, the sufficient density for star formation can be reached. Molecular clouds tend to seek balance between their gravitational pull inwards and magnetic pressure outwards, but short-scale fluctuations like a traveling shock wave can disturb this balance, allowing dense cores to compactify to an extent at which nuclear fusion can take place - the birth of a star. After multiple stars are created, their combined stellar winds reheat their surrounding, and finally, their supernova explosions release giant volumes of coronal gas into the interstellar medium again. A special case of this is

	HIM (Halo)	HIM	WIM	WNM	CNM	MC
temperature T (K)	2×10^6	10^6	8000	6000	100	15
Volume filling factor	20-80%		$\leq 2\%$	50%	$\leq 2\%$	$\leq 2\%$
Mass fraction	$\leq 1\%$	$\leq 1\%$	$\leq 1\%$	20%	40%	40%
speed of sound v_S (km s^{-1})	130	90	8	7	1	0.35
particle density ρ_{Gas} (cm^{-3})	10^{-3}	4×10^{-3}	0.1	0.4	30	$10^2..10^6$
mean free path λ_{mfp} (cm)	4×10^{19}	$2 \times 10^{1}8$	6×10^{12}	8×10^{11}	3×10^6	10^4
magnetic field B_{reg} (μG)	5	2	5	5	5	15
plasma β	0.28	3.5	0.11	0.33	0.42	0.046
degree of ionization	≈ 1	≈ 1	0.01..0.05	0.01..0.05	10^{-3}	$10^{-8}..10^{-6}$
damping	collisionless	collisional	collisional	ion-neutral	ion-neutral	ion-neutral

Table 1.1. Typical parameters for different ISM phases. Phases are described in the text, details in [2, 4, 12]. "Plasma β" is the ratio of kinetic gas pressure to magnetic pressure.

superbubble creation, which is important for our direct local environment in the ISM, so an outline is sketched in appendix A.1.

Additional to the matter components just explained, the Milky Way holds further a large-scale magnetic field, and the interstellar radiation field.

1.2.3. The galactic magnetic field(s) (GMF)

Magnetic fields hold an important role in galactic dynamics, considering that most of the ISM is ionized. Owing to the absence of magnetic monopoles, magnetic fields are very sustainable (up to the canceling of opposite fields, "magnetic reconnection"). In fact, magnetic pressure is crucial for the stability of the Galactic Disc, as it acts as a counterforce against its gravitational collapse. Furthermore, it is accounted a driving force in the large-scale evolutionary processes like the formation of spiral arms and ISM dynamics [13], as well as the smaller-scale transport of angular momentum required for the collapse of star forming regions [14] and dynamics of the ISM.

In most astrophysical conditions, the ISM plasma can be taken as a perfectly conducting fluid. Then it arises from Ohm's law and Faraday's law of induction [15], that the magnetic flux can not change in a way perpendicular to the movement of the fluid. This is *Alfvén's theorem* [16], it is said that the magnetic field is "frozen in" the matter, thus accompanying its movement (or vice versa, if the magnetic pressure becomes large).

The GMF is actually the superposition of various magnetic fields over a wide range of scales. It can be overall described as composition of two fields:

Turbulent magnetic fields: From Alfvén's theorem, it directly follows that the turbulent movement of the gas causes a significant small-scale random component of the magnetic field. For illustration, Fig. 1.3 shows the course of small-scale magnetic field orientation in a view of the Galactic Disc, superimposed on the density of dust grains. Magnetic turbulence becomes amplified by several mechanisms, as magnetohydrodynamical (MHD) instabilities at phase boundaries, the compression of magnetic fields by supernova shocks and stellar winds, or a self-generation effect called the small-scale dynamo (further reading e.g. [17]).

The mathematical description of turbulent fields is commonly done by spectral decomposition into MHD waves (magnetosonic and Alfvén waves, see. appendix A.3). Interactions of these MHD waves lead to so-called *turbulent cascades*, the mixture of magnetic fields of different spatial scales. This causes a shift of spectral energy between larger-scale and smaller-scale modes: Energy can be removed from the turbulent field by wave damping mechanisms, or, at very small scales (high spectral energy), thermal dissipation into heat energy.

For the scope of this work, it is very interesting for it to have been observed [18] that the turbulent magnetic field in the so-called *HI shells of superbubbles* is concentrated in

filaments of large magnetic pressure. This might play a role in cosmic ray propagation not considered before, and is revisited in chapter 3, where our local environment is discussed.

Regular large-scale field: There seems to be an ordered magnetic component in the Milky Way, following the large-scale structure of the galactic spiral arms (reversing its direction in the inter-arm regions) [13]. It is of about $2 - 6\,\mu$G strong. Similar shapes are also observable in distant galaxies, as demonstrated in Fig. 1.4 for the galaxy IC342 which we can see directly perpendicular to its disc. It is remarkable that the magnetic spiral structure is even seen in galaxies which are not visibly showing these structures, i.e. are not classified as Spiral Galaxies at all. The Milky Way GMF, as it is currently understood, is sketched in Fig. 1.2. The large-scale field currently is believed to be largely attributable to the α-ω-*dynamo* effect, by which the differential (non-uniform) rotation of the galaxy causes the magnetic field to stretch in azimuthal direction (ω effect) and convection forces transforms this flow back into vertical flow (α effect). This dynamo is then further driven by the feeding of smaller-scale energy (creating order out of chaos). While the exact physics of the α-ω−dynamo are not completely understood, this is also believed to be the driving mechanism behind the geomagnetic and solar magnetic field.
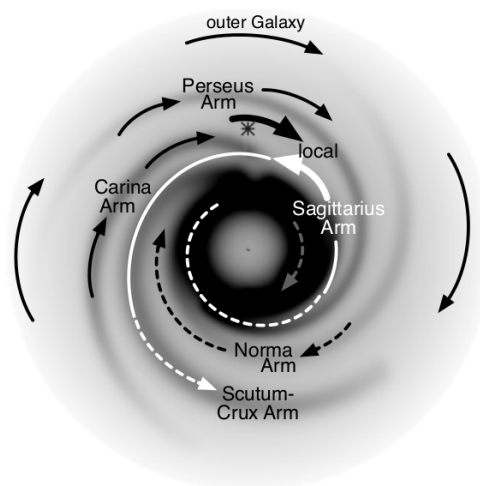
Figure 1.2. Model of the large-scale magnetic field in the Milky Way disc [19], based on Faraday rotation measure of pulsars and extragalactic sources. The bold arrows in the local and Sagittarius Arm are the only widely accepted magnetic field directions. The long white arrow in this model is the only further spiraling direction; other black arrows follow circular paths. Dashed arrows are given with less certainty than solid ones.

Measurement of the large-scale GMF is one of the showcase examples on what methods one has to resort to determine a vast structure from a single, embedded location. Magnetic field measurements thus derive combined information, gained from as many independent observables as possible. To gain directional information, one searches for several aspects of photonic emission over a broad range of wavelength. A review is given in [19], which names five different techniques, applicable for different spatial scales: For example, inside compact molecular clouds the Zeeman splitting (due to the magnetic coupling of the GMF

to the magnetic moments of the molecules) can be a direct tracer, while much gathered information about the spiral arms and the Galaxy as a whole is inferred from the Faraday rotation measurement, a quantity designing the amount of rotation that linear polarized light (emitted e.g. by pulsars or external galaxies) underwent, a product of the thermal electron density and overall magnetic field strength in each line-of-sight direction. Furthermore, cosmic ray electrons are emitting Synchrotron radiation in these fields (see below).

The energy density of the total magnetic field is observed to be of same order $\sim$ 1eV as the thermal motion of the interstellar matter. A large-scale electrical field is not expected, a consequence of the high conductivity of the ISM.
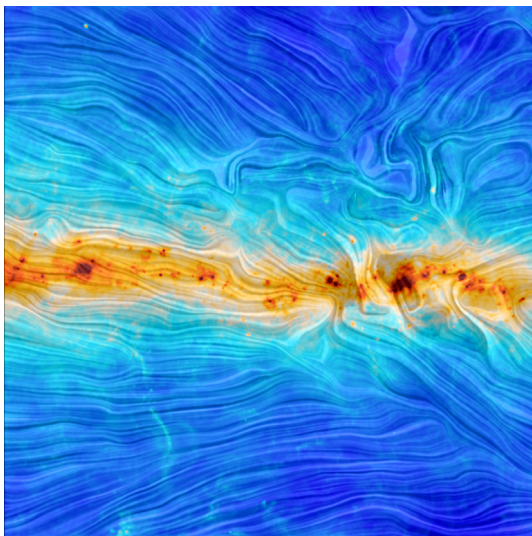
Figure 1.3. Turbulent magnetic field orientations (white lines) superimposed on the dust grain distribution. Shown is a region in the Milky Way disc in direction of the Carina nebula (seen as the structure to the right). [20]
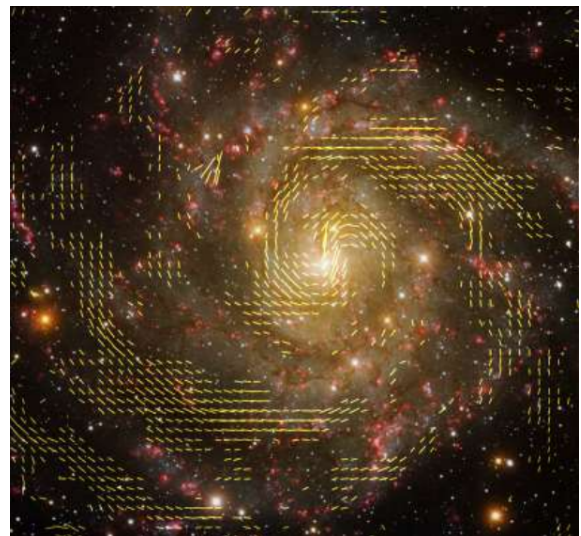
Figure 1.4. The face-on Spiral Galaxy IC342, with polarization vectors (yellow arrows) of the magnetic field superimposed [13]. This clearly shows the alignment of the magnetic field with the spiral arms.

1.2.4. The interstellar radiation field (ISRF)

The interstellar gas and dust also is in constant dynamical exchange with the interstellar photons, the ISRF: The state of ionization and thermal states of gas and dust (e.g. photoelectric heating) is shaped by the constant absorption and emission of photons. For example, the continuous effect of UV radiation acting on a molecular cloud can lead to its total disintegration, or trigger star formation. Also, radiation pressure acting against the higher-latitude gas causes these layers to outflow, giving rise to galactic winds (described below).

Three contributions play a role for cosmic ray interactions. These hold roughly the same amount of energy density, but at different frequencies (depicted in Fig. 1.5).

- Cosmic Microwave Background (CMB), the direct relic of the Big Bang photon field cooled down to $T \approx 3\,K$. As a consequence, it is distributed very isotropic nowadays. Its peak frequency is at $\nu \sim 1..2 \cdot 10^{11}\,\text{Hz}$ ($\omega \sim 1\,meV$)

- Starlight, mostly in the visible range and the ultraviolet (UV) range, with peak frequency at $\nu \sim 10^{15}\,\text{Hz}$ ($\omega \sim 1..2\,\text{eV}$). This component is rather easy to trace and shows a steady rise towards the Galactic Center.

- Dust emissions, caused by heating by absorbing optical/UV radiation and then re-emitting in the infrared range (as described above). It mainly peaks at about $\nu \sim 5..6 \cdot 10^{13}\,\text{Hz}$ ($\omega \sim 10\,\text{meV}$), plus some distinct line spectra at higher frequencies. It is roughly coupled to the HI distribution.
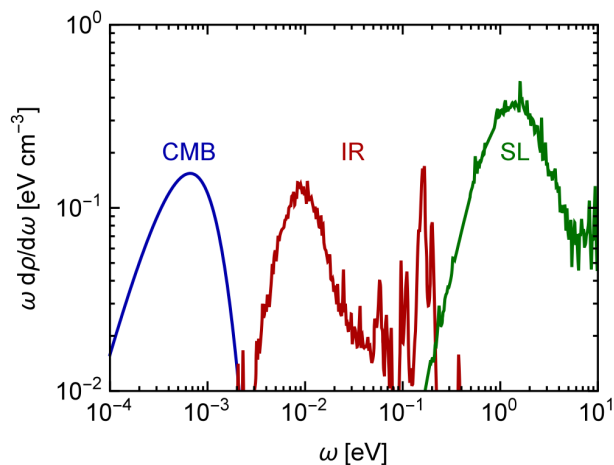
Figure 1.5. The spectral density of the interstellar radiation field near the Sun [21, 22]. The CMB (blue), dust emission / infrared (red) and starlight (green) components are the only photon fields considered relevant for CR propagation.

Other photonic fields are neglected for cosmic ray interactions, as their contribution in energy density is already one order below or less. These include nebular emissions (from molecular and fine-structure transitions), radio waves, Synchrotron radiation and γ-rays (the latter are usually counted as a part of the *uncharged cosmic ray* population) The next largest contributor to the cosmic photon fields are nebular (molecular and fine-structure) emissions, however already about one order weaker in average energy density, so their contribution to the ISRF is neglected. that are high in energy, but too low in overall density to hold a large portion of the ISRF energy density.

1.3. Cosmic Rays (CR)

In the previous section, we have gathered the galactic conditions significantly shaping the overall movement and kinetics of the cosmic ray population. We can thus now continue to discuss the *phenomenology* of cosmic rays ("CR" from here on) and their transport processes. As mentioned before, we keep the *theoretical* outline for the next chapter.

Fig. 1.6 (left) gives a combination of all-particle CR flux measurements, over a 12-decade energy range as present in 2013 [23]. The spectrum is displayed in log-log scale to emphasize the power-law shapes, and scaled with an energy factor E^2 for better display (a customary habit in CR physics). In fact, the overall spectral shape is strikingly well described by a power law dependence over wide ranges in energy, with some breaks that are commonly called the "knee" ($E \sim 3 \, \text{PeV}$), the "second knee" ($E \sim 0.4 \, \text{EeV}$) and the "ankle" ($E \sim 4 \, \text{EeV}$. Above ($E \sim 50 \, \text{EeV}$), a cutoff in CR flux is predicted because at these energies, collisions $p + \gamma_{\text{CMB}} \longrightarrow \Delta^+ \longrightarrow n + \pi^+ / p + \pi^0$ with the ubiquitous Cosmic Microwave Background photons become possible, exciting a Δ^+ resonance ("Greisen-Zatsepin-Kuzmin limit"). This reaction is efficient enough to decelerate any faster particles, although surprisingly, some events have been measured above.

For comparison, the topmost energies of man-made accelerators available at that time are shown (red arrows). With steepingly decreasing flux, it of course becomes increasingly more difficult to precisely observe the CR fluxes at high energies: Observed at the Earth surface, the particle flux at the energy of the knee is about $\sim 1 \, \text{particle}/(\text{yr m}^2)$, and down to $\sim 1 \, \text{particle}/(\text{century km}^2)$ above the ankle. These are *ultra-high-energy cosmic rays* (UHECR) observed with ground arrays detectors like KASCADE, the Pierre Auger Observatory, or the antarctic IceTop and (underground) IceCube experiments. Below the knee, however, it is viable to use space-born detectors, the most recent missions being PAMELA on the space station Resurs-DK1 and the currently-measuring AMS-02 on the International Space Station (ISS). For galactic cosmic rays (GCR), it is theorized that there is *no "PeVatron"*, no object or mechanism capable of accelerating CRs to PeV energies (although this theory is currently under debate). The observation and interpretation of galactic and extragalactic cosmic rays are actually nearly separated fields, with this work only concerned about the propagation of GCR at energies below 1 TeV.

Before the discussion of the propagation of galactic cosmic rays, some insight follows already from three basic observations:

1. the mean thermal energy density of the gas, the magnetic and photonic energy density, and the cosmic rays is all in *equipartition* $\approx 1 \frac{\text{eV}}{\text{cm}^3}$. This is interpreted as a condition of equilibrium that could have been acquired by enduring interactions between all components. Therefore, the galactic environment can be assumed not to change significantly during the time of source injection and observation.

2. Comparing the chemical composition (element abundances) of cosmic rays (Fig.[24]) with the local galactic abundances - as measured in meteorites and inferred from observation of the solar photosphere [25] - showcases: *Primary* elements (red ones) show good agreement because the fusion processes inside the sun are the same as
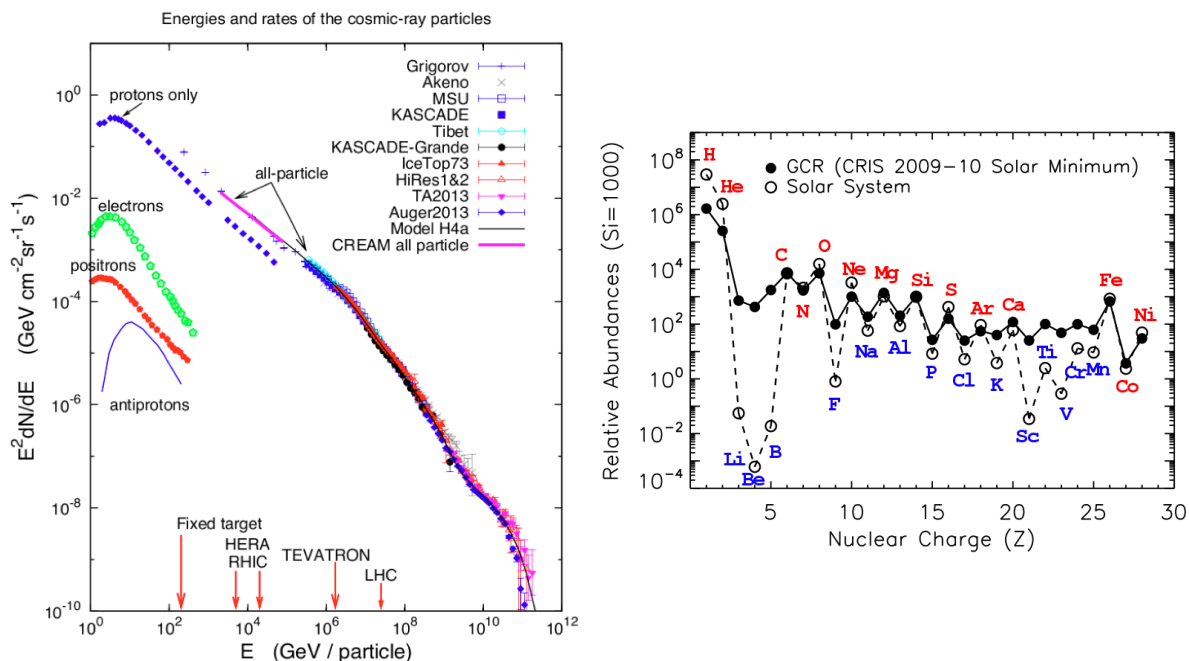
Figure 1.6. Left panel: Cosmic ray spectrum measurements [23]. The spectral features are explained in the text. Data of lepton and antiproton components are as measured by the PAMELA experiment. Energy scales of collider experiments are shown for scale (red arrows). **Right panel:** Relative chemical composition seen in CRs (black) compared with local abundance measurements in the Solar System (hollow), normalized at 10^3 for Silicon [24]; marked red are primary, blue are secondary particle species.

these enriching the cosmic ray sources, while *secondary* elements are produced after the CR have left the primary acceleration sites.

3. Naively considering a free stream of CR, directed outwards from the Galactic Center, where significantly more material is concentrated, would imply cosmic rays to be rather young (as they travel nearly at the speed of light $c \approx 0.3\frac{\text{pc}}{\text{kyr}}$, they would be on average 10..30 kyr old. This contradicts isotopic measurements (e.g. of ^{10}Be and ^9Be, as explained below), which imply a residence time at the Myr scale. Their trajectory must be considerably longer and this advocates the idea of a random-walk in which frequent scattering causes particles to change course, described as *diffusive propagation*.

At this time, there is by no means a *standard model* of CR propagation, but the basic observations motivate what is commonly referred to as a *standard paradigm*: Cosmic rays are first accelerated in sources, from which they undergo diffusive scattering throughout the Galaxy, bounded by a Galactic Halo region beyond which they freely escape. Up to a certain height over the disc, there are interactions with the gas to account for. The exact details of the astrophysical processes are then up to the level of model complexity, ranging from very reduced setups as depicted in Fig. 1.7 to advanced models as presented in chapters 2 and 3.
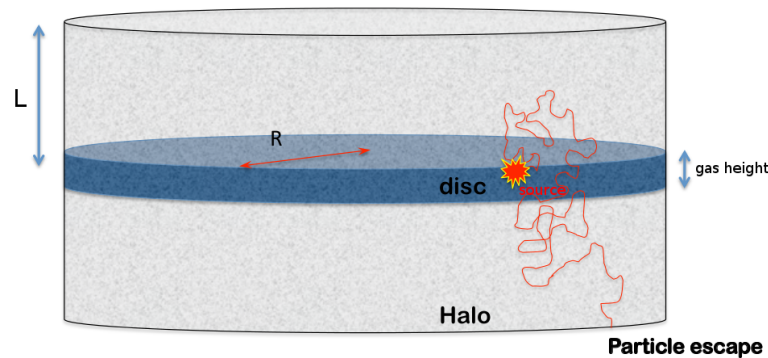
Figure 1.7. Simple transport models of Galactic cosmic rays are reduced to the basic requirements of the standard paradigm: their acceleration in *sources*, interactions with the *gaseous disc*, and the extended diffusion through the *Galactic Halo*, at whose boundary they escape into intergalactic space. This boundary defines a *propagation box* of half-height *L* and radius *R*. [26]

We now give a review of the range of astrophysical phenomena that are currently embodied in the standard paradigm. Afterwards, we will return to a description of our solar neighborhood in the Galaxy and discuss the possible effect of our local environment, the Local Bubble, on CR propagation in our direct vicinity. This is then the topic of this work, which has not been investigated before.

1.3.1. Acceleration of cosmic rays

While it is still under current debate, which galactic environments should in total be accounted for in providing the source cosmic ray population, and especially, what their maximum acceleration power is, there are two widely accepted mechanisms suited to explain the acceleration of the large part of galactic cosmic rays. These are named *first-* and *second-order Fermi acceleration* after Fermi's original 1949 paper [27] in which the notion of "collision against an irregularity in the cosmic field" was introduced. It might be noted, that as magnetic fields don't perform work, any increase in kinetic energy always requires an electrical field - and as there is no such large-scale field, the presence of electric fluctuations is indispensable for any acceleration [4]. In the current picture, these "irregularities" are identified as turbulent magnetohydrodynamical wave fields, which are ubiquitous throughout the Galaxy (see above under GMF). Each single collision brings then a statistical change in energy which can be either positive or negative, but the collective exchange ultimately heads for statistical equilibrium, which means net energy gain for the CR population.

First-order Fermi acceleration is a mechanism applicable in an environment of a strong, supersonic shock. A *shock* is a coherently moving phase transition, i.e. a discontinuity in pressure, density as well as velocity with respect to the surrounding medium. With v_{shock} being the group velocity of the shock front, a singular scattering upstream (see Fig. 1.8) brings an energy gain, averaged over all possible scattering angles:

$$\Delta E \propto v_{\text{shock}} E \qquad (1.1)$$

For acceleration to CR energies of the GeV and above, a CR particle has undergo many such energy gains. With the surrounding sufficiently magnetized, this can be accomplished by frequent scattering back and forth the shock front (see Fig. 1.8). As a result, this is most efficient if the particle's gyroradius is comparable to the spatial scale of the shocked region, while slower particles are overrun by the shock movement and leave the shock upstream. The maximum energy for a particle of charge Z to be reached, if the shock region has an extension of ΔR and mean magnetic field B, is then

$$E_{\mathrm{max}}/(\gamma eZ) \lesssim B \cdot \Delta R , \qquad (1.2)$$

idealized if the acceleration works completely efficient. This process is also called **diffusive shock acceleration** (DSA) for the above reason. It is called "first-order" Fermi mechanism because there is a first-order dependence $\Delta E \propto v_{\mathrm{acc}}^1$ as opposed to the second-order scenario presented next.

Second-order Fermi acceleration can take place everywhere in the galaxy where turbulent magnetic fields move as a coherent packet[5] versus the background magnetic field. These can be the product of distant supernova shocks, stellar winds or chaotic instabilities, or many more, but the details do not matter, as slowly moving magnetic perturbations are omnipresent in the ISM. In contrast to the first-order mechanism, there is less confinement to small regions of space necessary, no "shocked" environment is required. This is also called *stochastic acceleration* (SA).

The net energy gain per collision is then of *second* order in propagation speed of the magnetic turbulences v_A ("Alfvén velocity"), see the sketch in Fig. 1.9,

$$\Delta E \propto v_A^2 E . \qquad (1.3)$$

It is worth remarking that this difference in order, quadratic v_A^2 versus linear v_{shock}^1 is often claimed to be the reason that DSA is per se a much more efficient process. This is a fallacy, as the first-order DSA works only with a large number of crossing the shock wave. Under this circumstance, another dependence $\propto v_{\mathrm{shock}}$ enters the energy gain term, and as

$$\left(\frac{\Delta E}{E}\right)_{\mathrm{DSA}} \propto v_{\mathrm{shock}}^2 \qquad \text{vs.} \qquad \left(\frac{\Delta E}{E}\right)_{\mathrm{SA}} \propto v_A^2 , \qquad (1.4)$$

the real reason is only that the shock velocities as observed in SNR surroundings, $v_{\mathrm{shock}} \sim 20.000 \frac{\mathrm{km}}{\mathrm{s}}$, are multiple orders above the stochastic movement of the turbulent magnetic fields, $v_A \sim 30..100 \frac{\mathrm{km}}{\mathrm{s}}$. DSA is considered the main process in the initial *source* acceleration. SA in contrast is possible anywhere throughout the Galaxy and thus plays a role in reacceleration during propagation.

---

[5]This is sometimes described a "magnetized cloud", but there does not need to be a actual (gaseous) cloud.
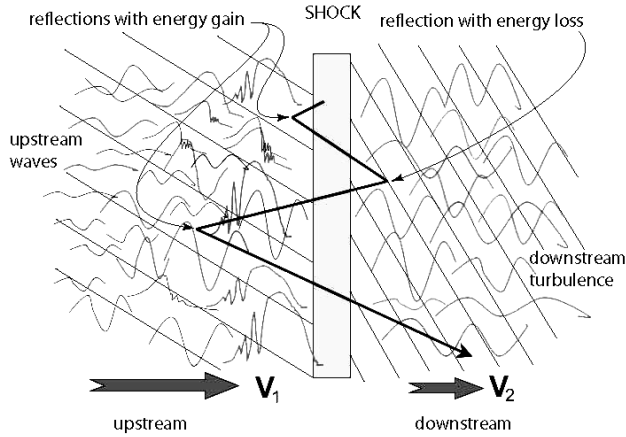
Figure 1.8. Diffusive shock acceleration (First-order Fermi acceleration) happens when CRs cross a moving shock ($v_{\text{shock}} = v_1 - v_2$). By diffusive scattering, the process can repeat many times, until the shock dissolves.
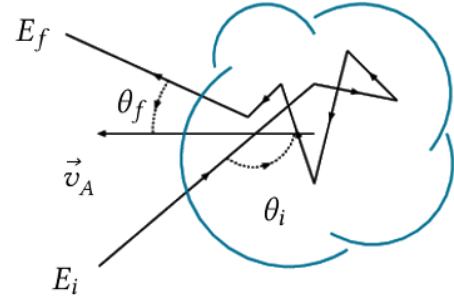
Figure 1.9. Stochastic acceleration (Second-order Fermi acceleration) happens when CRs enter magnetic turbulent structures of relative movement velocity v_A. This is a reacceleration process during propagation.

1.3.2. Power-law injection spectra

The acceleration mechanisms presented above are favorable because they predict a plausible shape of the *injection spectrum*, i.e. the spectrum CR particles assume directly after leaving the acceleration region. This is likely to be a power-law $\frac{dN}{dE}(E) \sim E^{-\alpha}$, as the locally measured CR spectra also show such shapes. Consider an acceleration process linear in energy, combined with a fixed chance of escape (constant in time), into the interior of the shock/cloud region, where little further energy gain takes place. This defines an acceleration time scale τ_{acc} as $\left(\dot{E} = \tau_{\text{acc}}^{-1}E\right)$, and an escape time scale τ_{esc} defined via $\left(\dot{N} = -\tau_{\text{esc}}^{-1}N\right)$. In total, the injection spectrum is

$$\frac{dN}{dE} = \frac{dN}{dt}\bigg/\frac{dE}{dt} = \left(-\tau_{\text{esc}}^{-1}N\right)\Big/\left(\tau_{\text{acc}}^{-1}E\right) = \left(-\frac{\tau_{\text{acc}}}{\tau_{\text{esc}}}\right) \cdot \frac{N}{E} \tag{1.5}$$

$$\frac{dN}{N} = \left(-\frac{\tau_{\text{acc}}}{\tau_{\text{esc}}}\right)\frac{dE}{E} \tag{1.6}$$

$$N \propto E^{-\tau_{\text{acc}}/\tau_{\text{esc}}} \tag{1.7}$$

$$\Rightarrow \frac{dN}{dE} \propto E^{-\tau_{\text{acc}}/\tau_{\text{esc}}-1} \tag{1.8}$$

This consideration is, again, already featured in Fermi's 1949 publication [27]. This feature is one of the important reasons why today, these are still considered valid. However, these are simple arguments that do not give a solid prediction of the actual *injecton index* $\alpha = (-\tau_{\text{acc}}/\tau_{\text{esc}} - 1)$. For protons, generally a value $\alpha \sim 2.1..2.3$ is considered. However, some transport models account for the possibility that the index is not constant over the whole energy range, by allowing multiple *injection breaks*, in between which $\alpha \sim 1..3.5$ might be adopted. Such breaks in injection spectrum might account for

certain inefficiencies in the acceleration mechanism, or over-efficiencies in the confining mechanism, or they can overall be seen as an *effective* injection spectrum, that is containing multiple source types of different power-law injection.

1.3.3. Sources of primary cosmic rays

We might now consider the nature of the *sources*, i.e. the sites of primary acceleration ("injection"). As demonstrated in Fig. 1.6 (right), primary CR components are isotopes that are synthesized in typical stellar fusion reactions (as proton-proton chain fusion, CNO cycle, alpha and triple-alpha processes, ...). These particles can either be produced in the accelerator themselves or be already present in the ISM, as ejected from stellar winds or as thermalized relics of Myr-old supernovae remnants. There are then several candidates inside our galaxy considered powerful enough to accelerate to the TeV scale. As estimated in (1.2), such a source region must either be large or equipped with an immense magnetic field.

1.3.3.1. Supernova Remnants (SNRs)

A supernova, the violent explosion occurring with the death of a star, releases an enormous amount of energy as a blast wave into the surrounding gas and dust, typically of the order 10^{44} J. The process of SN evolution is sketched in appendix A.1. They develop strongly compressed and magnetized shocks, remaining for thousands of years after the actual supernova has faded after a few years. The so-called *supernova remnants* (SNR) are deemed the most significant site of galactic cosmic ray acceleration, as they meet the criteria required for acceleration up to several TeV energies. The long-standing shock structures allow for a efficient diffusive shock acceleration (see above). Secondly, they appear with a galactic average frequency of about $\frac{1}{30\,\text{yr}}$, giving an energetic argument as this meets the order of power estimated to sustain the overall CR energy density (extrapolated from the local energy density of $1\,\frac{\text{eV}}{\text{cm}^3}$:

$$P_{\text{SN}} \sim \frac{10^{44}\,\text{J}}{1/30\,\text{yr}} \sim 10^{35}\,\text{J/s} \quad \gg \quad P_{\text{CR}} \sim 10^{33..34}\,\text{J/s} \;. \tag{1.9}$$

For a third reason, they automatically account for the chemical composition of primary cosmic rays. Debate has not settled, however, how the galactic SNR distribution exactly looks like. While there are 294 SNR cataloged in Galactic longitude l and latitude b, as seen in Fig. 1.10, their exact distance yet to be determined.
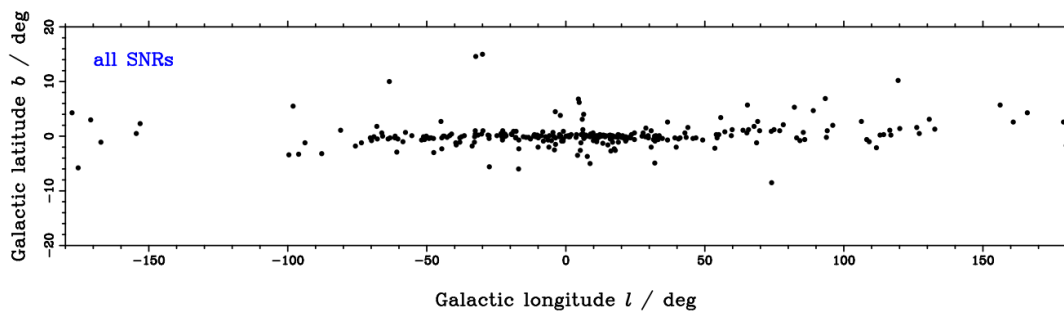
Figure 1.10. The distribution in galactic longitude *l* and galactic latitude *b* (*b* = 0 is the Galactic plane) of 274 SNR in the Green Catalog, [28]. Since 2014[29], 20 more SNRs have been included.

The distance of a single SNR might for example be [30] estimated by the amount of HI absorption in their light, but this requires then knowledge of the gas distribution, which especially leads to uncertainty in the inner Milky Way region. Several source distributions, [30, 31, 2, 32, 33] (showed in Fig. 1.11), have been constructed in order to reproduce observations, e.g. the EGRET γ-ray data [34] or radio pulsar measurements [33]. which take the maximum to lie about $R \sim 3..4$ kpc from the Galactic Center, coincident with the maximum of the molecular H_2 distribution,

Figure 1.11. Suggestions of SNR distributions, showcasing the uncertainty coming from distance measurements. References in text.

as well as the location of *OB* associations. Most SNR are usually believed to lie within galactic heights $|z| < 100..200$ pc near the galactic plane, so that high-latitude pulsars in Fig. 1.10 are rather close to the Sun.

One of the photogenic showpieces of SNR is the Crab Nebula (Fig. 1.12). As its associated supernova already was observed by Chinese astronomers in the year 1054, it is now one of the most studied extrasolar objects. It is also very illuminative because the product of its core-collapse is a pulsar (called PSR B0531+21) which is still very active, as revealed by X-ray observations such as by the Chandra space telescope, but also in the optical range as backed by ROSAT data [35]. Fig. 1.13 shows this pulsar inside its wind nebula (see next paragraph), visible at the bright dot in the center, of which two jets emerge perpendicular to an accretion disc. This pulsar is especially interesting as very few pulsars have been recorded in human history since their creation, e.g. their age and total energy output can only roughly be estimated.
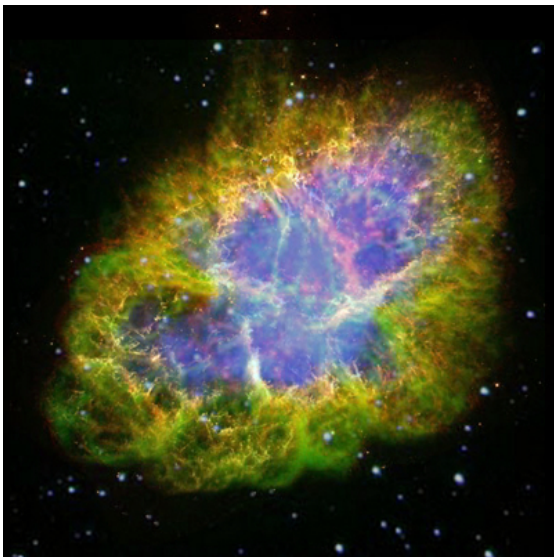
Figure 1.12. The Crab Nebula, a SNR, as seen in the optical range. [36]

Figure 1.13. The Crab PWN, seen inside the Crab Nebula (Fig 1.12) in X-rays. [37]

1.3.3.2. Pulsars and Pulsar Wind Nebulae (PWN)

Pulsars are highly magnetized, fast rotating neutron stars – as a leftover from a massive stars' core collapse. The large gravitational in-fall squeezes electron and nucleons together $\left(p+e^- \longrightarrow n+\nu_e\right)$ until mostly neutrons are left. The collapse only comes to a hold because the number of quantum mechanical states is limited: Due to the fermionic nature of neutrons, the Pauli principle prohibits two neutrons to share the same state. Neutron stars are thus immensely dense *degenerate matter* $\left(\text{density } \sim 3..6 \cdot 10^{17} \, \text{kg} \, \text{m}^{-3}\right)$ and occupy only a sphere of a few 10 km radius. However, this degenerate state only exists in the very core of the neutron star, while towards the surface, heavier nuclei can be left in the star like doped impurities, and the surface is covered with residual electrons. The star is rotating heavily, due to the conversation of angular momentum during the compactification: In the end, the embedded charges rotate at velocities up to $0.7c$. This heavy rotation of charges creates the *magnetosphere*, pictured in Fig. 1.14. Due to the immense strength of this electromagnetic field, e^- escape the neutron star surface, and then move inside the so-called *light cylinder* (for some directions, closed field lines back to the neutron star surface are possible, while for other directions, these would contradict the speed of light limitation, so particles can escape). Thereby, they are radiating *curvature radiation* photons (Bremsstrahlung in the extremely curved pulsar magnetosphere). In this environment, these can directly seed an electromagnetic cascade creating $10^4..10^5$ $e^\pm$ pairs from a single surface e^- [38].

As pulsars are born into SNRs, they are surrounded by the subrelativistically expanding supernova blast wave. The first relativistic $e^\pm$ are then thought to impact the blast wave from the inside, and by that, a *termination shock* is created, traveling back inwards to the neutron star. This termination shock is it, then, that can then accelerate further $e^\pm$ pairs up to TeV energies [39]. The region between the termination shock and the outer SNR

ejecta is called the Pulsar Wind Nebula, shining from the hot, accelerated leptonic pulsar wind (Fig. 1.13).

The pulsar theory of CR acceleration is supported by the detection of GeV-γ-ray point sources identified as pulsars [40]. Such an acceleration of γ-ray would need an environment as described above and would subsequently also predict the highly energetic leptons just mentioned. The total power injected into CRs is also estimated to be $P_{\mathrm{PWN}} \approx 10^{34}$ J/s [40], but only accelerating primary electrons and positrons, no nuclei. It is assumed that their injection spectrum would not be a pure power-law, but one with a *cut-off*:

$$\left.\frac{dN}{dE}\right|_{\mathrm{inj}} \propto E^{-\Gamma} \cdot \exp\left(-\frac{E}{E_{\mathrm{cut}}}\right) \tag{1.10}$$

a consequence of the energy losses happening between the departure from the neutron star and entrance into the PWN [41] (see also below, for leptonic energy losses).
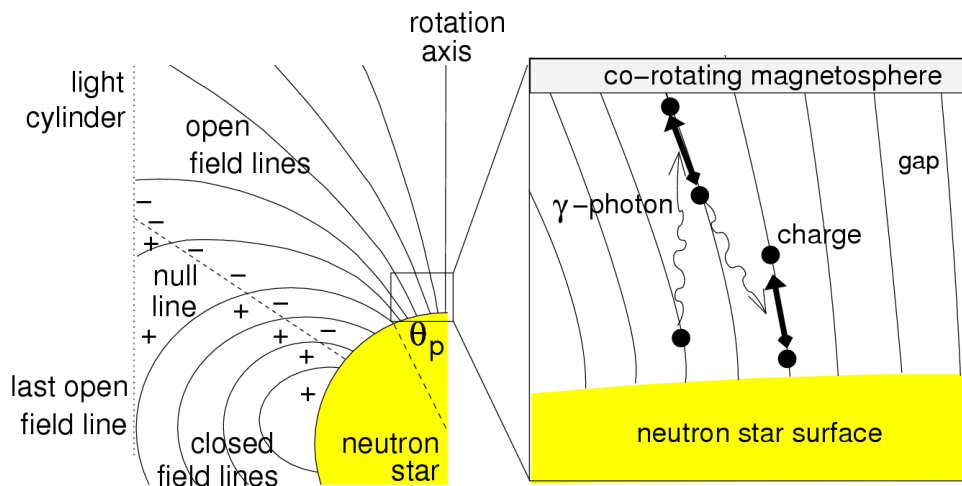
Figure 1.14. Left panel: Schematic view of a pulsar (yellow circle). Surface charges create the large magnetic field. At a certain declination, a particle leaving the surface can not follow one closed field line back to the surface again, because it would need to move faster than light. These are called *open field lines* and define the *light cylinder*. **Right panel:** Charged particles produce γ-rays and $e^{\pm}$ pairs (as large as 10^5 pairs from one surface charge) in the strong magnetic field. From [42].

1.3.3.3. Further astrophysical sources

Superbubbles Superbubbles are mergers of multiple supernova remnants that allow for a far greater extension, because their expansion becomes less decelerated. Our current understanding of their formation is sketched in appendix A.1. As our very local environment, the vicinity of the heliosphere, is located in such a bubble, the formation of these structures is of interest for this work, thus a summary of superbubble formation is given in appendix A.1. Superbubble environments have been suggested as additional site of CR

acceleration, similar in nature but of up to 10..100× as large and thus, by (1.2), possibly accelerating to a significant higher maximum particle energy.

Stellar winds from massive stars   Suggestions exist that the stellar winds from young stars of the hottest type O and B are powerful enough to affect the energy balance of the ISM. These have mass-loss rates so high that during their main-sequence lifetime, up to 50% can be radiated away, and this can result in a power of about $P_{OB} \approx 10^{34}$ J/s throughout the Galaxy [40].

Black Hole (Sagittarius A*)   As recently as in March 2016, the H.E.S.S. collaboration [43] released a publication, finding a PeV-capable acceleration site in the Galactic Center. Their observation of a very hard γ-ray spectrum hints to the presence of a PeV proton population within $R < 10$ pc galactic radius, which is likely to be correlated with the black hole hypothesized at Sagittarius A*. This is just a remark, as the galactic black hole has not been considered as a source of cosmic rays so far.

1.3.3.4. An exotic source: Dark Matter (DM)

As was already anticipated in the introductory part, it is currently out of the question that (DM) comprises an integral part of the Milky Way - essentially due to the lack of universally accepted alternatives describing the entirety of phenomena the DM hypothesis can describe (e.g. the dynamics of rotation, velocity, interacting galaxy clusters like the Bullet Cluster (Fig. 1.15) and more).
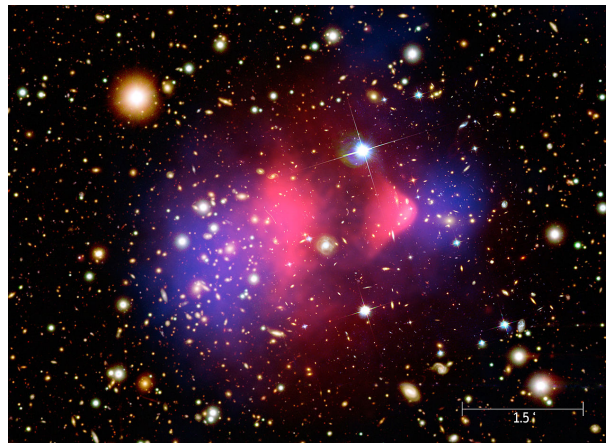
Figure 1.15. The difference between the baryonic gas observed in X-ray emissions (marked red) and the entirety of gravitationally interacting matter seen by the gravitational lensing effect (marked blue), in the Bullet Cluster [44].

The possible relevance of the presence of a DM halo for CR propagation is not because of its gravitational effects (which are generally negligible for the galactic cosmic ray densities), but due to it giving an additional, *exotic* origin of CRs in addition to the astrophysically known SNRs/PWNe.

Too little is currently known about the actual nature of this mass component, but regularly, attempts are made to assign to it some properties of a *particle nature*, as fields coupled by a gauge theory of some kind like the other established particles in the Standard Model. Widely accepted as best effort therein is the hypothesis of the "weakly interaction massive particle" (WIMP), which couples to the weak interaction of the Standard Model, which is of partial theoretical beauty because it could show the right self-annihilation cross section to be compatible with its thermal production in the early universe; so no new interactions would need to be introduced into the $SU(3)_\mathrm{c} \times SU(2)_\mathrm{L} \times U(1)_\mathrm{Y}$ gauge theory which is the fundament of the Standard Model in its current state. Further, a suggestive WIMP candidate would be given, if any supersymmetric extension of the Standard Model came to be verified, by the "lightest neutralino" of such an extension. Other particle explanations contain the "axion" (linked to the strong CP problem) or a particle from a Kaluza-Klein theory (a five-dimensional extension of the Standard Model).

Assuming a particle nature of DM and a certain coupling to the Standard Model (e.g. weak), the annihilation or decay of this particle would result in the production of Standard Model particles as γ-rays, neutrinos and matter-antimatter pairs, illustrated in Fig. 1.16. The latter are, then, especially an interesting source component of antimatter particles, as these are rare in galactic cosmic rays and DM production would more likely be visible in the local flux measurements. However, the spectral shape of this contribution is then only determinable under further assumptions about the particle nature. It might be noted, that this contribution would likely be observed rather isotropic, from the required flatness of the spatial DM halo distribution near the Sun.
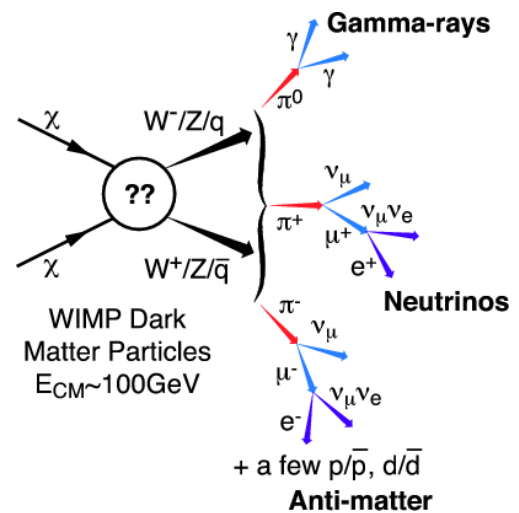
Figure 1.16. A WIMP particle χ of unknown nature could annihilate (or decay) in mostly γ-rays, neutrinos and $e^\pm$ pairs. The significance of hadronic final states as $p\bar{p}$ depends on the WIMP mass.

1.3.4. Particle interactions
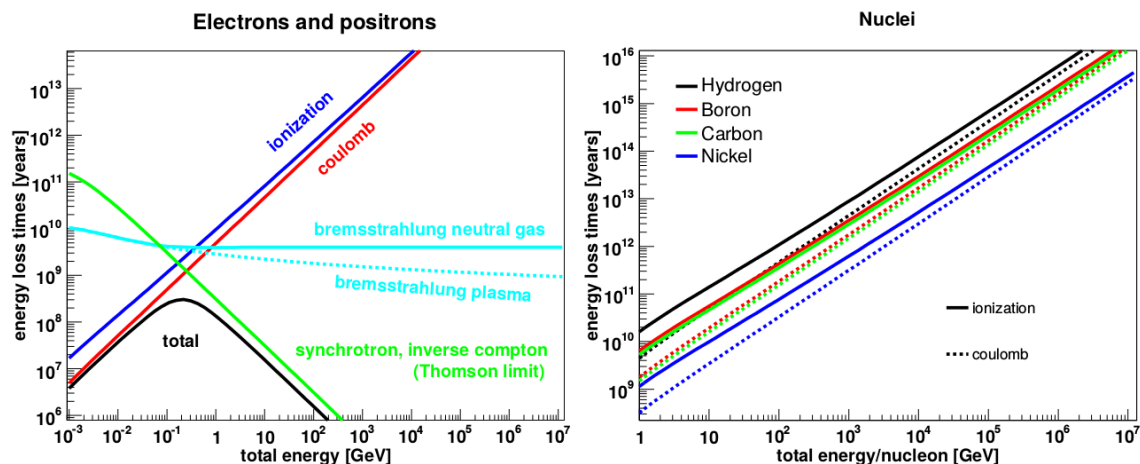
Figure 1.17. Visualization of the energy loss time scales, for CR leptons in the **left** and for CR hadrons in the **right** panel. Small times mean efficient energy loss. Synchrotron and Inverse Compton lines take the magnetic field and radiation field at energy density $1\,\mathrm{eV\,cm^{-3}}$, the other energy losses refer to ISM gas densities taken as average values $n_{\mathrm{ISM}} \approx 10^{-2}\,\mathrm{cm^{-3}}$ over a typical CR trajectory (neglecting ISM Helium). From [45].

On their way through the galaxy, CR particles are subject to various interactions with the surrounding ISM. Subsequently, the leptonic particles will radiate a significant share of their energy away as photons. In total, current models account for five energy loss processes (in short "energy losses"), but three of them are negligible for protons and heavier nuclei (hadronic CR species). In total, the loss of energy $\dot{E}$ defines the energy loss time scale τ that decreases with energy loss efficiency,

$$\tau(E) = \frac{E}{\dot{E}(E)} \tag{1.11}$$

These time scales, for exemplary values of the ISM, are visible in Fig. 1.17. For (left) electrons and positrons (the leptonic component of cosmic rays), these are several orders shorter than for nuclei (right), making the energy loss a significant feature of their propagation.

1.3.4.1. Lepton-specific energy losses

A number of energy loss mechanisms is only considered for electrons and leptons, because they become insignificant with CR particle mass of 1 GeV (protons) or more. These effects will be described first, because of the particular impact they have on leptonic source models.

Synchrotron radiation: Moving through the galactic magnetic (regular) fields, ultrarelativistic charged particles cause radiation according to the relativistic generalization of Maxwell's equations. The resulting power is given by Larmor's formula as

$$P_{\text{sync}}(\vec{r}, E) = \frac{4}{3}\sigma_{\text{T}} \cdot \left(\beta(E)\gamma(E)\right)^2 \cdot \epsilon_B(\vec{r}) \qquad (1.12)$$

with the relativistic kinetic quantities β and γ, the regular magnetic energy density ϵ_B and the Thomson cross section $\sigma_{\text{T}} = 66.5\text{fm}^2$ (for electrons). By σ_{T} and γ, the power has a mass dependence $P_{\text{sync}} \sim m^{-4}$, explaining why this effect can be neglected for protons or heavier nuclei.

Figure 1.18. Synchrotron radiation: As $e^{\pm}$ circulate along a magnetic field line, they are constantly radiating photons to conserve momentum.

Equation (1.12) shows a linear dependence in ϵ_B, so the energy loss via Synchrotron radiation will be generally larger in models that use a stronger galactic magnetic field. Together with the Inverse Compton effect, this radiation is responsible for the rapid decrease in leptonic spectra towards higher energies. This will be shown in chapter 3 and be the topic of chapter 4, applied to the local positron measurement.

Inverse Compton scattering: Compton scattering is widely known as the deceleration of a photon in the collision with an electron, speeding that electron up.
Inverse Compton scattering, then, means that a lepton can lose its energy in the interaction with a low-energy photon, which are abundant in the *interstellar radiation field* (ISRF). From a quantum electrodynamics point of view (Fig. 1.19, this process is described by the same interaction as Synchrotron (in the Thomson limit, for high energies QED corrections lead to the Klein-Nishina formula), but given as interaction partner a real photon instead of a virtual photon from the

Figure 1.19. Feynman graph of the basic QED process. This describes Synchrotron, Inverse Compton and Bremsstrahlung effects.

GMF. In the Thomson limit the radiating power is similar to (1.12), but with the photon energy density ϵ_{ν}:

$$P_{\text{IC}}(\vec{r}, E) = \frac{4}{3}\sigma_{\text{T}} \cdot \left(\beta(E)\gamma(E)\right)^2 \cdot \epsilon_{\nu}(\vec{r}) \qquad (1.13)$$

The ϵ_{ν} is sufficiently given from the three main ISRF constituents, CMB, starlight and dust emission as described in the previous section, Fig. 1.5. Due to the higher invariant mass of this process, the photon participating is usually accelerated up to very high energies, i.e. the Inverse Compton effect produces γ-rays, which can be detected at Earth.

Bremsstrahlung: Bremsstrahlung is the third process described by the QED process seen in Fig. 1.19, but it is of minor importance (slow τ in Fig. 1.17), compared with the Synchrotron radiation and Inverse Compton effects. Here, the interaction is between the CR lepton and the magnetic field of the interstellar gas particles. For the neutral ISM components H_2, HI, the interaction is with the nuclear magnetic field of the gas, while for

the *HII* plasma, there is a net charge and slightly larger magnetic field (see the difference between the turquoise lines in Fig. 1.17.

The deceleration due to the Bremsstrahlung emissions can usually be dropped in discussions (but are computed in numerical codes, anyway). However, Bremsstrahlung plays a role as another γ-ray component, being produced throughout the ISM, where CR leptons and ISM gas meets.

Further, but insignificant interactions: For completeness, we mention [46] who investigated two leptonic effects usually not accounted for in CR propagation; the $e^{\pm}$ pair annihilation (of a CR e^+ with a thermal ISM e^-) and the triplet-pair production process (a CR e^- colliding with a soft ISRF photon), i.e.

$$e^+ + e^-_{\mathrm{ISM}} \longrightarrow 2\gamma \tag{1.14}$$

$$e^- + \gamma_{\mathrm{ISRF}} \longrightarrow e^- + (e^+ + e^-) \,. \tag{1.15}$$

They find, by numerical computation, no significance of these processes. Note that for (1.14), the CR density generally is too low. This also holds for annihilation of antiprotons, another CR antimatter component.

1.3.4.2. All-particle energy losses

As was stated, Synchrotron and Inverse Compton effects, which lead to efficient deceleration in the high-energy regime for leptons, are negligible because the $P \sim m^{-4}$ dependence means a suppression by 12 orders magnitude. Therefore, high energy nuclei fill the whole galactic volume, i.e. a hadronic CR particle in this regime can be measured at Earth if it was created over 10 pc away. For stable low-energy hadrons, little changes in the spectrum are also expected in the low-energy range, noting that the energy loss time scale there $\tau \sim 10^9$ Myr is of the order of the escape time inferred from $^{10}Be/^9Be$ measurements [47]. Nevertheless, they will be briefly given:

Coulomb interaction with the charged ISM (*HII* component): As HII regions consist of highly ionized hydrogen and Helium, the energy loss is dominated by the Coulomb scattering off thermal electrons.

Ionization of neutral ISM (H_2, HI component): Traveling through atomic *HI* or molecular H_2 clouds, it becomes possible for the charged CR to strip an electron of the gas atoms/molecules.

As will be shown below, the energy range in which these two ISM-gas-related effects become relevant is one that is also strongly affected by the heliosphere (see under *Solar Modulation*). Therefore their effect is usually disguised in model predictions. However, a correct treatment is necessary for ratio observables like *B/C*, as the different charge in *B* and *C* affects the energy losses differently.

1.3.4.3. Secondary production of cosmic rays

In contrast to the last section, the collisions from cosmic rays with the interstellar medium become interesting for *inelastic scattering*: When the energy of the collision exceeds the binding energy of the CR nucleus itself, it becomes fragmented and hereby creates a secondary particle as the high-energy daughter particle of this reaction. This is also called *spallation*. Several spallation reactions are important because their ratio of secondary particles to primary particles are well measured, as in the example of the B/C, which is a measure for the amount of collisions [4]

$$^{12}C + p_{\text{ISM}} \longrightarrow {}^{10}B, {}^{11}B + \ldots \tag{1.16}$$

$$^{14}N + p_{\text{ISM}} \longrightarrow {}^{10}B, {}^{11}B, {}^{12}C, {}^{13}C + \ldots \qquad \longrightarrow {}^{10}B, {}^{11}B + \ldots \tag{1.17}$$

$$^{16}O + p_{\text{ISM}} \longrightarrow {}^{10}B, {}^{11}B, {}^{12}C, {}^{13}C, {}^{14}N, {}^{15}N + \ldots \qquad \longrightarrow {}^{10}B, {}^{11}B + \ldots \tag{1.18}$$
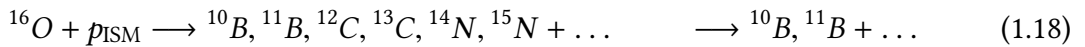
Target particles can also be unionized $(H)_{\text{ISM}}$ atoms in colder regions, as well as $(He)_{\text{ISM}}$ particles, which are usually assumed to be $\approx 11\%$ of the ISM hydrogen abundance. A kinetic description of the fragmentation of relativistic ^{12}C and ^{16}O projectiles is given in [48]. These reaction are then responsible for the gap between the relatively high abundance of B in CR compared with the solar system (Fig. 1.6 right). The observable B/C ratio is thus a measure for the amount of interstellar gas the CR have "seen" on average, or the *grammage* defined as the column density

$$X(E) = \int\limits_{\text{trajectory}} dl \, n_{\text{ISM}}(\vec{r}) \, . \tag{1.19}$$

It has been inferred that, for low energies, $X \sim (6 - 9)\,\text{g cm}^{-2}$ [4] and from B/C and N/O observations[49], that above rigidities $\rho > 20\,\text{GV/nucleon}$ a decrease a grammage $X(\rho) = 6.9 \cdot (\rho/(20\,\text{GV/nucleon}))^{-0.6}\,\text{g cm}^{-2}$ is traversed.

An important test of our understanding of the propagation paradigm as well as the cross sections of secondary production processes is given by *antimatter* observations: positrons e^+, antiprotons $\bar{p}$ and, of minor relevance, antideuterons, $\bar{d}$. Positrons are usually created via π or K^+ production channels, e.g. [4], see [50, 51, 52] for a review of the production of antiparticle cross sections.

$$p + p_{\text{ISM}} \longrightarrow \pi^0 + \ldots \longrightarrow e^- + e^+ + \ldots \tag{1.20}$$

$$p + p_{\text{ISM}} \longrightarrow \pi^+ + \ldots \longrightarrow \mu^+ + \nu_\mu + \ldots \longrightarrow e^+ + \nu_e + \bar{\nu}_\mu + \nu_\mu \tag{1.21}$$

$$p + p_{\text{ISM}} \longrightarrow K^+ + \ldots \longrightarrow \mu^+ + \nu_\mu + \ldots \longrightarrow e^+ + \nu_e + \bar{\nu}_\mu + \nu_\mu \tag{1.22}$$

$$p + p_{\text{ISM}} \longrightarrow K^+ + \ldots \longrightarrow \pi^0 + e^+ + \nu_e + \ldots \tag{1.23}$$
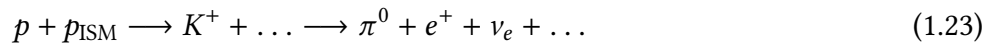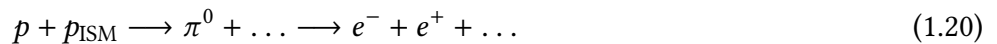
The correct description of e^+ production is especially an intriguing topic, as due to the large energy losses, e^+ of energy $E > 10\,\text{GeV}$ do not travel large distances. The observation of such an energetic positron population is thus challenging our understanding of CR sources and propagation, a topic to be discussed in chapter 4.

Another important secondary production process is the one of γ-rays produced via interstellar π^0-production,

$$p + p_{\text{ISM}} \longrightarrow \pi^0 + \ldots \longrightarrow \gamma\gamma + \ldots \tag{1.24}$$
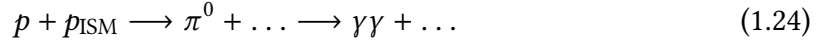
which gives an important contribution to the *diffuse γ-ray flux*, i.e. the γ cosmic rays that is not directly emitted in the SNRs, PWNe, or other source accelerators. The π-decay γ-production is then, in a given line of sight (LOS), amounting to the total of

$$\phi_\gamma(E) = \int\limits_{\text{LOS}} dl \, n_{\text{ISM}}(\vec{r}) \, N_p(\vec{r}, E) \, \sigma(E) \,, \tag{1.25}$$

with N_p the CR proton density, n_{ISM} the ISM gas density and $\sigma(E)$ the production cross section. Further contributions come from from *He*, in CR and in the ISM gas. By this, γ-rays are *tracing* distant CR densities (combined with the ISM density), that are experimentally inaccessible otherwise. Similarly, the other diffuse γ-ray components produced by the leptonic Bremsstrahlung and Inverse Compton interactions are mostly tracing the distant CR electron population, combined with the ISM gas, and the ISRF, respectively [53].

1.3.4.4. Radioactive Decay

As many of the CR isotopes are unstable, they are subject to radioactive decay during propagation. This fact can be made use of in estimating their average age (coining these isotopes "cosmic clocks"). Conveniently, isotopes are regarded whose half-life is in the Myr range, to be comparable to the assumed time of residence (escape time) in the Galaxy, as two commonly taken examples ^{10}Be (half-life 1.6 Myr) and ^{26}Al (half-life 0.9 Myr), amongst others as ^{14}C, ^{36}Cl, ^{54}Mn (not discussed here). While primary ^{26}Al is abundant in the sources, ^{10}Be is a purely secondary product. From the low values of ^{10}Be abundance, it can be concluded that the escape time is on average larger than a few ^{10}Be half-lives, estimated by [54] as $\tau_{\text{esc}} = 15^{+7}_{-4}$ Myr. Furthermore, comparing this information with the grammage given above [4], an average density of ISM matter of $0.4..0.6 \frac{\text{atoms}}{\text{cm}^3}$ is derived. Being only a fraction of the average ISM density in the galactic plane $n_{\text{ISM}} \gtrsim 1 \frac{\text{atoms}}{\text{cm}^{-3}}$, this means that CR spend only $\sim \frac{1}{3}$ of their lifetime in rather high ISM densities, the other $\sim \frac{2}{3}$ in thin environments, as the galactic halo.

A complication in the study of cosmic clocks is, that the decay processes in the ISM are not necessarily happening at a rate equal to Earth laboratories. While β-decay is a purely nuclear process, the other relevant decay process is by *K*-capture, i.e. when the nucleus weakly interacts with the innermost e^- of the atomic shell, similar to β^+ decay but assisted by an electron (sometimes called EC or ϵ decay),

$$X \longrightarrow Y + e^- + \bar{\nu}_e \qquad\qquad \beta^- \text{ decay} \tag{1.26}$$
$$X \longrightarrow Y + e^+ + \nu_e \qquad\qquad \beta^+ \text{ decay} \tag{1.27}$$
$$X + e^- \longrightarrow Y + \nu_e \qquad\qquad K \text{ capture} \tag{1.28}$$

Therefore, *K* capture takes longer in the electron-poor ISM as lifetime measurements on Earth would predict. However, as ^{10}Be is purely subject to β^- decay, the above lifetime argument is unaffected by this.

1.3.5. Diffusion and Leaky-Box models

As explained at the beginning of this chapter, cosmic ray propagation must be a diffusive process in order to explain the high level of isotropy observed in the arriving cosmic rays. Yet, this scattering can not be by direct collisions, as these interactions would lead to any nuclei heavier than protons to fragment before they reach Earth, in contrareity to the actual chemical composition Fig. 1.6. Also, for a proton of kinetic energy $E \sim 1\,\text{GeV}$, for interaction with the interstellar gas, the Coulomb cross section σ and collision rate τ_{coll}^{-1} are (with a mean gas density of $n_{\text{ISM}} \approx 1 \text{cm}^{-3}$),

$$\sigma \approx 10^{-30}\,\text{cm}^{-3} \tag{1.29}$$

$$\tau_{\text{coll}}^{-1} = n_{\text{ISM}}\sigma v = 3.16 \cdot 10^{-20}\,\text{s}^{-1} \tag{1.30}$$

$$\tau_{\text{coll}} = 3.16 \cdot 10^{19}\,\text{s} \gg 4.32 \cdot 10^{18}\,\text{s} \quad \text{(age of the universe)}\,. \tag{1.31}$$

So these collisions happen far too infrequently. Therefore, scattering of cosmic rays has to be *collisionless*. It is thus suggested that this is accomplished by resonant interaction with the surrounding magnetic turbulent field, as this would lead to the desired non-fragmentive diffusion. Frequent magnetic deflections, then, keep the cosmic rays from streaming freely from the inner galaxy, rich in SNRs, to the intergalactic space and the spatial CR source distribution is "blurred". In chapter 2, a discussion of this will be given in a microscopic, magnetohydrodynamical picture. Here, it will be sufficient to consider that this approach leads to rigidity-dependant (rigidity $\rho = p/(Ze)$) galactic diffusion coefficient, parametrized by a power-law

$$D(\rho) \propto \rho^\delta \qquad \propto (E/Z)^\delta \ (E \gg mc^2) \tag{1.32}$$

and this can be interpreted with the help of a very simplified model, the so-called *leaky box* (a variation of what was already seen in Fig. 1.7): Therein, it is assumed that all particles are injected homogeneously into one galactic volume, with no further assumptions about the diffusion process but only stating free escape the volume boundary, with rigidity-dependent escape (or confinement) time $\tau_{\text{esc}}(\rho) \propto \rho^{-\delta}$ (intuitively shorter for faster particles). CR densities are simply described as (assuming ρ dimensionless, e.g. relative to 1 GV)

$$\frac{\partial N(\rho)}{\partial t} = N_{\text{inj}}(\rho) - \tau_{\text{esc}}^{-1}(\rho)N(\rho) + \ldots \tag{1.33}$$

$$\approx N_0 \cdot (\rho)^{-\alpha} - \rho^\delta N(\rho) \tag{1.34}$$

where ... describe further terms, as decay or secondary production (see below). For particles where these terms do not play a role, e.g. protons, this predicts a local spectrum

at the earth, if equilibrium is reached

$$\dot{N}(\rho) = 0 \qquad \Rightarrow \qquad N(\rho) = N_0 \cdot \rho^{(-\alpha-\delta)} \tag{1.35}$$

Indeed, it has been observed that the source component of protons has a significantly larger high-energy component than the one locally observed. With CR protons being nearly immune to energy loss, this change in spectral shape is thus attributable to the diffusion process, or time-dependent escape from the galaxy.

Further terms for leaky-box models

The predictive power of leaky-box models is astounding. Considering the secondary-to-primary ratios or cosmic clock observables, one might formulate equations like (1.33) for multiple particle species N_i and then on the right hand side include simple terms like

$$\text{fragmentation} \left(- n_{\text{ISM}} v \sigma_i N_i \right) \text{ and decay} \left(- N_i/\tau_i \right), \tag{1.36}$$

with $\sigma_i = \sum_j \sigma_{ij}$ the total fragmentation cross section, σ_{ij} the cross section for production $i \rightarrow j$ of daughter species j from mother species i and $\tau_i = (\sum_j \tau_{ij})^{-1}$ its total radioactive decay time, τ_{ij} the corresponding decay time for the $i \rightarrow j$ channel. Both effects then serve as additional source terms for particle type j, so one accordingly adds

$$\text{fragmentation} \left(+ \sum_{i>j} n_{\text{ISM}} v \sigma_{ij} N_i \right) \text{ and decay} \left(+ \sum_{i>j} N_i/\tau_{ij} \right) \tag{1.37}$$

to the leaky-box equation of N_j. Within this simple picture, the grammage is

$$X = v \, n_{\text{ISM}} \, \tau_{\text{esc}} \, . \tag{1.38}$$

Other terms, e.g. to account for energy losses, are not discussed here but also commonly used. [4].

As a demonstration, B/C can then be estimated as function of rigidity ρ, with the production cross section $\sigma_{C \rightarrow B}$ of boron from carbon and the total fragmentation cross section $\sigma_{B,\text{frag}}$, as

$$\frac{N_B}{N_C}(\rho) = \frac{\sigma_{C \rightarrow B}}{\sigma_{B,\text{frag}} + X} = \frac{\sigma_{C \rightarrow B}}{\sigma_{B,\text{frag}} + (v n_{\text{ISM}} \tau_{\text{esc}})^{-1}} \propto \rho^{-\delta} \tag{1.39}$$

In Fig. 1.20, two simple leaky-box predictions are made for the choices of $\delta = \{\frac{1}{3}, 0.7\}$, in comparison with CREAM measurement [55]. It shows a general agreement with the linear (in double logarithmic representation) prediction done by the LB model, but gives these two values rather as lower and upper limit of possible choices. Roughly, this dependence is also seen in more complex, numerical propagation models, so with rising
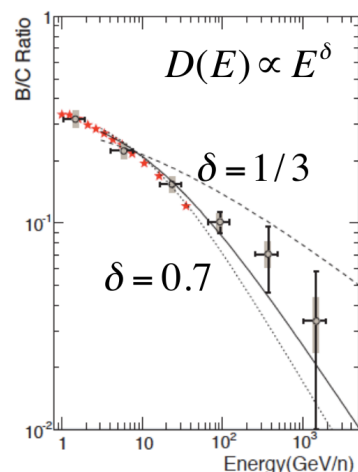
Figure 1.20. The high-rigidity end of *B/C* CREAM data is described by a Leaky-Box model within a range of different δ indices.

precision in CR measurements, closer restriction of δ will in principle be possible.

Note that in all cosmic ray transport models, the free escape into intergalactic space is considered at some height above and below the galactic plane. This distance, the *galactic half-height L*, is taken as a multiple of the thickness of the Galactic Disc (where the ISM concentrates). Cosmic rays are then filling the whole galactic *halo*, only loosely restricted $L \sim 2..30$ kpc [56]. In the diffusion approximation (coefficient D), this height is related to the escape time as $\tau_{esc} \approx L^2/D$, thereby being constrained by B/C and $^{10}Be/^9Be$ measurements, but severely uncertain due to the influence of other propagation processes.

Besides diffusive propagation, CR can also undergo convective transport, i.e. the combined drift and energy exchange exerted by a moving background ISM. This is called a *galactic wind*, a result of a strong gradient in magnetic and thermal gas pressure (thus, "wind"). This is usually considered between the Galactic Disc and the vertical boundary to the halo region. However, [57], wind velocities have been observed to be relatively small, of the order 10 $\frac{km}{s}$. Thus, galactic winds are not always considered to play a large role in CR propagation. On the other hand, it was theorized [58] that the interaction of the CR population with the magnetic turbulences create a turbulent instability, which accelerates the wind with rising height above the galactic plane up to values of several hundred $\frac{km}{s}$.

1.3.6. Our Solar neighborhood: The Local Bubble (LB)

The interstellar medium in our direct vicinity is in a very inhomogeneous shape. Fig. 1.21 [59] shows a schematic of the side-ways view of the closest regions, for a sector of dimensions about $460 \times 460 \, \text{pc}^2$ (left) and $120 \times 120 \, \text{pc}^2$ (these views capture slices of about 200 pc thickness in the projected direction, so that distances can appear smaller than in actuality). In this thesis, we will refer with the *solar neighborhood* to the closer $\sim 200 \times 200 \times 200 \, \text{pc}^3$ cuboid volume around the Sun, for which the view in Fig. 1.21 (right) is a good reference. It is remarked that in the volume shown in the left plot, most of the known stars are already included [59] (which demonstrates the sheer vastness of the Milky Way).

Very clearly, the HI regions appear to be structured in bubble-shaped filaments, which are the called *Superbubbles*. Superbubbles form by the merger of the supernovae or supernova remnants of the most massive stars (type O and B), when they develop in a temporal correlation. This, is actually not uncommon in such called OB-associations and it is estimated that ca. 75% of all galactic SNRs lie in a Superbubble environment [60]. It is now established, that the whole galactic ISM is spangled with topological structures like bubbles, cavities, filaments, tunnels, et cetera, a usual product of the dynamical transformation due to pressure equalization. For further understanding, an outline of Supernova and Superbubble formation is presented in the appendix.

The Sun is embedded, Fig. 1.21 (bottom) inside a Superbubble of its own, which is called *the Local Bubble.* The existence of such a bubble was first noticed in the 1970's by a Soft X-Ray component visible in a large portion of the sky, supposed to be emitted by
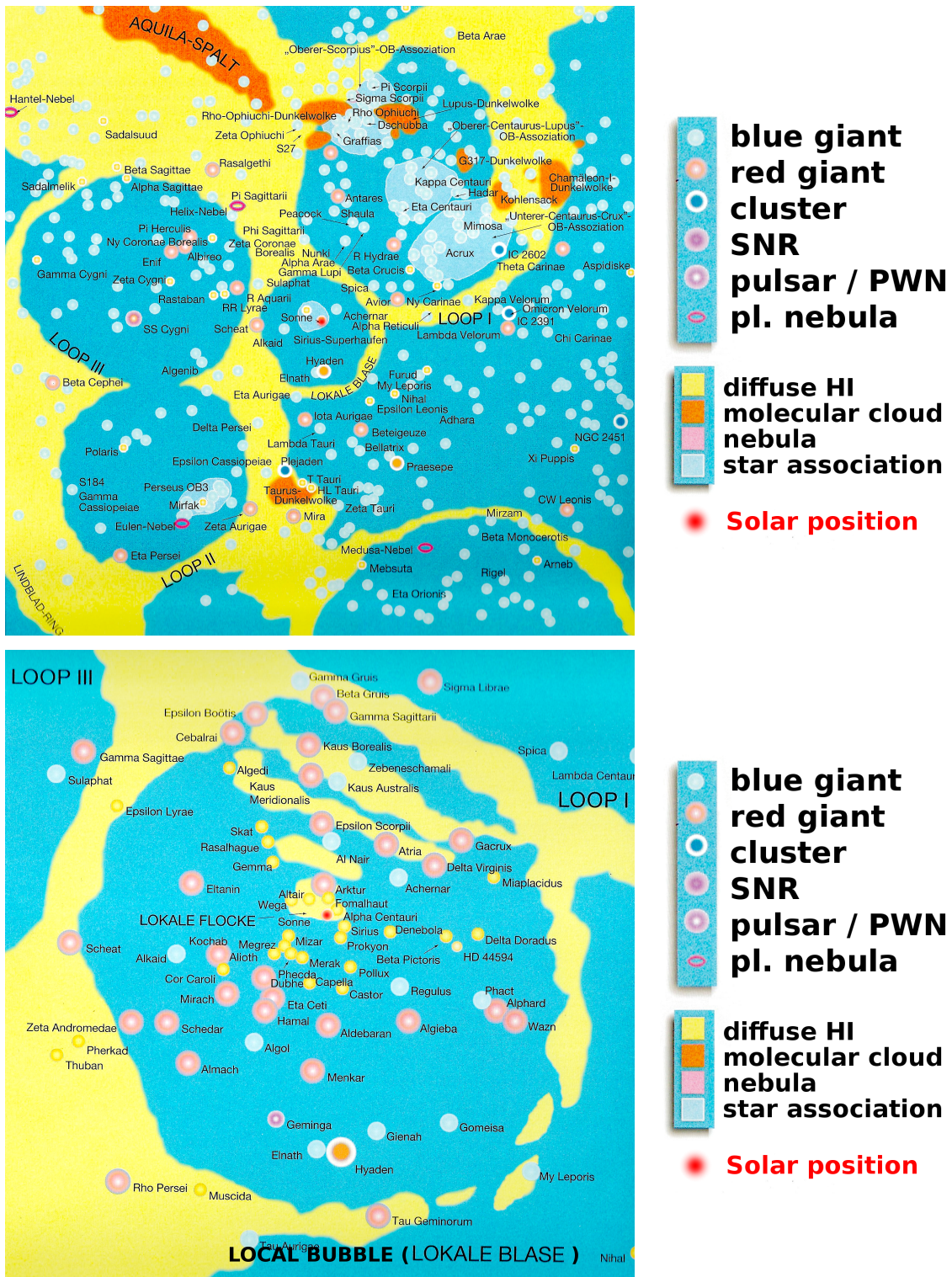
Figure 1.21. The gas distribution in the solar neighborhood, especially HI (yellow), show several structures of (Super-)bubbles, shell fragments and clouds (The blue regions are taken as hot, Coronal gas). This is likely a standard environment in ISM structure at small scales, a product of its constant state of metamorphosis. The **top** panel shows a ca. $460 \times 460 \, \text{pc}^2$ sector and the **bottom** panel a closer one of ca. $120 \times 120 \, \text{pc}^2$. The Sun is nearly central in each view and also approximately in the center of the *Local Bubble*. These maps were created using combined measurements of dust extinction, radio emission of the 21cm line, and distance estimates from stars in star birth regions [59].

hot Coronal Gas (see above). As sounding rocket flights did not show strong large-scale angular fluctuations [61] it was concluded that this gas should be confined in a local cavity and absorption measurement of the hydrogenic Lyman α line in the spectra of close-by stars affirmed a underdensity of local HI gas. Its origin as a product of multiple SNRs was proposed only as recently as 2001 [62], and even more currently, numerical simulations reproduced the evolution of the Local Bubble from its original SN explosions (see [63] or the Nature publication by Breitschwerdt from this year [64]), in agreement with ^{60}Fe measurements in the Earth's crust attributed to these SNe. A review of astronomical observations at the state of research in 2009 is given in [65].

Today, the corresponding precursor OB stars are believed to be members of the Sco Cen association, while the Sun[6] entered this volume only a few Myr ago. It is thus only a coincidence that the current position of the Sun is near the center of the Local Bubble. Also, as visible in Fig. 1.21 (right), the location of the Sun inside the Local Bubble is within a small HI cloud called the Local Fluff ("Lokale Flocke" in the figure) of only a few pc size.

Detailed measurements of the HI distribution in and around the Local Bubble have been performed by [66, 67, 68]. NaI absorption lines towards hundreds of close-by stars trace the overdense gas distributions, this can be combined by observation of the color excess $E(B - V)$ in starlight (difference in extinction in the B and V frequency band) due to scattering off interstellar dust. Recent results are shown in Figs. 1.22 and 1.23. These show a clear cavity embedded in denser clouds, to which we will refer to as the *Bubble Interior* and the *Bubble Walls*, respectively. The structure is not a perfect bubble, as during the expansion into the highly inhomogeneous environment, some connections were made with the surrounding structures. Especially, the Local Bubble is seen as elongated towards the galactic halo than towards the galactic plane directions (see Fig. 1.23).

The question of the impact of the Local Bubble environment on the propagation of cosmic rays is of great importance for the interpretation of cosmic ray arrival directions. Yet, this subject has seen only little research [69, 70] so far, considering that observational advances about the Local Bubble structure only emerged in recent years. This will be one of the main topics of this thesis. In the standard picture, any small-scale structures in the ISM are averaged over larger scales of $\sim 500\,\text{pc}$ in order not to overcomplicate calculations. We suggest that fluctuations in the gas and magnetic fields can have a significant effect on the small-scale density of the local cosmic ray distribution, thus a *local transport model might deviate considerably* from a propagation model that smooths out these fluctuations.

Reasoning along the processes presented so far, the Local Bubble structure would affect

1. **Energy loss processes:** Fluctuations in the local ISM gas affect the energy losses via Bremsstrahlung, Coulomb and Ionization processes. Variation of the regular magnetic field will affect the energy loss by Synchrotron radiation. Similarly, variation of the starlight or emissions from the dust distribution would affect Inverse

---

[6]The sun is nowadays believed to be a *solitary* star, a star whose group association has dissolved long ago.

Compton energy losses. Therefore especially the leptonic CR component might be affected.

2. **Production of secondary particle:** The denser wall regions provide more target particles for the inelastic collisions spawning secondary particles. In the rarefied bubble interior, this production rate is then reduced. Both alterations could, in principle, affect predictions of B/C or the antimatter components e^+ and $\bar{p}$.

3. **Diffusion**: If the turbulent magnetic field is amplified or attenuated, the free mean path and scattering rate of CR particles changes. Currently, there is no observation of how the turbulent field behaves throughout the solar neighborhood. In chapter 3, we will construct a range of local transport models after we investigate the effects which would be responsible for either increase of decrease in magnetic fluctuations, in the interior and the wall regions individually.

Our study will, in chapter 3, implement these locally modified transport models (or just "local transport models") and investigate the flux predictions for p, e^- and e^+, the ratios $\bar{p}/p$, $^{10}Be/^9Be$ and B/C and further, the expected dipole anisotropies in the p, e^- and e^+ fluxes.
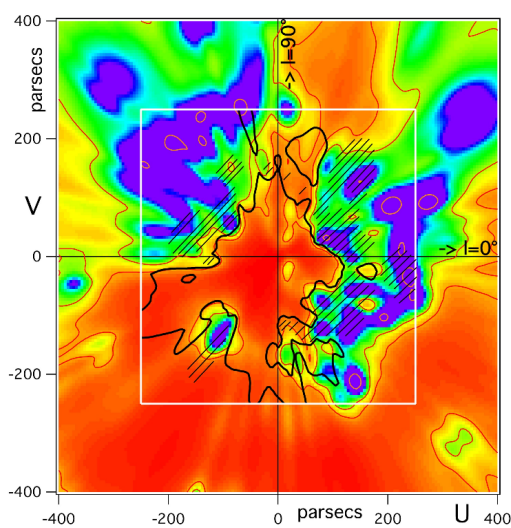
Figure 1.22. Viewed from above: The Local Bubble in the surrounding ISM, shown as black contour around the Sun (centered). Taken from [67], this plot displays hot, rarefied cavities as red and cold, dense clouds as blue. The galactic center is located towards the right. The blue dashed contour is an auxiliary line that is not of importance here. This distribution is inferred from dust extinction measurements.[71]
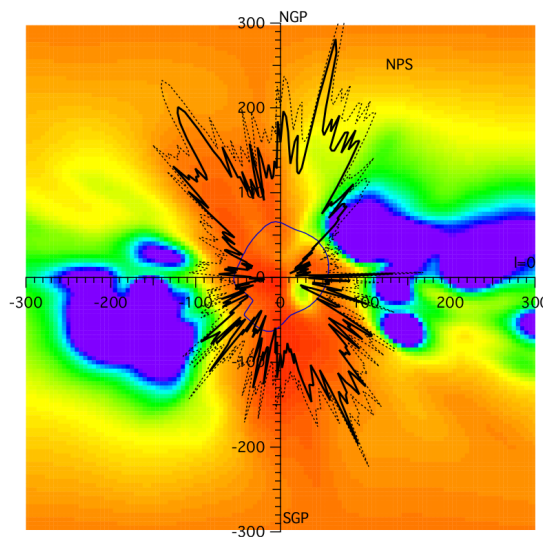
Figure 1.23. Sideways view: The Local Bubble in the surrounding ISM, shown as black contour around the Sun (centered). Taken from [68], the color scale is the same as described left. The Galactic Center is located towards the right, the North Galactic Pole to the top. The extruded black lines show the regions of soft X-ray emissions associated with the LB. This shows it is rather chimney-shaped than spherical.

1.3.7. Solar Modulation

Before discussion the propagation effect of the heliosphere, we want to put its size into perspective. The heliosphere is usually taken to have asymmetrical extension of about 100..160 AU, equal to 500..800 μpc. In 1977, NASA launched its spacecraft missions Voyager 1 and Voyager 2 to travel, on two different paths, towards the edge of the solar system. Fig. 1.24 shows a schematic view of the heliosphere including its outer boundary layers, and the respective position of the two probes back in a time when they met the *termination shock*. The termination shock is the theoretical distance to the sun at which particles in the solar wind are beginning to be dominated by the energy loss from interacting with the ISM. The solar wind consists of mainly protons (and some electrons and helium nuclei), emitted from the Sun. When decelerated in this region, the gas heats up and the termination shock is formed by the steady outflow of further particles. The *heliopause* is the outer edge, at which the stream of particles has no significant effect on the ISM anymore. Voyager I is believed to have crossed the heliopause in August 2012 and since then, is in interstellar space. This was registered by relative strong changes in magnetic field and particle density of the environment. Voyager II was expected to cross the heliopause in 2015 but so far, is still considered inside the heliosheath, the region directly interior the heliopause.

Voyager I and II are, as of October 4th 2016, in 136.4 AU and 112.4 AU distance from the Sun, respectively, and it took these spacecrafts 39 years to reach this distance. As these are scales below the milliparsec, the dimensions of the local bubble are about 5 orders in magnitude larger. So, while the Local Bubble is commonly ignored in the cosmic ray propagation picture, it is a enormous structure, and which astroparticle physics dominate its interior we have very little understanding of.
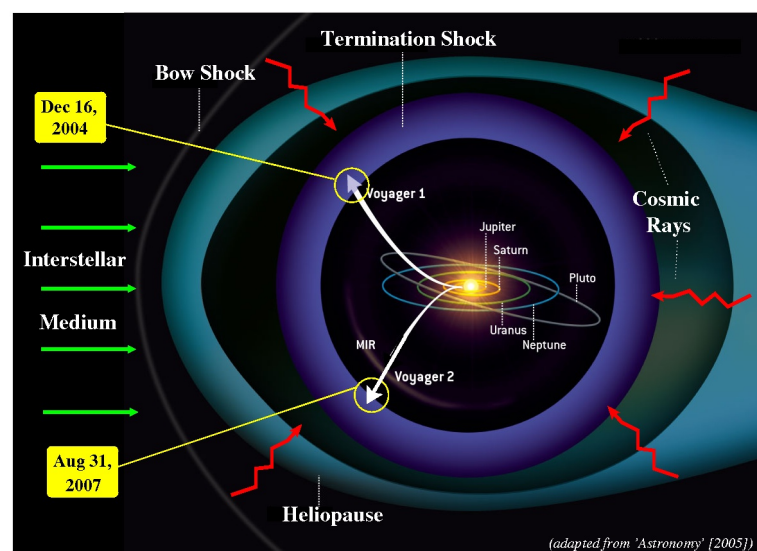
Figure 1.24. The heliosphere consists of multiple layers. The termination shock and the heliopause are two boundaries in which the Sun loses influence over the ISM each. The time when Voyager I and Voyager II have crossed the termination shock (launched in 1977) is marked and presents a glimpse of the vastness of this structure alone.

CR particles at low energies interact with the the solar wind and the heliospheric magnetic field (HMF). The HMF has a large turbulent component as well as a regular spiral structure, as it is is frozen into the outward-moving solar wind plasma, coming from the rotation Sun. This is called the Parker Spiral and illustrated in Fig. 1.25.

The study of the turbulent HMF field is at the moment a current topic, it is following a shape called the Fisk field (not shown here). Interaction with the HMF causes low energy CR particles to be deflected or decelerated, thus reducing their local flux. This so-called *solar modulation* and usually only considered effective for kinetic energies under a few GeV.

Solar modulation can be illustrated by the temporal variation of AMS-02 proton measurements [72] in Fig. 1.26. As the solar magnetic field follows the 11-year cycle of solar activity (visible in number of sun spots or frequency of

Figure 1.25. The Parker Spiral, the structure of the regular heliospheric magnetic field.

auroras in the geomagnetic field), the low-energy proton flux becomes deflected according to these cycles. With rising rigidity, the proton flux becomes increasingly independent from these timescales (compare red points vs. blue points). Fig. 1.26 shows the proton flux measured during different months between May 2011 and December 2013, normalized to the average flux over this period. For low rigidities (blue points), the variation is up to a factor 1.3..1.4 up and down over this interval in time.
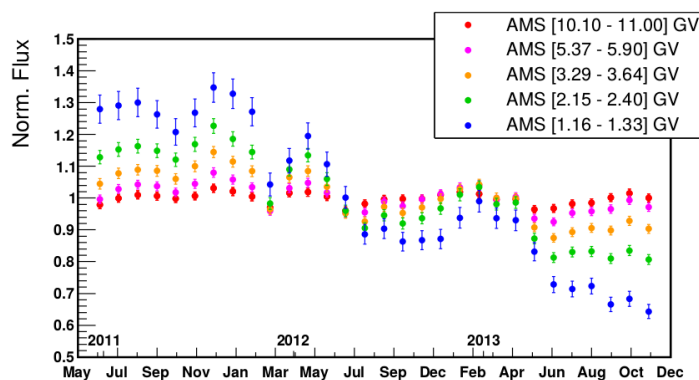
Figure 1.26. Solar modulation in AMS-02 proton flux: Depending on the time, the proton flux at different rigidities is affected differently (each rigidity bin is shown normalized to an average value). This is in accordance to the solar activity. From [72].

2. Modeling cosmic ray propagation: theoretical foundation

The mathematical framework of galactic cosmic ray propagation is given by the *transport equation* ("TE"), or rather the set of TEs, for every CR isotope each. This is a partial differential equation describing the temporal, spatial and kinetic evolution of the particle density $N(E, \vec{r}, t)$ throughout the galaxy. In anticipation, we give its state-of-the-art form as $(\partial_p \equiv \frac{\partial}{\partial p})$

$$\frac{dN}{dt} = \vec{\nabla}\left(D\vec{\nabla}N - \vec{V}_C\, N\right) + \partial_p\left(p^2 D_{\text{pp}} \partial_p\left(\frac{N}{p^2}\right)\right) - \partial_p\left(\dot{p}\, N - \frac{p}{3}(\vec{\nabla} \cdot \vec{V}_C)N\right) - \frac{N}{\tau} + Q \quad (2.1)$$

which will be comprehensively discussed in this chapter. Before doing so, it is worth mentioning that for most CR applications, it is well justified to assume that the CR population is old enough so that a state of equilibrium has been reaching, including the steady supply of freshly injected CR and the irreversible loss processes, i.e.

$$\frac{dN}{dt} = 0 \quad \text{(stationary state)} . \quad (2.2)$$

On the whole, the TE is the product of theoretical groundwork already raised in the 1960s by Ginzburg and Syrovaatski [73], refined since then, by [74], [Parker 1968b, 1969; Lerche 1969; (e.g. McKenzie & Völk 1982)] amongst others. A benchmark publication was given 1990 by Berezinskii, Ptuskin et al. [75], which contains the foundation of most of current CR research. A profound consolidation has been given by Schlickeiser 2002 [4]. The review of this chapter is based on these publications, supplemented by own work and other sources, where necessary.

The approach of this work is to assume a model set of TE parameters, use a numerical solving algorithm and then to discuss the outcome, scrutinizing it with the help of available experimental data. The publicly available code DRAGON, both used and modified by our study, is described later in this chapter. This approach utilizes the modern, powerful capacities of multi-core processors and clusters. The implementation of the TE in this code (and, too, the more widespread code GALPROP) is based on several assumptions, chosen in favor of computational performance and are challenged where we find it adequate. For simpler scenarios, it is also possible to solve eqn. (2.1) analytically, which is done in chapter 4 (along with a DRAGON comparison).

We now sketch the general derivation of the TE from first principles and basic assumptions. This will show why (2.1) serves as a valid transport equation. We then present the fundamental understanding of the various differential TE operators, and their implementation in a numerical framework like GALPROP or DRAGON. The specific solving

algorithm used in DRAGON is shortly described afterwards, along with a few important considerations for numerical treatment of the TE.

Finally, this chapter will contain some preparatory calculations required in order to interpret model predictions for CR anisotropies, as will be one of the main discussion points in chapter 3 and chapter 4, and the discussion of a simple TE describing a point source in a simple diffusion set up.

2.1. The transport equation (TE)

2.1.1. Plasma kinetics: Quasi-Linear Theory (QLT)

2.1.1.1. Derivation

Overall, the TE derives from the conservation of phase space (Liouville's theorem) in a magnetohydrodynamical (MHD) system. This basic perturbative approach dates back to Jokipii [74], which is again based on Vlasov's description of a *collisionless* relativistic plasma [76] (first published 1938). With *phase-space density* $f(\vec{r}, \vec{p}, t)$ the *Vlasov* equation is a direct consequence of Liouville's theorem - and basically only the statement of the derivative chain rule inserting an electromagnetic Lorentz force term $\dot{\vec{p}}$, and a source density term q on the right-hand side:

$$\frac{df}{dt} = \frac{\partial f}{\partial t} + \dot{\vec{r}}\frac{\partial f}{\partial \vec{r}} + \underbrace{Ze\left[\vec{E} + \vec{\beta} \times \vec{B}(\vec{r}, t)\right]}_{\dot{\vec{p}}} \frac{\partial f}{\partial \vec{p}} = q(\vec{r}, \vec{p}, t)\,, \qquad (2.3)$$

with the velocity $\vec{\beta} = (\gamma mc)^{-1}\vec{p}$, the relativistic gamma factor γ, mass m the particle's mass and Z its charge number, and $\vec{E}, \vec{B}$ the electromagnetic field vectors. The connection between phase-space density $f(\vec{r}, \vec{p}, t)$ and particle density $N(\vec{r}, p, t)$ is ($p \equiv |\vec{p}|$)

$$\int d^3p\, f(\vec{r}, \vec{p}, t) = \int dp\, N(\vec{r}, p, t) \quad \text{(total particle number } N(\vec{r}, t)) \qquad (2.4)$$

$$\Rightarrow N(\vec{r}, p, t) = \int d\Omega_p\, p^2 f(\vec{r}, \vec{p}, t) = 4\pi p^2 f(\vec{r}, p, t) \qquad (2.5)$$

where the latest step holds for isotropic $f(\vec{r}, \vec{p}, t) = f(\vec{r}, |\vec{p}|, t)$ only. Please note that in a *collisional* plasma, the right side of (2.3) would have to be amended by a Boltzmann collision term $(\dot{f})_{\text{coll}}$, as direct collisions would constitute abrupt leaps in phase space, deviating from Liouville's theorem.

We linearize (2.3) in each quantity $X \in \{f, \vec{B}, \vec{E}\}$ by a large-scale solution X_0 and a small fluctuation part δX, as is common practice in perturbation theories. Then, the distinction is made that the X_0 are isotropic and in temporal equilibrium, or at least varying slowly in time compared with δX (also, we will consider time-independent source terms $q = q(\vec{r}, \vec{p})$).

The δX parts will then consist either of completely random fluctuations or, if correlated via magnetohydrodynamic (MHD) equations, propagating waves.

- Phase-space density: $f(\vec{r}, \vec{p}, t) = f_0(\vec{r}, |\vec{p}|) + \delta f(\vec{r}, \vec{p}, t)$

- Magnetic field: $\vec{B}(\vec{r}, t) = \vec{B}_0(\vec{r}) + \delta\vec{B}(\vec{r}, t)$

- Electric field: $\vec{E}(\vec{r}, t) = \vec{E}_0(\vec{r}) + \delta\vec{E}(\vec{r}, t)$

- In our case, the regular electric field component can be set $\vec{E}_0 = 0$, as the plasma is approximated as a perfect conductor.

The magic of interstellar plasma physics now "only" lies in understanding the nature of the fluctuations $\delta\vec{B}, \delta\vec{E}$ - for the equations governing them are in principal merely Maxwell's equations including the generalized Ohm's law, coupled to fluid motions given by the continuity equations for mass, energy and momentum. But the entirety of this already accounts for a range of astrophysical plasma phenomena which are deemed relevant for cosmic ray transport.

After putting the expansions for $f, \vec{B}, \vec{E}$ into the Vlasov equation (2.3), the quasilinear approach is to drop term $O(\delta^2)$, by which every term coupling two fluctuational quantities vanish. Regardless of their origin, the fluctuations of the electromagnetic field $\delta\vec{B}(\vec{r}), \delta\vec{E}(\vec{r})$ can always be represented by their Fourier-transformed fields $\delta\vec{B}(\vec{k}), \delta\vec{E}(\vec{k})$, a.k.a. their decomposition into spatial plane waves of wave vector $\vec{k}$ and frequency ω^α. The superscript α denotes the different wave *modes* of propagation, i.e. waves of different dispersion relation $\omega^\alpha = \omega^\alpha(\vec{k})$. The different MHD modes - slow magnetosonic, fast magnetosonic and Alfvén waves - are shortly discussed in appendix . The Fourier transformed quantities can finally be correlated by virtue of Faraday's law of induction (2.8):

$$\delta\vec{B}(\vec{r}, t) = \sum_\alpha \int d^3k \, e^{-i\omega^\alpha(\vec{k})t + i\vec{k}\vec{r}} \, \delta\vec{B}(\vec{k}) \tag{2.6}$$

$$\delta\vec{E}(\vec{r}, t) = \sum_\alpha \int d^3k \, e^{-i\omega^\alpha(\vec{k})t + i\vec{k}\vec{r}} \, \delta\vec{E}(\vec{k}) \tag{2.7}$$

$$\text{with } \delta\vec{B}(\vec{k}) = \frac{c}{\omega^\alpha(\vec{k})} \left(\vec{k} \times \delta\vec{E}(\vec{k}) \right) \tag{2.8}$$

It is now not a very instructive move to exercise the complete calculation step by step. For this, I recommend the literature mentioned above to the inclined reader, foremost [75], also Kennel & Engelmann [77]. For the further review, it is favorable to use cylindrical coordinates around the direction of the regular magnetic field $\vec{B}_0$, i.e. $\vec{k} = (k_\parallel, k_\perp, \phi)$ and equivalently $\dot{\vec{r}} = \vec{v} = (v_\parallel, v_\perp, \varphi)$ with the parallel coordinates

$$\vec{k} \cdot \vec{B}_0 = k_\parallel \, |\vec{B}_0| \,, \qquad \dot{\vec{r}} \cdot \vec{B}_0 = v_\parallel \, |\vec{B}_0| \,, \tag{2.9}$$

and $k_\perp, v_\perp$ perpendicular to $\vec{B}_0$, accordingly. The *pitch-angle* is defined as the angle between $\vec{B}_0$ and the direction of movement $\vec{v}$, $\mu = \cos \sphericalangle(p_\parallel, p_\perp)$. The isotropic part $f_0(\vec{r}, p$ can be

gained from $f(\vec{r}, \vec{p}, t)$ by averaging away the azimuthal momentum information φ (we note a bar, $\bar{f}$):

$$f(\vec{r}, \vec{p}) \longrightarrow \bar{f}(\vec{r}, p, \mu) \equiv \frac{1}{2\pi} \int_0^{2\pi} d\varphi \, f(\vec{r}, \vec{p}) \tag{2.10}$$

By the manipulations required to achieve this [77], one gets after some manipulation:

$$\frac{\partial \bar{f}}{\partial t} + v_\| \frac{\partial \bar{f}}{\partial r_\|} = \sum_\alpha \int d^3 k \sum_{s=-\infty}^{\infty} \delta\left(\omega^\alpha(\vec{k}) - k_\| v_\| - s\omega_H\right) \left(\ldots \frac{\partial}{\partial p_\|} + \ldots \frac{\partial}{\partial p_\perp}\right) \bar{f} \tag{2.11}$$

in which the $(\ldots)$ parts contain combinations of the wave vector components $k_\|, k_\perp$, the velocity components $v_\|, v_\perp$, the wave frequency $\omega^\alpha(\vec{k})$ of mode α, its corresponding electric field fluctuations $\delta E_\|, \delta E_\perp$, the relativistic cyclotron frequency $\omega_H = ZeB_0/(\gamma mc)$ as well as Bessel functions $J_s(k_\perp v_\perp / \omega_H)$, over whose order s is summarized.

This is mentioned here because of the significant appearance of the *resonance condition* within the $\delta(\ldots)$-function, requiring

$$\omega^\alpha(\vec{k}) - k_\| v_\| = s\omega_H \,, \quad s \in \mathbb{Z} \tag{2.12}$$

meaning, in physical interpretation: the left side of eqn (2.12) - which simply is the wave frequency Doppler-shifted to the particle movement ("as seen from the cosmic ray particle's reference frame") - must match the cyclotron frequency an integer number of times. Rephrased in spatial scales, this means that wave-particle interaction (scattering) only appears in the wave components in which the wavelength matches particle gyroradius. This emphasizes why turbulent fields allow for much more efficient scattering than than simple monochromatic fluctuations: In astrophysical environments, a large range of wave vectors are present. A momentum-changing interaction with one wavelength can then subsequently match the wavelength of another fluctuation, and so on.

Usually, the particles can be taken as highly magnetized, $\omega_H \gg k_\perp v_\perp$ for which only interactions with $|s| \leq 1$ have to be considered. Furthermore, it can be considered that magnetic pressure is strong compared to the thermal pressure, so it holds that

$$\text{speed of sound} \quad v_S = \sqrt{\frac{kT}{m}} \ll \frac{B_0}{\sqrt{4\pi \rho_{\text{ISM}}}} = v_A \quad \text{Alfvén velocity} \,, \tag{2.13}$$

for which in the case of high ω_H large contributions only result from Alfvén waves with $\omega^\alpha(\vec{k}) = \pm|k_\||v_A$ and fast magnetosonic waves with $\omega^\alpha(\vec{k}) = \pm k v_A$. Realistic interstellar values are of the order $v_A = 50 \frac{\text{km}}{\text{s}}$. Consideration can also safely be restricted to $k = k_\|$, because modes with $k_\perp \neq 0$ are subject to strong MHD damping processes. With these conditions, the Alfvén and fast magnetosonic modes are both transverse modes propagating at v_A (with opposite polarization). Thus, $\delta E_\| = 0$ and the $s = 0$ component from (2.12) vanishes, reducing the resonance condition to ($\omega_{\text{res}}^\alpha \equiv \omega^\alpha(k_{\text{res}})$ and $r_G = \frac{mv}{ZeB_0}$ the Larmor

gyroradius):

$$k = k_\parallel = \mp \frac{\omega_H}{v\mu - \omega_{\text{res}}^\alpha/k} = \mp \frac{ZeB_0}{pc(\mu - \omega_{\text{res}}^\alpha/(kv))} \tag{2.14}$$

$$\Rightarrow k_{\text{res}} \equiv \left| \frac{ZeB_0}{pc\mu} \right| = \frac{1}{r_G|\mu|} \qquad (v_A \ll v \approx c) \ . \tag{2.15}$$

As other modes do *not* contribute, given the above simplifications, the kinetic equation (2.11) now reads in full form

$$\frac{\partial \bar{f}}{\partial t} + \mu v \frac{\partial \bar{f}}{\partial r_\parallel} = \pi^2 Z^2 e^2 \sum_\alpha \left(\frac{\omega_{\text{res}}^\alpha}{k_{\text{res}} c} \right)^2 \frac{1}{p^2} \left(\frac{\partial}{\partial p} p + \frac{\partial}{\partial \mu} \left(\frac{k_{\text{res}} v}{\omega_{\text{res}}^\alpha} - \mu \right) \right) \tag{2.16}$$

$$\times \frac{p(1 - \mu^2) W^\alpha(k_{\text{res}})}{|v\mu - \omega_{\text{res}}^\alpha/k|} \left(\frac{\partial}{\partial p} + \left(\frac{k_{\text{res}} v}{\omega_{\text{res}}^\alpha} - \mu \right) \frac{1}{p} \frac{\partial}{\partial \mu} \right) \bar{f} \ , \tag{2.17}$$

every differential operator acting on every term on its right. The *turbulent spectrum* $W^\alpha(k)$ of energy density of wave mode α appears as a replacement of the $\delta \vec{B}^\alpha$ terms, averaging over the phase and polarization of the waves

$$\int_0^\infty dk_\parallel \, W^\alpha(k_\parallel) = \int_{-\infty}^{+\infty} dk_\parallel \, \frac{1}{4\pi} \left| \delta \vec{B}^\alpha(k_\parallel) \right|^2 \ . \tag{2.18}$$

Now, we can gain further insight by linearizing (2.17) in $|\omega_{\text{res}}^\alpha/(kv)| = |\pm v_A/c| \ll 1$ (neglecting quadratic and higher orders) and thus generally qualifying only wave modes to contribute when they move along ($\vec{k}^+ \uparrow\uparrow \vec{B}_0$) or opposed ($\vec{k}^- \uparrow\downarrow \vec{B}_0$) to the regular magnetic field. The quantity

$$\nu_\mu^\alpha \equiv 2\pi^2 |\omega_H| \frac{k_{\text{res}} W^\alpha(k_{\text{res}})}{B_0^2} \tag{2.19}$$

then appears as a coefficient of unit (time)$^{-1}$ in otherwise dimensionless terms and is interpreted as the effective pitch-angle scattering rate by mode $\alpha = \{+, -\}$, gaining

$$\frac{\partial \bar{f}}{\partial t} + \mu v \frac{\partial \bar{f}}{\partial r_\parallel} = \sum_{\alpha = +, -} \frac{v_A^2}{p} \left(\frac{\partial}{\partial p} + \alpha \frac{v}{v_A} \frac{\partial}{\partial \mu} \right) \frac{1 - \mu^2}{2} \nu_\mu^\alpha \frac{p^3}{v^2} \left(\frac{\partial}{\partial p} + \alpha \frac{v}{v_A} \frac{1}{p} \frac{\partial}{\partial \mu} \right) \bar{f} \ . \tag{2.20}$$

For time intervals much larger than the anisotropic scattering relaxation time $\Delta t \gg (\sum_\alpha \nu_\mu^\alpha)^{-1}$ the anisotropic distribution part δf in $\bar{f}$ is only small, i.e.

$$\bar{f}(\vec{r}, t, \mu) = f_0(\vec{r}, t) + \delta f(\vec{r}, t, \mu) \quad \Leftrightarrow \quad f_0(\vec{r}, t) = \frac{1}{2} \int_{-1}^{1} d\mu \, \bar{f}(\vec{r}, t, \mu) \tag{2.21}$$

finally reducing (2.17) to a kinetic equation of the isotropic distribution function $f_0(\vec{r}, t)$

$$\frac{\partial f_0}{\partial t} - \frac{\partial}{\partial r_\parallel} D \frac{\partial f_0}{\partial r_\parallel} + \frac{1}{3p^2} \frac{\partial p^3 u_w}{\partial p} \frac{\partial f_0}{\partial r_\parallel} - \frac{\partial u_w}{\partial r_\parallel} \frac{p}{3} \frac{\partial f_0}{\partial p} - \frac{1}{p^2} \frac{\partial}{\partial p} p^2 D_{\text{pp}} \frac{\partial}{\partial p} f_0 = 0 \ , \tag{2.22}$$

by definition of the *Fokker-Planck coefficients*, hereby called the **spatial diffusion coefficient** D, the effective **wave convection velocity** u_w, and the **momentum diffusion coefficient** D_{pp} (the term $\frac{\partial \delta f}{\partial r_{\parallel}}$ has been removed by partial integration)

$$D \equiv \frac{v^2}{2} \int_0^1 d\mu \, \frac{1 - \mu^2}{v_\mu^+ + v_\mu^-} \tag{2.23}$$

$$u_w \equiv v_A \int_0^1 d\mu \, \frac{v_\mu^+ - v_\mu^-}{v_\mu^+ + v_\mu^-} \tag{2.24}$$

$$D_{pp} \equiv \frac{p^2 v_A^2}{v^2} \int_0^1 d\mu \, 2(1 - \mu^2) \frac{v_\mu^+ v_\mu^-}{v_\mu^+ + v_\mu^-} \ . \tag{2.25}$$

We will return to a interpretation of these terms in the context of our transport equation parameters, after discussing a realistic model of spectral density function $W^\alpha(k)$ below. At this point, it is to be remarked that W^α can also be taken to be equipartitioned between the forward $+$ and backward $-$ component relative to the regular magnetic field. In this isotropic case, then, D and D_{pp} further simplify while u_w vanishes completely.

A similar derivation in 3 Cartesian coordinates x, y, z (instead of the aligning with the direction of the magnetic field $\vec{B}_0/|\vec{B}_0|$) is more tedious, but similar in application, giving

$$\frac{\partial f_0}{\partial t} - \vec{\nabla} D_{ij} \vec{\nabla} f_0 + \frac{1}{3p^2} \frac{\partial (p^3 \vec{u}_w)}{\partial p} (\vec{\nabla} f_0) - (\vec{\nabla} u_w) \frac{p}{3} \frac{\partial f_0}{\partial p} - \frac{1}{p^2} \frac{\partial}{\partial p} p^2 D_{\mathrm{pp}} \frac{\partial}{\partial p} f_0 = 0 \ , \tag{2.26}$$

and then finally, replacing the isotropic phase-space distribution function f_0 by the particle density $f_0 \to N = \frac{1}{4\pi p^2} f_0$ slightly changes the structure of the fourth and fifth term, giving it now full resemblance of the TE (2.1) (the u_w-term is discussed below)

$$\frac{\partial N}{\partial t} - \vec{\nabla} D_{ij} \vec{\nabla} N + \frac{1}{3p^2} \frac{\partial (p^3 \vec{u}_w)}{\partial p} (\vec{\nabla} N) - (\vec{\nabla} u_w) \frac{p^3}{3} \frac{\partial}{\partial p} \frac{N}{p^2} - \frac{\partial}{\partial p} p^2 D_{\mathrm{pp}} \frac{\partial}{\partial p} \frac{N}{p^2} = 0 \ . \tag{2.27}$$

2.1.1.2. Application

The applicability of quasilinear theory to the propagation of galactic cosmic rays was inspired by analogy to the findings of the inter*planetary* medium in the solar system (see e.g. Jokipii [74], [78] or [79]). The heliosphere likewise served as a laboratory for galactic phenomena, as space probes like Helios-2 (1976-1981) or the ongoing mission WIND (since 1994), were used to examine the local environment *in situ*. Fig. 2.1 (from [80]) shows the combination of spectral density measurements, exhibiting good agreement with the expectations from turbulent cascades. The

Figure 2.1. Helios-2 (low-frequency) and WIND (high-frequency) measurements of the turbulence spectrum in the interplanetary medium.

$W(k) \sim k^{-5/3}$ shape is predicted by the assumption of Kolmogorov [81] that the rate of energy transfer between the modes is independent on the wave number k itself, showing good agreement with the observed power spectrum. In this regime, turbulence can be pictured by a combination of vortices (eddies) whose interaction create smaller eddies until their energy goes into the thermal motion (see schematic Fig. 2.2). The markers in Fig. 2.1 then give the so-called *standard length scales* in the turbulent medium, which measure of the spatial scale of the largest turbulent eddies ("correlative scale"), the scale for which viscous dissipation begins to affect the cascade ("Taylor scale") and the smallest eddy scale ("Kolmogorov scale").

The Kolmogorov spectrum $W(k) \sim k^{-5/3}$ is a hydrodynamical prediction which holds when the magnetic field is weak and turbulent motions are mainly given by fluid mechanics (it is also found valid in fluctuations of the Earth atmosphere [82] and the thermal ISM electron spectrum [83]). In case of a strong mean magnetic field, the theory of Kraichnan [84] and Iroshnikov [85] predicts $W(k) \sim k^{-3/2}$. These are two common assumptions for cosmic ray diffusion models [21, 4], giving both acceptable descriptions of CR observations

Figure 2.2. Turbulent fields can be depicted as eddies of different scale. Energy cascade is then a shift towards smaller, more curled eddies.

considering the uncertainty in other propagation effects. To parametrize our ignorance thereof, it is customary to assume a general spectral index $(2 - \delta)$, chosen for convenience (as will seen below) to describe $W^\alpha(k)$ fully isotropically, i.e.

$$W^+(k) = W^-(k) = W(k) = \frac{1}{(1-\delta)} \frac{1}{k_B} \left(\frac{k}{k_B} \right)^{2-\delta} \left| \frac{\delta B}{4\pi} \right| \tag{2.28}$$

with k_B given as the inverse of the basic spatial scale $\lambda_B = 2\pi k_B^{-1}$ of the variations in the regular magnetic field B_0. To evaluate D from $W(k)$, it is necessary to regularize the divergent integral (a complication of previously dropping terms of $O((v_A/v)^2)$ in the resonance condition), but this can be done by assuming spatial variations of the magnetic

field only in between scales of $10^{-6}..10^2$ pc. D can then be given conveniently [75]

$$D \approx 3 \cdot 10^{28} \, \frac{\mathrm{cm}^2}{\mathrm{s}} \, \left| \frac{\delta B}{B_0} \right|^{-2} \cdot \frac{v}{c} \left(\frac{pc}{7Z \, \mathrm{GeV}} \right)^{\delta} , \tag{2.29}$$

or a function of *rigidity* $\rho \equiv p/(Ze)$. (2.29) takes $|\delta B/B_0|$ at basic scale λ_B, i.e. in this formula this ratio is taken as a constant factor that parametrizes the general level of ISM turbulence. We will use this fact in our consideration of transport in the solar vicinity, below.

2.1.2. The diffusion term

From the derivation above, we have seen that the TE (2.1) describes the diffusive behavior of cosmic rays as a ionized, collisionless plasma, in a constant state of scattering off the turbulent MHD fluctuations in the ISM. By the sole term *diffusion* we from now on specifically mean the spatial diffusion term

$$\left(\dot{N} \right)_{\mathrm{Diff}} = \vec{\nabla} \left(D \vec{\nabla} N \right) = \left(\vec{\nabla} D \right) \left(\vec{\nabla} N \right) + D \, \vec{\nabla}^2 N , \tag{2.30}$$

which is given by the *spatial diffusion coefficient D*. The MHD/QLT background of D is then modeled after (2.29)

$$D(\rho) = D_0 \beta^{\eta} \left(\frac{\rho}{\rho_0} \right)^{\delta} \tag{2.31}$$

as a function of particle rigidity ρ relative to an arbitrary reference rigidity ρ_0. In (2.31), the $r_{\parallel}$-dependence in (2.22) was extended to three spatial, Cartesian coordinates. More general models of *anisotropic* diffusion [86] take D_{ij} to be a second-grade tensor, assuming different diffusion properties between directions parallel and perpendicular to the background regular magnetic field. In our models, this is not considered necessary, i.e. D is a scalar function of the energy as well as, possibly, on location. However, many transport models use a spatially homogeneous D.

Note that another parameter $\beta \to \beta^{\eta}$ was introduced to allow for a deviation from QLT at low velocities, e.g. to account for Alfvén wave dissipation [87]. Furthermore, models might to allow for a "broken" power-law, i.e. a transition $\delta \to \delta_{\mathrm{high}}$ above a certain break rigidity ρ_b. This can be made plausible in order to describe B/C measurements in models with a large D_{pp} term (see below, *diffusive reacceleration*).

Customary taken values are $\delta \in [0.3; 0.7]$, $\eta \in [-2; 2]$. The choice of exponent $\delta = \frac{1}{3}$ then resembles the Kolmogorov spectrum, $\delta = \frac{1}{2}$ the Kraichnan spectrum. Other choices just describe deviations from these idealized description of interstellar turbulence. It is taken to be universal throughout the galaxy, as no conclusions were yet to be made about the spatial structure of the turbulent magnetic GMF component [88].

Simple solution: Linear diffusion length.   Considering the diffusion term alone, the TE approximately has the basic Green's function, i.e. solution to a pointlike source distribution concentrated at $\vec{r} = \vec{r}_0$ for $t = 0$ as widely known:

$$\frac{\partial N}{\partial t} = \delta(\vec{r} - \vec{r}_0)\,\delta(t) + D\vec{\nabla}^2 N \tag{2.32}$$

$$\Rightarrow\; N(\vec{r}, t) = \frac{1}{(\sqrt{4\pi D t})^3} \cdot \exp\left(-\frac{|\vec{r} - \vec{r}_0|^2}{4Dt}\right) \tag{2.33}$$

The *diffusion length* $\Delta x(t)$ is defined as the Gaussian width of this solution, after a time t:

$$|\vec{r} - \vec{r}_0| = \Delta x(t) \equiv 2\sqrt{Dt} \tag{2.34}$$

as a useful measure in estimating the propagation distance of protons and heavier nuclei (especially in how fast they reach the boundary of the propagation box), whereas for leptons leptons, their energy loss also has to be taken into account. We consider this in section 2.5.2, below.

2.1.3. The convection term

The following terms in the TE are accounted for convection effects:

$$\left(\dot{N}\right)_{\text{Conv}} = \underbrace{-\vec{\nabla}\left(\vec{V}_C\,N\right)}_{\text{advective motion}} + \underbrace{\partial_p\left(\frac{p}{3}(\vec{\nabla}\cdot\vec{V}_C)N\right)}_{\text{convective acceleration}}, \tag{2.35}$$

that means that convection describes the effect being carried along the background motion (*drift*, or *advection*), but also exchanging energy, leading to acceleration or deceleration depending on the relative direction. Usually convection is described as caused by *galactic winds*, which enter the transport equation as wind velocity $\vec{V}_C$, a function of place but constant in energy.

On a more detailed level, we recall - from the above sketch of QLT - eq. (2.24) in which the quantity u_w appeared, describing a similar convective behavior from the particle interactions with the turbulent MHD waves, which appear in the final form (2.27) as

$$\frac{\partial N}{\partial t} = \ldots - \frac{1}{3p^2}\frac{\partial p^3 \vec{u}_w}{\partial p}(\vec{\nabla}N) + (\vec{\nabla}\vec{u}_w)\frac{p^3}{3}\frac{\partial}{\partial p}\frac{N}{p^2} \tag{2.36}$$

The presence of a galactic wind, i.e. large-scale motion of the interstellar medium by a wind of velocity $\vec{V}_C$, can be implemented in the QLT derivation [75] by incorporating substitutions (2.37) with $V_{C\|}$ the component of the drift parallel to the magnetic field. These lead to a shift in the resonance condition (2.12), i.e.

$$\omega^\alpha(k) \longrightarrow \omega^\alpha(k) + V_{C\|}\,k \tag{2.37}$$

$$u_w \longrightarrow u_w + V_{C\|} \tag{2.38}$$

In the full 3D solution in galactic coordinates, then, the drift velocity $\vec{u}_C$ appears as a shift in the convective scattering velocity $\vec{u}_w$:

$$\frac{\partial N}{\partial t} = \ldots - \frac{1}{3p^2} \frac{\partial p^3 \left[\vec{u}_w + \vec{V}_C \right]}{\partial p} (\vec{\nabla} N) + (\vec{\nabla} \left[\vec{u}_w + \vec{V}_C \right]) \frac{p^3}{3} \frac{\partial}{\partial p} \frac{N}{p^2} \qquad (2.39)$$

In this galactic picture, it will be easier not to differentiate between forward- and backward-scattering on the turbulent fields. As seen in (2.24) and the text below, it follows that $\vec{u}_w$ vanishes. As we further assume no momentum dependence in the interaction with the galactic wind, (2.35) follow.

In CR transport models, convection is not always accounted for. However, as the wind velocity can have a strong divergence $\vec{\nabla} \vec{V}_C$ in vertical direction (becoming strong at high galactic heights), it might play an important role in the outer halo (cf. chapter 1). A common parametrization is thus

$$\vec{V}_C = v_C \cdot \left(\frac{dv_C}{dz} \right) \cdot z \cdot f_v(R) \qquad (2.40)$$

with constant v_C and constant dv_c/dz. The wind is modeled as directed only away from the Galactic Disc, and further it might be a function $f_v(R)$ of radius R from the galactic center, likely to be stronger in regions where more gas and supernova remnants are located inside the disc. Another way of parametrization has been implemented in Dragon (e.g. [56]), which modifies (2.40) for a $|\vec{V}_C| \propto z^2$ dependence in the disc region $|z| < 110\,\text{pc}$, which will not be discussed here.

2.1.4. The reacceleration term

The third result from QLT is this term second order in momentum and with no spatial derivative. Algebraically, it resembles the diffusion term but with p taking the place of spatial coordinates, plus an "advective" movement in momentum space. Note how the second term is usually positive (as $\partial_p N < 0$), thus describing the mean *gain* of energy, while the first momentum "diffusion" term is not directed (symmetrical around zero).

$$\left(\dot{N} \right)_{\text{Reacc}} = \frac{\partial}{\partial p} \left(p^2 D_{pp} \frac{\partial}{\partial p} \frac{N}{p^2} \right) = \underbrace{\frac{\partial}{\partial p} \left(D_{pp} \frac{\partial}{\partial p} N \right)}_{\text{momentum diffusion}} + \underbrace{\frac{\partial}{\partial p} \left(-\frac{2D_{pp}}{p} N \right)}_{\text{adiabatic momentum gain}} \qquad (2.41)$$

This is coined "diffusive reacceleration" at is it able to energize the cosmic rays during propagation, by resonant interaction of the turbulent MHD wave modes with the particle.

Physically, $(\dot{N})_{\text{Reacc}}$ describes the effect of *stochastic reacceleration* (presented in chapter 1), the 2$^{\text{nd}}$-order Fermi acceleration mechanism. The rate in which energy is shifted from the MHD waves to given by the D_{pp} as in (2.25), which can be expressed by the spatial

diffusion coefficient D in our parametrization of wave spectrum $W^\alpha(k)$[89]:

$$D_{pp} = p^2 v_A^2 \left(\frac{4}{3} \cdot \frac{1}{\delta(2-\delta)(4-\delta)(2+\delta)} \right) \left| \frac{\delta B}{B_0} \right|^{-2} \cdot D^{-1} \tag{2.42}$$

$$v_A^2 = \frac{B_0^2}{4\pi \rho_{\text{ISM}}} \quad (\rho_{\text{ISM}} \text{ is the density of the charged gas components}). \tag{2.43}$$

As a remark: In the GALPROP/DRAGON modelization, the strength of this term is not fixed. Instead, a free choice "v_A" is allowed. This is then internally only used to scale $D_{pp} \propto p^2 v_A^2 D^{-1}$, and in general not equal to the real Alfvén velocity v_A as in (2.43), which specifies the speed of MHD wave propagation. This has to be kept in mind when interpreting numerical models, whereas a choice $v_A = 50..100 \frac{\text{km}}{\text{s}}$ is usually regarded as "high reacceleration model", $v_A < 5 \frac{\text{km}}{\text{s}}$ as "low-reacceleration".

2.1.5. The primary source term

The generic CR source term,

$$\left(\dot{N} \right)_{\text{Source}} = Q(p, \vec{r}, t) \,, \tag{2.44}$$

is conveniently separated into a injection spectrum function $Q_{\text{inj}}(\rho)$ and a spatial distribution $Q_{\text{SNR}}(\vec{r})$. In conventional models, SNR are seen as the main primary source of galactic cosmic rays and other contributions are dismissed. $Q_{\text{SNR}}(\vec{r})$ then models the distribution of SNR occurrence as a function rather smooth in space (cf. Fig. 1.11) and constant in time. $Q_{\text{inj}}(\rho)$ is taken as a function of rigidity $\rho = p/(Ze)$ relative to a reference value, as e.g. 1 GV:

$$Q(\vec{r}, E) = Q_{\text{SNR}}(\vec{r}) \cdot Q_{\text{inj}}(p) = Q_{\text{SNR}}(\vec{r}) \cdot Q_0 \cdot (\rho/1\,\text{GV})^{-\alpha}. \tag{2.45}$$

The SNR distribution function chosen for this study follows the suggestion by the GALPROP authors, defined to reproduce the CR distribution inferred by a EGRET γ-ray analysis [34]. It is cylinder symmetrical around the galactic center $R = 0$,

$$Q_{\text{SNR}}(R, z) = \left(\frac{R}{8.3\,\text{kpc}} \right)^\alpha \cdot \exp\left(-\beta \left(\frac{R - 8.3\,\text{kpc}}{8.3\,\text{kpc}} \right) - \frac{|z|}{h} \right) \cdot \Theta(R - 15\,\text{kpc}) \,. \tag{2.46}$$

which assumes the radial parameters ($\alpha = 1.25, \beta = 3.56$) as well as the disc source height $h = 0.2\,\text{kpc}$, and is zero for galactocentric distance $R > 15\,\text{kpc}$. 8.3 kpc appears as the model position of the Sun, Q_{SNR} is chosen this way to equal $Q_{\text{SNR}} = 1$ at our location.

The actual supernova frequency and overall strength is stated by the normalization parameter Q_0. When solving the TE in stationary state, is it very convenient to ignore this constant throughout the calculation and only afterwards assign it a value that seems suitable to describe one given data point, e.g. one energy interval of an observed proton flux. It should be noted that the TE is *linear*, thus this rescaling does not affect the propagation properties per se. Moreover, this means that the solutions to different source functions

(and otherwise fixed transport parameters) are additive:

$$\dot{N}_1 = \text{TE}\left(Q_1\right) \tag{2.47}$$

$$\dot{N}_2 = \text{TE}\left(Q_2\right) \tag{2.48}$$

$$\Rightarrow \dot{N}_{1+2} = \text{TE}\left(Q_1 + Q_2\right) \tag{2.49}$$

which is useful if one considers the effect of singular point sources added on top of a given "background" distribution, as we will do in chapter 4.

As mentioned before, the CR injection spectrum might be a multiply broken power-law. DRAGON transport models were enhanced to allow up to 3 continuous breaks:

$$Q_{\text{inj}}(\rho) = Q_0 \cdot \begin{cases} (\rho/\rho_0)^{-\alpha_0} & \rho \leq \rho_0 \\ (\rho/\rho_0)^{-\alpha_1} & \rho \in [\rho_0, \rho_1] \\ (\rho/\rho_1)^{-\alpha_2}(\rho_1/\rho_0)^{-\alpha_1} & \rho \in [\rho_1, \rho_2] \\ (\rho/\rho_2)^{-\alpha_3}(\rho_2/\rho_1)^{-\alpha_2}(\rho_1/\rho_0)^{-\alpha_1} & \rho \geq \rho_3 \end{cases} \tag{2.50}$$

Free escape: boundary sinks   As described in the first chapter, the turbulent magnetic fields responsible for the diffusive scattering can, of course, only extend up to a certain distance from the Galactic Disc. This is called the *propagation box* and at some maximum radial distance from the center, R_{max} and at the chosen galactic half-height L above and below the plane, the CR density is supposed to drop to zero. In three spatial dimensions, this is forced as Dirichlet boundary conditions on the surface of the propagation box:

$$N(x = \pm R_{\text{max}}, y, z, p) = N(x, y = \pm R_{\text{max}}, z, p) = N(x, y, z = \pm L, p) = 0 \tag{2.51}$$

while R_{max} is usually just a parameter chosen for convenience, the half-height L is a fully relevant transport parameter. Due to its correlation on CR escape time, this choice is e.g. affecting the cosmic clock $^{10}Be/^9Be$. Numerically, it is very simple to just apply this condition through every computation step until the stationary state has been reached (in more complex analytical models, a method of mirror force is sometimes used).

2.1.6. Energy loss terms

We briefly go through the terms responsible for energy loss processes, particle loss by decay or fragmentation, and secondary source production, as these terms in the TE are rather straightforward.

For instance, the energy loss term (or momentum loss, in this choice of coordinate),

$$\left(\dot{N}\right)_{\text{ELoss}} = \partial_p\left(\dot{p}N\right) = \frac{\partial}{\partial p}\frac{\partial p}{\partial t}N \,, \tag{2.52}$$

is the direct result of the chain rule. One of the great advantages of numerical modelization - as opposed to analytical simplifications like the leaky-box - is that the energy loss term can be computed at any point in space specifically, taking into account realistic models of

gas distributions $n_{\text{ISM}}(\vec{r})$ (for ionization of and Coulomb interaction, Bremsstrahlung via the ISM gas), the regular magnetic field component $B_0(\vec{r})$ (for Synchrotron radiation) and the interstellar radiation field density $\epsilon_\nu(\vec{r})$ (for Inverse Compton scattering). Thus, this can combine the picture of diffusive CR propagation with precise theoretical calculations from other fields of particle physics. The total $\dot{p}$ in any point is then to be calculated as one function of location $\vec{r}$ and momentum p:

$$\dot{p}(\vec{r}, p) = \dot{p}_{\text{ion}}(n_{\text{ISM}}(\vec{r}), p) + \dot{p}_{\text{Couloumb}}(n_{\text{ISM}}(\vec{r}), p) \qquad \text{(all species)} \qquad (2.53)$$

$$+ \dot{p}_{\text{BS}}(n_{\text{ISM}}(\vec{r}), p) + \dot{p}_{\text{Sync}}(B_0(\vec{r}), p) + \dot{p}_{\text{IC}}(\epsilon_\nu(\vec{r}), p) \qquad \text{(leptons only)} \qquad (2.54)$$

The $n_{\text{ISM}}(\vec{r})$ gas distributions of H_2, *HI* and *HII* regions will be described more closely in chapter 3 and thus skipped here. The implementation of GMF and ISRF are based on γ-ray observations and described [90]. For the ISRF, several observations of dust and stellar emissions are combined, mainly by the COBE satellite. For a sense of imagination, the total ISRF (CMB + starlight + dust emissions) shows a roughly exponential shape peaking at the Galactic Center with a peak energy density of $\sim 10 \text{eVcm}^{-3}$. For details, see [90]. The regular GMF is idealized as a simple function

$$B_0(R, z) = B_\odot \cdot \exp\left(-\frac{R - R_\odot}{r_0} - \frac{|z|}{z_0}\right) \qquad (2.55)$$

with an overall normalization $B_\odot = 6.1\,\mu\text{G}$ (taken at Solar position $R = R_\odot$) and two scales which, with choices $r_0 = 10\,\text{kpc}$ and $z_0 = 2\,\text{kpc}$, have shown to be in agreement with the longitude and latitude distribution of the Galactic Synchrotron emission at 408 MHz (see also 2000ApJ...537..763S). Note that the direction information of the magnetic information does not matter in the picture of isotropic diffusion.

In subsection 2.4.2, we illustrate the overall impact of the totality of energy loss processes on a sample transport model.

2.1.7. Particle loss terms

Similarly, the particle conversion processes by radioactive decay and fragmentation processes terms (usually coined "catastrophic particle loss" as they remove particles from the mother species)

$$\left(\dot{N}\right)_{\text{PLoss}} = \frac{N}{\tau} = \underbrace{\frac{N}{\tau_R}}_{\text{radioactive}} + \underbrace{n_{\text{ISM}} \cdot v \cdot \sigma_{\text{frag}} \cdot N}_{\text{fragmentation}}, \qquad (2.56)$$

can be given with detailed tables of isotopic decay times τ_R (taking into account the Lorentz boost factor of the particle) and fragmentation cross sections σ_{frag}. As in our leaky-box example in chapter 1, consistency is then given when the amount of particles lost by these interactions are then added to the source term Q of each corresponding daughter particle. This is also called the "spallation network".

2.2. Solar modulation: The force-field approximation
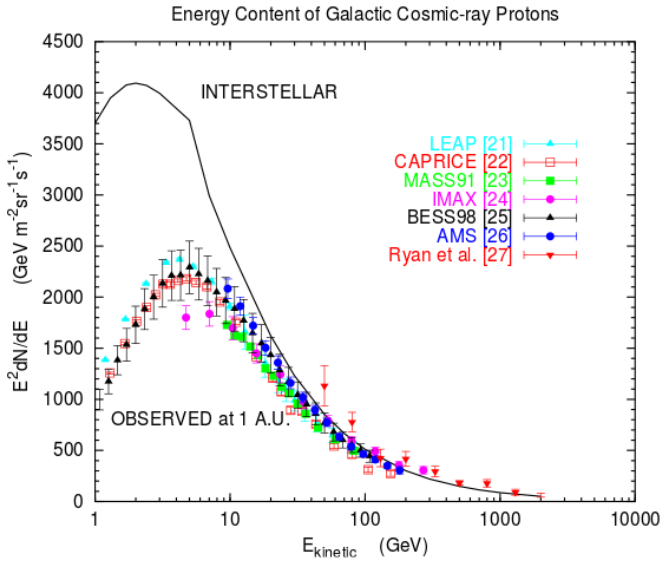
Figure 2.3. Model prediction for interstellar proton flux scaled with energy E^2 (black line) shows a huge low-energy deviation compared to data. This is attributed to the solar modulation in the heliospheric field [45].
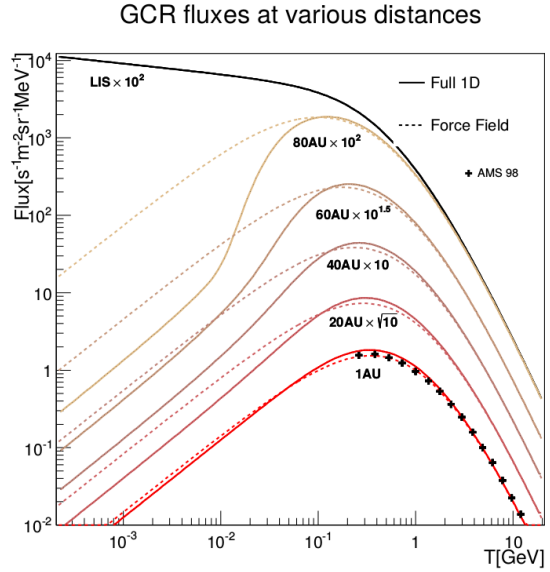
Figure 2.4. FFA is compared with the full simulation of the 1D Parker equation (2.57). It is shown that these methods agree for the result at 1 AE (Earth position). Shown are proton fluxes, scaled by a constant for each distance, for better visualization. Differences become large for large distances, especially below $0, 5$ GeV. Simulation by [91].

The effect of solar modulation was described in chapter 1 as the deceleration of low-energy cosmic rays by propagation through the solar system. This is illustrated in Fig. 2.3, where the black line demonstrates the local *interstellar* solution, outside the heliosphere.
In this exemplary transport model, The predicted proton flux is about a factor 2 (at $E = 3..5$ GeV) to 4 (at $E = 1$ GeV) above the actual observation.

This can be understood by the heliospheric propagation properties. In principle, a heliospheric transport equation, the Parker equation [92], can be constructed similar to the galactic TE (2.1), with the interstellar solution acting as a boundary condition from outside. Model descriptions are then able to give good agreements with locally observed, as is shown in Fig. 2.4: The effect of the heliospheric propagation is shown at various distances from the sun. At the distance of the earth distance (1 AU), this model shows to describe the AMS-01 1998 proton data depicted as black crosses. For this heliospheric model, the graph shows two common approaches, the "Full 1D" solution of the one-dimensional Parker equation and the "Force Field" approximation. The stationary 1D Parker equation looks like [93]

$$\frac{\partial N}{\partial t} = \vec{\nabla}\left(K\,\vec{\nabla}N\right) - \left(\vec{V_S} + \vec{V_D}\right)\vec{\nabla}N + \frac{p}{3}\left(\vec{\nabla}\vec{V_S}\right)\frac{\partial N}{\partial p} \; = 0 \;, \qquad (2.57)$$

This contains a the diffusion term for coefficient K, a convection term with the solar wind velocity $\vec{V}_S$ and additional advective drift velocity $\vec{V}_D$. There is no extra source term considered. The continuous inflow of galactic cosmic rays is considered by requiring

$$N(r,p)\Big|_{\text{heliopause}} = N_{\text{LIS}}(p) \,, \tag{2.58}$$

which might then be solved by numerical codes like HELMOD [94] or HELIOPROP [95]. It is more common, as less computational expensive, to apply the *force-field approximation*: We assume a radial symmetry and an isotropic diffusion coefficient $K \sim p$ (linear in momentum) and omit the drift term $\vec{V}_D$, thereby reducing (2.57) to

$$\frac{\partial N}{\partial r} + \frac{pV_S}{3K}\frac{\partial N}{\partial p} = 0 \,. \tag{2.59}$$

The adherence to the boundary condition (2.58) can be ensured with the help of an auxiliary quantity, the *modulation potential* Φ:

$$\Phi = \frac{1}{3Zec} \int_{r}^{\text{heliopause}} dr' \, \frac{V_S(r')}{K(r')} \tag{2.60}$$

$$N(p) = N^{\text{LIS}}(p + Zec\Phi) \cdot \left(\frac{p}{p + Zc\Phi}\right)^2 \qquad \text{(in momentum } p\text{)} \tag{2.61}$$

$$N(E) = N^{\text{LIS}}(E + Ze\Phi) \cdot \frac{E(E + 2mc^2)}{(E + Ze\Phi)(E + Ze\Phi + 2mc^2)} \qquad \text{(in kinetic energy } E\text{)} \tag{2.62}$$

for particle charge Ze and mass m. It is then customary for model-data comparison to choose a modulation parameter $\Phi \sim 300..1500\,\text{MV}$ best fit to describe a given set of data. As visible in Fig. 2.4, the force field approximation is equivalent to the full 1D Parker equation down to $E \approx 10^{-2}\,\text{MeV}$. It is considered sufficient to describe the model uncertainties due to the solar modulation effects, but it is to be stressed that the parameter Φ does not really reflect a measurable property of the solar activity.

The solar modulation effect as described here does not account for *anisotropic diffusion* effects. In our derivation of QLT, we first described wave-particle interactions separately for directions parallel and perpendicular to the regular magnetic field. Later, we assumed a simplified scenario in which the coupling of the MHD waves to the regular magnetic field is not strong, so that the galactic diffusion coefficient D act equally and independently on the three galactic coordinates (the diffusion tensor is proportional to the unit matrix). It is not clear to which extend this holds, either in the galaxy (e.g. [86]) or the heliosphere (e.g. [96]).

2.3. Dipole anisotropy of arrival directions

Now, we have finished the theoretical description of the transport of CR densities throughout the Galaxy and the solar system. Experimental devices do not actually measure the density N itself, but the intensity I of the local CR flux. This is then seen as an isotropic part and an anisotropic, directed component, written as

$$I(p) = I_0 \cdot (1 + \delta \cos \Theta_\delta) = I_0 \cdot (1 + \vec{\delta} \cdot \vec{e}_r) \,, \tag{2.63}$$

with the isotropic intensity I_0 related to the CR density N and velocity v as

$$I_0(p) = \frac{v \cdot N(p)}{4\pi} \approx \frac{c}{4\pi} N(p) \,, \tag{2.64}$$

and the *dipole anisotropy* δ designates the relative strength of the directed CR component. The direction Θ_δ is defined between the intensity maximum $I_{\max}$ and minimum $I_{\min}$. If written in galactic coordinates (x, y, z), δ is composed by three vectorial dipole anisotropies $\vec{\delta} = (\delta_x, \delta_y, \delta_z)$, $|\vec{\delta}| = \delta$. The galactic unit vector $\vec{e}_r$ might be written using the galactic longitude l and latitude b:

$$\vec{e}_r = \begin{pmatrix} -\cos b \cos l \\ \cos b \sin l \\ \sin b \end{pmatrix} . \tag{2.65}$$

The connection between cosmic ray *flux F* and *flux intensity I* is, by angular integration

$$\vec{F} = \int d\Omega \, I(p) \, \vec{e}_r = I_0(p) \cdot \frac{4\pi}{3} \vec{\delta}(p) = \frac{c}{3} N(p) \vec{\delta}(p) \tag{2.66}$$

This can be equated with the diffusive flux given by QLT. We revert to the phase-space description of $\bar{f}(\vec{r}, p, \mu) = f_0(\vec{r}, p) + \delta f(\vec{r}, p, \mu)$. There, the flux F_r of phase-space density towards a direction r is defined via

$$\frac{\partial F_r}{\partial r} = \frac{\partial \bar{f}}{\partial t} \quad \Rightarrow \quad F_{r_\parallel} = \frac{v}{2} \int_{-1}^{1} d\mu \, \mu \delta f = -D \frac{\partial f_0}{\partial r_\parallel} - \frac{u_w + V_{C\parallel}}{3} p \frac{\partial f_0}{\partial p} \,, \tag{2.67}$$

using (2.22) and amending u_w by the galactic wind velocity. Because we assumed isotropic scattering and the local wind velocity is negligible, the second term vanishes. Then, the density flux in three Galactic coordinates reduces to Fick's first law,

$$\vec{F} = -D \vec{\nabla} N \,. \tag{2.68}$$

By combination of (2.66) and (2.68), we gain an interpretation of anisotropy in terms of CR density gradient, with λ_{mfp} the diffusive mean free path length in three dimensions [97]:

$$\boxed{\vec{\delta} = \frac{3D}{c} \frac{\vec{\nabla} N}{N} = \lambda_{\mathrm{mfp}} \frac{\vec{\nabla} N}{N}} \tag{2.69}$$

2.3.1. Identities for combined dipole anisotropies

In the following, a few useful identities will be derived. These will be helpful to refer to in chapter 4. In this chapter, for every single flux intensity I_i its anisotropy vector $\vec{\delta}_i$ and isotropic intensity I_{i0} defined in analogy to the previous section:

$$I_i = I_{i0} \cdot (1 + \vec{\delta}_i \cdot \vec{e}_r) \, . \tag{2.70}$$

Effective anisotropy in sum fluxes.   Consider several flux contributions I_i that are to be added, e.g. the flux intensities of two particle species, or from two different sources. The dipole anisotropy in the sum flux is

$$I^{\text{sum}} = \sum_i I_i = \overbrace{\left(\sum_i I_{i0} \right)}^{I_0^{\text{sum}}} \cdot \overbrace{\left(1 + \sum_i \frac{I_{i0}}{I_0^{\text{sum}}} \vec{\delta}_i \cdot \vec{e}_r \right)}^{(1 + \vec{\delta}_{\text{eff}} \cdot \vec{e}_r)} \tag{2.71}$$

$$\Rightarrow \vec{\delta}_{\text{eff}} = \sum_i \frac{I_{i0}}{I_0^{\text{sum}}} \vec{\delta}_i \tag{2.72}$$

Effective anisotropy in flux ratios.   Likewise, with ratio observables of the type N/D, as e.g. B/C or e^+/p, (numerator N, denominator species D), the effective dipole isotropy is

$$\frac{I_N}{I_D} = \frac{I_{N0}}{I_{D0}} \cdot \frac{1 + \vec{\delta}_N \cdot \vec{e}_r}{1 + \vec{\delta}_D \cdot \vec{e}_r} \approx \frac{I_{N0}}{I_{D0}} \left(1 + \vec{\delta}_N \cdot \vec{e}_r - \vec{\delta}_D \cdot \vec{e}_r \right) \tag{2.73}$$

$$\Rightarrow \vec{\delta}_{\text{eff}} = \vec{\delta}_N - \vec{\delta}_D \tag{2.74}$$

the conclusion in (2.73) follows from the geometric series expansion to leading order,

$$\frac{1}{1+x} = \sum_{n=0}^{\infty} (-x)^n = 1 - x + O(x^2) \tag{2.75}$$

Higher order anisotropies. For an arbitrary flux intensity $I = I(\Omega)$ containing angular information Ω e.g. expressed in galactic longitude l and latitude b, or otherwise, there exists an unique decomposition into spherical harmonics $Y_{lm}(\frac{\pi}{2} - b, l)$ due to their orthogonality ($\pi 2 - b$ chosen for convenience). The complex coefficients of this series expansion are usually called a_{lm} and the *multipole power* C_l of the l-th order multipole combines the quadratic values of all a_{lm} belonging to this order:

$$I(\Omega) = \sum_{l=0}^{\infty} \sum_{m=-l}^{l} a_{lm} \, Y_{lm}(\frac{\pi}{2} - b, l) \tag{2.76}$$

$$a_{lm} = \int d\Omega \, I(\Omega) \, Y_{lm}^{*}(\frac{\pi}{2} - b, l) \tag{2.77}$$

$$C_l = \frac{1}{2l+1} \sum_{m=-l}^{l} |a_{lm}|^2 \tag{2.78}$$

These are standard denotation in spherical harmonic analysis. With increasing l, the Y_{lm} describe smaller angular structure. The spherical harmonics of order l divide the whole 4π-sphere into segments of $\frac{2\pi}{l}$ each: The monopole power C_0 is the overall average, the dipole power C_1 describes angular variations of half the sphere (e.g. "forward-backward", "north-south", "east-west"), the quadrupole power C_2 is then a measure of total correlated scales of quarter-sphere area and so on. Examples are given in the *sky-map* representation in Fig. 2.5: Galactic longitude l is given in horizontal and latitude b given in vertical direction, with the center of the skymap pointing at the Galactic Center ($l = b = 0$). Shown are the spherical harmonics for dipole Y_{1m} (left), quadrupole Y_{2m} and octopole Y_{3m} order, with the real Y_{l0} function in the top row and then each real and imaginary part of the Y_{lm} for increasing m.
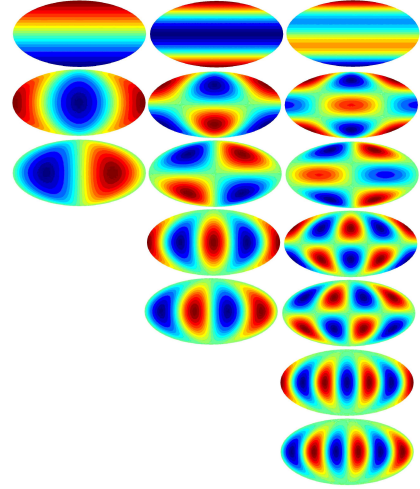
Figure 2.5. Skymap visualization of the first spherical harmonics.
From top to bottom: $m = 0$ (purely real), $m = 1$ real part, $m = 1$ imaginary part, etc. to $m = l$. **(left)** dipole $l = 1$ **(middle)** quadrupole $l = 2$ **(right)** octopole $l = 3$.

Usually, analysis of cosmic ray arrival directions is limited to only a few orders. While the dipole anisotropy is already low, the higher orders are often not considered at all (contrary to other fields, e.g. cosmic microwave background measurements). This will be verified for our leptonic transport scenario in chapter 4. However, measurements of higher-order multipole information in the cosmic ray arrival directions might shed light on the anisotropic nature on heliospheric transport processes.

"Fake" quadrupole anisotropy from denominator dipole anisotropy. From this consideration, we can estimate the quadratic term from (2.75) as a further contribution to (2.73). In an flux ratio like e^+/p (positron flux relative to proton flux), the dipole anisotropy from the denominator would then appear as a small quadrupole term in the overall flux ratio:

$$\frac{I_N}{I_D} \approx \frac{I_{N,0}}{I_{D,0}} \left(1 + \vec{\delta}_{\text{eff}} \cdot \vec{e}_r + (\vec{\delta}_D \vec{e}_r)^2 + O(\delta_D^3) \right) \tag{2.79}$$

In this e^+/p example, a proton dipole anisotropy from the Galactic Center $\vec{\delta}_D = \delta_p \vec{e}_x$ gives

$$\delta_p^2 \cos^2 b \cos^2 l = \delta_p^2 \left(\sqrt{\frac{8\pi}{15}} Y_{22} + \sqrt{\frac{8\pi}{15}} Y_{2-2} - \sqrt{\frac{4\pi}{45}} Y_{20} + \sqrt{\frac{4\pi}{9}} Y_{00} \right) \tag{2.80}$$

with the spherical harmonics $Y_{lm}(\frac{\pi}{2} - b, l)$, amounting to a quadrupole power of (the definition of multipole powers is recalled below)

$$C_2 = \delta_p^4 \cdot \frac{1}{5} \left[\frac{4\pi}{45} + 2 \cdot \frac{8\pi}{15} \right] = \frac{52\pi}{225} \delta_p^4 = 0.73 \, \delta_p^4 \tag{2.81}$$

for a small background proton anisotropy of $\sim 1\%$, this is $7.3 \cdot 10^{-9}$, a tiny contribution. But as the analysis of experimental data, like AMS-02, is also interested in quadrupole anisotropies, this is nevertheless to be mentioned.

2.3.2. Cumulative energy intervals

Anisotropy limits, as they are given by up-to-date measurements as AMS-02 [98, 99], are usually given as upper limits at 95% confidence level, within which the measured events are compatible with fully isotropic arrival directions. Moreover, these are taken in *cumulative* intervals of kinetic energy over a wide energy range typically far exceeding the actual detector resolution. Thereby all events over a given energy are regarded up to a limiting energy E_{max}, not only up to the start of the next energy interval. Doing so has the advantage of far greater event statistics. To compare DRAGON model predictions with such observations, we also implement this way of cumulation over large energy bins. In our model predictions of dipole anisotropy, the spectral flux density $N(E)$ is replaced by

$$N_{\text{cumul}}(E) = \int_E^{E_{\text{max}}} dE' \, N(E') \tag{2.82}$$

$$\vec{\delta}(E) = \frac{3}{c} \frac{\int_E^{E_{\text{max}}} dE' \, D(E') \vec{\nabla} N(E')}{\int_E^{E_{\text{max}}} dE' \, N(E')} \tag{2.83}$$

with the upper energy limit E_{max} chosen in comparison to what a specific experiment chose as limit. The anisotropy limits used for AMS-02 proton measurements cumulate up to $E_{\text{max}} = 1.8\,\text{TeV}$, while for anisotropies of leptonic fluxes like e^-, e^+ or the ratio e^+/p, they state $E_{\text{max}} = 350\,\text{GeV}$ (above this energy, the detector shows a drop in proton rejection

capability, i.e. it is not distinguishable whether a single particle was a positron or electron or a misidentified proton).

2.4. Numerical codes: Discretizing the Galaxy

For numerical solvers of partial differential equations, there exists a range of possibilities (standard literature herefore e.g. is [100]). This is necessarily accompanied by discretizing any physical coordinates (position, momentum, time) within an adequate grid resolution, e.g. $dt \to \Delta t$. The essential challenge for the transport equation, however, is to describe the physical processes relevant *over a wide range of time-scales*, A choice $\Delta t \gtrsim 1\,\mathrm{Myr}$ would be adequate to account e.g. for the large escape time (diffusion throughout the halo) or ^{10}Be decay half-life, but would greatly overestimate fast processes the high-energy leptonic energy losses in every step. A choice more precise for the latter, $\Delta t \sim 100\,\mathrm{yr}$, would then require an utopically large number of steps to find a state of equilibrium in slow processes like diffusion. Hence, the *state of equilibrium has to be achieved at different time scales independently*.

The Galaxy is then discretized in each dimension by choice of a grid, now with x being representative for each coordinate x, y, z, p unless otherwise stated, and quantities like the CR density $N(x, p)$ accordingly,

$$x \longrightarrow x_i, \qquad\qquad i = 0, 1, \dots, \tag{2.84}$$

$$N(x, p) \longrightarrow N_i = N(x_i) \qquad i = 0, 1, \dots \; . \tag{2.85}$$

Further a *finite-differencing scheme*, has to be chosen to discretize the first and second derivatives. For this work, it will be important that the grid steps $(x_{i+1} - xi)$ are not constant everywhere. This is referred to as *non-equidistant spacing* or as a *non-uniform spatial grid*. The preparatory work of this thesis was our own implementation of non-uniform grids in DRAGON and the numerical tests thereof, which is why a few of the arising complications have to be discussed here.

In the given TE, there are no mixed differential operators, i.e. each term only acts on a single coordinate. In this case, it is possible to apply the operators sequentially, reducing the amount of equations that have to be solved in every propagation step ("operator splitting"). For spatial coordinates, we then choose the central schemes

$$\frac{\partial N}{\partial x} \longrightarrow \frac{1}{2} \left(\frac{N_{i+1} - N_i}{x_{i+1} - x_i} + \frac{N_i - N_{i-1}}{x_i - x_{i-1}} \right) \tag{2.86}$$

$$\frac{\partial^2 N}{\partial x^2} \longrightarrow \frac{1}{\frac{1}{2}(x_{i+1} - x_{i-1})} \left(\frac{N_{i+1} - N_i}{x_{i+1} - x_i} - \frac{N_i - N_{i-1}}{x_i - x_{i-1}} \right) . \tag{2.87}$$

Each differencing scheme introduces an inevitable deviation from the mathematical derivative which is called *truncation error*. It will be shown that this restricts the choice of non-uniform grids in order to avoid large artificial errors. We will focus this discussion on

the differencing schemes for the spatial variables, because the momentum variables did not have to be modified in this work. However, most steps would be analogous for the momentum grid, which is out of practicality chosen in a logarithmic fashion, $p_i = p_0 \cdot (\Delta \log p)^i$ (with fixed $\Delta \log p$, the momentum resolution).

Time is implemented as a progressive variable, i.e.. there is no temporal grid. As mentioned above, internal quantizations Δt have to be chosen in order to propagate the numerical TE through time. From any previous solution N_i^{prev} in a calculational step at time t, the TE dictates behavior at the next step N_i^{next} at time $t + \Delta t$ (for better visual clarity, I use the labels next/prev instead of the common designation $t + \Delta t$ and t.):

$$\frac{\partial N_i}{\partial t} \equiv \frac{N_i^{\text{next}} - N_i^{\text{prev}}}{\Delta t} \tag{2.88}$$

The exact implementation of this transition, however, is crucial for the stability and accuracy of the algorithm. In Dragon, a *Crank-Nicolson* (CN) implicit scheme [101] is used, which guarantees independence of the choice of Δt from the spatial and momentum grid spacings [100]. As a downside, it is known to cause spurious *oscillations* when there are steep gradients between two neighboring grid points. As this has shown to be a serious problem in grid creation, the appearance of these oscillations is explained in appendix A.2. Implicit propagation schemes function by stating a system of linear equations for the N^{next} and N^{prev} densities at *all*[1] points involved, i.e. $N_{i-1}^{\text{prev}}, N_i^{\text{prev}}, N_{i+1}^{\text{prev}}, N_{i-1}^{\text{next}}, N_i^{\text{next}}, N_{i+1}^{\text{next}}$. This then forms a matrix which is inverted in order to *implicitly* solve for $N^{t+\Delta t}$ from N^t.

By the splitting of operators, every term in the TE takes on the form of some linear differential operator $\mathcal{D}$, acting like

$$\mathcal{D} N_i = \alpha_i^{(1)} N_{i-1} - \alpha_i^{(2)} N_i + \alpha_i^{(3)} N_{i+1} \tag{2.89}$$

this defines the CN coefficients $\alpha_i^{(1..3)}$, which for every grid point x_i contain the connection between the neighboring grid points. The CN decomposition of $\left(\partial N / \partial t = \mathcal{D}N + Q \right)$, given any constant[2] source function Q, reads:

$$\frac{N_i^{\text{next}} - N_i^{\text{prev}}}{\Delta t} = \frac{1}{2} \left(\mathcal{D} N_i^{\text{next}} + \mathcal{D} N_i^{\text{prev}} \right) + Q_i \tag{2.90}$$

$$= \alpha_{i-1}^{(1)} \left(N_{i-1}^{\text{next}} + N_{i-1}^{\text{prev}} \right) + \alpha_i^{(2)} \left(N_i^{\text{next}} + N_i^{\text{prev}} \right) + \alpha_{i+1}^{(3)} \left(N_{i+1}^{\text{next}} + N_{i+1}^{\text{prev}} \right)$$
$$+ Q_i \tag{2.91}$$

---

[1] as opposed to *fully explicit* methods that define an equation F for $N_i^{\text{next}} = F(\{N^{\text{prev}}\})$ and to *fully implicit* methods that define an equation G as $N_i^{\text{prev}} = G(\{N^{\text{next}}\})$ that needs to be inverted. The Crank-Nicolson method is a way of *averaging* between those methods.

[2] the case of time-dependent sources would require splitting $Q_i \longrightarrow \frac{1}{2} Q_i^{\text{next}} + \frac{1}{2} Q_i^{\text{prev}}$, consistently.

which can easily be transformed to a tridiagonal $(d \times d)$ -matrix equation (for d grid points):

$$
\left(\mathbb{1} + \frac{\Delta t}{2} \begin{pmatrix} \alpha_0^{(2)} & -\alpha_0^{(3)} & 0 & \cdots \\ -\alpha_1^{(1)} & \alpha_1^{(2)} & -\alpha_1^{(3)} & \cdots \\ 0 & -\alpha_2^{(1)} & \alpha_2^{(2)} & \cdots \\ \cdots & \cdots & \cdots & \cdots \end{pmatrix} \right) \cdot \begin{pmatrix} N_0^{\text{next}} \\ N_1^{\text{next}} \\ N_2^{\text{next}} \\ \cdots \end{pmatrix}
$$

$$
= \left(\mathbb{1} + \frac{\Delta t}{2} \begin{pmatrix} -\alpha_0^{(2)} & \alpha_0^{(3)} & 0 & \cdots \\ \alpha_1^{(1)} & -\alpha_1^{(2)} & \alpha_1^{(3)} & \cdots \\ 0 & \alpha_2^{(1)} & -\alpha_2^{(2)} & \cdots \\ \cdots & \cdots & \cdots & \cdots \end{pmatrix} \right) \cdot \begin{pmatrix} N_0^{\text{prev}} \\ N_1^{\text{prev}} \\ N_2^{\text{prev}} \\ \cdots \end{pmatrix} + \begin{pmatrix} Q_0 \\ Q_1 \\ Q_2 \\ \cdots \end{pmatrix} \Delta t , \tag{2.92}
$$

thus being of a basic form[3] $\left(S \vec{N}^{\text{next}} = \vec{R} \text{ with tridiagonal matrix } S \right)$, which can be solved directly for $\vec{N}^{\text{next}}$ employing the Thomas algorithm[102]. It is then assumed that each of the TE operators $\mathcal{D}$ operate on a specific time scale. If Δt is of the order of this scale, repeated iteration of (2.92) will drive the system into equilibrium. The number of repetitions is usually chosen $N_{\text{rept}} = 30..60$.

To achieve overall stationarity, the value of Δt is stepwise refined. Starting from a large $\Delta t = \Delta t_{\text{max}}$, a rough distribution can be solved ($N_{\text{rept}} \times (2.92)$ in each direction x, y, z, p) that holds the stationary state for all effects contributing at that order. Then, Δt is decreased by a factor $f_{\Delta t}$ e.g. $\Delta t = \frac{1}{4} \Delta t_{\text{max}}$ and from the rough distribution, every operator relevant at $\frac{1}{4} \Delta t_{\text{max}}$ is driven into equilibrium by $N_{\text{rept}} \times (2.92)$. The whole procedure is repeated with $\Delta t = \frac{1}{16} \Delta t_{\text{max}}, \frac{1}{64} \Delta t_{\text{max}}$, etc. until a minimum scale $\left(\Delta t \leq \Delta t_{\text{min}} \right)$ is reached below which no significant astrophysical processes are considered.

To take care for the free escape condition, the boundary values are forced in every repetition,

$$
N_0^{\text{next}} \overset{!}{=} 0 \tag{2.93}
$$

$$
N_{d-1}^{\text{next}} \overset{!}{=} 0 , \tag{2.94}
$$

for each spatial direction. No boundary condition is applied for the momentum grid, i.e. particles from the lowest momentum bin become removed from the system if further decelerated.

As conclusion, the operator-splitting, time-scale-refining, CN scheme implemented in DRAGON is believed to adequately describe the physical effects of cosmic ray propagation. In equilibrium, and accounting for the boundary conditions, there will then be a prediction of the galactic density distribution of every CR isotope, which can be evaluated at the local interstellar flux outside the heliosphere. To compare this model prediction with observed

---

[3] tridiagonal matrices have only diagonal and neighboring entries.

CR fluxes, the effects of solar modulation have still to be regarded, as done below.

Before that, I want to shed some insight on the grid-dependent truncation error for the inhomogeneous diffusion operator, as this will be used in chapter 3.1.

2.4.1. Discretization of inhomogeneous diffusion

The diffusion term (2.30), reduced to one coordinate for simplicity ($D_i = D(x_i, y_j, z_k)$), reads

$$\left(\dot{N}\right)_{\text{Diff}} = -\frac{\partial D}{\partial x}\frac{\partial N}{\partial x} - D\frac{\partial^2 N}{\partial x^2} \tag{2.95}$$

$$\Rightarrow \mathcal{D}_{\text{Diff}} N_i = -\left[\frac{dD}{dx}\right]\left(\frac{N_{i+1} - N_i}{x_{i+1} - x_i} + \frac{N_i - N_{i-1}}{x_i - x_{i-1}}\right)$$

$$- \frac{D_i}{x_{i+1} - x_{i-1}}\left(\frac{N_{i+1} - N_i}{x_{i+1} - x_i} - \frac{N_i - N_{i-1}}{x_i - x_{i-1}}\right) \tag{2.96}$$

The inhomogeneous diffusion term $\propto [dD/dx]$ obviously vanishes for a diffusion coefficient constant everywhere, and for small gradients over several kiloparsecs a differencing scheme analogous to (2.86) can be chosen. We, however, will ultimately want to consider very local fluctuations of a factor of 10..100 over a few tens of parsec. Thus, we need to minimize the truncation error. With the abbreviation

$$\Delta x^+ \equiv x_{i+1} - x_i \tag{2.97}$$

$$\Delta x^- \equiv x_i - x_{i-1} \tag{2.98}$$

$$\Delta x \equiv \frac{1}{2}(x_{i+1} - x_{i-1}) \tag{2.99}$$

the function values at neighboring grid points are described by the corresponding Taylor expansion (N' the first derivative etc.)

$$N_{i+1} = N + (\Delta x^+)N' + \frac{1}{2}(\Delta x^+)^2 N'' + \frac{1}{6}(\Delta x^+)^3 N''' + O((\Delta x^+)^4) \tag{2.100}$$

$$N_{i-1} = N - (\Delta x^-)N' + \frac{1}{2}(\Delta x^-)^2 N'' - \frac{1}{6}(\Delta x^-)^3 N''' + O((\Delta x^-)^4) \,, \tag{2.101}$$

and thus the truncation error η on $[dN/dx]$ as chosen in (2.86) is of first order in N'':

$$\eta_{dN/dx} = (2.86) - N' = \left[0\right] N + \left[0\right] N' + \left[\frac{\Delta x^+ - \Delta x^-}{4}\right] N'' + \left[\frac{\Delta x^{+2} + \Delta x^{-2}}{12}\right] N'''$$

$$\tag{2.102}$$

While this is acceptable for the CR density N itself (N was considered sufficiently smooth in the QLT derivation), we found that the error on $[dD/dx]$ is minimized if constructed as

$$\frac{dD}{dx} \longrightarrow \left[-\frac{\Delta x^+}{2\Delta x \Delta x^-} \right] D_{i-1} + \left[\frac{\Delta x^+ - \Delta x^-}{\Delta x^+ \Delta x^-} \right] D_i + \left[\frac{\Delta x^-}{2\Delta x \Delta x^+} \right] D_{i+1} \qquad (2.103)$$

resulting in the truncation error after substituting $D_{i\pm1}$ with their respective Taylor expansions:

$$\eta_{dD/dx} = (2.103) - D' = \left[0\right] D + \left[0\right] D' + \left[0\right] D'' + \left[\frac{\Delta x^+ \Delta x^-}{12\Delta x} \left(\Delta x^+ - \Delta x^- \right) \right] D''' \quad (2.104)$$

And the combined truncation error to leading order

$$\eta_{[dD/dx][dN/dx]} = (2.86) \times (2.103) - D'N' = \left[\frac{\Delta x^+ \Delta x^-}{12\Delta x} \left(\Delta x^+ - \Delta x^- \right) \right] D'''N'$$
$$+ \left[\frac{\Delta x^+ - \Delta x^-}{4} \right] D'N''$$
$$+ \left[\frac{\Delta x^{+2} + \Delta x^{-2}}{12} \right] D'N''' \qquad (2.105)$$

As can be seen, for a uniform grid the first two terms vanish. In order to minimize this error for a non-uniform grid, then, this means that the distribution of x_i must accommodate the course of D' and higher derivatives, i.e. where gradients are thought to be large, a fine resolution is required.

Similarly, the truncation error on the homogeneous diffusion term $[D \, d^2N/dx^2]$ is

$$\eta_{[D \, d^2 N/dx^2]} = D \times (2.87) - DN'' = \frac{2}{3}(\Delta x^+ - \Delta x^-)DN''' \qquad (2.106)$$

We will refer to these quantities as they in the discussion of our non-uniform grid choice, section 3.2).

2.4.2. Overall impact of energy losses

In chapter 3, we will argue that the structure of the ISM in the solar neighborhood might have a profound effect on the energy losses and the diffusion coefficient, locally. Thus, it is now helpful to advance our understanding of these terms in the following subsections. With DRAGON, we shed some light on the full impact of the energy loss terms. In order to assess the overall effect, we take the reference model BG, described in chapter 3, and then temporarily remove the energy loss terms in the DRAGON code. We can then compare the standard BG with a hypothetical no-energy-loss world. The details of the reference model BG are of no relevance here, we only want to emphasize the differences the energy loss terms make. Note that the BG model is not designed to accurately describe the high-energy AMS-02 e^- and e^+ fluxes. Figs. 2.6, 2.7, 2.8 show the result of our model evaluation for electrons, positrons and protons, showing each, in their left part, the reference in red and the no-energy-loss prediction in blue. The local interstellar fluxes are shown as dashed lines and, as solid lines, solar modulation is fit to agreement with AMS-02 e^- and e^+ data and PAMELA p data, respectively (also drawn in).

For leptons (Figs. 2.6 and 2.7), the energy losses reduce the local fluxes to about a factor of $\frac{1}{3}$ to $\frac{1}{2}$ for medium energies $E \in [0.5, 100]$ GeV. With rising energies, the importance of the energy losses even rises: This is due to the $\dot{E} \propto -E^2$ dependence of Synchrotron and Inverse Compton radiating powers. Towards lower energies, the Ionization and Coulomb interactions gain dominance, but this is completely in the solar modulation range where local fluxes are strongly influenced (for comparison, in these plots the modulation parameter was fixed so that it agrees with the AMS-02 measurements [103] in the low-energy range, for the standard scenario. The energy loss processes are charge-symmetric; the differences between the ratio between electrons and positrons is only due to the much larger electron densities. Due to the large impact of the high-energy radiation processes on the local leptonic fluxes, it shows that is indeed crucial how the local GMF and ISRF actually look like.
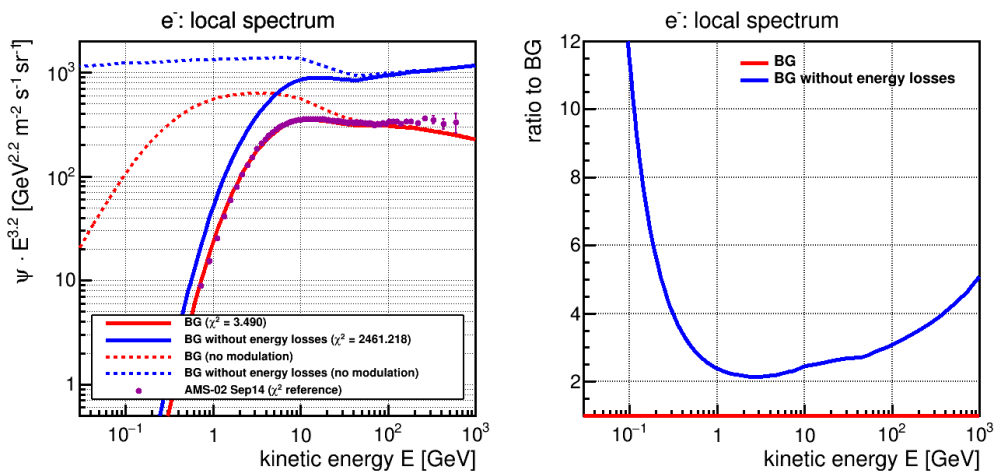
Figure 2.6. For the local electron flux prediction (scaled with $E^{3.2}$) in red, the blue line shows a comparison with no-energy-loss propagation. The **left** panel shows the spectra after solar modulation (solid) and the unmodulated interstellar spectra (dashed), using the same modulation potential $\Phi = 875$ MV. The **right** panel shows the ratio between the two unmodulated spectra.
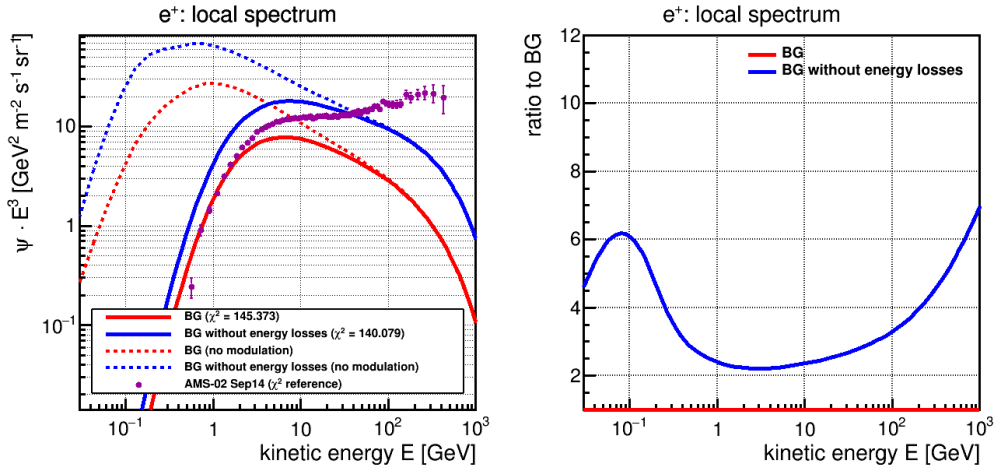
Figure 2.7. For the local positron flux prediction (scaled with E^3) in red, the blue line shows a comparison with no-energy-loss propagation. The **left** panel shows the spectra after solar modulation (solid) and the unmodulated interstellar spectra (dashed), using the same modulation potential $\Phi = 680\,\text{MV}$. The **right** panel shows the ratio between the two unmodulated spectra.

In contrast, the proton spectrum (fig 2.8) prediction is nearly unchanged by the absence of energy losses. While there are large deviations for $E < 0.3\,\text{GeV}$ due to the absence of Coulomb interactions, and to a smaller part Ionization processes, these fall completely in the solar modulation range: For the same modulation parameter $\Phi = 540\,\text{MV}$, the two proton spectra coincide. For very low energies $E \ll Ze\Phi$, the force-field-modulation (2.62) reduces to $N(E) \propto E \cdot N^{\text{LIS}}(Ze\Phi)$ only. The difference in energy losses are thereby irrelevant, which means the proton flux predictions are very robust against uncertainties in the interstellar gas density.
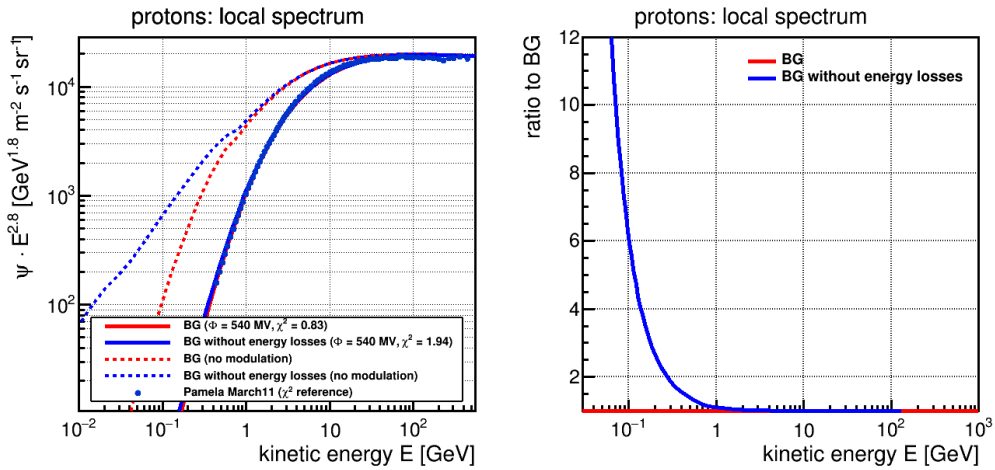
Figure 2.8. For the local proton flux prediction (scaled with $E^2.8$) in red, the blue line shows a comparison with no-energy-loss propagation. The **left** panel shows the spectra after solar modulation (solid) and the unmodulated interstellar spectra (dashed), using the same modulation potential $\Phi = 540\,\text{MV}$. The **right** panel shows the ratio between the two unmodulated spectra.

2.4.3. Overall impact of the diffusion coefficient

Similarly, we can investigate simple modifications of the the diffusion coefficient, i.e. scattering efficiency of cosmic rays on the turbulent magnetic field. In models of CR propagation, the diffusion coefficient prefactor D_0 is only constrained, by the influence of CR escape time on the $^{10}Be/^9Be$ or B/C measurements, if a certain height $2L$ of the propagation box is assumed.

To illustrate the effect different choices of D_0 have at fixed $2L$, we take a model as above and vary D_0 by a factor of 0.01, 0.1, 10 or 100. We show, in Fig. 2.9 the impact on the local proton flux, which is mostly primarily created, and the local positron flux, completely by secondary production. Recall that a *increase* in D_0 means *faster* diffusion, i.e. the edge of the propagation box is reached earlier. A *decrease* in D_0 is *slower* diffusion, i.e. the distribution of primary particles is closer to the source distribution. It can be seen that the scenarios of faster diffusion (green, yellow) only have a slight effect on the proton spectrum. For slower diffusion (cyan, blue) the spectrum is closer to the source injection spectrum. These proton spectra are set to be normalized at $E = 95$ GeV in every scenario.
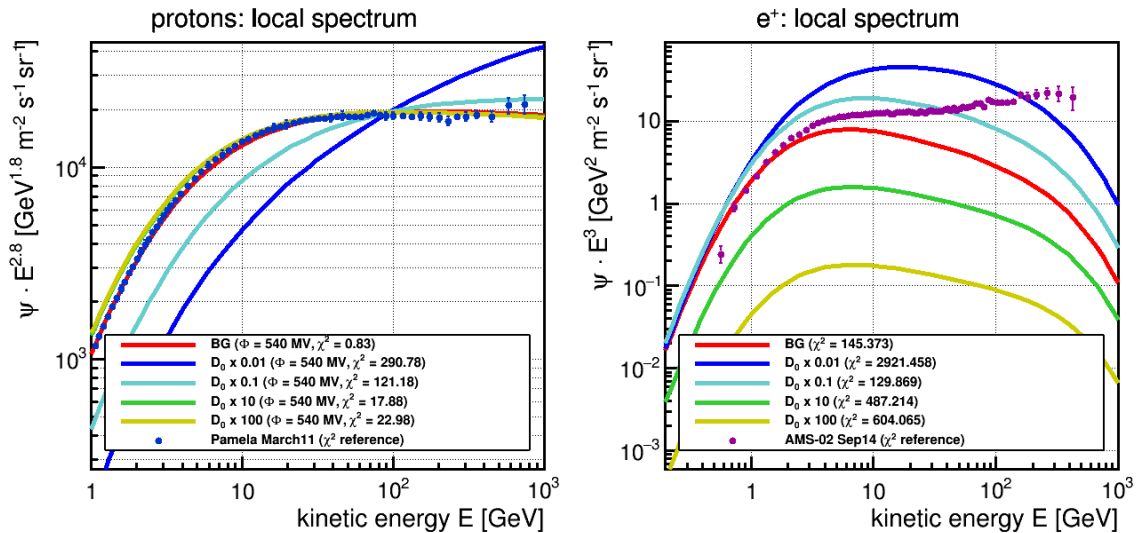
Figure 2.9. Variation of D_0: A reduction of diffusion coefficient ("slower diffusion") equals a higher scattering rate, longer galactic residence time and statistically more particle interactions, while an increase ("faster diffusion") leads to the opposite. The effect on local spectra is shown in the **left** panel for protons (scaled with $E^{2.8}$) and in the **right** panel for positrons (scaled with E^3).

The secondary production of e^+ is affected strongly by the choice of D_0. Positrons come mainly from proton-gas collisions, of which there are fewer in scenarios of fast diffusion (green, yellow). In slow diffusion (cyan, blue), collisions are greatly enhanced and secondary production rises. This is also illustrated by the production of boron from carbon in the B/C (Fig. 2.10 left).
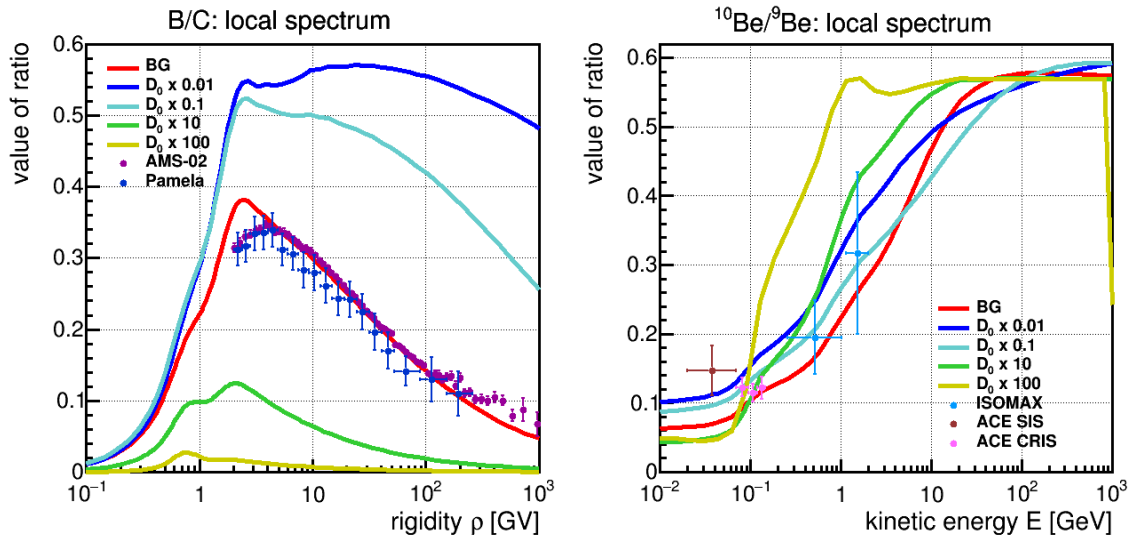
Figure 2.10. Variation of D_0: A reduction of diffusion coefficient ("slower diffusion") equals a higher scattering rate, longer galactic residence time and statistically more particle interactions, while an increase ("faster diffusion") leads to the opposite. The effect on local spectra is shown in the **left** panel for B/C and in the **right** panel for $^{10}Be/^9Be$.

Moreover, the change in escape time corresponding to variation of D_0 shows very different predictions for $^{10}Be/^9Be$. This observable is more complex in this interpretation, because both ^{10}Be and ^9Be are created in collisions. After these, the decay of ^{10}Be takes place. So, for the fastened diffusion (green, yellow) there is less time to decay, which is why the ratio assumes a flat, near constant behavior for high energies. This is the same value that was assumed for the reference model at high energy, $E \gtrsim 100$ GeV, by the same reason. On the other side, if diffusion becomes slower (cyan, blue) all ^{10}Be particles have a longer time to decay, but at the same time, secondary production is increased and both isotopes are created more frequently. The latter effect dominates the low-energy $^{10}Be/^9Be$, increasing the value over the ACE observation.

This illustrates the constraining power of the $^{10}Be/^9Be$ and B/C observables. A further plus in considering these is the cancellation of overall source normalization in a model.

2.5. Simplified model for a pulsar-like source

For the discussion of point sources like pulsars, we will give the analytical solution of a simplified transport equation now. It is also instructive for a general understanding of simple TEs, which however is a very restricted model and does not allow for the entirety of propagation effects presented here. This model drops convection, reacceleration and all nuclear interactions, i.e. describes only the production of $e^{\pm}$ pairs, as we expect coming from PWNe (see chapter 1).

2.5.1. Analytical solution

We only consider a simple scalar, spatially homogeneous diffusion term $D(E)$ and an approximation of $b(E) = -\dot{E}$, the high-energy loss function, for Synchrotron and Inverse Compton effects only.

$$\frac{\partial N}{\partial t} = \vec{\nabla}\left(D(E)\,\vec{\nabla}N\right) + \frac{\partial}{\partial E}\left(b(E)N\right) + Q_{\text{PS}}(E, \vec{r}, t) \qquad (2.107)$$

$Q_{\text{PS}}(E, \vec{r}, t)$ is the point source term, with an injection spectrum of *cutoff-power-law* shape (as was suggested in section 1.3.3.2, this is due to the combination of shock acceleration and Synchrotron radiation inside the PWN):

$$Q_{\text{PS}}(E, \vec{r}, t) = Q_0 \cdot \underbrace{\left((E/1\,\text{GeV})^{-\Gamma} \cdot \exp\left(-E/E_{\text{cut}}\right)\right)}_{Q(E)} \cdot \delta(\vec{r} - \vec{d}) \cdot \delta(t - t_0)\,, \qquad (2.108)$$

The "burst-like" $\delta(t)$ behavior in time is applied as the major part of the particle output is expected in the first few kyr of pulsar lifetime. After about 10..100 kyr, still short on galactic timescales, the spin-down of the pulsar (according to the magnetic dipole radiation model) has slowed down enough not to further release a large amount of particles. It is also thought that the lifetime of the PWN, necessary to supply the environment for efficient shock acceleration, has dissolved after 20 kyr [41].

As mentioned in chapter 1, the pulsar injection spectral index Γ and cutoff-energy E_{cut} are not determined. These are taken as model parameters, with generally admitted range $\Gamma \in [1; 2], E_{\text{cut}} \in [100\,\text{GeV}, 10\,\text{TeV}]$, as suggested by [41, 104]. Then, the following simple functions are assumed for diffusion coefficient and energy loss rate function:

$$D(E) = D_0 \cdot (E/(1\,\text{GeV}))^{\delta} \qquad (2.109)$$

$$b(E) = b_0 \cdot E^2\,. \qquad (2.110)$$

For the discussion here, the choice of diffusion parameters is not important, only that it has the usual shape of a power-law in rigidity (note that for leptons, rigidity $\rho/(1\,\text{GV})$ and kinetic energy $E/(1\,\text{GeV})$ are nearly the same, so $D(E)$ can be given in kinetic energy directly). The approximation of $b(E)$ is justified noting that from the Synchrotron radiation

power (1.12), it directly shows $b(E) = P_{\text{sync}}(\vec{r}, E) \sim \gamma^2 \sim (E + mc^2)^2 \approx E^2$ (same for P_{IC} from (1.13)). The two effects combined, with an average GMF and ISRF energy density, are parametrized as $b_0 = 1.4 \cdot 10^{-16}\,\text{GeV}^{-1}\text{s}^{-1}$ [105] (calculated from the model implemented in GALPROP). This equals $b_0 = 4.4 \cdot 10-6\,\text{GeV}^{-1}\,\text{kyr}^{-1}$. From the definition of $b(E)$, it follows directly,

$$\dot{E} = -b(E) = -b_0 E^2 \tag{2.111}$$

$$-\int_{E_0}^{E} \frac{dE'}{E'^2} = b_0 \int_{t_0}^{t} dt' \tag{2.112}$$

$$\frac{1}{E} - \frac{1}{E_0} = b_0(t - t_0) \tag{2.113}$$

that there is a maximum energy $E_{\text{max}} = (b_0 t)^{-1}$, called *cooling break*, a particle can have after a time t if it was injected at $t_0 = 0$ with an arbitrarily high energy $E_0 \to \infty$. Or vice versa, the initial energy E_0 a electron of energy E could have had a time t ago, is

$$E_0 = \frac{E}{1 - E b_0 t} \tag{2.114}$$

therefore an analytical connection can be made to the solution of a simple, non-energy-losing point source (2.33) [41]. Introducing

$$R_{\text{diff}}^2 \equiv 4 \int_{E}^{E_0} dE' \, \frac{D(E')}{b(E')} \;, \tag{2.115}$$

the transport equation then has a solution

$$N(E, \vec{r}, t) = \frac{b(E_0)}{b(E)} \frac{Q(E_0)}{(\sqrt{\pi} R_{\text{diff}})^3} \exp\left(-\frac{(\vec{r} - \vec{d})^2}{R_{\text{diff}}^2}\right) \tag{2.116}$$

$$= \frac{Q_0}{(\sqrt{\pi} R_{\text{diff}})^3} (1 - E b_0 t)^{\Gamma - 2} \left(\frac{E}{1\,\text{GeV}}\right)^{-\Gamma} \cdot \exp\left(-\frac{E}{E_{\text{cut}}} \frac{1}{1 - E b_0 t}\right) \cdot \exp\left(-\left(\frac{\vec{r} - \vec{d}}{R_{\text{diff}}}\right)^2\right) .$$

The availability of a simplified, analytical function is very convenient because it allows for immediate investigation for the effects of varying injection spectrum (Γ, E_{cut}), distance $|\vec{d}|$ or time after injection t. As we modeled the burst-like source term as $\delta(t)$, we can take $t = t_{\text{age}}$ the pulsar age, which generally is estimated from its momentarily observed rotation properties in the magnetic dipole radiation spin-down model, as briefly described in equations (4.10) and (4.10) later on.
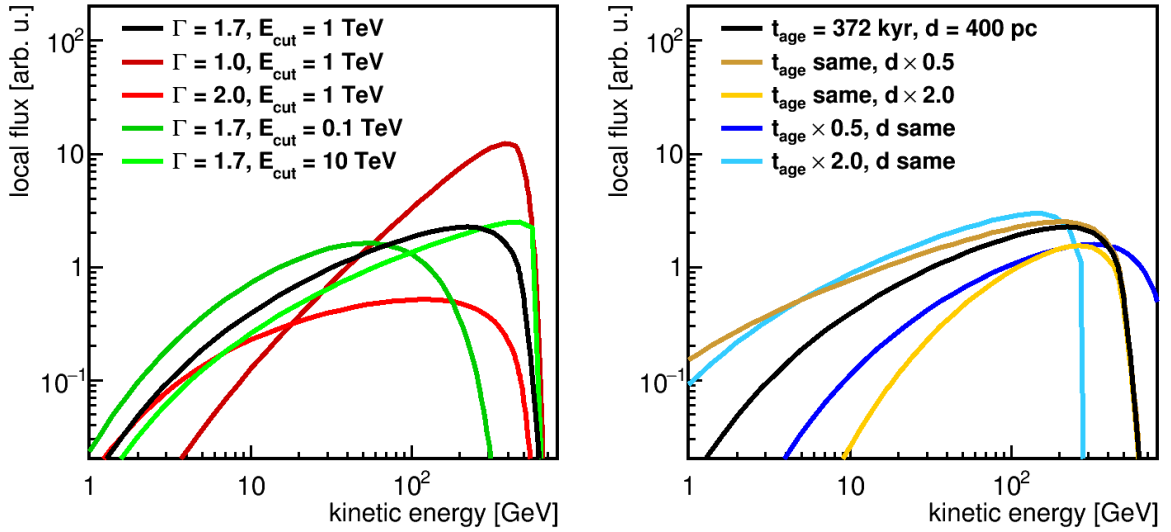
Figure 2.11. We show a Geminga-like analytical pulsar solution (black) given by (2.116) (scaled with E^3, but overall value is irrelevant for this demonstration). In the **left** panel, we vary the injection parameters Γ (green) and E_{cut} (red) within generally assumed intervals and see a large possibility of spectral shapes. In the **right** panel, we keep injection fixed and vary the physical parameters distance d (yellow) and age t_{age} (blue) each by a factor 2 up and down. While for t_{age} usually only small variations are considered, the methods of distance estimation for several pulsars is very weak (cf. Tab. 4.1).

For a sample calculation of a local e^+ flux, we model a point source after properties that could describe the Geminga pulsar within our current knowledge, see Fig. 2.11. The black line refers to a choice $\Gamma = 1.7, E_{\text{cut}} = 1\,\text{TeV}, d = 400\,\text{pc}, t_{\text{age}} = 372\,\text{kyr}$ (for the parameter limits currently given for this pulsar, I refer to chapter 4). The normalization Q_0 is chosen at a reasonable value for theoretical total $e^{\pm}$ output, but this value is fixed just to demonstrate the impact of the other parameters. In Fig. 2.11, the left graph shows the the (red) variation of injection index within the generally assumed range $\Gamma \in [1, 2]$, and (green) variation of cutoff energy $E_{\text{cut}} \in [0.1, 10]\,\text{TeV}$. The right graph shows the difference it makes when the pulsar is twice or half its assumed distance d or age t_{age}.

Propagation length. The above definition of R_{diff}^2 gives the *propagation length*

$$R_{\text{diff}} = 2\sqrt{D(E)\,t\,\frac{1 - (1 - Eb_0 t)^{1-\delta}}{(1-\delta)Eb_0 t}} \tag{2.117}$$

as a modification of the diffusion length (2.34) with the energy loss function accounted for. This definition (2.115) is introduced as a mathematical tool [41], a substitution to restore the simple diffusion equation (2.32) from the energy-loss equation (2.107), and so analogously appears as the Gaussian width of the CR distribution after time t. It can then be interpreted as a mean value for the distance the leptons have traveled. However, it does not mean that sources farther away $|\vec{d}| > R_{\text{diff}}(E, t)$ are incapable of contributing *something* to the local flux (the density only drops to $e^{-1} \approx 0.37$ of its maximum value at R_{diff}), but in general an extra source at such distance can not account for a coherent local

high-energy population.

Below, we suggest a way for a more accurate determination of R_{diff} when facing spatially varying energy losses, as present in the models of GMF and ISRF energy densities. This is interesting in order to restrict the proximity of possible sources of local $e^{\pm}$ flux measurements. This is an important inspect in the discussion of the high-energy positron population as done in chapter 4.

2.5.2. Propagation length with inhomogeneous energy losses

We suggest an iterative method of determining a more precise value for (2.117) from (2.115). Naturally, this length only has a statistical meaning, as the diffusion picture can not describe single-particle trajectories (in principle, a cosmic ray electron arriving with energy $100\,\text{GeV}$ moves at nearly speed of light $c \approx 0.3\,\frac{\text{pc}}{\text{yr}}$ despite energy losses, so within its maximum age of $t = (b_0 \cdot 100\,\text{GeV})^{-1} = 2.3\,\text{Myr}$ it could have traveled a total path length of about $680\,\text{kpc}$). We thus need to assume the direction in which a source could be located and *trace back* the propagation distance only in this direction. We will present our calculation for three limiting cases, for particles

- coming from a source straight in direction of the Galactic Center (GC) where $b(E, \vec{r})$ is large,

- coming from a source straight in direction of the Galactic Anticenter (GAC), directly opposed the GC, where $b(E, \vec{r})$ is decreasing and

- coming from a source straight in direction of the Galactic North Pole (GNP), one of the directions in which total $b(E, \vec{r})$ assumes minimum values. (this is for estimation only, as there are not much galactic sources to be expected in this direction.)

A particle arriving at our local position with energy E has been injected somewhere with initial energy E_{init}. Step-by-step, we take the propagation over a distance ΔR and change in energy ΔE to be governed by a locally constant $b(E, \vec{r})$. We illustrate our back-tracing method for the first path, moving towards the GC in -x direction. From the integrand of (2.115), it then follows from the local value $b(E, x_\odot)$, that from a slightly higher energy $E_1 = E + \Delta E$, the particle could have originated from distance ΔR_1, with

$$(\Delta R_1)^2 = \frac{D(E_1)}{b(E_1, x_\odot)} \Delta E \tag{2.118}$$

towards there, taking the value at $b(E_1, x_\odot - \Delta R_1)$, the particle could have had a higher energy $E_2 = E_1 + \Delta E$ to move a distance ΔR_2,

$$(\Delta R_2)^2 = \frac{D(E_2)}{b(E_2, x_\odot - \Delta R_1)} \Delta E \tag{2.119}$$

and so on until, for a initial energy $E_{\text{init}} = E_{\text{arr}} + n\Delta E$, the total distance d is given as

$$d^2(E_{\text{arr}}, E_{\text{init}}) = \sum_{i=1}^{n} (\Delta R_i)^2 = \sum_{i=1}^{n} \frac{D(E_{\text{arr}} + i\Delta E)}{b(E_{\text{arr}} + i\Delta E, x_\odot - \sum_{k=1}^{i-1} \Delta R_i)} \Delta E \qquad (2.120)$$

We implemented a numeric routine which were fed the DRAGON model values of $b(E, \vec{r})$, evaluating the total energy loss function by linear interpolation in $\vec{r}$ and logarithmic interpolation in E where necessary. $D(E)$ was parametrized according to our basic model, presented in chapter 3 ($D_0 = 2.29 \cdot 10^{28} \frac{\text{cm}^2}{\text{s}}, \delta = 0.58$). Our results are seen in Figs. 2.12 (GC), 2.13 (GAC) and 2.14 (GNP) for leptons (left) and protons (right) each.
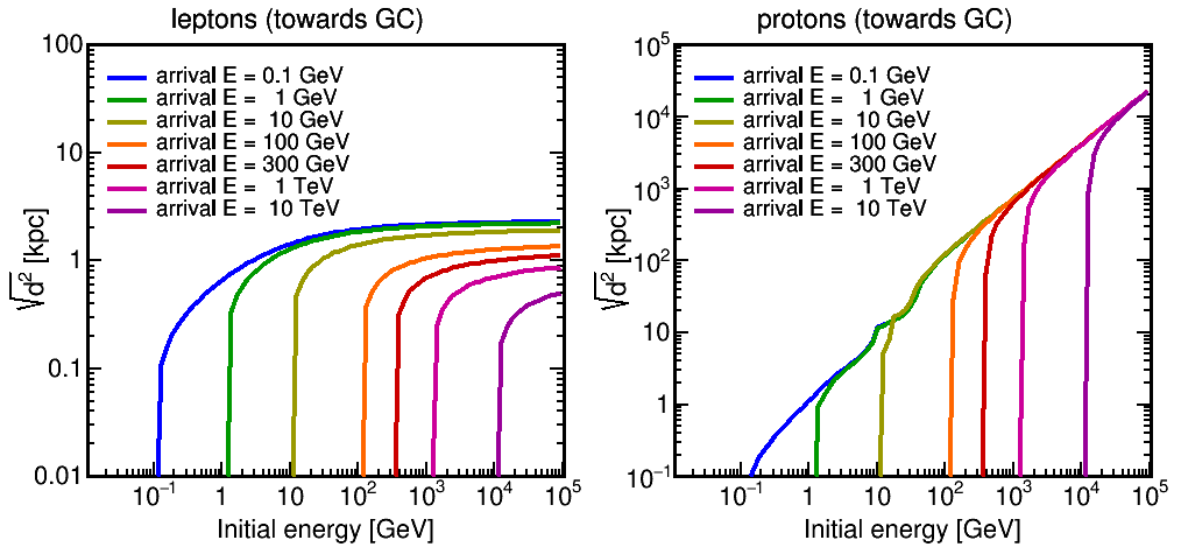
Figure 2.12. Calculation of the propagation length $\sqrt{d^2}$ by our iterative back-tracing scheme (2.120), evaluated in direction of the Galactic Center; the y-axis shows the likely distance of the source, according to a given initial energy (x-axis) and arrival energy (color), **left** panel for $e^\pm$ and **right** panel for p.

It becomes clear that the strong energy losses for leptons make the propagation length assume a plateau distance, around 2 kpc for the highest initial energies in GC direction (Fig. 2.12). In GAC direction (Fig.2.13 left), the maximum is as about 3 kpc for the lowest energies. The GNP direction (Fig 2.14 left), shown as a estimate at maximum 7 kpc. To compare the source estimations for leptons that contribute at 300 GeV (where the measured positron flux suggests extra sources, as described in the following section), we compare the maximum distances of the *crimson* line each, with a maximum propagation length $d \approx 1$ kpc (GC), $d \approx 1.1$ kpc (GC) and $d \approx 1.7$ kpc (GNP). It is stressed, again, that the increased values of propagation length towards the Galactic Pole(s) are only hypothetical as very little source candidates exist at high latitudes (cf. the SNR distribution at Fig. 1.10).

For a proton (and heavier nuclei accordingly), it holds that energy losses are sufficiently small to allow very distant sources. The structure seen for $d \approx 6..12$ kpc resembles the increased gas densities in the 2..4 kpc ring region around the GC. For large propagation distance over $d \gtrsim 20$ kpc, the graph is actually underestimating the propagation length

and are not reliable, because these exceed the propagation box, so the propagation at these distances can not be described in the diffusive picture anymore. In GAC direction, this is already true at about 7-8 kpc.
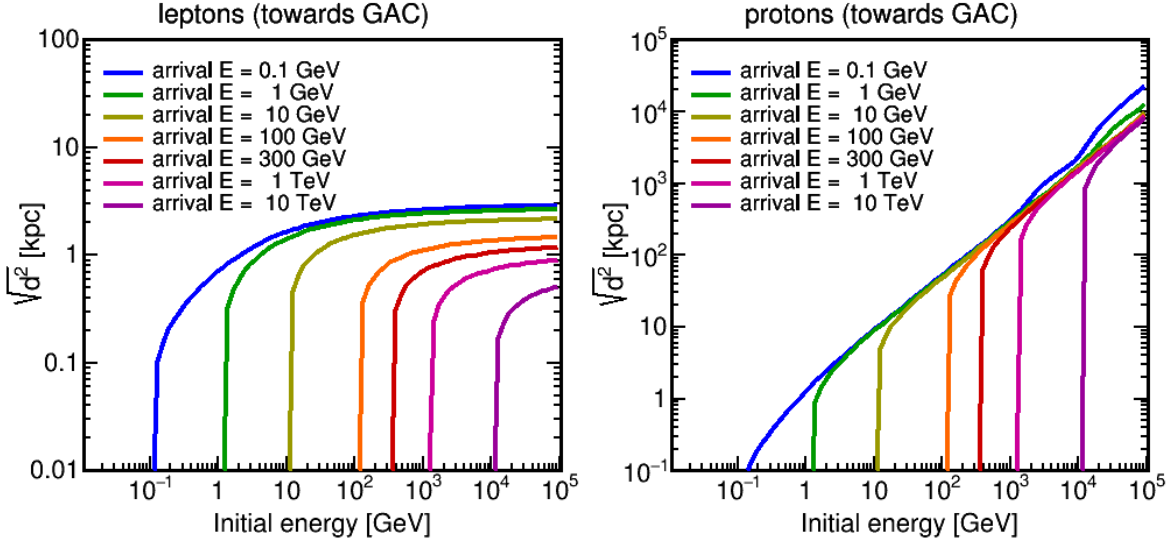
Figure 2.13. Calculation of the propagation length $\sqrt{d^2}$ by our iterative back-tracing scheme (2.120), evaluated in direction of the Galactic Anti-Center; the y-axis shows the likely distance of the source, according to a given initial energy (x-axis) and arrival energy (color), **left** panel for $e^{\pm}$ and **right** panel for p.
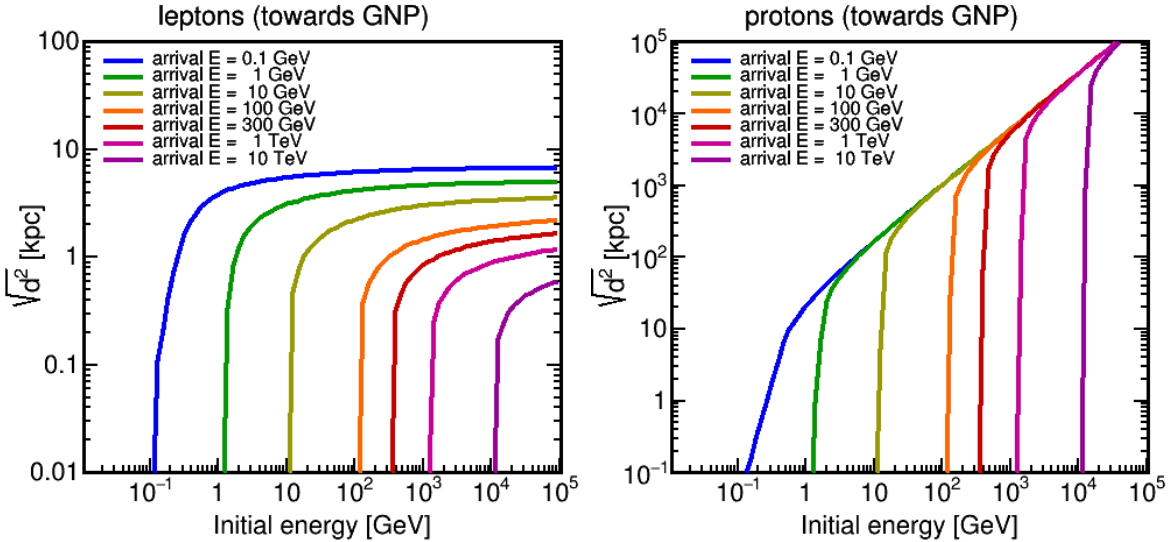
Figure 2.14. Calculation of the propagation length $\sqrt{d^2}$ by our iterative back-tracing scheme (2.120), evaluated in direction of the Galactic North Pole; the y-axis shows the likely distance of the source, according to a given initial energy (x-axis) and arrival energy (color), **left** panel for $e^{\pm}$ and **right** panel for p.

2.6. Interlude: Open questions in propagation modelization

With the chapter presented right now, we laid the mathematical-theoretical groundwork of cosmic ray propagation. After defining the model source and transport parameters, the transport equation governs the temporal evolution of the cosmic rays density distribution $N(\vec{r}, E, t)$. We demonstrated an analytical solution in the simplified example of a single $e^{\pm}$ point source under restriction to the very basic transport processes, and the numeric approach in finding a steady-state solution $\delta_t N = 0$ as implemented in the DRAGON code.

The fact that numerical transport models are widely used nowadays is owing to the advent of modern, powerful computational resources. Currently, the world of numerical codes is advanced by the implementation of a more precise description of the Galaxy (e.g. source distributions), of further of physical effects (e.g. pionic energy loss) and improved accuracy thereof (e.g. production cross sections). With the advent of new, complex extensions of GALPROP [95], DRAGON 2 [21] or PICARD [106], future propagation models will allow predictions with a lesser extent of the generalizing assumptions that were implemented in previous packages for simplicity. With rising access to powerful computational resources, the inclusion of a full variety of transport processes becomes feasible.

For illustration, one of the most commonly held assumptions in widespread models is the isotropy and homogeneity of the diffusion coefficient, which seems unlikely considering the range of astrophysical scenarios in which magnetic turbulence would be amplified, diminished or given a strong coupling to the direction of the regular field. Further, the usual assumption of cylindrical symmetry, as present e.g. in the gas distribution and simple GMF models completely neglect the galactic spiral arm pattern. Also, the simple solar force-field modulation does not allow a realistic modelization of the anisotropic diffusion properties inside the heliosphere.

The inclusion of local effects in galactic transport models is not done only because it finally became possible. It is the current advancements in precision measurement, of fluxes and arrival directions, which make it possible to identify several *features* in cosmic ray spectra that are at odds with such simplified models. In light of the most recent publications, we will now turn to a few of the currently open issues to which no simple answer from the field of propagation models is yet given.

PAMELA, Fermi and AMS-02 positron "excess" measurements

By the 2009 PAMELA publication [107] of the positron fraction, $\frac{e^+}{e^- + e^+}$ or $\frac{e^+}{e^{\pm}}$, it first became known what was later named the "anomalous rise" or "positron excess" (cf. Fig. 2.15. At about a kinetic energy of $E \approx 5..7\,\text{GeV}$, the observed positron fraction of about $\frac{1}{20}$ is well in agreement with propagation models, in which the positronic component is produced by proton-proton collisions in the ISM only (see Fig. 1.3.4.3). Then, the range of conventional model description (gray range) predicts a decrease with higher energies, due to the shape of the proton spectrum and the efficient Synchrotron and Inverse Compton energy losses for leptons at these energies.

Instead, the observation shows a clear rise above $E \gtrsim 10\,\text{GeV}$ to up to over $\frac{1}{10}$ at $E \approx 100\,\text{GeV}$. It was then also seen in 2012 by the Fermi collaboration [108] (yet with rather large uncertainties) and then finally confirmed by the 2014 publication by AMS-02 [109], with unprecedented precision, that this rise is indeed reproducible in measurement. From the AMS-02 data, it is seen that the spectral shape is smooth, i.e. no finer structures are distinctly present. Further, above $E \gtrsim 300\,\text{GeV}$ a flattening of the rise in positrons is suggested, especially as there exists another point of published data not shown in the figure, at $e^+/(e^\pm)(350..500\,\text{GeV}) = 0.1471 \pm 0.0278$ (statistical error) [109]). AMS-02 also gave [103] separate flux measurements for e^- and e^+, making sure that the rise in positron fraction was also a rise in positron flux, not probably a decrease in electron flux.

A number of ideas has subsequently been proposed in order to explain this *energetic positron population*, with a larger share of introducing new sources as pulsars or Dark Matter annihilation, but also some attempts in modifying underlying assumptions about the secondary e^+ production in the ISM structure. As this positron population is the topic of chapter 4, a short review of the suggestions and their implications on other cosmic ray species is presented there.
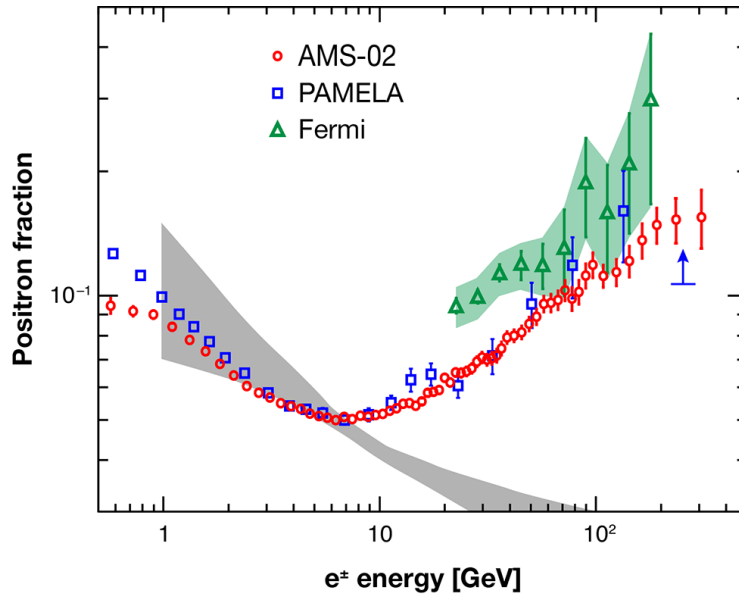
Figure 2.15. Recent measurements of the positron fraction $\frac{e^+}{e^- + e^+}$ (or $e^+/e^\pm$) as function of kinetic energy, by the PAMELA, Fermi-LAT and AMS-02 experiments. The gray band is the prediction of common models of cosmic ray propagation which can not explain the rise in data, a highly actual topic addressed in chapter 4 of this thesis. After the publication of this plot, AMS-02 added one more data point $e^+/e^\pm(350..500\,\text{GeV}) = 0.1471 \pm 0.0278$. [Refs. in text]

PAMELA and AMS-02 antiproton "excess" measurement.

Similarly, the conventional modelization of purely secondary production of $\bar{p}$ in the ISM predicts the $\bar{p}/p$ ratio as a declining function of energy, above a few tens of GeV. Instead (Fig. 2.16), the measurement [presented by A. Kounine at the AMS Days at CERN 2015] is "flat" at about $\bar{p}/p \approx 2 \cdot 10^{-4}$. This is in agreement with previous observation by PAMELA [110], but with too little statistics to exclude the decline.

Suggestions [111] have been made in order to investigate model compliance with additional astrophysical sources or Dark Matter contributions, but considering all uncertainties (colored bands in Fig. 2.16), the measurement is not exceedingly conflicting the models. This has the reason that for $\bar{p}/p$ model predictions, the uncertainties are not only from the parametrization of the primary sources (blue band) and the transport properties (yellow band), but also from the theoretical uncertainties depending on the cross section formulae (red band). As opposed to positrons which are only participating in electroweak couplings, secondary production of hadronic species like antiprotons requires QCD interactions which are typically more difficult to estimate.
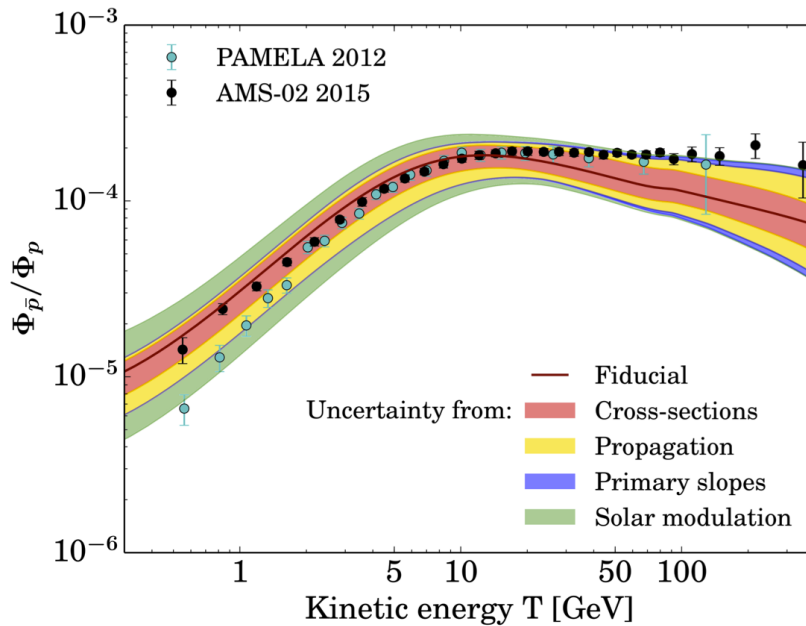
Figure 2.16. Recent measurements of the antiproton ratio $\bar{p}/p$ as function of kinetic energy T, by the PAMELA and AMS-02 experiments. The black line is a single numerical model prediction representing the theoretical expectation, which decline towards higher energies while the data shows a flat behavior. The colored bands show that uncertainties in cross sections (red), propagation parameters (yellow) and primary source injection slopes (blue), the data currently show no large anomaly. [Refs. in text]

AMS-02 proton and Helium measurement showing a "spectral hardening".

High precision measurement of the proton flux, by AMS-02 [112, 113], has revealed that above a particle energy of about 300..400 GeV/nucleon, the spectral shape is not compatible anymore with a "unbroken" power-law $N_p(\rho) \propto \rho^{-\gamma}$ (single index γ). Such "spectral hardening", which was also observed as a feature in the helium flux above 300..400 GeV/nucleon. [114]), is compatible with the measurement of the first CREAM balloon flight [115]. This can be caused by [116]

1. an intrinsic feature of the source acceleration mechanism, which would then need a more proper understanding of the shock systems in SNRs;

2. an intrinsic feature of the diffusion properties in the ISM, which would then require a more detailed picture of MHD scattering than QLT provides;

3. the presence of a local source mostly contributing at either low or high rigidities, which would raise the question for their nature.

This feature is therefore a showcase example of the correlation between source and transport properties. By improving the description of the Galaxy in numerical transport models, new insight therefrom is to be gained.
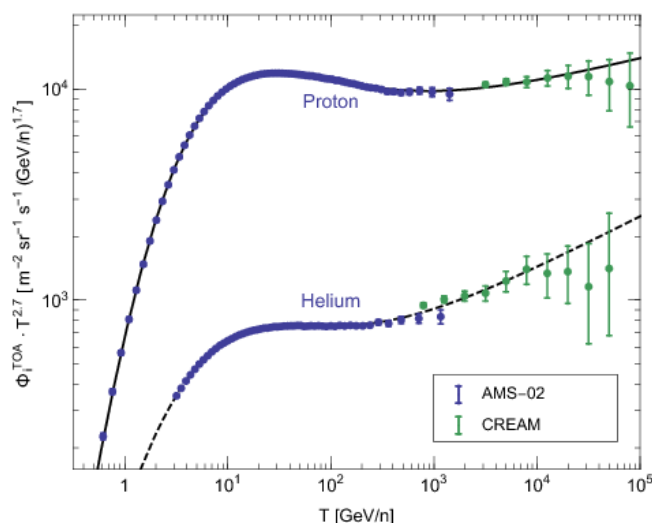
Figure 2.17. Recent measurements of the proton and helium flux (scaled with $T^{2.7}$ as a function of kinetic energy T per nucleon n) by AMS-02, and 2011 data by CREAM. The lines are fits done by [113], indicating a spectral break at $T \sim 300..400 \, \text{GeV}/n$. [Further refs. in text]

Description of the Fermi diffuse γ-ray sky.

Finally, propagation models, designed for describing the local measurements of charged cosmic rays, are generally not able to give a good description of the *γ-ray sky*, as in the publicly available PASS7 set, a 6-year measurement by the Fermi collaboration.
This means, the propagation models predict very different line-of-sight-integrated (LOS) γ-ray spectra in different directions, which are the superposition of LOS γ-ray spectra from

- (top) CR proton collisions with the ISM and subsequent *pi* decay,

$$pp \to \pi^0 \to \gamma\gamma$$
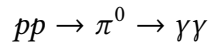
- (middle) CR electron Bremsstrahlung emission

$$e\gamma_{\mathrm{GMF}} \to e\gamma$$
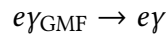
- (bottom) CR electron Inverse Compton radiation

$$e\gamma_{\mathrm{ISRF}} \to e\gamma \ .$$
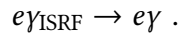
Therefore, each LOS direction holds information about the overall CR p density (π decay, and with a minor contribution from CR *He*) and overall CR e^- density (Bremsstrahlung and IC).

To quantify the model deviation, direction-dependent *scaling factors* can be applied to the single γ-ray contributions. This is done in ongoing work by de Boer et al. at KIT [117], who show that further γ-ray components (coming from source CR and from molecular clouds) are to be considered in order to describe the Fermi data. Fig. 2.18 shows, as sky maps, the logarithm of these scaling factors as blue to red values as $\log(\mathrm{SF}) \in [-1.3, 1.3]$, i.e. $\mathrm{SF} \in [0.05; 20]$. These factors do, of course, require much more understanding overall; however, an illustration is made by the observation that every component requires a significantly reduced density $\sim 0.05..0.1$ inside the inner Galactic Disc (the thin blue line visible in the center of each sky map). This might mean that this transport model largely overestimates the CR densities in the Galactic Plane.

The information to take from this is: γ-rays act as a *tracer*, they hold information about the galactic (non-local) cosmic ray distribution, coupled to another distribution of a galactic quantity each (the gas distribution, magnetic field or the radiation field). Improving galactic transport models might be a key to understanding the γ-ray sky, but as transport models are constrained by the local measurements, by conclusion, a more thorough understanding of the transport in the local environment is required.
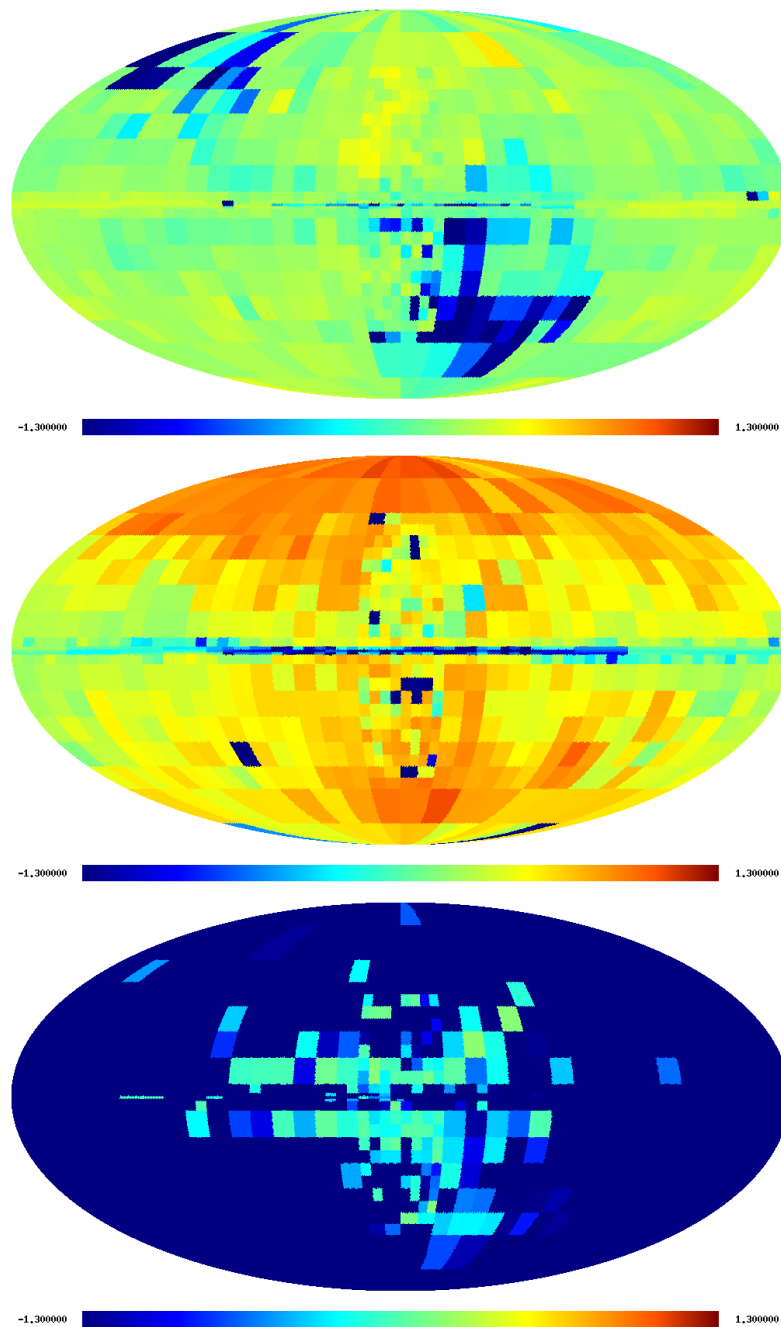
Figure 2.18. These skymaps show the required direction-dependent scaling factors that have to be multiplied to each model LOS to describe the Fermi PASS7 diffuse γ-ray data. The binning were chosen in order to optimize the varying statistics in each region of the sky. From **top** to **bottom**, the γ-ray contributions are given by π decay, Bremsstrahlung and Inverse Compton effect. Color scales go from 0.05 (blue) to 20 (red).

3. Local transport of cosmic rays

Numerical propagation models are designed to contain a generally large number of free parameters, in most general cases. While simple transport model approximations are used to readily gain general insight about a specific transport effect - as in leaky-box or simplified diffusion models - they are not designed to consistently predict *combined* measurements of multiple cosmic ray species. This is especially a declared goal as with the ongoing AMS-02 measurements, a set of high-precision, multi-species spectra will be available by the same detector and consistent analysis group. Advanced models of CR transport are then desirable that give a coherent picture of the complete set, if possible.

Furthermore, it is conceptually self-evident that for a realistic description of galactic cosmic ray propagation, the inhomogeneity of the astronomically observed physical quantities - gas density, magnetic field etc. - can not be neglected. As much progress has been made since the advent of GALPROP in the mid-1990's, CR model studies have now shifted to improving the physical accuracy of implemented formulae and distributions, as well as to improving the performance of the numerical algorithm - both utilizing and supporting the advancements in interpretation of observed CR data.

Advancing precision in measurements of local cosmic ray fluxes and their arrival directions is putting pressure on the presumptions in current numerical transport models. From the perspective of four current samples of understanding deficiency, it was deduced *Only by selectively scrutinizing these presumptions, the true correlation between cosmic ray sources, their propagation and their local measurements can be revealed.*

In this chapter we will, for the first time, perform a model study of the impact of our solar neighborhood on cosmic ray propagation. Introduced in chapter 1, the solar neighborhood is here taken as the $200 \times 200 \times 200 \, \text{pc}^3$ region around the solar system (centered around the Sun). This study is then structured in the definition of our reference model (coined "BG" as it will also serve as a *background* model for the study of positron point sources in chapter 4). Then a non-uniform, locally adapted grid is constructed in order to achieve a reasonable number of spatial grid points in the solar neighborhood. In adherence to section 1.3.6, we then build models of local transport, varying the local quantities defining energy loss and diffusion; for which we evaluate the changes in flux for $p, e^-, e^+, \bar{p}/p, {}^{10}Be/{}^9Be$ and B/C, as well as the dipole anisotropy of protons δ_p, electrons plus positrons $\delta_{e^\pm}$, and the relative anisotropy of $\delta_{e^+/p}$ of positrons relative to protons. Furthermore, we view the dipole anisotropy of *protons relative in energy*, i.e. protons with energy $E > 40 \, \text{GeV}$ compared to lower-energy protons in the range $E \in [40, 80] \, \text{GeV}$.

3.1. Choice of a galactic transport reference model

First, we need to define our reference model. We base our search on the results of Simon Kunz, our former colleague at KIT, who performed a global parameter scan with the help

of a Markov chain Monte Carlo method [56], driven by the evaluation of a combined χ^2 taken over four observables, with the measurements available at that time (which was before the AMS-02 publications), extracted from the Database of Charged Cosmic Rays [118]:

$$\chi^2 = \sum_{\text{observables}} \sum_{\text{data}} \sum_{\text{bin}}^{\#\text{bins}} \left(\frac{\text{DRAGON prediction} - \text{data}}{\text{error on data}} \right)^2 \frac{1}{\#\text{bins}} \tag{3.1}$$

- p flux measurement from PAMELA [119];

- $\bar{p}/p$ ratio measurement from PAMELA [120];

- $^{10}Be/^9Be$ ratio measurement from ACE-CRIS [121] and ISOMAX [122];

- B/C ratio measurement from PAMELA [123]

- e^- flux measurement from PAMELA [124].

The models of Kunz were evaluated based on a generic DRAGON model template with up to 25 free parameters, in which the Markov chain Monte Carlo method had the advantage of covering broad ranges of parameter space, i.e. not focusing on a very special region when a value of χ^2 minimum had been found. The transport parameters were allowed in a range each listed in the second column of Tab. 3.1. The Markov chains resulted in the evaluation of over 10^7 models, of which the 450 models with lowest total χ^2 were selected here, under the name "K450".

We show the model envelope of the K450 set on the spectra of $p, \bar{p}/p, B/C, {}^{10}Be/{}^9Be$ (Figs. 3.1 to 3.4) in comparison with the corresponding data (see above), and spectra of e^-, e^+ (Figs. 3.5 and 3.6) in comparison with most recent AMS-02 data [103] Also, we consider the model predictions of dipole anisotropies, given in *cumulative* energy bins as introduced before (section 2.3.2), and compare these with AMS-02 ($\delta_{p/p}, \delta_{e^+/p}$) [99] and Fermi-LAT ($\delta_{e^\pm}$) [125] upper limits (UL) within 95% CL (Figs. 3.7 to 3.10).

The analysis of dipole anisotropies from detectors like AMS-02 is considerable easier to handle if relative fluxes are considered, e.g. e^+/p (positrons relative to protons). Detector effects like limited acceptance are then assumed to cancel from both observables, to reduce the contribution of "fake" anisotropies from the method of measurement. For leptonic observables, protons pose a suitable reference as their low energy loss implies a smaller dependence on the actual source locations and the local flux should appear more isotropic. For proton fluxes themselves, the observable dipole anisotropy in *protons relative in energy* $\delta_{p/p[40,80]}$ is given (which we might abbreviate to $\delta_{p/p}$): Assuming an anisotropy in the proton flux towards higher energies $E \gtrsim 80$ GeV, it can be considered small for intermediate energies $E \in [40, 80]$ GeV, so the latter can pose as a reference to the higher-energy flux. The AMS-02 upper limits in our study are preliminary values from the ongoing AMS-02 analysis of Stefan Zeissler [99] from our group at KIT. As the methods in determining dipole anisotropies in the absolute flux of one CR species are currently under development,

these values are to be published by the end of the year.

Fig. 3.7 shows the predictions of *absolute* proton dipole anisotropy δ_p, of all K450 models enveloped as a blue band. Fig. 3.8 shows the corresponding dipole anisotropy of protons relative in energy, $\delta_{p/p}$. The red line is the result of the model introduced below. By comparison, the predictions in both cases appear similar, indicating that the dipole anisotropy in δ_p is mostly given by the higher-energy range. In Fig. 3.8, we also see that the blue band of K450 is not everywhere compatible with the AMS-02 UL from [99]. These models were defined in 2013 and could not account for the limits of 2016. This showcases the new possibilities to use the observable dipole anisotropy as a constraint for models of CR propagation. The K450 models are all in agreement with Fermi-LAT [125] limits on $e^\pm$ anisotropy (Fig. 3.9 and AMS-02 [99] limits on e^+/p anisotropy (Fig. 3.10).

Model selection criteria.   For this work, we choose one model of reference which we call BG from now on. It is shown as a bright red line in the figures. We will then propose local model modifications, based on various assumptions about the Local Bubble and discuss their impact on the predictions. Of course, a different choice of reference model would later result in different predictions, but as this is the first study of the local transport in the solar neighborhood, we are less interested in the exact numerical values of our predictions than in the overall change of shape in our observables. In principle, a study on a broader range of reference models can be repeated using the implementations we made to the DRAGON code, which was published since [95].

For our reference model BG, we found it adequate to select for the following criteria:

1. The injection spectrum for nuclei is taken to be an universal, single-index power-law for all primary nuclei. This means the source injection spectrum of a primary particle species like carbon differs from the proton injection spectrum only by a constant factor in overall *source abundance* (in *rigidity*, accounting for the charge). Also, we assume no break in the rigidity dependence of the diffusion coefficient, $\delta = \delta_h$. Thereby the proton spectrum should in principle follow a simple power-law and we can investigate whether any spectral feature emerges from local transport scenarios.

2. The convection term should be neglected, i.e. we choose the model on the criterion of low wind velocity, and then set it to zero ($v_{C,0} = \frac{dv_C}{dz} = 0$).

3. The diffusive reacceleration term is also neglected ($v_A = 0$). (This is actually a convenient choice for performance, because from the physical processes described below, we do not know yet how to treat the reacceleration term consistently. Also, high-reacceleration models have shown to require a considerably larger number of algorithm iterations to reach a steady-state.)

4. For the reason of computing time, we prefer a model with low halo half-height L. Large halos, evidently, require a larger amount of grid points in z direction to be modeled correctly. Because one can not adjust L without also Because of that, we

advise ourselves to take a reference model that naturally needs a low halo half-height $L < 3\,\mathrm{kpc}$.

5. The electron injection spectrum is, in our model, taken to be completely decoupled from the nuclei's injection. For preparation of the next chapter, we *tune* the parameters so that it well describes the AMS-02 e^- measurement [103] *under addition of the difference in e^+ flux between AMS-02 observation and model prediction*. By that, both spectra will be described well if a charge-symmetric extra component is accounted for. We allow up to two spectral breaks in the e^- spectrum.

The complete set of parameters is listed in Tab. 3.1 (third column). This is always represented as red line in this chapter (as in Figs. 3.1 to 3.10).

Parameter		K450 range	BG model
Halo half-height L	[kpc]	[0.3845, 30]	2.8
Nuclei injection spectrum index α_0		[0.3648, 3]	2.2721
Nuclei injection spectrum break rigidity ρ_0	[GV]	[0.0870, 100]	–
Nuclei injection spectrum index α_1		[1.7159, 2.6969]	2.2721
Nuclei injection spectrum break rigidity ρ_1	[GV]	[100, 1000]	–
Nuclei injection spectrum index α_2		[0.0017, 3]	2.2721
Nuclei injection spectrum break rigidity ρ_2	[GV]	[100, 1000]	–
Nuclei injection spectrum index α_3		[0.0017, 3]	2.2721
Electron injection spectrum index α_0^{el}		[0.5880, 1.8596]	2.6009
Electron injection spectrum break rigidity ρ_0^{el}[GV]		[2.9200, 6.5398]	9.1213
Electron injection spectrum index α_1^{el}		[2.4311, 2.6489]	2.9043
Electron injection spectrum break rigidity ρ_1^{el}[GV]		[26.2500, 92.8571]	40.0266
Electron injection spectrum index α_2^{el}		[2.0429, 2.6489]	2.5467
Electron injection spectrum break rigidity ρ_2^{el}[GV]		[262.5000, 812.5000]	–
Electron injection spectrum index α_3^{el}		[1.0492, 3.0000]	2.5467
Diffusion prefactor D_0	$[10^{28}\mathrm{cm}^2\mathrm{s}^{-1}]$	[0.1694, 9.4677]	2.29
Diffusion rigidity index δ		[0.3404, 1.2]	0.576
Diffusion break rigidity ρ_D	[GV]	[21.2894, 3500]	–
Diffusion rigidity index above break δ_{high}		[0.0046, 1.2]	0.576
Diffusion velocity exponent η		[-2, 2]	0.632
Alfvén velocity v_A	[km s^{-1}]	[0.1049, 49.3921]	0.0
Convection base velocity $v_{C,0}$	[km s^{-1}]	[0.0152, 29.1684]	0.0
Convection velocity gradient[1] $\frac{dv_C}{dz}$	[km s^{-1} kpc^{-1}]	[0.2361, 46.0649]	0.0

Table 3.1. List of the most relevant DRAGON transport model parameters. The **left** column names the parameters, the **middle** column the range in which the K450 models are defined [56]. In the **right** column we see the choice of each parameter in the reference model BG (fixed throughout this study). Parameters are given as described in chapter 2, cf. there for more details. ([1] three more detailed parameters of convection velocity were dropped in this list.)

There is another model shown in the B/C plot as a blue line in Fig. 3.4. The difference to BG is that it was a convection velocity parameter $v_C = 10\,\frac{\mathrm{km}}{\mathrm{s}}$ instead of $v_C = 0$ (cf. the

second condition above). This was the original value of the model that appeared best to us from the K450 set. Again: As this is the first study of the impact of the Local Bubble, we specifically required a reference model with a high degree of simplicity. As the choice $v_C \to 0$ gives no conflict with any of the other data either, it is thus the better choice of reference.

As a general note: In any of the following considerations, we treat the solar modulation parameter as a nuisance parameter only. The value of the potential Φ does not carry a physical meaning, and we will allow it to be applied freely in a range $\Phi \in [0, 2]$ GV, for every observable separately to reach ideal data description.
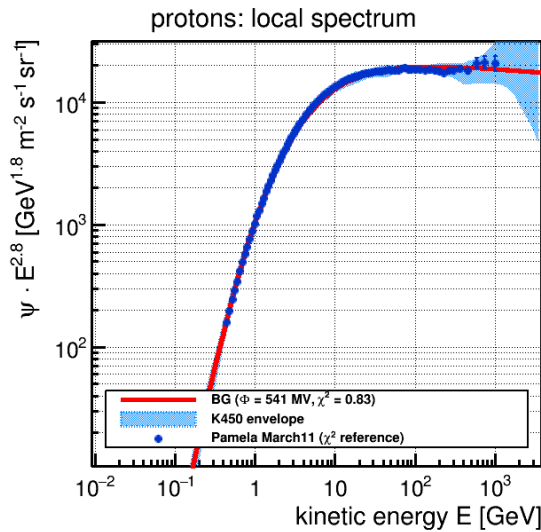
Figure 3.1. Energy spectrum of protons, scaled with $E^{2.8}$ for display. BG is the chosen reference model for this study (red). K450 is a set of results from a complete parameter scan [56] (blue), with parameter range given in Tab. 3.1. The K450 scan was performed on PAMELA proton data. [119], solar modulation is set to best fit the data.
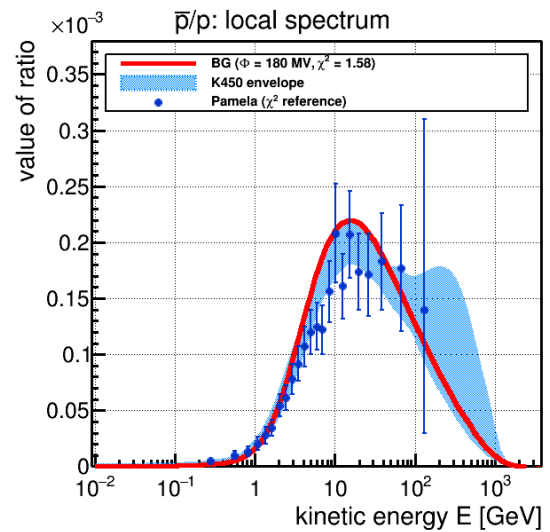
Figure 3.2. Energy spectrum of $\bar{p}/p$. BG is the chosen reference model for this study (red). K450 is a set of results from a complete parameter scan [56] (blue), with parameter range given in Tab. 3.1. The K450 scan was performed on PAMELA $\bar{p}/p$ data. [120], solar modulation is set to best fit the data.
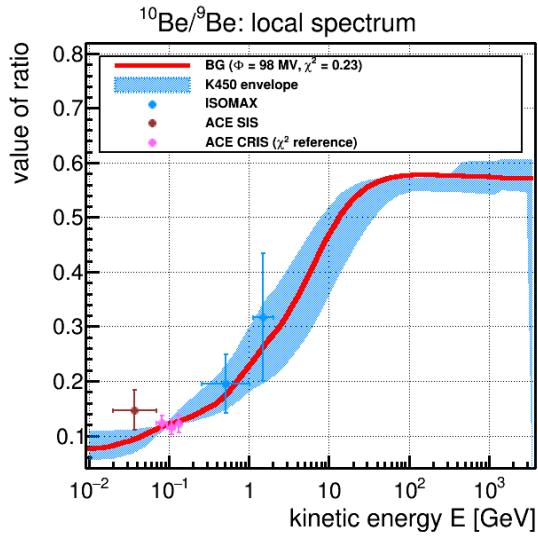
Figure 3.3. Energy spectrum of $^{10}Be/^9Be$. BG is the chosen reference model for this study (red). K450 is a set of results from a complete parameter scan [56] (blue), with parameter range given in Tab. 3.1. The K450 scan was performed on ACE-CRIS [121] and ISOMAX [122] $^{10}Be/^9Be$ data, solar modulation is set to best fit the data.
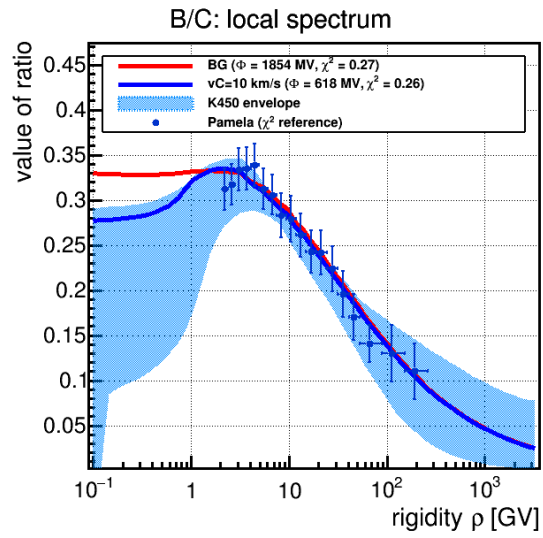
Figure 3.4. Energy spectrum of B/C. BG is the chosen reference model for this study (red). K450 is a set of results from a complete parameter scan [56] (blue), with parameter range given in Tab. 3.1. The K450 scan was performed on PAMELA B/C data. [123]. The blue $v_C = 10$ km s^{-1} model was the original model from the K450 set, from which we created BG by setting $v_C \to 0$ for simplicity. Solar modulation is set to best fit the data.
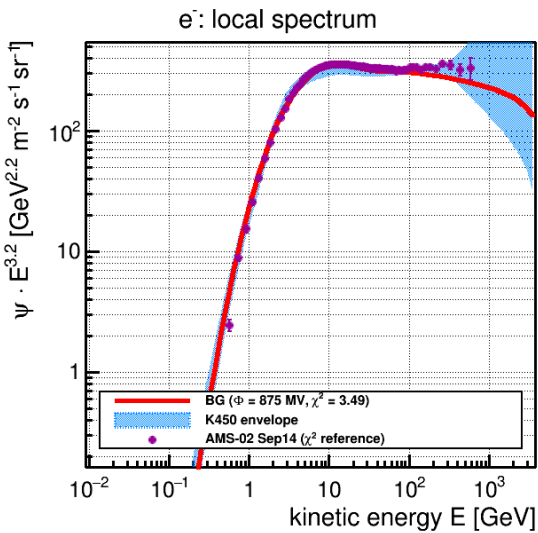
Figure 3.5. Energy spectrum of electrons e^-, scaled with $E^{3.2}$ for display. BG is the chosen reference model for this study (red) it was tuned to leave a gap to the AMS-02 data [103] (shown) (explained in text). K450 is a set of results from a complete parameter scan [56] (blue), with parameter range given in Tab. 3.1. The K450 scan was performed on PAMELA e^- data [124] (not shown), solar modulation is set to best fit the AMS-02 data.
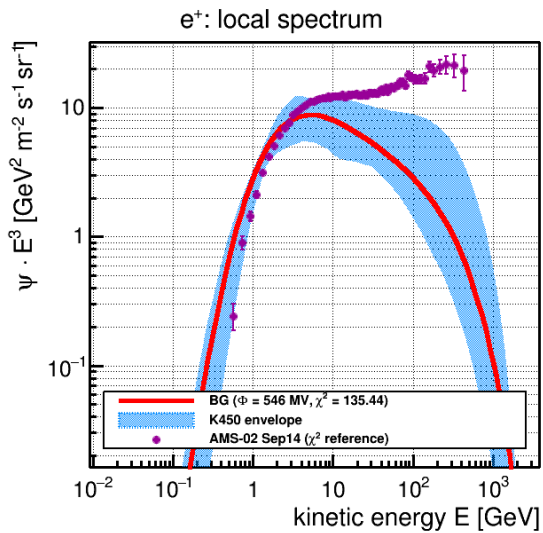
Figure 3.6. Energy spectrum of positrons e^+, scaled with E^3 for display. BG is the chosen reference model for this study (red). Description of the K450 [56] (blue) is poor, this is the problem known as "positron excess". AMS-02 data are shown [103], solar modulation is set to best fit the low-energy data.
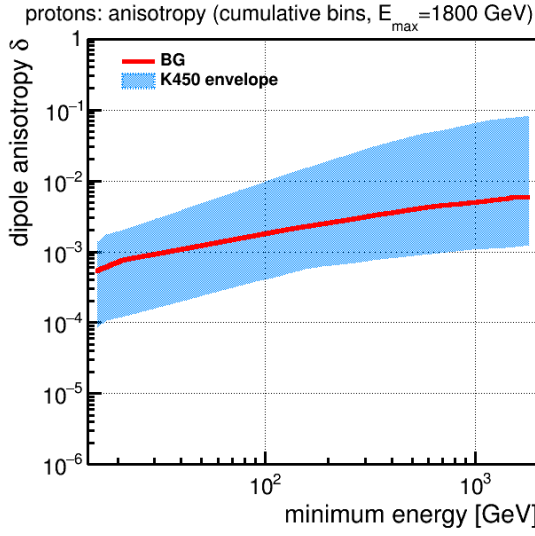
Figure 3.7. Dipole anisotropy of protons δ_p, in cumulative energy bins up to $E = 1.8\,\text{TeV}$. BG is the chosen reference model for this study (red). K450 is a set of results from a complete parameter scan [56] (blue), with parameter range given in Tab. 3.1. Anisotropy limits for protons are currently only available in the form of proton relative in energy UL, see Fig. 3.8
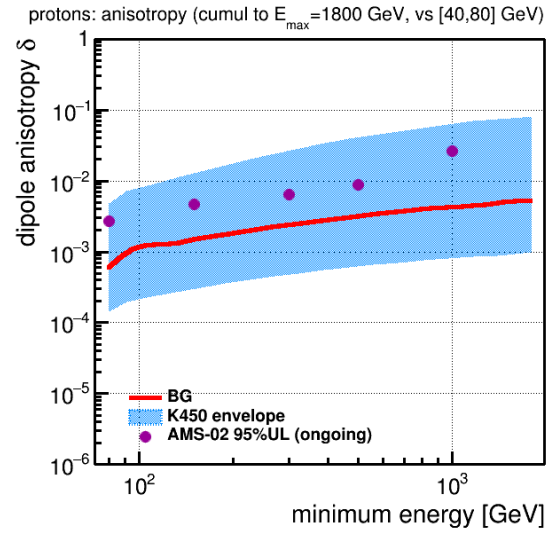
Figure 3.8. Dipole anisotropy of protons over protons relative in energy $\delta_{p/p}$, in cumulative energy bins up to $E = 1.8\,\text{TeV}$. BG is the chosen reference model for this study (red). K450 is a set of results from a complete parameter scan [56] (blue), with parameter range given in Tab. 3.1. AMS-02 upper limits are from the ongoing work of [99]. Some K450 models disagree with current UL.
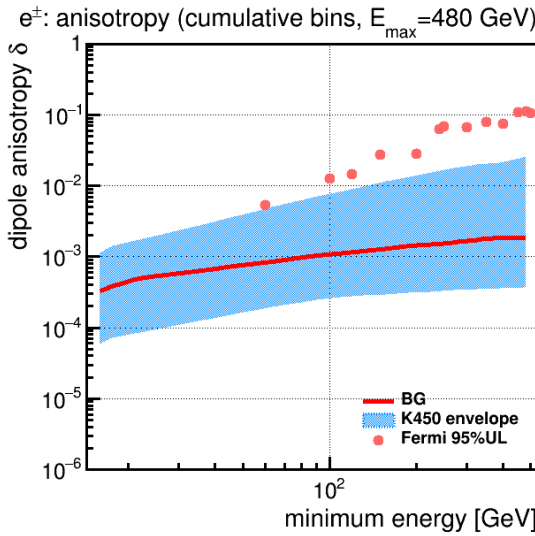
Figure 3.9. Dipole anisotropy of the leptonic sum flux $\delta_{e^\pm}$, in cumulative energy bins up to $E = 480\,\text{GeV}$. BG is the chosen reference model for this study (red). K450 is a set of results from a complete parameter scan [56] (blue), with parameter range given in Tab. 3.1. Fermi-LAT [125] upper limits are shown.
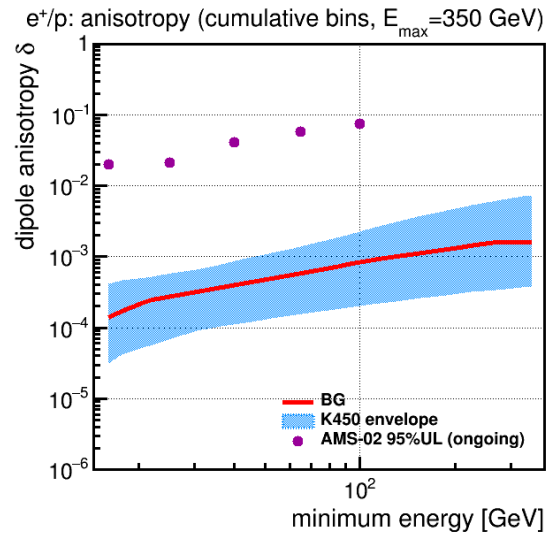
Figure 3.10. Dipole anisotropy of the relative positron to proton flux $\delta_{e^\pm}$, in cumulative energy bins up to $E = 350\,\text{GeV}$. BG is the chosen reference model for this study (red). K450 is a set of results from a complete parameter scan [56] (blue), with parameter range given in Tab. 3.1. AMS-02 upper limits are from the ongoing work of [99].

85

3.2. Non-uniform grid refinement in the solar neighborhood

We defined the solar neighborhood as the local cuboid of $\sim 200 \times 200 \times 200\,\text{pc}^3$ size, centered around the Sun. This embeds the Local Bubble. Judging from the dust extinction measurements Figs. 1.22, 1.23 and 1.21, the actual size of the hot gas cavity (the bubble interior) is indeed only of a size $\lesssim 100\,\text{pc}$, in galactic x and y directions. In order to conduct studies at Local Bubble scale, a grid spacing of a few tens of parsec is required. This is a resolution much finer than the customarily chosen grid spacings of 200 pc, e.g. the default configuration in the Galprop *WebRun service* uses a spacing of 200 pc in Galactic vertical z direction and even only a spacing of 1 kpc in Galactic radial direction R: Usually, the solar neighborhood becomes *completely averaged out.*

In need of a strongly enhanced spatial grid resolution, we face the problem of extending the computational expense of running the algorithm, up to the point where even modern CPUs get close to their capacity. For a desirable grid spacing of $1\,\text{pc} \longrightarrow 10\,\text{pc}$ in every spatial direction, a uniform grid refinement would correspondingly imply a factor of 8000 in pure memory usage, and possibly a much longer computational time, as the Dragon solver then in every step needs to invert a Crank-Nicolson matrix 400 times as large. These simple estimations show why a *non-uniform, locally adapted* grid is required.

The predictive power of any numeric calculation is limited by the order of truncation error, as introduced in section 2.4 and stated for our discretization of the inhomogeneous diffusion terms. Therein, any sudden changes in grid step size will largely amplify the error. This is illustrated in Fig. 3.11: A hard change in grid spacing (seen left) is lead to completely artificial solutions which showed weird spatial oscillations in CR density. A smooth transition grid (as seen right) is required for the treatment of locally fine spacings.

These oscillations are a known effect in Crank-Nicholson algorithms and their origin is further described in appendix A.2. This problem especially appears if physical quantities near these regions do show a strong gradients where the grid is modified (as was found with steep source distributions and diffusion coefficients). We implemented a number of numerical grids in order to give good agreement in comparison with a uniform grid, first without changing any other parameters. Then we refined these grids by enabling local diffusion coefficient $D(\vec{r})$ up to a factor of $\frac{1}{100}$ to 100 differing from the galactic average. When a gradient in $D(\vec{r})$ between two neighboring grid points was too hard, the oscillatory behavior typical for strong gradients in CN schemes emerged (explained in more detail in appendix A.2); the grid had to be further refined then.
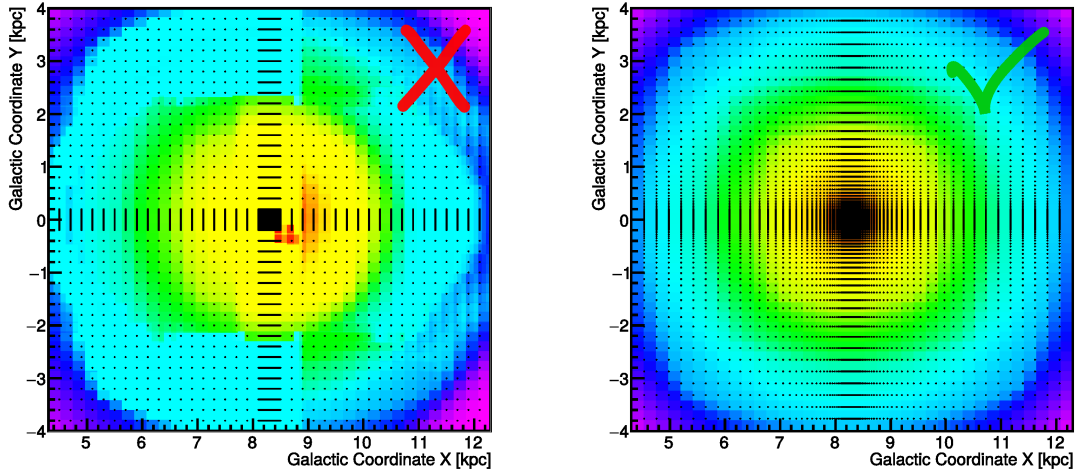
Figure 3.11. Visualization of grid truncation error: Local nonuniform grid adaption can not be chosen arbitrarily. A smooth source distribution is propagated in two grids (color axis arbitrary). In the **left** panel, we see hard changes in grid spacing that lead to a distortion of the solution with oscillations from truncation error with chaotic looking amplification. In the **right** panel, the sufficiently smooth grids do not show such erratic behavior. (this example is illustrated on a reduced $8 \times 8 \times 8 \, \text{kpc}^3$ propagation box around the Sun).

Finally, a grid choice was found to work well that was constructed from *inside* the Local Bubble. The construction works as follows, independently for every dimension: Around the position of the Sun $x_\odot$, a number of N_I points in each direction was defined in an equidistant fashion, i.e. constant spacing

$$\Delta x_i = 10 \, \text{pc} \quad \text{for the inner } N_I \text{ points}$$

Then, a small fixed "curvature" $c \approx 1.2$ was applied, gradually increasing

$$\Delta x_{N_I+j} = 10 \, \text{pc} \cdot c^j \quad \text{for each further } j\text{th point}$$

i.e. increasing slowly to 12 pc, 14.4 pc etc. After a certain number of points, at about 4 kpc distance from the Sun in each direction, the grid spacing was manually increased as large as 1 kpc or higher. This was chosen sufficiently far away from the Local Bubble region. To show the principally grid-given part of truncation error, the Δx-coefficients in

Figure 3.12. By comparing the leading order truncation errors cofactors (2.105)/(2.106), a measure of the "hardness" of changes in grid spacing is given. The grid from Fig. 3.11 (right) was extended to the whole galaxy, the values of these cofactors on the positive X axis are shown here. High cofactors equal more abrupt changes, which are critical if they appear in regions of high gradient in CR density, diffusion coefficient, etc.

(2.105), (2.106), are evaluated. If these are large, it is estimated that the grid is prone to propagation errors if gradients in the CR density or other physical parameters are large

there. The total error then comes by multiplication with the actual quantities there, this means that "dangerous" grid regions might be safe if no large gradients appear. Fig. 3.12 shows for illustration the values for the grid we adopted, on the positive x axis.

The comparison of the DRAGON solutions for the adapted grid and a uniform grids are, with the BG model chosen above is given for energy spectra in Fig. 3.13 and for spatial distributions in Fig. 3.14. Shows the ratio of the CR density as calculated for the adapted grid, relative to the solution for the uniform grid, for the energy spectra of e^- (left) and p (right). There is a general decrease towards low energies similar in both species, but only significant in the energy range in the solar modulation range, where uncertainties are generally large. This difference can therefore be compensated by choosing the solar modulation potential as best fit to data. The difference in spatial distribution are given in Fig. 3.14 within the Galactic plane ($z = 0$). For e^- and p at low and high energy, these plots again show the ratio (adapted grid)/(uniform grid). There is a large homogeneous region in the galactic plane in which the deviation is below 5% (7% for protons at higher energies). Outside the Galactic Disc, $R = \sqrt{X^2 + Y^2} > 15\,\mathrm{kpc}$, deviation rises up to over 20% up and down, which are not regions of great significance. Overall, the distribution in the low energy range does, for e^- and p, decrease about $3 - 5\%$.

To conclude, we see our adapted grid as equally suitable for cosmic ray studies as the uniform reference grid. The uniform grid shown before uses customary grid spacings of 200 pc in z direction and 500 pc in each x and y directions. In contrast, the adapted grid thus has a locally improved resolution of a factor 20 in z and 50 in x and y, while only containing a factor 9.6 as many grid points in total (i.e. memory usage does not blow up dramatically). Furthermore, Tab. 3.2 lists the definition of this grid, which will be used throughout our study.
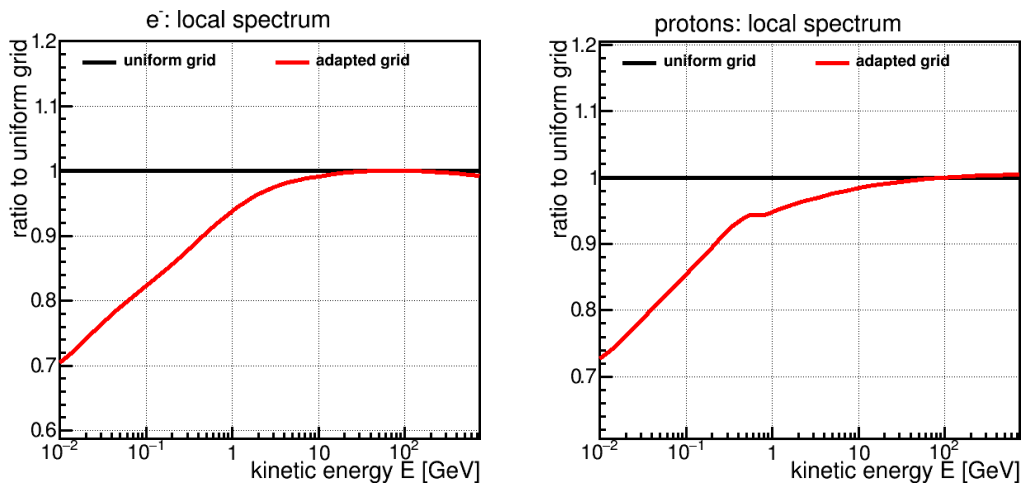
Figure 3.13. Choice of uniform grid, energy spectrum deviations: The ratio of particle spectrum in our locally adapted grid, relative to the particle spectrum in the uniform grid, are seen. The **left** panel shows the relative deviation of e^- spectra, the **right** panel the relative deviation of p spectra. Above kinetic energy $E \gtrsim 1$ GeV, the deviation is below 5% for both species. The low-energy deviations of up to 30% are considered negligible because the solar modulation parameter can be reduced to correct this decrease.
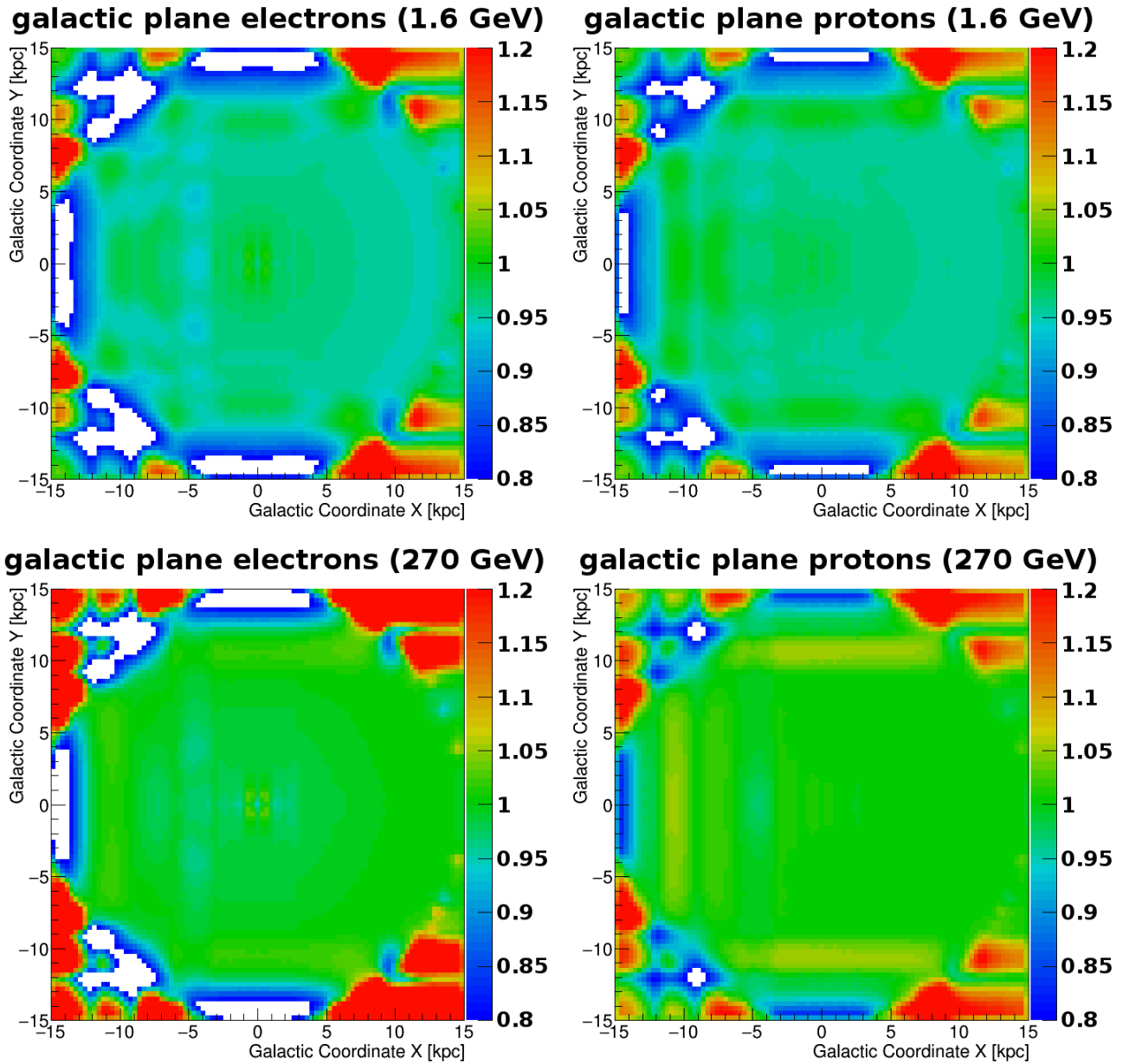
Figure 3.14. Choice of uniform grid, spatial deviations in the Galactic plane: In each plot, we see the particle distribution in our locally adapted grid, relative to the particle distribution in the uniform grid. Panels **left** show e^-, panels **right** show p. **Top** panels show the case of low energy ($E \approx 2\,\text{GeV}$), **bottom** panels the case of high energy ($E \approx 270\,\text{GeV}$). There is a nearly-uniform decrease in energy at low energies, also visible in Fig. 3.13. The deviations shown here are considered acceptable.

X	Y	Z	X	Y	Z	X	Y	Z
			...	...	...	...	...	...
-15			7.948	-0.352	-0.352	8.543	0.243	0.243
-12			7.989	-0.311	-0.311	8.575	0.275	0.275
-9			8.025	-0.275	-0.275	8.611	0.311	0.311
-6			8.057	-0.243	-0.243	8.652	0.352	0.352
-3			8.085	-0.215	-0.215	8.698	0.398	0.398
-2	-15		8.109	-0.191	-0.191	8.75	0.45	0.45
-1	-12		8.13	-0.17	-0.17	8.808	0.508	0.508
0	-9		8.148	-0.152	-0.152	8.873	0.573	0.573
1	-8		8.164	-0.136	-0.136	8.945	0.645	0.645
2	-7		8.178	-0.122	-0.122	9.024	0.724	0.724
3	-6		8.19	-0.11	-0.11	9.111	0.811	0.811
3.4	-5.5		8.2	-0.1	-0.1	9.206	0.906	0.906
3.7	-5		8.21	-0.09	-0.09	9.31	1.01	1.01
4	-4.5		8.22	-0.08	-0.08	9.423	1.123	1.123
4.3	-4		8.23	-0.07	-0.07	9.546	1.246	1.246
4.535	-3.765		8.24	-0.06	-0.06	9.679	1.379	1.379
4.758	-3.542		8.25	-0.05	-0.05	9.822	1.522	1.522
4.981	-3.319		8.26	-0.04	-0.04	9.975	1.675	1.675
5.204	-3.096		8.27	-0.03	-0.03	10.142	1.842	1.842
5.427	-2.873	-2.8	8.28	-0.02	-0.02	10.323	2.023	2.023
5.65	-2.65	-2.65	8.29	-0.01	-0.01	10.518	2.218	2.218
5.873	-2.427	-2.427	**8.3**	**0.0**	**0.0**	10.727	2.427	2.427
6.082	-2.218	-2.218	8.31	0.01	0.01	10.95	2.65	2.65
6.277	-2.023	-2.023	8.32	0.02	0.02	11.173	2.873	2.8
6.458	-1.842	-1.842	8.33	0.03	0.03	11.396	3.096	
6.625	-1.675	-1.675	8.34	0.04	0.04	11.619	3.319	
6.778	-1.522	-1.522	8.35	0.05	0.05	11.842	3.542	
6.921	-1.379	-1.379	8.36	0.06	0.06	12.065	3.765	
7.054	-1.246	-1.246	8.37	0.07	0.07	12.3	4	
7.177	-1.123	-1.123	8.38	0.08	0.08	13	4.5	
7.29	-1.01	-1.01	8.39	0.09	0.09	13.5	5	
7.394	-0.906	-0.906	8.4	0.1	0.1	14	5.5	
7.489	-0.811	-0.811	8.41	0.11	0.11	14.5	6	
7.576	-0.724	-0.724	8.422	0.122	0.122	15	7	
7.655	-0.645	-0.645	8.436	0.136	0.136		7.5	
7.727	-0.573	-0.573	8.452	0.152	0.152		8	
7.792	-0.508	-0.508	8.47	0.17	0.17		9	
7.85	-0.45	-0.45	8.491	0.191	0.191		12	
7.902	-0.398	-0.398	8.515	0.215	0.215		15	
...	...	...	...	...	...			

Table 3.2. This list our grid choice, tabulated. It has $112 \times 112 \times 83$ grid points and is shown centered around the Sun (thus the columns start in different rows). The **solar bin** is marked red, the inner, 10pc resolution region in blue. The surrounding neighborhood in which we still expect some minor influence of the Local Bubble is marked in magenta.

3.3. Physical motivation of local transport models

We have now defined our galactic transport model (Tab. 3.1) and our local grid (Tab. 3.2) and can proceed with the actual *local model definition.* We will start with a discussion of the motivation(s) of the physical effects likely to play a role.

From the observations that lead to the discovery and acceptance of its existence, we consider the Local Bubble to consist of two distinct phases, based on Figs. 1.21, 1.22 and 1.23:

- The LB **Interior**, a hot ($T \sim 10^6$ K), dilute gas, resembling the Coronal Gas phase. As the Local Bubble is intruded by clouds of denser gas, as the Local Fluff, especially increasing towards the direction of the Loop I superbubble, we do not consider the gas density to be as low as the reference value for Coronal gas (Tab. 1.1). We do not further consider the inlets of denser clouds value of interior density of $\frac{1}{10}$ relative to the local average gas density. We simplify its structure as a spherical shape of radius 100 pc in the Galactic Plane, and consider the vertical extension either to be same, or elongated.

- the LB **Walls**, the denser structures of HI gas surrounding the local cavity. These are cold clouds ($T \sim 100$ K) that piled up after the superbubble shock expansion had lost enough pressure, in order not to evaporate them (cf. "Snowplow phase", appendix A.1). Therefore, the Walls are not a continuous shell, but disrupted or open in some directions. For the average gas density, we thus take an average gas concentration of a factor 10 compared to the average value and then simplify the structure as uniformly surrounding the Interior.

For any of the bubble structures outside the Walls (sometimes referred to as Swiss Cheese [126]), we assume that they can well be averaged out and ignored, as these are taken to be distributed stochastically (the special importance of the Local Bubble comes only from the fact that we live inside).

While the gas density can be based on astronomical observations - and deviations from the local average might or might not be relevant to cosmic ray diffusion - there are no observations to compare the local magnetic field with the local average values, both for the regular and the turbulent component. From (2.29), we know that the relative amplitude of magnetic turbulence $|\delta B/B_0|$ enters the diffusion coefficient via the prefactor

$$D_0 \propto \left| \frac{\delta B}{B_0} \right|^{-2} .$$

(3.2)

This means that by fluctuations of the local turbulent amplitude of a factor 10 up or down, D_0 could vary by a factor 100 down or up. There are a number of physical effects that could lead to such a variation in both phases. As the physical actuality is not known, our models will investigate several possibilities. It follows a description of phenomena either leading to MHD wave damping (i.e. rise in D_0) or amplification of turbulent fields (i.e. drop in D_0), as found in astrophysical environments.

3.3.1. Bubble Interior, Fast Diffusion: MHD Wave Landau Damping

In regions of higher temperature and levels of ionization, the diffusion coefficient might be significantly enhanced, as e.g. suggested by [127]. This is attributed to the damping of δB wave modes due to so-called *linear Landau damping* [128], a energy exchange process between a type of MHD waves (magnetosonic) and surrounding thermal plasma. The velocity distribution of the hot gas $f(v)$ is approximated as Maxwellian, see Fig. 3.15).
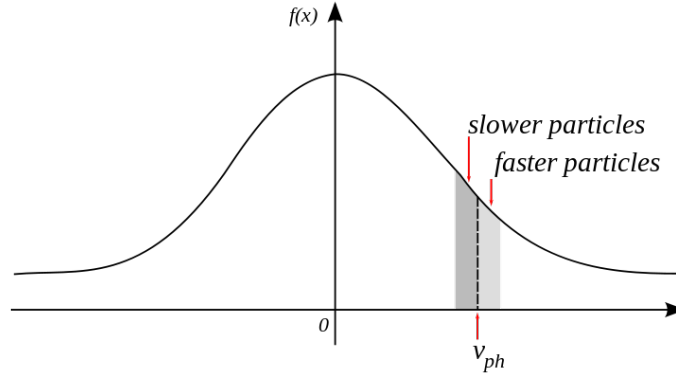
Figure 3.15. Landau damping by the exchange of a wave component v_{Ph} with the slower component of the gas, heating it up. The wave loses energy.

Resonant interaction between a δB wave component of given phase velocity v_{Ph} with a thermal particles of comparable velocity causes the latter to stochastically speed up or slow down, i.e. diffuse in momentum space. This is enhanced because in actuality, nonlinear wave-particle interactions cause a broadening of the resonance condition [75]. For the wave, this implies an energy loss in form of a exponential wave damping

$$\delta B(k) \propto e^{-\kappa(k)t} \tag{3.3}$$

with damping exponent

$$\kappa(k) \propto -\frac{1}{k^2}\left(\frac{\partial f}{\partial v}\right)_{v_{\mathrm{Ph}}} > 0 \tag{3.4}$$

Landau damping plays a significant role in *high-β* plasmas [129], β being the ratio of thermal to magnetic pressure:

$$\beta = \frac{2v_{\mathrm{sound}}^2}{v_A^2} = \frac{8\pi p}{B^2} \tag{3.5}$$

(p thermal pressure, B regular magnetic field), whereas a $\beta \gtrsim 0.1$ is considered "high-β"[130]. In [127], Spangler estimates a Local Bubble interior $\beta \approx 9$, further suggesting that an lower value of the regular magnetic field B in the bubble could increase β even more. A brief review of astrophysical wave damping is given in [129] and further reading e.g. in [131] and references therein.

3.3.2. Bubble Interior, Slow Diffusion: Turbulent amplification during shock expansion

On the contrary, the interior regions of SNR and Superbubbles are usually showing high degrees of turbulence, meaning a decrease in D_0. Fig. 3.16 shows, as an example, a numerical simulation of a core-collapse supernova explosion [132]. In the first picture, we see the reverse-shock wave, falling inwards to the core. Movement of a dense fluid against a significant more diluted one causes the creation of Rayleigh-Taylor instabilities[2], the fractal structures standing out especially in the second and third picture. In the third picture, the reverse shock hits the core, further swirling up the interior material. If the Alfvén theorem holds, i.e. the magnetic field is following the movement of the gas, these instabilities ultimately lead to strong turbulent cascades, pumping energy into a wide range of wave modes $\delta B(k)$. The effect of Rayleigh-Taylor instability is also very prominently seen in some SNR, e.g. as the bright filaments in the Crab Nebula 1.12).
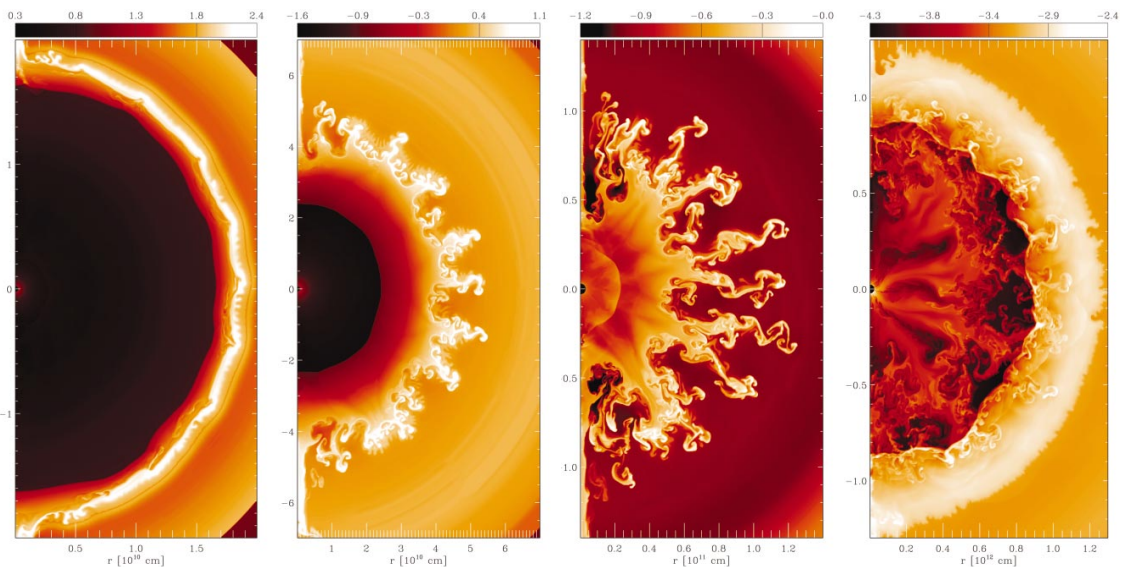
Figure 3.16. Temporal evolution of the particle densities inside a non-spherical core-collapse supernova, numerical simulation by [132]. This shows the inward-traveling reverse shock (bright circle left in the first picture), back to the core (which it meets in the third picture) This illustrates the possible high levels of turbulence inside supernova remnant structures like the Local Bubble.

However, little about the internal structure of the Local Bubble is known so far. It is still open to debate whether the Alfvén theorem is applicable inside the SNR, because it loses its validity in fluids of finite conductivity [133]). If so, no connection between the observation of turbulent gas and turbulent magnetic fields can be made. The idea of a drop in diffusion coefficient is indeed supported by [134], who argue that by CR shock acceleration itself, magnetic turbulence in the shocks is amplified by a instability effect; also [135] indicates $|\delta B/B| > 1$. An extensive review of interstellar turbulence is given by [136].

---

[2](The same instabilities lead to the distinct shape of atomic mushroom clouds.)

To summarize, the behavior of D_0 in the Interior region is depending on which one of the two effects dominates. This is not known. We thus intend to evaluate models of both types. Similarly, the Wall regions could show two competing effects for magnetic turbulence:

3.3.3. Bubble Walls, Fast Diffusion: Collisional MHD wave damping

Turbulent δB wave components can also lose energy in a partially ionized, dense gas as present in the cold bubble wall regions, by *ion-neutral friction* [137, 129, 138]: The MHD oscillations of δB are coupled to the movement of the charged particles in the medium, mostly electrons, plus the smaller amount of ionized hydrogen. The neutral hydrogen is thermalized at about 100 K and thus has a low mean particle velocity. Particle collisions between the two phases will then, on average, shift energy from the faster charged particle to the slower neutral particle, removing kinetic energy from the oscillation. By further collisions, this energy then gets randomly distributed in the thermal phase (hence it is *friction*).

Compared to the average ISM, this effect is expected to be stronger when the degree of ionized gas is *low* (as in cold atomic clouds, typically at 1%[12]). There, the damping via ion-neutral friction is more effective as the neutral phase has large inertia, enabling it to efficiently dissipate energy away from the turbulent field. In contrast, a high degree of ionization leads to a high ion-neutral collision rate: This excites the neutral phase to oscillate and not to dissipate the wave energy thermally. This is illustrated in fig 3.17 [139].

Figure 3.17. Collisions in a partially ionized medium transfer energy from the ion oscillation to neutrals, leading to frictional dissipation. This damping is stronger in a less ionized medium. Fig. based on [139].

As a second effect, this energy drain can be amplified by *charge exchange* collisions in the partially ionized phase [140]: If the density is high enough, frequent $p + H \rightarrow H + p$ collisions can occur by transferring the hydrogen's valence electron. This replaces one particle of the oscillating phase with one particle of the thermal phase, moving completely randomized, leading to further deceleration of the δB oscillations.

Further reading about the wave damping mechanism by ion-neutral and its effect on cosmic ray propagation is found in [141] and references therein.

A drop in diffusion coefficient in the wall regions is also assumed by [69], with the reason that the *regular* magnetic field B_0 could be highly increased, thus leading to a rise in $D_0 \propto |\delta B/B_0|^{-2}$.

3.3.4. Bubble Walls, Slow Diffusion: Turbulent amplification during pile-up

On the other hand, the piling up of the bubble walls might have, in fact, *enhanced* its turbulent field significantly. Cold clouds around a supernova expansion can form after its adiabatic phase, the Sedov-Taylor phase, is not as energetic anymore as to rather evaporate any surrounding cold material. As mentioned above, the pile-up of gas clouds happens after the pressure gradient between expanding supernova shocks and the clouds has become softer. However, turbulent boundary instabilities can also occur in the material upstream. These include Rayleigh-Taylor instabilities and Kelvin-Helmholtz-instabilities, the latter one occurring when two phases of different velocity are sheared against each other. With the δB frozen in, the diffusion coefficient $D \propto |\delta B/B_0|^{-2}$ in the bubble wall would then be decreased compared to the rest of the ISM.

Investigations of the interactions of shock waves with interstellar clouds have been e.g. done by [142, 143]. Fig. 3.18 shows an extreme example, in which a strong shock wave (propagating upwards) meets a gas cloud (initially a spherical gray volume, in picture (a)). The cloud is pushed along the shock (upwards) and at its boundary, Kelvin-Helmholtz instabilities arise as distinct shapes (clearly visible in (d) and (e)). From (e) on, the turbulent amplification inside the cloud has completely distorted its shape.
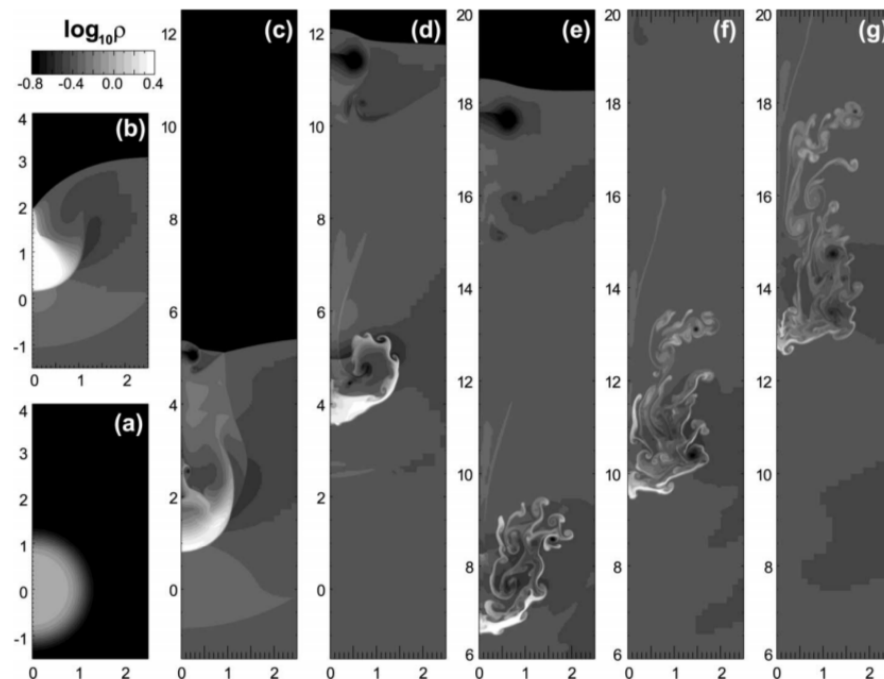
Figure 3.18. Numerical simulation of a small cloud (gray area in (a) that is hit by a shock wave (traveling from bottom to top). The temporal evolution is (a) to (f) in that order. At the cloud surface fluid instabilities form, most notably the Kelvin-Helmholtz instabilities that look like wave crests. In this extreme case, this lead to the destruction of the cloud, while in weaker scenarios, it could only lead to an increase in turbulence within the cloud. From [143].

To summarize, in both the overdense walls and the rarefied bubble cavity, there are two possibilities: Either the internal level of magnetic turbulence gets enhanced in respect to the outside, by the expansion itself, or on the contrary, wave damping processes remove energy from the turbulent field. Before we proceed to implement these changes as in inhomogeneous models of D_0, we discuss the two effects of altering the local gas distribution: the secondary production and three of the energy losses are coupled to the ISM gas density.

3.3.5. Particle interactions in the solar neighborhood

We address the local modification of the gas distribution first, because it illustrated our model implementation of the Local Bubble shape.

Here, it will be shown that locally modifying the gas density according to the Local Bubble, the secondary production can have a profound effect, especially on observables that are largely given as secondaries ($\bar{p}$, e^+, boron), while the energy losses fluctuations usually have little effect on the particles.

3.3.5.1. Secondary production

The secondary particle source function, as a product of primary particles inelastically scattering on any interstellar gas, is given straightforward and only depends on the respective densities of primary CR and hydrogen gas (with a given cross section $\sigma(E'; E)$, E the kinetic energy of the produced particle (e.g.[144])),

$$Q_{\text{sec}}(\vec{r}, E, t) = n_{\text{H}}(\vec{r}) \cdot \int dE' \, N_{\text{prim}}(E', \vec{r}, t) \, \sigma(E'; E) \qquad (3.6)$$

$$\text{total } n_{\text{H}} = n_{HI} + n_{HII} + n_{H2} \qquad (3.7)$$

plus a similar contribution from interaction with interstellar helium. For antiprotons, the iteration of this process is taken into account: Secondary antiprotons interact with the gas to produce *tertiary* antiprotons. This is considered relevant for the low-energy region, $E \leq 0.5\,\text{GeV}$, where it was calculated that the total $\bar{p}$ flux should consist of more tertiary $\bar{p}$ than secondary $\bar{p}$ [145].

In the astronomical observations of the Local Bubble, as reviewed in chapter 1, there is no information about the local n_{HII} and n_{H2} density. The latter might be assumed zero in the $\sim 10^6\,\text{K}$ hot Local Bubble (H_2 molecules would not survive this). Probably there is no complication, because secondary production only scales according to the sum of the gas phase densities (3.7), but in order to test this we suggest varying the single gas components and comparing the outcome, e.g. for the $\bar{p}$ component (whose production is then two-told coupled to the gas density).

3.3.5.2. Energy loss

To shortly revisit the considerations of chapter 1 (especially Fig. 1.17), we have in total five energy losses commonly considered. With the gas components n_H, the ISRF energy density U_{ph} and the galactic (regular) magnetic field energy density $U_B = (8\pi)^{-1}B_0^2$ (see section 1.3.4). The energy losses depend on these ISM distributions as:

Ionization rate $\propto (n_{\mathrm{H2}} + n_{\mathrm{HI}})$ all cosmic rays

Coulomb interaction $\propto (n_{\mathrm{HII}})$ all cosmic rays

Bremsstrahlung in neutral gas $\propto (n_{\mathrm{H2}} + n_{\mathrm{HI}})$ leptons only

Bremsstrahlung in plasma $\propto (n_{\mathrm{HII}})$ leptons only

Synchrotron $\propto B_0^2$ leptons only

Inverse Compton $\propto n_{\mathrm{ph}}$ leptons only

The local gas densities from the Galprop model are $n_{\mathrm{HI/H2/HII}} = 0.911/0.596/0.034\,\mathrm{cm}^{-3}$. Thus, if we vary each distribution by a fixed factor up or down and see as a result only variations in $\bar{p}$ flux of these factors (relative to the total gas density, they are $(HI/H2/HII) = (59\%/39\%/2\%)$, we can safely assume that the energy losses in the different phases play no role and the distribution of local gas only has to be accounted for secondary (and tertiary) production. Then, we can modify n_H as a whole without spending attention to the exact composition $HI/H2/HII$.

In advance, we might assume that the local Bremsstrahlung emissions do not play a significant role, as they generally do not. Also, from the low density of HII, locally the Coulomb-mediated energy losses should be relatively weak. It is probably safe to estimate that even if our surrounding would be unusually dense for the ISM, the increased ionization losses would not contribute much for nuclei, as the volume is small compared to the galactic halo. Also, low energies have the relative freedom in solar modulation, which could compensate for any changed in low-energy loss.

We have the tools to study local modifications of the Dragon gas distribution easily, so we suggest just to evaluate the effects. We construct four models for the gas density, and we address the question of local increase or decrease of the regular magnetic field (for Synchrotron energy losses) and ISRF (for Inverse Compton losses), respectively.

Relevance of single gas components?

From the section about grid choice 3.2, we do already know that we are advised to implement any modification of any parameter in a *smooth* way. This might be less critical for the gas distribution, but for flexibility, we directly address this now. To achieve a dilution of the Interior gas to a factor $\frac{1}{10}$ and in the Walls, at distance, we compose of Gaussian shapes a function $f_{\mathrm{Gas}}(d) = f(|\vec{r} - \vec{r}_\odot|)$ of distance d as shown in Fig. 3.19.

This way, the position-dependent modification of the gas is sufficiently smooth over the numerical grid. For simplicity, the sun is taken directly at the center of this shape. At $d = 0$, the modification is applied at full strength. The transition to the bubble walls starts at $d = 80\,\mathrm{pc}$, is at maximum at $d = 100\,\mathrm{pc}$ and is then extended to a "tail" region until about $d \approx 180\,\mathrm{pc}$, in which modification effects are not expected to be strong anymore. This function was tested amongst others and worked for our choice of grid.
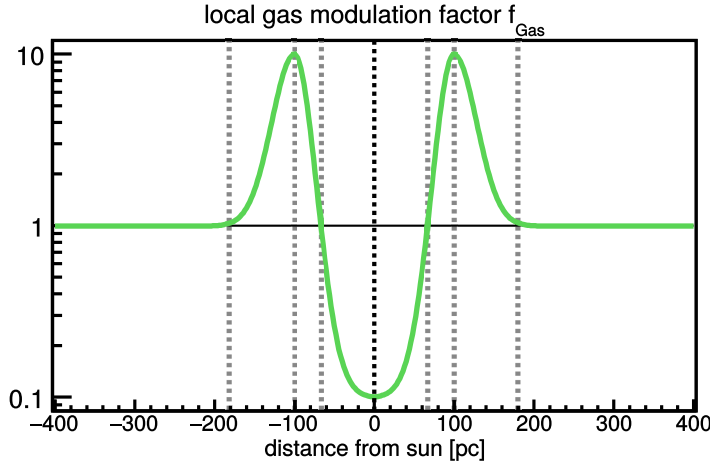
Figure 3.19. We suggest a smooth function to describe wall-and-interior behavior of the local gas. The value on the y-axis is the factor that gets applied to the gas density at a given distance. With this parametrization, the Interior region is spanning from $d \in [-80, 80]\,\mathrm{pc}$, the Walls show the largest density at $d = \pm 100\,\mathrm{pc}$ and beyond, there is a tail structure to assure smooth propagation conditions.

This method assumes a certain symmetry of the the Local Bubble. For the ModHI, ModH2, ModHII, ModGas models, we assume a spherical shape

$$f(\vec{r}) = f\left(\sqrt{d_x^2 + d_y^2 + d_z^2}\right) . \tag{3.8}$$

For reference, in diffusion models we will either use the same assumption, or assume a cylindrical shape (as Fig. 1.23 shows, there is a certain elongation in z direction)

$$f(\vec{r}) = f\left(\max\left(\sqrt{d_x^2 + d_y^2}, |d_z|\right)\right) , \tag{3.9}$$

or, one might assume a different function in vertical behavior, as is it not entirely clear at all whether the Coronal gas in the Local Bubble is directly connected with the Galactic Halo, which motivates further models of local transport, with a separate (e.g. Gaussian) shape $f_z(d_z)$,

$$f(\vec{r}) = f\left(\sqrt{d_x^2 + d_y^2}\right) \cdot f_z(d_z) . \tag{3.10}$$

We further assume the homogeneity of the bubble, especially of the Bubble Walls as one closed surrounding and of the Interior as one thin medium, without inclusion of any clouds or filaments. Comparing with Figs. 1.22 and 1.23, this might appear as a crude

oversimplification. At this point in the study, however, we see no further use in overly complicated assumptions: We want *to estimate the impact of the Local Bubble on galactic transport models in general.* This is especially emphasized considering that the Local Bubble structure is still under active investigation, and especially considering that we have no theory yet to predict the behavior of the diffusion coefficient in these regions, due to little restriction from magnetic field observations. Instead, we will return to these assumptions for the evaluation of our specific models, if we consider it illustrative.

We define the four simple *local gas* models

- ModHI: $n_{HI}(\vec{r}) \longrightarrow n_{HI}(\vec{r}) \times f_{\mathrm{Gas}}(\vec{r})$

- ModH2: $n_{H2}(\vec{r}) \longrightarrow n_{H2}(\vec{r}) \times f_{\mathrm{Gas}}(\vec{r})$

- ModHII: $n_{HII}(\vec{r}) \longrightarrow n_{HII}(\vec{r}) \times f_{\mathrm{Gas}}(\vec{r})$

- ModGas: $n_{H}(\vec{r}) \longrightarrow n_{H}(\vec{r}) \times f_{\mathrm{Gas}}(\vec{r})$ $(n_H \equiv n_{HI} + n_{H2} + n_{HII})$

and we will further define a bubble-interior shape to either increase or decrease a physical quantity inside the Local Bubble, as we will do in models of *local magnetic field / radiation field* setups. We will perform these for an understanding of the hypothetical impact on leptonic fluxes, at the current time we do not know of a specific behavior of both of these fields in the real Local Bubble. For modifications that do not regard any special behavior inside the bubble walls, we suggest the functions shown in Fig. 3.20, here named f_{Mag} or f_{ISRF} because we first apply them to magnetic field and ISRF, but of general use in our definition of diffusion scenarios. In these cases, the bubble interior is taken to extend up to a distance of $d = 100\,\mathrm{pc}$, then smoothly fading away until $d = 200\,\mathrm{pc}$.
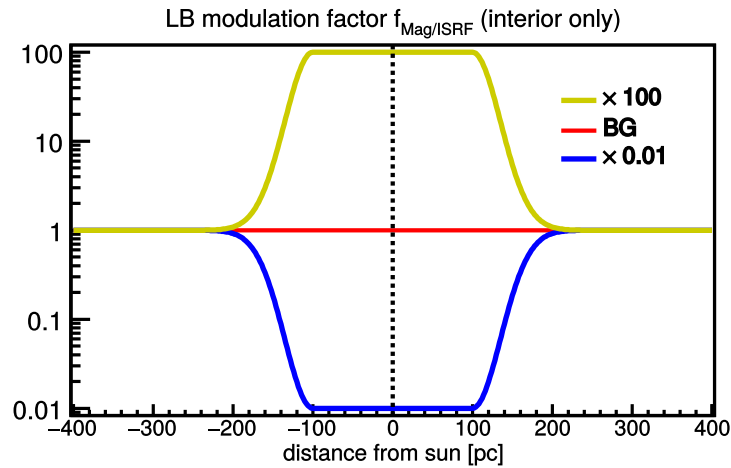
Figure 3.20. We suggest a smooth function to describe a sole increase (yellow) and decrease (blue) of a factor 100, of the magnetic field or the radiation field, in the Local Bubble Interior. The value on the y-axis is the factor that gets applied to the particular quantity at a given distance. With this parametrization, the Interior region is spanning from $d \in [-100, 100]\,\mathrm{pc}$, and then fading smoothly for further distances, to assure smooth propagation conditions.

We will gain a first glimpse on the importance of local transport models that account for a more realistic gas distribution. For local transport models that account for a more realistic diffusion coefficient - or account for *a range of assumptions* about realistic diffusion in the galactic neighborhood - we will then define similar functions similar to the templates just described. We implemented this range of functions in our local version of DRAGON and would, in principle, also be able to modify parameters as the source density, the convection velocity, or even the reacceleration strength. There is only no good motivation for such a study, at the current stage.

3.4. Evaluation

3.4.1. Transport models with locally modified gas distribution

We first address the question of fluctuations in the gas distribution alone and compare models ModGas, ModHI, ModH2 and ModHII versus the reference BG. The local proton spectrum prediction (Fig. 3.21) is only affected insignificantly, in similarity to the BG vs. "no-energy-loss" comparison in section 2.4.2, Fig. 2.8. This confirms that energy loss for hadronic CR particles is not to be considered relevant for cosmic rays, neither at the local nor at the galactic scale.

We now can use the antiproton prediction (Fig. 3.22) as suggested above, as an indicator for the amount of secondary production. Secondary production rates (3.6) are linearly coupled to the gas densities. By application of the local gas factor (Fig. 3.19) they rise (in the Walls) or drop (in the Interior) accordingly. Fig. 3.22) shows that indeed, there is a constant factor at all energies, and these factors for the three models are summarized in Tab. 3.3. It is visible that indeed, the factors in overall more-production of $\bar{p}$ correspond just to the local percentages of each particular gas component.

The point for antiprotons remains a point for positrons (Fig. 3.23). These spectra show, compared with BG, a stronger energy dependence of the rise in secondary production, but when comparing different gas modifications in relation to modifying all H, the overall effect is just according to the local percentage of this contribution.

modified component	unmodified local density (% of all H)	average rise in antiprotons
HI	0.911 cm^{-3} (59%)	4.9% (64%)
H2	0.596 cm^{-3} (39%)	2.6% (34%)
HII	0.034 cm^{-3} (2%)	0.2% (2.6%)
all H	1.541 cm^{-3} (100%)	7.6% (100%)

Table 3.3. By accounting for the gas overdensity in the Local Bubble Walls, secondary production rates rise. This is considered for antiprotons $\bar{p}$. The increase is purely due to the increased target density, as shown by the agreement of the percentages in the second and third column (i.e. the type of gas does not play a role).
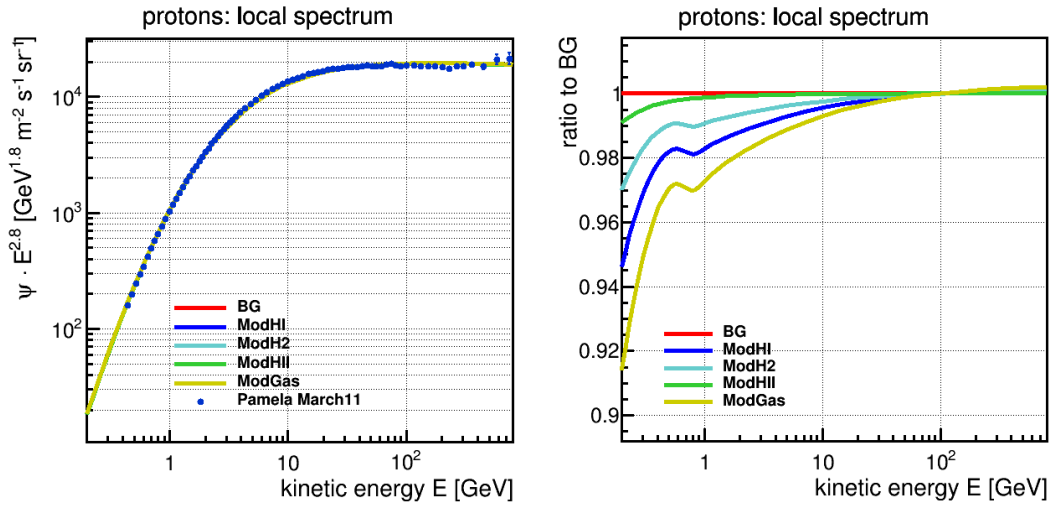
Figure 3.21. The reference model (red) in comparison to the modifications by the f_{Gas} function Fig. 3.19, of only the *HI* component (ModHI), only the *H*2 component (ModH2), only the *HII* component (ModHII), or all gas components (ModGas). The **left** panel shows the proton flux (scaled with factor $E^{2.8}$). The **right** panel shows the ratio of the proton flux in each local gas model to the reference model. Overall, little deviations are seen.
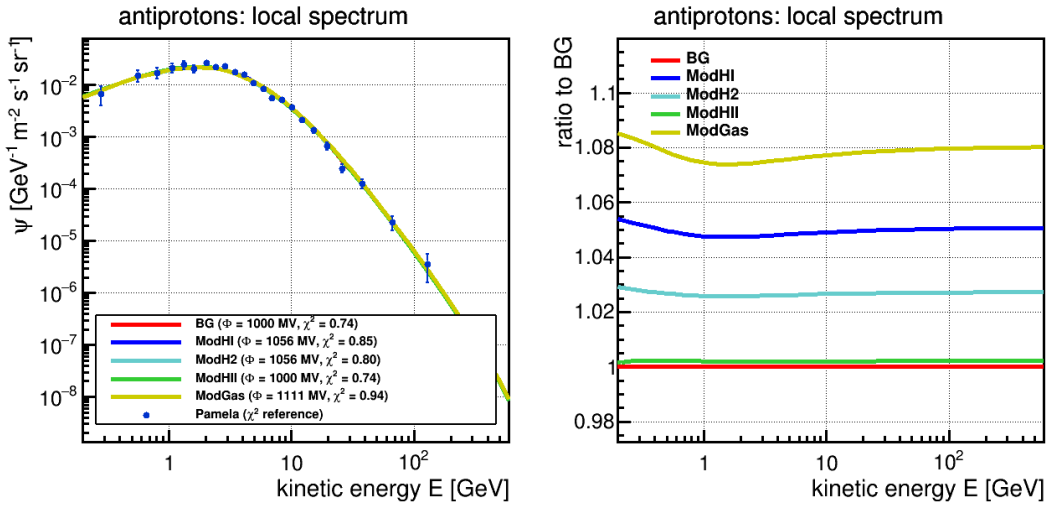
Figure 3.22. The reference model (red) in comparison to the modifications by the f_{Gas} function Fig. 3.19, of only the *HI* component (ModHI), only the *H*2 component (ModH2), only the *HII* component (ModHII), or all gas components (ModGas). The **left** panel shows the antiproton flux. The **right** panel shows the ratio of the antiproton flux in each local gas model to the reference model. The local gas modifications each lead to a constant rise in antiproton production, summarized in Tab. 3.3.

The shape of the ratios for positrons (Fig. 3.23) are likely due to the small effect of Bremsstrahlung, which becomes slightly enhanced in the gas (as these models did not employ changes in the magnetic/radiation field, and the total propagation time is not altered by only modifying the gas, Synchrotron/IC losses are expected to stay the same). We have now shown that the detailed description of the local gas distribution is negligible for the account of the energy losses in the gas, but relevant for secondary productions. If
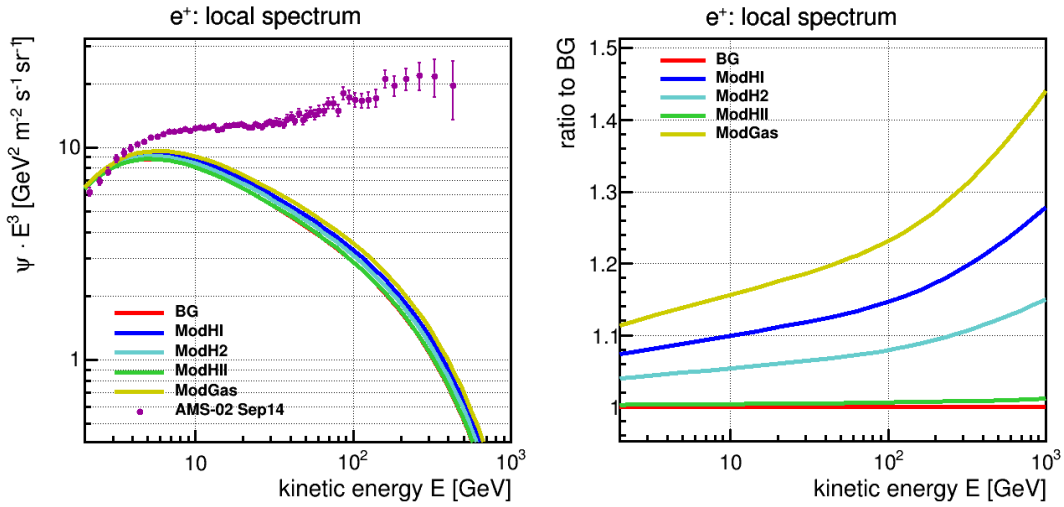
Figure 3.23. The reference model (red) in comparison to the modifications by the f_{Gas} function Fig. 3.19, of only the *HI* component (ModHI), only the *H*2 component (ModH2), only the *HII* component (ModHII), or all gas components (ModGas). The **left** panel shows the positron flux (scaled with E^3). The **right** panel shows the ratio of the positron flux in each local gas model to the reference model. The local gas modifications each lead to a constant rise in antiproton production

one considers a modification of the diffusion coefficient, as we do later on, this might lead to an extra component of nearby produced secondary particles, which is not large however. We also showed that there is not need to further investigate the particular gas components, but it is sufficient to examine overall modification of the total local gas distribution instead.

Next, we turn to the high-energy energy loss processes that are only relevant to the $e^{\pm}$ observables due to their low mass. Emission processes for Synchrotron and Inverse Compton radiation depend on the energy density of the background magnetic field, and interstellar photonic field, respectively. These effects might be more important, as they already are in galactic transport models, and limiting the assumed position of lepton sources (see section 2.5.2).

Because the energy loss time for leptons at high energies is influenced by the sum of energy density of the magnetic field and the radiation field,

$$\tau = \frac{E}{\dot{E}} = \frac{E}{\dot{E}_{\text{IC}} + \dot{E}_{\text{Sync}}} \propto \frac{1}{U_{\text{ph}} + U_B} \tag{3.11}$$

$$\approx \frac{1}{2U_B} \quad \text{(assuming equipartition)}, \tag{3.12}$$

it is evidently not very instructive to look at only the decrease of one of the electromagnetic energy densities. For example, a drop of $U_B \to 0.01 U_B$ would only imply a increase of $\tau \to 2\tau$ for U_{ph} unchanged, and vice versa. However, if one component increases by a large amount, e.g. $U_B \to 100 U_B$, the energy loss time scale will follow $\tau \to 2 \cdot 10^{-2}\tau$ for U_{ph} unchanged. Therefore, the energy loss time scales might even be dramatically reduced and potential $e^{\pm}$ sources would have to be closer than estimated in section 2.5.2. While in principle, it would be possible to use the iterative scheme we previously introduced and

apply it to such a scenario, we do not do this as we do not currently see motivation for such an increase.

Therefore we use the Interior-Only modification function of Fig. 3.20 only to discuss five basic, exaggerated models for general insight:

- Sync ×100(< 100pc): increase the GMF energy density $U_B \rightarrow 100U_B$ (equals an increase of regular magnetic field strength $B_0 \rightarrow 10B_0$),

- IC ×100(< 100pc): increase the ISRF energy density $U_{\mathrm{ph}} \rightarrow 100U_{\mathrm{ph}}$,

- Sync/IC losses ×0.01(< 100pc): decrease both energy densities $U \rightarrow 0.01U$

in which a LB radius of 100 pc is assumed as in Fig. 3.20, and for further comparison

- Sync/IC losses ×0.01(< 300pc): decrease both energy densities $U \rightarrow 0.01U$ within 300 pc radius

- Sync/IC losses ×0.01(galaxy wide): decrease both energy densities $U \rightarrow 0.01U$ in the whole galaxy (this comes then close to the no-energy-loss model of chapter 2)

The results on positrons and electrons look very similar (as expected, these are charge-symmetric processes), see Fig. 3.24 for e^- and Fig. 3.25. for e^+ predictions. To conclude, these extreme models show

- A locally strong increase in either the galactic magnetic field or the interstellar radiation field in the Local Bubble could reduce $e^\pm$ flux at high energies $E \gtrsim 200\,\mathrm{GeV}$ down a factor $30 - 50\%$, thus, sources would have to be even closer.

- A local decrease, even if for both fields over a relatively large 300 pc radius, not enhance the high-energy lepton flux to over 10% up, thus, sources could not be expected much further than before.

- The galactic reduction ×0.01 shows again that indeed these energy losses are crucial, but the majority of energy is lost near the sources, not near the Earth.
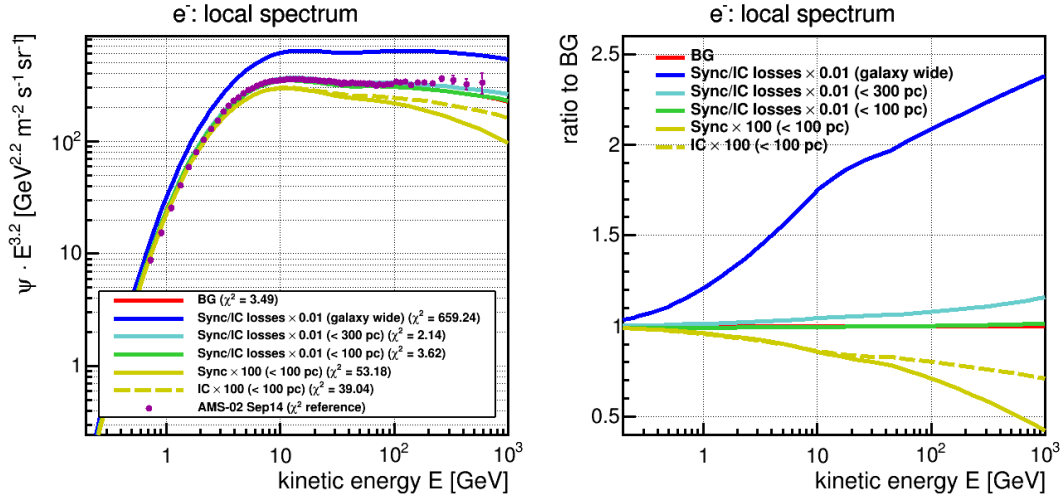
Figure 3.24. The impact of strong local fluctuations in the GMF or ISRF on leptonic fluxes, comparing the reference model BG (red line) with one model of increased GMF (Synchrotron losses) and ISRF (IC losses) each (yellow lines) by a factor 100, and two models in which both quantities are reduced by a factor 0.01, for the previously used LB radius 100 pc (green, very close to BG) and a larger radius 300 pc (turquoise, also similar to BG). Comparison is also shown in a galactic reduction of both quantities to a factor 0.01, which is very close to a "no energy loss" model. The **left** panel shows electron fluxes (scaled with $E^{3.2}$. The **right** panel shows the ratio of electron fluxes for each model to the BG model. The difference between the yellow lines is due to the radiative IC corrections (Klein-Nishina) at high energies. The electron ratios look very similar to the positron ratios Fig. 3.24 (right)
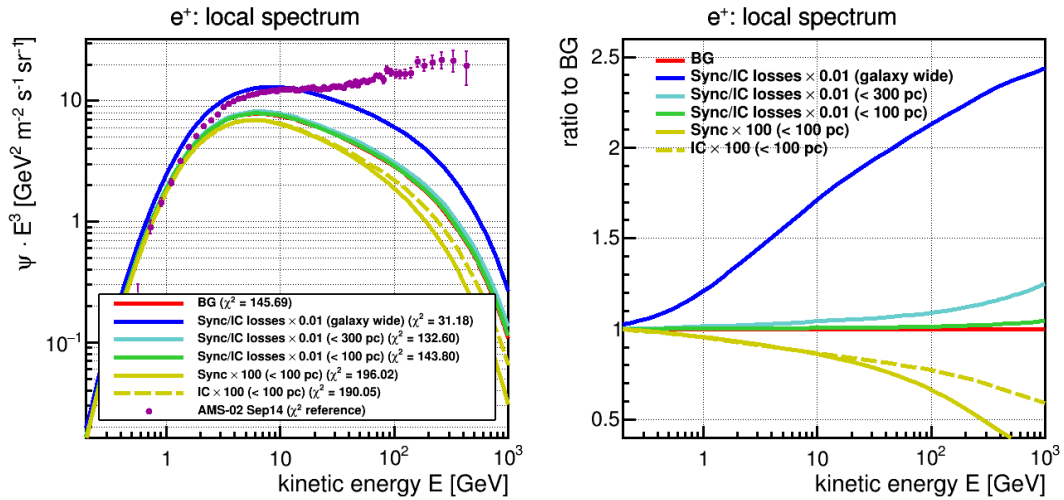
Figure 3.25. The impact of strong local fluctuations in the GMF or ISRF on leptonic fluxes, comparing the reference model BG (red line) with one model of increased GMF (Synchrotron losses) and ISRF (IC losses) each (yellow lines) by a factor 100, and two models in which both quantities are reduced by a factor 0.01, for the previously used LB radius 100 pc (green, very close to BG) and a larger radius 300 pc (turquoise, also similar to BG). Comparison is also shown in a galactic reduction of both quantities to a factor 0.01, which is very close to a "no energy loss" model. The **left** panel shows positron fluxes (scaled with E^3). The **right** panel shows the ratio of positron fluxes for each model to the BG model. The difference between the yellow lines is due to the radiative IC corrections (Klein-Nishina) at high energies. The positron ratios look very similar to the electron ratios Fig. 3.24 (right)

3.4.2. Transport models with locally modified diffusion

Up to now, we have shown how the local gas distribution might affect secondary production, but local energy losses are nearly unaffected by it. Local amplification in GMF or ISRF might increase the energy loss of leptons heavily, but a local deficiency could not explain a significant extension of the leptonic propagation length. We now turn to the presented theories of local diffusion coefficient.

Based on the previous considerations, we have built a total of 34 transport models. These consist of several combinations of model function shapes, similar to the shapes of Figs. 3.19 and 3.20. These can appear very different, so their full description is given in appendix A.4, while here, just a review of the considered shape is briefly given.

The "type" labels given in there follow this nomenclature:

- Slow-Wall-Fast-Interior setups **(type "A")**

- type "A" with chimney-like elongation in vertical direction **(type "TA")**

- Fast-Wall-Slow-interior setups **(type "B")**

- type "'B" with chimney-like elongation in vertical direction **(type "TB")**

- Slow-Interior setups **(type "c")**

- type "c" elongated in vertical direction **(type "e")**

- Fast-Interior setups **(type "C")**

- type "C" elongated in vertical direction **(type "E")**

- Slow-Wall setups **(type "d")**

- Fast-Wall setups **(type "D")**

Unless a setup is explicitly described elongated in vertical direction (into the Galactic Halo), the modifications are implemented spherically symmetric around the Sun. For each setup, we considered a case in which the gas distribution was kept unmodified and one in which its local fluctuations were considered. The latter were designated with a **suffix "g"**. Also, in many cases we considered it interesting to implement different modification strengths, e.g. maximum/minimum factor that was applied to the diffusion coefficient and/or gas distribution. For instance, the model named c100g is a Slow-Interior "c" setup, with a maximum drop in D of a factor 100, and the modification of the gas was implemented, etc.

Before this discussion, we want to *emphasize* that the number of models presented here reflect the degree of missing knowledge about the magnetic turbulence inside the Local Bubble. At this point, we do not mean to *exclude* certain models. **We want to demonstrate that by the lack of knowledge of our solar neighborhood, a very vast range of model prediction can be made about dipole anisotropy**.

The three models which we want to illuminate in detail here are based on rather simple assumptions (see Fig. 3.26)

- c10g: $D \rightarrow \frac{1}{10}D$ in the Interior, with rarefied gas $n_H \rightarrow \frac{1}{10}n_H$.

- C10g: $D \rightarrow \frac{1}{10}D$ in the Interior, with rarefied gas $n_H \rightarrow \frac{1}{10}n_H$.

- c100: $D \rightarrow \frac{1}{100}D$ in the Interior, no modification made to the gas.
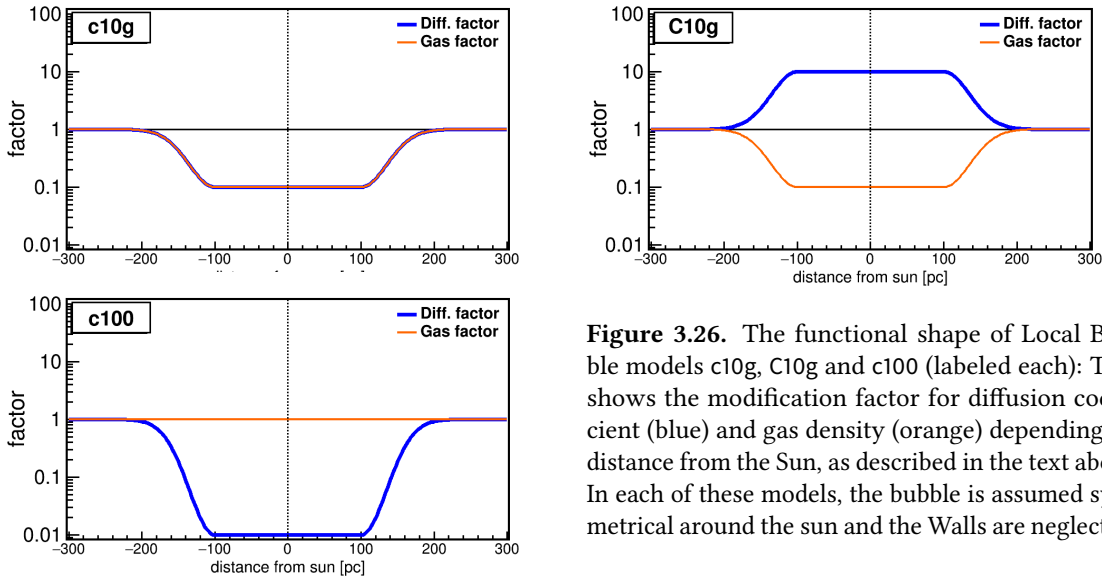
Figure 3.26. The functional shape of Local Bubble models c10g, C10g and c100 (labeled each): This shows the modification factor for diffusion coefficient (blue) and gas density (orange) depending on distance from the Sun, as described in the text above. In each of these models, the bubble is assumed symmetrical around the sun and the Walls are neglected.

With these simple models, we can already illustrate a variety of effects. Generally, c10g and C10g show very little deviation from the reference model BG in the χ^2 description of the spectra (p, $\bar{p}/p$, B/C, $^{10}Be/^{9}Be$, e^-, e^+) themselves (while the B/C spectral shape of c10g differs at low energies, the PAMELA data is described equally, or slightly better). For c100, the measured data of hadronic spectra is poorly described. There is a divergent effect in the prediction of anisotropy ($\delta_{p/p}$, $\delta_{e^\pm}$, $\delta_{e^+/p}$), in that C10g raising anisotropy, and the other two models reducing them by a significant factor. In general, most models showed a varying decreasing effect on dipole anisotropy, which is summarized after the discussion of these three cases in Tab. 3.4.

The description of the local proton spectrum does not show large differences (Fig. 3.27 (left)). In general, it is well described in most of the models we looked at. These are only changed little in spectral shape, and as the normalization condition in DRAGON was imposed so that

$$\psi_p(E = 95.49 \text{ GeV}) \overset{!}{=} 0.0503 \, \frac{1}{\text{GeV}^{-2}\text{m}^{-2}\text{s}^{-1}\text{sr}} \, , \tag{3.13}$$

the source strength in each model was adjusted accordingly (we will refer to this fact as "source renormalization"). As mentioned before, the models show different effects on the

proton/proton anisotropy $\delta_{p/p}(16..350\,\text{GeV})$ (Fig. 3.27 (right)): While for C10g, the increase by a factor 3 is critical in comparison with the AMS-02 limits, the isotropization in the other models can be as severe as by a factor 6 (c10g) or even a factor 50 (c100).
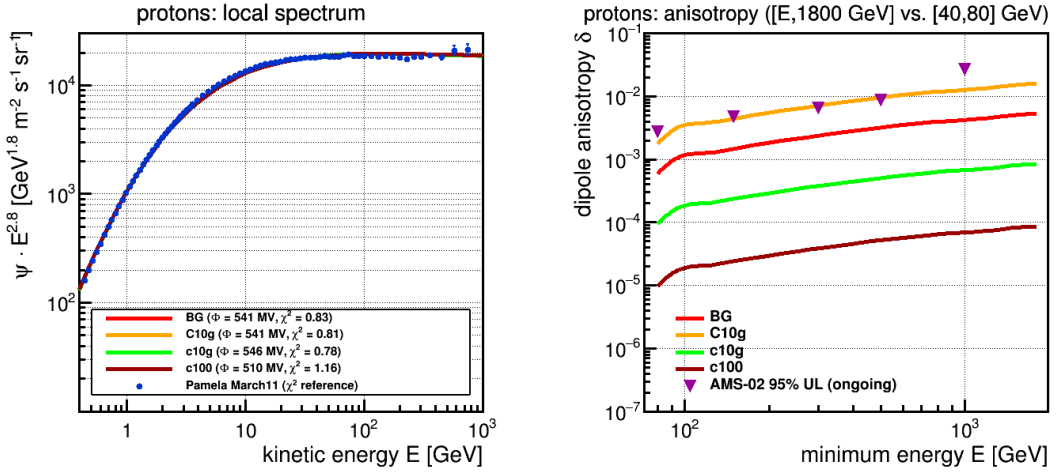
Figure 3.27. For the three exemplary models c10g, C10g and c100, we show that in comparison with the reference model BG, in the **left** panel, the local proton flux (scaled with $E^{2.8}$) does not change much and is in agreement with the PAMELA measurement [119] and in the **right** panel, that the predicted dipole anisotropy of protons relative in energy $\delta_{p/p}$ can rise or decrease, depending on the local model assumptions.

This can be understood by looking at the spatial distribution of protons, as shown in Fig. 3.28 for the examples of x direction (left) and z direction (right), both through the position of the sun at $\vec{r}_\odot = (8.3, 0, 0)$ kpc and taken at $E = 200\,\text{GeV}$ each. In the C10g model (orange), the mean free path length in the Bubble Interior is increased, less scattering takes place. This causes the particles, when the stationary state is reached, to assume a rather similar value in this region, compared to the outside gradient. In the z direction, the distribution appears symmetrical for BG, and the increased free path length leads to a more smoothened out distribution into the Galactic halo. However, this overall smoothening of the gradient $|\vec{\nabla}N|/N$ is only at a factor $\sim 1/3$, while the increase in D of a factor 10 causes the aforementioned increase in anisotropy $\delta \sim D|\vec{\nabla}N|/N$.

The models c10g and c100 show an increase of scattering rate (slow diffusion) throughout the Interior. Compared to the reference model, at each position a smaller influx from the neighboring positions is experienced. In a single-particle picture, protons entering from the outside are less likely to get scattered out again. Towards the center of the bubble, this escape out of the bubble becomes smaller, this effect thus leads to an central overdensity, which is quite weak for model c10g, but very significant for c100. Far outside the Local Bubble, the distribution assumes the same shape as the BG model, but due to source renormalization at the solar position, this model assumes an overall reduced source strength (about 73%). In x direction, the maximum of this Gaussian-like shape is not at the solar position $x = 8.3$ kpc, but slightly to the left as the BG distribution has a gradient in this direction (such a gradient is not there in z direction, so the Sun lies at the maximum, by construction).
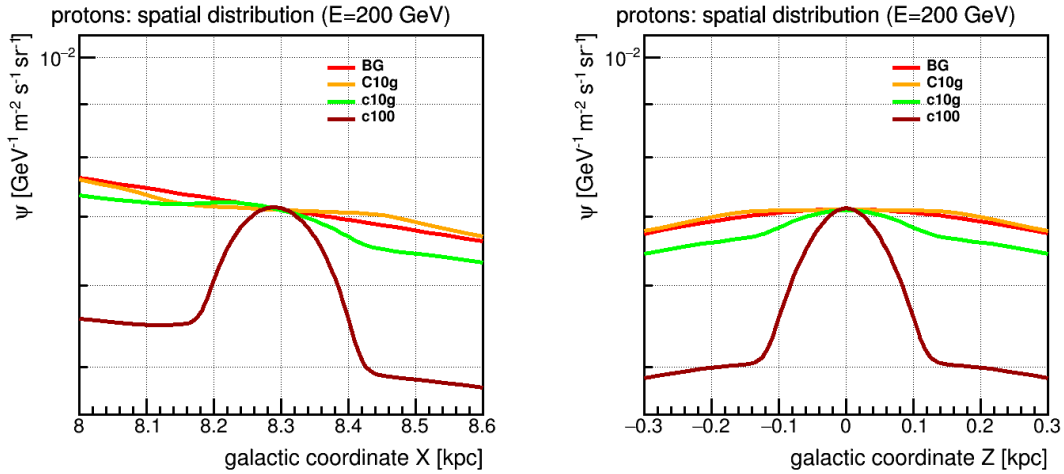
Figure 3.28. For the three exemplary models c10g, C10g and c100, we show the proton distribution at $E = 200\,\mathrm{GeV}$, in the **left** panel in x direction and in the **right** panel in z direction. The source strength normalization was chosen to describe the proton spectrum at $E = 95\,\mathrm{GeV}$. It is seen that these different assumptions lead to very different density distributions, in the case of TA10 flattening the density in the solar neighborhood out and in the case of c100 creating a local increase with large density gradients in the solar neighborhood.

So, in these models, the prediction in dipole anisotropy is very dependant on the position of the actual borders of the Local Bubble (or equivalently, on the position of the Sun inside it). Minor steps of a few tens of parsecs in one direction can imply stronger or weaker gradients. However, as in both cases the local gradient is not exceeding the factor 1/10 or 1/100 that is applied to the diffusion coefficient, this manifests as a drop in anisotropy[3] $\delta \propto |\vec{\nabla} N|/N$. This means, that due to the locally increased scattering of the particles the cosmic ray flux appears more isotropic, regardless of the medium-scale density gradient at scales of a few hundred parsecs. An increase in isotropy would only be experienced if, as for c100, the medium-scale gradient would exceed a factor of 100 compared to the BG model.

Note that a structure like the one in c100 is rather uncorrelated with the outer gradient, and in such a model the local dipole anisotropy is very sensitive to the exact position of the sun: The flux would appear isotropic if coincidentally located at the peak of this overdensity, while in the more likely cases of being located further, e.g. 40-50 pc away, the strong gradients would determine the dipole component. Depending on the overall diffusion coefficient, the latter scenarios would be challenged by the measured upper limits. This is a general distinction in which models like c100 appear unlikely.

The spectra of e^- and e^+ are shown in Fig. 3.29. As the primary electrons are source-renormalized on their own, the spectra do not show a considerable difference in absolute height. The changes in spectral shape are negligible for models C10g/c10g (deviation $\leq 4\%$) and also minor for c100, as the solar modulation parameter could compensate the spectral deviation (χ^2 values are mainly given by the purposely missing high-energy component).

---

[3]The gradient is taken between the neighboring grid points ±10 pc.

For the positrons (Fig. 3.29 (right)), there is also nearly no difference between BG and C10g/c10g, but in c100 the e^+ flux is overall increased, by roughly a factor of 2: As the local CR protons spend an increased time in the Bubble, more collisions with the gas can happen, and the secondary production of e^+ rises.
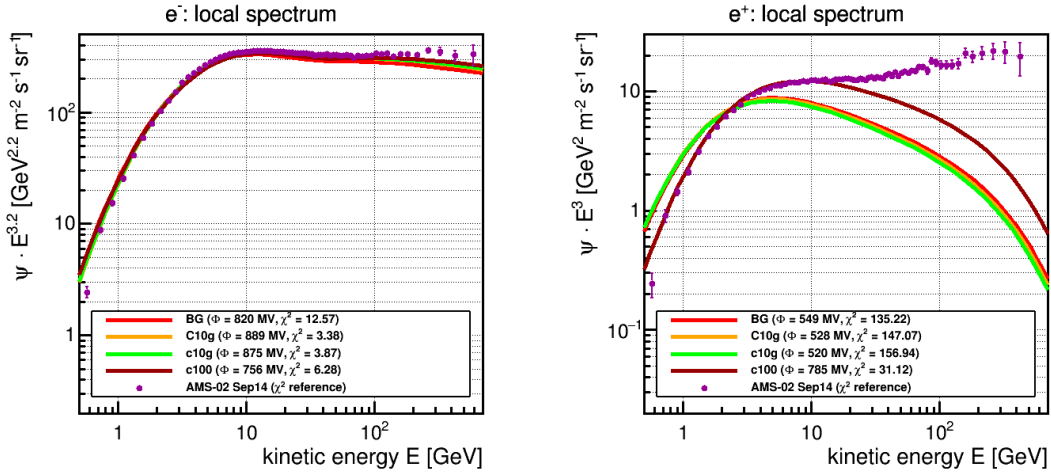
Figure 3.29. For the three exemplary models c10g, C10g and c100, we show the difference in leptonic spectra, seen in the **left** panel for electrons (scaled with $E^{3.2}$) and in the **right** panel for positrons (scaled with E^3. The differences are similar for both species, but more visible in positrons because these only have a secondary component. In comparison with the reference model BG, the TA10 model does not significantly deviate from the reference BG model, while the slowed diffusion in c100 and subsequently larger secondary production rate leads to a overall increase of positrons. Solar modulation is best fit to data.

We further investigate the positron-over-proton anisotropy $\delta_{e^+/p}$ and, for illustration, the x distribution through the solar position, for $E = 200\,$GeV (Fig. 3.30). For the energy range $E = 16..350\,$GeV, $\delta_{e^+/p}$ rises to 293% vs. the reference model for C10g and drop to 23%/3% for c10g/c100. Overall, the shape of the distribution is comparable to the proton distribution in Fig. 3.28 (left), but since positrons are not source-normalized on their own, the lines are shifted in absolute value. The effect of reduced Interior gas density in C10g/c10g appears minor, but would gain importance in models with even slower Interior diffusion, e.g. in c100g (not shown here). For c100, more positrons are largely created inside the Local Bubble, and the strong Gaussian-like shape already seen in the proton distribution is replicated. Again, the total change in $\delta_{e^+/p}$ is given by both the flattening of the distribution (which again could be a steepening in models like c100 when the sun is assumed elsewhere) and the pure factor in D, with the latter dominating the question whether the anisotropy rises or falls. However, since the BG model shows e^+/p dipole anisotropies of more than a factor 100 below the AMS-02 upper limits, there is no conflict.

We finally analyze the model prediction of $^{10}Be/^9Be$ and B/C (Fig. 3.31). For model C10g, there is no real difference to the reference BG in both observables, and for c10g differences only appear for B/C in the low-energy range where data do not exist (the χ^2 is similar to C10g). In contrast, c100 shows large deviations, similar to the predictions made for a galactic decrease in D_0, Fig. 2.10: In this scenario the secondary production leads to a local increase of production same for ^{10}Be and ^9Be isotopes and thus the low-energy $^{10}Be/^9Be$ increases (moving closer to the flat value each model shows in the high-energy region);
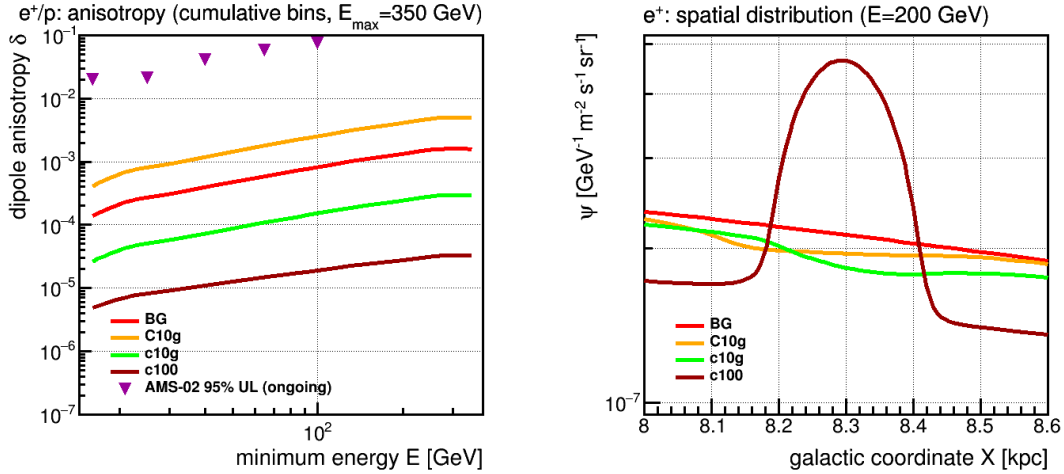
Figure 3.30. For the three exemplary models c10g, C10g and c100, we show the difference in comparison with the reference model BG, in the **left** panel on the predicted dipole anisotropy of e^+/p and, in the **right** panel, in the local e^+ distribution in x direction, at $E = 200$ GeV. These differences look similar to the changes seen in protons (Figs. 3.27 right and 3.28 left).

and also to the increase of processes like $p + C \rightarrow B + \dots$ amongst others. Thereby, this model does not describe the observations. In c10g, the increase of secondary production rate from diffusion time is countered with the decrease of target material for inelastic collisions: The rarefication of gas in this model hinders the over-production of B or ^{10}Be. This way, this model leads to better agreement with the BG prediction than without gas modification. It is an open question whether modifications in other galactic transport parameters in c100-like models can lead to a better description; for example, an overall increase in D_0 would likely lower the overall B/C, but on the other hand, further increase $^{10}Be/^9Be$.
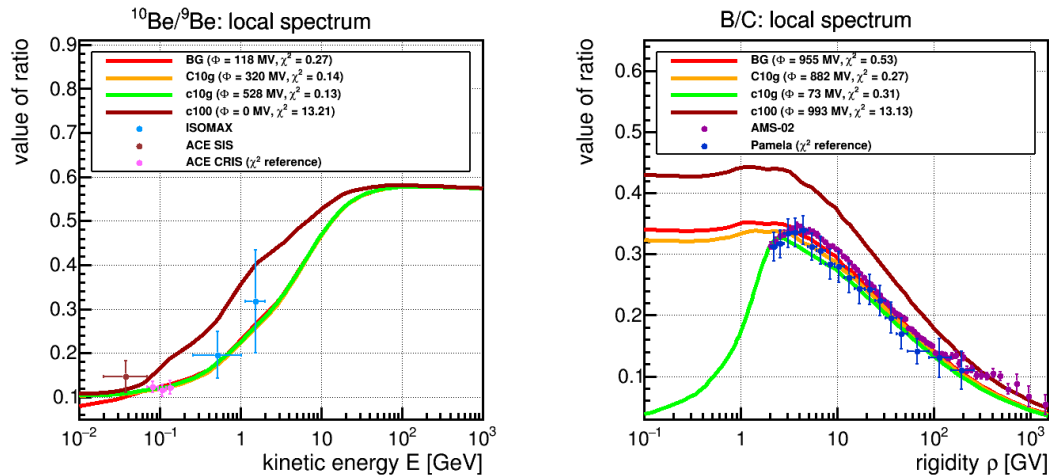
Figure 3.31. For the three exemplary models c10g, C10g and c100, we show the difference in prediction, in the **left** panel of $^{10}Be/^9Be$, and in the **right** panel of B/C. In both cases, the TA10 model does not affect the data description largely (a slight improvement in χ^2 is seen, cf. legends), but the c100 model gives a very poor model description. This is the result of the increase in secondary production (mainly visible in B/C, right) and in propagation time (mainly visible in $^{10}Be/^9Be$, left).

3.4.3. Impact on hadronic observables and on local dipole anisotropies

After we saw the three cases of TA10, e10g and c100 in more detail, we come to the summary and comparison of all model, in terms of their hadronic data description and dipole anisotropy prediction compared to the reference BG. This summary is presented in Tab. 3.4, while extensive details of each of the 34 models are given in appendix A.4. In Tab. 3.4, the χ^2 values for the model description of p, $\bar{p}/p$, $^{10}Be/^9Be$ and B/C against the respective measurements (the data that BG was selected for, see subsection 3.1).

A word of caution has to be emphasized for the models that show significant degradation in χ^2 (especially the models marked "red" in Tab. 3.4). These are not, as a general statement, excluded assumptions of the local transport processes. As was previously argued, the propagation parameters like halo-height L and diffusion constant D_0 are chosen for a galactic transport model like BG in such a way that the $^{10}Be/^9Be$, B/C and $\bar{p}/p$ data are met. If, by local enhancement of secondary production processes, these are not described correctly anymore, the galactic transport parameters could be re-tuned in a way as to compensate for this local enhancement (specifically, in the Bubble Walls). Further, transport processes could be reintroduced into the model (convection, reacceleration), which have only been neglected in BG for simplicity. At this point, *this study has not had the goal to pursue this*, but the framework has now been created to allow for such studies.

We also show, in Tab. 3.4 to the right side, the relative value of $\delta_{p/p_{[40,80]}}$ (80 GeV..1.8 TeV), $\delta_{e^{\pm}}$ (16..480 GeV) and $\delta_{e^+/p}$ (16..350 GeV), in relative % to the BG model prediction. All models are in each value in agreement with the observed 95% CL upper limits of Fermi-LAT and AMS-02, respectively. Overall, most models reduce the three shown dipole anisotropies, but to a different amount; and some models greatly increased them. In Tab. 3.5, the values are listed again, sorted in relative change for each of the $\delta_{p/p_{[40,80]}}$, $\delta_{e^{\pm}}$ and $\delta_{e^+/p}$.

A few similarities stand out:

1. While the local gas modificiations under consideration can have a profound impact on the χ^2 values, its effect on the dipole anisotropy is rather small (largest for $\delta_{e^+/p}$ due to secondary production).

2. The **Fast-Interior** block is nearly completely made of green models, i.e. improving data description. The CR density distributions become locally flattened, due to the factor on D the anisotropy values rise about a factor 2-3.

3. The **Slow-Interior** block is mostly red except for the two "weaker" models c10g,e10g that also reduce the interior gas density (counteracting the longer time of residence). These models show a drop in anisotropy from 1/5 down to 1/50, but the distributions are "bumpy", i.e. more sensitive to the location of the Sun (for example, the relative $\delta_{p/p_{[40,80]}}$ value is between 1% and 5% in the closer 20 pc vicinity).

4. Similar for the **Slow-Wall** scenarios: It generally holds that heavy *slow down* (low diffusion setting) leads to a worsening of $^{10}Be/^9Be$, B/C, $\bar{p}/p$ description.

111

5. The **Wall-Only** scenarios **with gas** (d⋆g, D⋆g) are all marked red due to the over-production of secondaries in the Wall gas (in all of these models, a factor 10 was chosen for the Wall gas overdensity, which is likely overestimating the actual average throughout the whole Local Bubble wall regions). This does not apply for the **chimney-elongated** models, which are in good agreement with the data.

6. Generally, the combined scenarios of **Slow-Wall+Fast-Interior** and **Fast-Wall+Slow-Interior** each show χ^2 values similar to the behaviour of the corresponding Wall-Only scenarios alone. The actual factor on the Interior diffusion coefficient is then only impacting the value of the dipole anisotropies (but note that A100 and d100 show similar predictions there).

7. For **Slow-Wall+Fast-Interiors** models, comparing the anisotropy values for the spherically symmetrical A10(g) with the elongated TA10(g), it appears crucial for both the χ^2 and the anisotropy values whether the Local Bubble is connected with the Galactic Halo or not. For $\delta_{e^+/p}$ in particular, the secondary positron production can counteract the relative flattening of the density distributions, i.e. for TA10(g)).

8. The **Fast-Wall+Slow-Interior** models show an efficient isotropizing behaviour of factors 1/10 down to 1/300, even in models compatible with data.

9. The models often become labelled red because in particular, the χ^2 of $^{10}Be/^9Be$ is red (description of $\bar{p}/p$ seems redundant of B/C except for some expections like c100g).

10. The other blocks of models are generally mixed, and sometimes fall into the red block because of a single χ^2.

11. In two extreme modification scenarios (A100g, d100g), secondary production rates are so enhanced that the e^+ prediction lies over the AMS-02 data. These are then models that are, already with weaker modification factors, showing the secondary production excess in $\bar{p}/p$, $^{10}Be/^9Be$ or B/C.

In the models of green and black classification, i.e. those in which no model readjustment is required for hadronic observable description, we see the strongest *isotropizing* effect in the green C100(g) bubbles, and the strongest *anisotropizing* effect in the black e10(g) bubbles. For these three dipole anisotropies, then, an uncertainty of orders

$$\delta_{p/p} : \quad 0.3..344\% \tag{3.14}$$

$$\delta_{e^{\pm}} : \quad 0.3..345\% \tag{3.15}$$

$$\delta_{e^+/p} : \quad 0.2..364\% \tag{3.16}$$

is just given by the local diffusion properties.

	Model	χ^2_p	$\chi^2_{\bar{p}/p}$	$\chi^2_{^{10}Be/^9Be}$	$\chi^2_{B/C}$	rel. $\delta_{p/p_{[40,80]}}$	rel. $\delta_{e^\pm}$	rel. $\delta_{e^+/p}$	
	BG	**0.83**	**1.58**	**0.23**	**0.27**	**100%**	**100%**	**100%**	
Slow W. + Fast I.	A10	0.85	1.78	1.01	0.42	150%	148%	158%	
	A10g	1.04	5.15	44.22	9.94	119%	119%	161%	
	A16	0.86	1.91	1.82	0.56	79%	78%	82%	
	A16g	1.13	7.01	54.70	15.34	79%	79%	120%	
	A100	2.35	9.65	9.28	11.19	15%	13%	26%	
	A100g	4.05	91.11	60.77	61.42	13%	12%	35%	$e^+!$
	TA10	0.83	1.51	0.15	0.25	73%	76%	233%	
	TA10g	0.93	2.22	0.69	0.89	73%	76%	364%	
Fast W. + Slow I.	B10	0.83	1.57	0.21	0.27	10%	10%	9%	
	B10g	0.91	2.59	3.29	1.65	10%	10%	7%	
	B100	0.85	1.69	0.70	0.33	0.3%	0.4%	0.6%	
	B100g	0.92	2.70	1.35	1.54	0.3%	0.4%	0.2%	
	TB10	0.83	1.54	0.18	0.27	11%	11%	11%	
	TB10g	0.93	2.22	0.69	0.89	11%	11%	9%	
Slow I.	c10	0.86	1.90	2.55	0.56	16%	16%	19%	
	c10g	0.78	0.97	0.13	0.32	16%	16%	23%	
	c100	1.16	7.01	13.22	10.01	2%	2%	3%	
	c100g	0.63	0.31	0.12	10.85	2%	2%	3%	
	e10	0.87	2.05	3.80	0.76	19%	18%	20%	
	e10g	0.77	0.85	0.13	0.54	19%	18%	23%	
Fast I.	C10	0.83	1.55	0.18	0.27	300%	301%	272%	
	C10g	0.81	1.34	0.14	0.25	300%	301%	293%	
	C100	0.83	1.56	0.19	0.27	344%	345%	289%	
	C100g	0.81	1.32	0.15	0.25	344%	345%	325%	
	E10	0.82	1.47	0.36	0.25	208%	222%	293%	
	E10g	0.80	1.25	0.11	0.24	208%	222%	294%	
Slow W.	d10	0.85	1.75	0.90	0.39	64%	63%	70%	
	d10g	1.11	6.62	66.13	15.20	64%	64%	94%	
	d100	1.00	3.77	8.40	3.87	15%	15%	24%	
	d100g	3.43	79.53	125.72	90.07	15%	16%	39%	$e^+!$
Fast W.	D10	0.83	1.56	0.18	0.27	59%	59%	55%	
	D10g	0.91	2.61	4.83	1.79	59%	59%	45%	
	D100	0.83	1.58	0.26	0.27	10%	10%	9%	
	D100g	0.95	3.22	8.48	3.09	10%	10%	7%	

Table 3.4. Local transport models can have an enormous impact on the prediction of hadronic observables $\bar{p}/p$, $^{10}Be/^9Be$ and B/C, and little impact on the local proton flux p. We analyzed 34 models described in detail in appendix A.4. Here, we show the χ^2 of data description [refs. given in text] for the reference model BG and all 34 local models. A color code is used according to the improvement ($(\chi^2 \leq \chi^2_{[BG]})$) or impairment ($(\chi^2 \in [1;3])$ / $(\chi^2 > 3)$) of data description relative to BG. For the $\bar{p}/p$ column, the purple and red ranges are ($\chi^2 \in [3;5]$) / ($\chi^2 > 5$). Each model is assigned the "worst" of all four χ^2 values in the first column. The $e^+!$ symbol marks that for models A100g, d100g, secondary e^+ production is exceeding the AMS-02 data at intermediate energies.

113

Model	$\delta_{p/p_{[40,80]}}$	Model	$\delta_{e^\pm}$	Model	$\delta_{e^+/p}$
B100	0.3%	B100	0.4%	B100g	0.2%
B100g	0.3%	B100g	0.4%	B100	0.6%
c100	2%	c100	2%	c100g	3%
c100g	2%	c100g	2%	c100	3%
B10	10%	B10	10%	B10g	7%
B10g	10%	B10g	10%	D100	9%
D100	10%	D100	10%	B10	9%
D100g	10%	D100g	10%	TB10g	9%
TB10	11%	TB10	11%	TB10	11%
TB10g	11%	TB10g	11%	c10	19%
A100g	13%	A100g	12%	e10	20%
A100	15%	A100	13%	e10g	23%
d100	15%	d100	15%	c10g	23%
d100g	15%	d100g	16%	d100	24%
c10	16%	c10	16%	A100	26%
c10g	16%	c10g	16%	A100g	35%
e10	19%	e10	18%	d100g	39%
e10g	19%	e10g	18%	D100g	45%
D10	59%	D10	59%	D10g	45%
D10g	59%	D10g	59%	D10	55%
d10	64%	d10	63%	d10	70%
d10g	64%	d10g	64%	A16	82%
TA10	73%	TA10	76%	d10g	94%
TA10g	73%	TA10g	76%	A16g	120%
A16	79%	A16	78%	A10	158%
A16g	79%	A16g	79%	A10g	161%
A10g	119%	A10g	119%	TA10	233%
A10	150%	A10	148%	C10	272%
E10	208%	E10	222%	C100	289%
E10g	208%	E10g	222%	C10g	293%
C10	300%	C10	301%	E10	293%
C10g	300%	C10g	301%	E10g	294%
C100	344%	C100	345%	C100g	325%
C100g	344%	C100g	345%	TA10g	364%

Table 3.5. Local transport models can have an enormous impact on the predicted dipole anisotropies. We show the relative difference in predicted dipole anisotropy for every of the 34 models we analyzed, compared to the prediction of the BG model. The **left** table shows this for protons relative in energy $\delta_{p/p_{[40,80]}}$, the **middle** table for the leptonic sum flux $\delta_{e^\pm}$ and the **right** table for positrons relative to protons $\delta_{e^+/p}$.

3.4.4. Impact of galactic CR densities on γ-ray production

As seen so far throughout this chapter, the model description of the local proton spectrum is essentially unaffected by the local modifications we introduced. This was attributed to the source renormalization applied by DRAGON, which computes the injection of all nuclei with a composition factor relative to the proton source abundance. Every cosmic ray species is the computed relative the absolute proton source strength, except for the primary electron component whose source abundance is decoupled from protons. Every secondary production process is also just proportional to the overall primary proton abundance. Ratio observables like B/C, of course, are independent of the absolute source strength as it cancels from both the numerator and denominator species.

However, the overall normalization of the galaxy-wide cosmic ray distribution has a direct effect on the γ-ray production. Their local spectrum carries explicit information about the amount of cosmic ray particles present throughout in every direction by their line of sight integral. Since galactic transport models have been known to usually overestimate the total flux of γ-ray arriving at Earth by about a factor $1.1 - 1.2\%$ ((averaged over all sky distribution), it is interesting how the γ-ray prediction will change when the galaxy-wide source strength is assumed at a lower level. The change in overall source strength is summarized in Tab. 3.6.
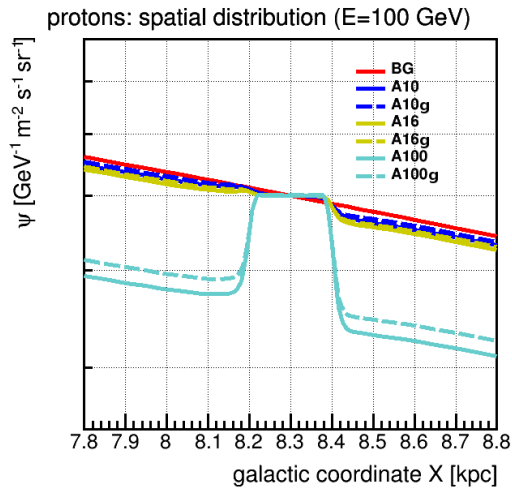
Figure 3.32. Showcase: Local proton distribution for type "A" bubbles. The drop in density outside the bubble comes from the source normalization, which assumes the sources at such a strength that the flux is fixed as 3.13. This difference in galactic CR density is thus a constant in energy.

The different γ-ray contributions change accordingly,

$$(\text{PCR}) + (\text{BR}) + (\text{IC}) + (\text{ISO}) \longrightarrow f_p \times (\text{PCR}) + f_e \times (\text{BR}) + f_e \times (\text{IC}) + (\text{ISO})$$

As the isotropic background is weak, we highlight these models in which both $f_p, f_e \lesssim 90\%$.

Difference in Skymap

This skymap, Fig. 3.33 shows the ratio of the total γ-ray sky for a A100 model, relative to its prediction for the galactic reference model BG at 1 GeV. Blue regions are completely

scaled down according to the reduced source normalization, red regions consist of line of sights, in which a larger share of γ rays is produced inside the Local Bubble.

Model	Protons f_p	Primary Electrons f_e
BG	100.00%	100.00%
A10	97.51%	94.32%
A10g	98.53%	95.25%
A16	96.16%	91.44%
A16g	97.05%	91.68%
A100	**70.18%**	**54.46%**
A100g	**73.57%**	**54.84%**
TA10	101.64%	103.68%
TA10g	102.03%	103.80%
B10	100.11%	100.27%
B10g	100.39%	100.35%
B100	98.45%	96.39%
B100g	98.72%	96.45%
TB10	101.67%	103.09%
TB10g	101.87%	103.14%
c10	96.16%	91.32%
c10g	**91.61%**	**83.73%**
c100	**72.70%**	**55.63%**
c100g	**71.29%**	**55.41%**
e10	106.02%	112.21%
e10g	105.96%	112.18%
C10	100.49%	101.22%
C10g	100.42%	101.20%
C100	100.16%	100.59%
C100g	100.08%	100.57%
E10	93.33%	86.39%
E10g	92.95%	86.30%
d10	97.85%	95.05%
d10g	98.75%	95.31%
d100	**83.71%**	**70.03%**
d100g	**87.86%**	**70.70%**
D10	100.32%	100.81%
D10g	100.61%	100.89%
D100	99.87%	99.94%
D100g	100.29%	100.06%

Table 3.6. Local transport models can change the expected source strength of galactic cosmic rays. This potentially has an impact on galactic γ-ray production. Here, the relative normalization factors are shown (100% equals the source strength assumed for the BG model).
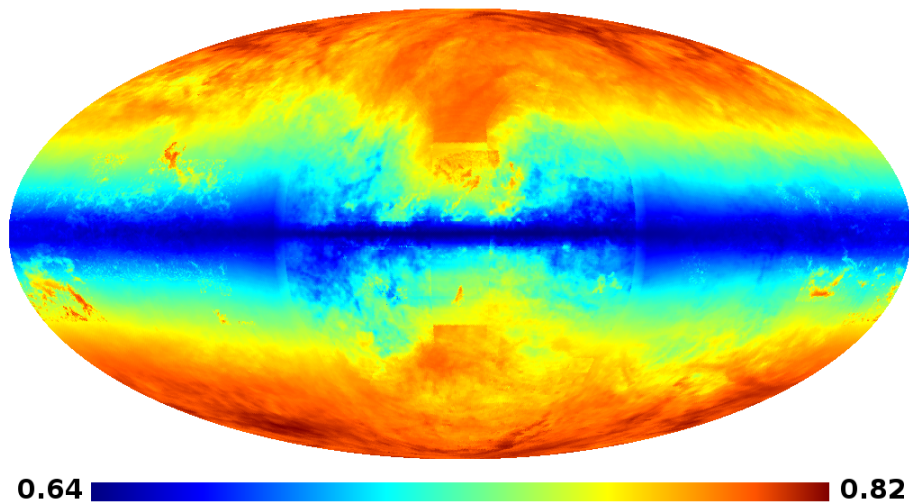
Figure 3.33. Ratio of the γ-ray sky at $E = 1\,\text{GeV}$ in a A100 model, divided by the reference model BG. The local diffusion model leads to galactic scaling factors in p and e^- distributions, the main CR primaries to create γ rays. This is therefore an inside-out view of a locally confined CR volume.

In this example a slightly larger LB model has been used (radius 160 pc). With a A100 model, the resulting global factor was 64%. This is then the difference between locally confined CRs (cf. Fig. 3.32 and the reduced galactic density. The factor of 64% is the "blue" value in Fig. 3.33. The perfect blue is visible in all directions in which only a negligible amount of γ-rays is created inside the Local Bubble, so mostly, the disc regions (the central blue band) in which the gas densities are high (and also the CR density is expected highest). With shifts in the color scale towards red, one is looking more into directions in which a larger share of γ-rays comes from the solar neighborhood itself. Towards the Galactic poles, the "perfect red" value is 82%, i.e. half of the γ-rays in these direction come from our direct vicinity. The red inlets at medium latitude and central longitude are likely regions in which the gas density is reducing (away from the disc), but CR protons are increased (as they are expected to be, towards the Galactic Center). For rising absolute latitude, the region becomes less and less affected. Towards the galactic poles, This factor approaches 82%, which means that these Lines of Sight are only half affected: half of the gamma rays come from within the local bubble region.

So, in some of the local transport models, the considerable difference of CR density inside and outside the Local Bubble can lead to a certain decoupling of the galactic γ-ray prediction. The arguments above have been made about the π-decay γ-rays, but similarly, the galactic reduction of electrons would trace this inside-out distribution, scaled with the magnetic field (for Bremsstrahlung γ-rays) or the ISRF (for Inverse Compton γ-rays). So far, the reproduction of the γ-ray sky is still an intriguing topic. By tackling the question of local cosmic ray transport, one might then also gain insight about the galactic CR distributions, e.g. if further local modifications of the magnetic field or the radiation fields were to be made.

3.5. Conclusion

By the construction of several local transport models, we have shown that any anisotropy in cosmic ray arrival directions is largely influenced by the details of our direct environment. The truth that the sun is located inside the Local Bubble is only one argument that makes it plausible that the local diffusion environment is strongly deviant from the galactic average conditions. As commonplace numerical models of galactic cosmic ray transport do not feature the required spatial resolution, a connection $\delta = \frac{3D}{c}|\vec{\nabla}N|/N$ between the local anisotropy in arrival directions and the coarse galactic density gradient $\vec{\nabla}N/N$ can, in general, not directly made.

It was demonstrated that there exists as variety of local transport models which does, for a given transport model, not deteriorate the model description of the locally measured proton flux, which was recently updated by the AMS-02 experiment with unprecedented precision. Also, local structures to not necessarily imply a strong impact on the existing measurements of the cosmic clock observable $^{10}Be/^{9}Be$ and the secondary-to-primary ratio B/C. While some of the investigated transport models were in disagreement with measurements of the latter observables, others left the original model prediction unchanged or lead to an improved model description.

Last, our models shows that the method of source normalization to data, as commonly used in Galprop/Dragon, can lead to a severe overestimation of the CR density throughout the galaxy. A more general approach of fixed-power sources is necessary in order to expand propagation models to γ ray predictions.

The extensions our group worked into the Dragon code have been adopted by the original Dragon authors and implemented in the currently ongoing Dragon2 project (cf. Fig. 3.34, release destined in spring 2017.
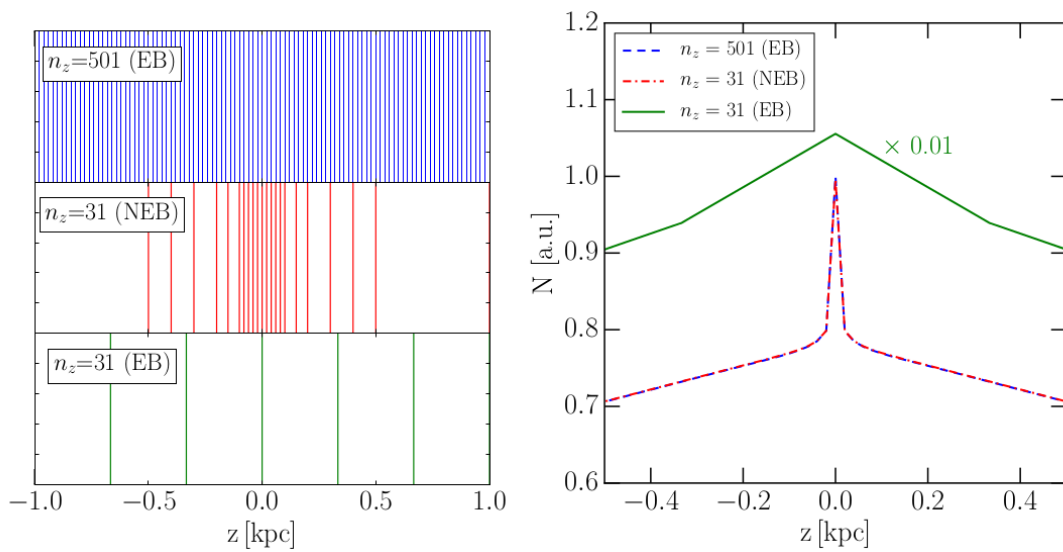
Figure 3.34. In the upcoming Dragon2, the implementation of a nonuniform as introduces by our work was accepted: Here the authors show another case of a very fine structure that is best described with a nonuniform grid. This is a calculation of a punctual drop in diffusion coefficient of three orders in magnitude. The panel **left** shows three different grids and the panel **right** the Dragon2 solution on each grid (in arbitrary units). Blue shows the choice of a fine uniform solution capable of resolving this structure. Red shows the choice of a locally adapted grid with only $\frac{1}{16}$ of grid points as the first case, but reproducing it exactly. Green shows the choice of a uniform grid with same number of grid points as the red case, which is incapable of resolving the structure correctly. From the preliminary Dragon2 publication [95].

4. Pulsar interpretation of the energetic positron component

We have shown, in the last chapter, that the solar neighborhood is in fact a very influential region on the propagation of cosmic rays. This is especially interesting for the electron and positron fluxes, which, unlike heavier CR species, are very prone to energy loss by radiation of Synchrotron X-rays and γ-rays by the Inverse Compton process.

As introduced before, the "energetic positron excess" describes the unexpected rise in positron fraction above $E \gtrsim 20\,\text{GeV}$ observed by the PAMELA, Fermi-LAT or AMS-02 experiments, in conflict with conventional transport models by far over the observational uncertainty.
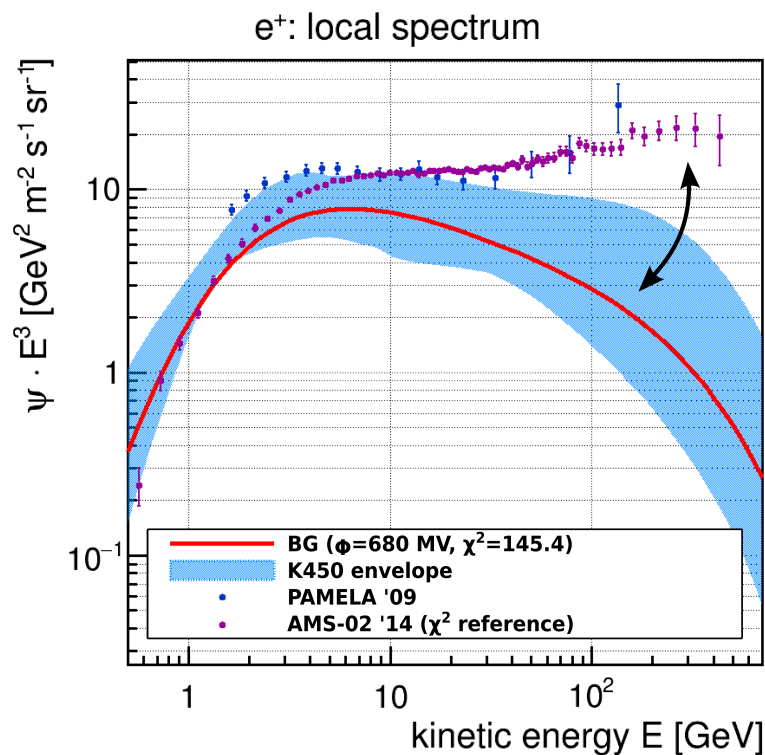
Figure 4.1. The energy spectrum (scaled with E^3) of positron shows an "excess": Above a kinetic energy over $E \gtrsim 10\,\text{GeV}$, current models (of purely secondary e^+ production) can not explain the gap to the e^+ flux measurements of PAMELA 2009 [107] and AMS-02 2014 [103]. The red line is our model BG, the blue band the K450 set of 450 good models [56] from the previous chapter.

The precise measurement of the positron and electron fluxes themselves by AMS-02 [103] have confirmed that it is indeed a population of high-energy positrons that is currently not modeled correctly. This is recalled by Fig. 4.1 for a whole range of 450 transport

models that were selected by goodness of describing PAMELA data for spectra of p [119], $\bar{p}/p$ [120], B/C [123] and data for $^{10}Be/^9Be$ from ACE [121] and ISOMAX [122].

4.1. Review of explanation approaches

Since the first publication by PAMELA, A number of competing ideas has been debated, and still topically is, in order to account for the presence of this energetic e^+ component. We hereby give a brief review about these ideas to illusstrate why so far, none of the explanations is universally accepted by the scientific community.

1. **Missing astrophysical sources.**
   Positrons, in the standard propagation picture, as created purely as the product of collisions by cosmic rays and the interstellar gas. While it is known since the 1970's [146] that pulsars produce $e^\pm$ pairs in their magnetosphere (as introduced in section 1.3.3.2), this production was considered energetically irrelevant in the overall CR paradigm. Only since the PAMELA observation, it was theorized that the surrounding PWN [147] could provide sufficient shock structures for first-order Fermi acceleration to become considerable [148].

   Fig. 4.2 shows one of these results [149]. It describes the positron fraction $e^+/e^\pm$ as the sum of a secondarily created e^+ contribution calculated from a GALPROP model, and a possible pulsar contribution, from the Geminga or Monogem pulsars, two widely known pulsars, estimated here at 160pc and 250pc [148]. Such models are, however, dependent on a lot of assumptions about the pulsar injection spectrum, as the astrophysical processes in pulsar magnetospheres and PWNe are not very well understood and therefore, not really restricted.
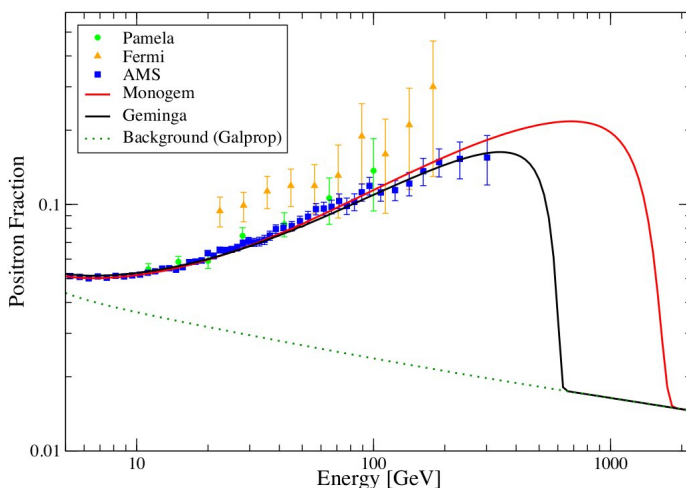
Figure 4.2. In the point source hypothesis, one (or several) point sources like pulsars are strong enough to account for the measured positron fraction [149]. Such an explanation is in principle difficult to constrain, as many astrophysical parameters are not known.

A major argument against the "pulsar hypothesis" is that a very confined, *point-like* source would likely increase the dipole anisotropy of positrons to an observable

amount [148]. For instance, the authors of [148] state two cases of a pulsar contributions to the local $e^\pm$ flux, one being excluded by the Fermi-LAT upper limits (UL) [125] as seen in Fig. 4.3. The details of the anisotropy prediction in such a pulsar scenarios are then of course dependent on the properties of the pulsar(s). In this chapter, we will investigate this argument under consideration of the Local Bubble, as has not yet been done before.

A major argument in favor of this hypothesis, however, is that the pulsar/PWN source mechanism only contributes $e^\pm$ pairs to the CR sources. Models of CR transport can thus be readily adopted, without problems arising in predictions of other CR observables, e.g. antiprotons.
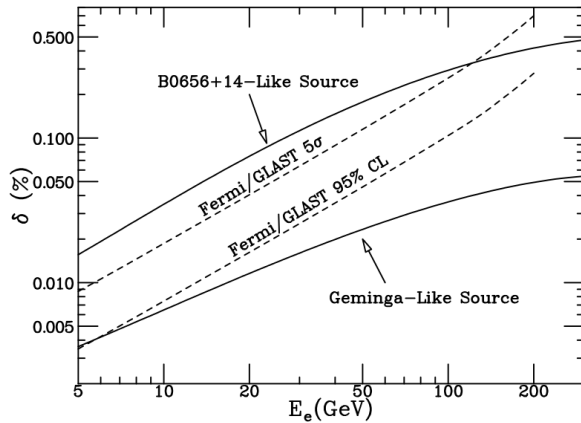
Figure 4.3. In the pulsar hypothesis, [148] state the level of expected dipole anisotropy for a Geminga-like source at 157 pc distance and 370 kyr age, as well as for a B0656+14-like source at 290 pc and 110 kyr age. The latter one would result in a dipole anisotropy that should have been detected by Fermi-LAT [148], while the Geminga-like source would be compatible.

2. **Missing contributions from exotic particles.**
On the other hand, the energetic positron component is interesting as it could be the contribution of a particle beyond the Standard Model. As explained in chapter 1.3.3.4, if the phenomenon of Dark Matter is ascribed to have a particle nature, and this particle is coupled to Standard Model particles via annihilation or decay, it would cause steady matter-antimatter pair production processes throughout the Galaxy. As opposed to the pulsar hypothesis, the DM hypothesis would generally also be expected to contribute to production of $p\bar{p}$, depending on the details of particle physics in the involved annihilation channels (DM $\rightarrow e^\pm, W^\pm, Z^0, \gamma, H, q\bar{q}, \ldots$) As mentioned before, the AMS-02 $\bar{p}$ measurement does not require a large exotic contribution.

DM considerations usually have the problem that the relic density constrains the annihilation cross section to $\langle \sigma v \rangle \simeq 3 \cdot 10^{-26} \text{cm}^3\text{s}^{-1}$, while the Galactic DM distribution can be fixed by numerical simulations of the gravitational attraction, so-called N-body simulations, e.g. [150]. Then, $e^\pm$ pair production (e.g. from a supersymmetric neutralino WIMP) appears far too low [151], unless it is "boosted" either by some unknown effect that increases the annihilation cross section but not the required thermal density, or by a close-by DM sub-halo, or clump, in which its density could

be locally increased without contradicting Galactic N-body simulations. Fig. 4.4 shows an example of DM $\rightarrow e^{\pm}$ production [152] by such an overdensity, which would explain the observed positron fraction by three different annihilation channels, each using DM masses of 1..2 TeV/c^2 and boost factors of about 40..50.
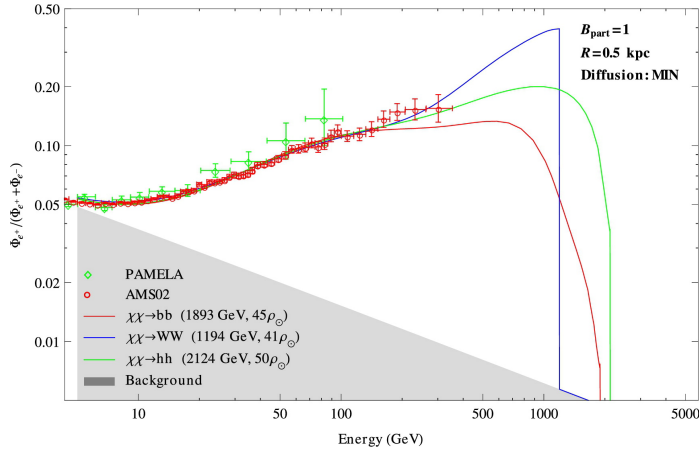
Figure 4.4. In the DM annihilation hypothesis, the positron fraction can be explained by $e^{\pm}$ pairs from an annihilation process, if a DM particle nature is assumed (e.g. WIMP). Models thereof usually need to account for at least one further specific presumption, as in this case [152] a local DM overdensity.

This hypothesis thus gives no natural explanation of the observed positrons either, but only for very specific assumptions about DM. Specifically, it is supposed to be very heavy (a review about the implications of PAMELA and AMS-02 measurements on DM properties is given e.g. in [153]). The question also remains whether WIMPs or other DM particles are to be detected in direct detection or collider experiments.

3. **Modified assumptions about SNR or ISM properties.**
   Further, suggestions have been made that no primary e^+ source has to be introduced. Several such mechanism have already been disfavored as early as 2009 [154], as they require further general assumption about CR propagation not generally in agreement with other CR observations. Some newer suggestions [155, 156] are not excluded yet. These include the positron production near SNRs (allowing diffuse shock acceleration for secondary e^+) or the consideration of interstellar $\gamma\gamma \rightarrow e^- e^+$ production [157], if efficient enough.

   No coherent analysis (e.g. by using numerical codes) was published, so far, that implements these assumptions and consistently describes hadronic spectra, secondary-to-primary ratios and cosmic clock observables simultaneously. As has been stressed throughout this work, with the current precision in measurement we find it crucial that such consistency is achieved.

To conclude, the e^+ observation currently provides a vivid field of new ideas in cosmic ray research, and the ongoing measurements of $e^{\pm}$ fluxes will constrain phenomenological models further. Especially the dipole anisotropy in arrival directions will then play a crucial role in model discrimination. We will now turn to the pulsar hypothesis in light of the Local Bubble transport models we earlier found to be in agreement with hadronic CR observations.

4.2. Anisotropy considerations: Exclusion of a single pulsar

We consider the BG model from chapter 3 as an adequate model providing the secondary positrons component. This is thus considered as a "background", on top of which we define a "signal" which we ascribe to one or multiple nearby sources. By adding pulsar models, the prediction of leptonic dipole anisotropy is likely to rise. We use the highly topical analysis of AMS-02 positron-over-proton data by Stefan Zeissler [99] to constrain the signal component. Over the maximum evaluated energy range, the e^+/p anisotropy UL from AMS-02 is (cf. Fig. 3.10)

$$\delta_{e^+/p}(16..350\,\text{GeV}) \leq 1.99\% \ . \tag{4.1}$$

We will now investigate the pulsar description of the e^- and e^+ spectra, as measured by AMS-02, in the light of uncertainties from the pulsar distribution. As will be shown, there exists a variety of possible models, which we will then further examined under various assumption of local transport models, based on last chapter's results.

Before we come to a realistic selection of known γ-ray pulsars that are likely to give significant contributions to the local $e^\pm$ flux, a simple estimate allows us to conclude, that *single-pulsar* scenarios are very unlikely. This is an estimation of the distance and age a single pulsar could have in order not to exceed the anisotropy limit. We can estimate the limit on the dipole anisotropy of signal alone. We separate the total flux intensity into two components

$$I_{\text{sum}} = I_{\text{BG}} + I_{\text{sig}} \ . \tag{4.2}$$

with each component giving a contribution to the e^+ anisotropy, written as a vector in Galactic coordinates x, y, z and a unit vector $\vec{e}_r$ as in section 2.3:

$$I_{\text{BG}} = I_{0,\text{BG}}(1 + \vec{\delta}_{\text{BG}} \cdot \vec{e}_r) \tag{4.3}$$

$$I_{\text{sig}} = I_{0,\text{sig}}(1 + \vec{\delta}_{\text{sig}} \cdot \vec{e}_r) \tag{4.4}$$

$$I_{\text{sum}} = I_{0,\text{sum}}(1 + \vec{\delta}_{\text{sum}} \cdot \vec{e}_r) \ , \tag{4.5}$$

The following calculation is executed in appendix A.5, and cut short here. From the flux prediction $I_{\text{BG}}(E)$ and the measurement $I_{\text{sum}}(E)$, one can estimate, for the cumulative energy bin $E \in [16, 350]$ GeV,

$$\vec{\delta}_{\text{sum}}(16..350\,\text{GeV}) = 9.3\% \, \vec{\delta}_{\text{BG}}(16..350\,\text{GeV}) + 90.7\% \, \vec{\delta}_{\text{sig}}(16..350\,\text{GeV}) \ . \tag{4.6}$$

This is now useful in estimating the limits of a *single-pulsar* explanation, given our BG model. We assume the analytical solution for a point source, (2.116) from section 2.5.1 to hold true for a pulsar and for which we can calculate the dipole anisotropy contribution

$\vec{\delta}_{\text{sum}}$ (2.69) analytically, gaining

$$\vec{\delta}_{\text{sum}}(16..350\,\text{GeV}) = 9.3\%\,\vec{\delta}_{\text{BG}}(16..350\,\text{GeV}) - 12.36\frac{[d/\text{pc}]}{[t/\text{kyr}]}\,\vec{e}_{\text{PS}} \qquad (4.7)$$

with $\vec{\delta}_{\text{BG}}$ the amplitude and direction of the background (secondary) positron flux, $[d/\text{pc}]$ the pulsar distance in pc, $[t/\text{kyr}]$ its age in kyr, and $\vec{e}_{\text{PS}}$ the normalized vector towards the pulsar location. If we now neglect the small $9.3\%\vec{\delta}_{\text{BG}}$ and assume the single pulsar to contribute all of the e^+ anisotropy, one obtains with the aforementioned AMS-02 limit[1] $\delta_{e^+/p}(16..350\,\text{GeV}) \leq 1.99\%$ on the second term:

$$[d/\text{pc}] \lesssim [t/\text{kyr}] \cdot 1.6 \cdot 10^{-3} \,. \qquad (4.8)$$

This means, with a typical pulsar age of 100-1000 kyr, d must lie within $1.6pc$ to the sun, and there is no candidate known so close[158]. For our background scenario BG, the contribution to the energetic positron population must be distributed between multiple sources, or the predicted anisotropy would exceed the measured limit. By the shape of the blue band in 4.1, for other models in the K450 set that would require a only a weaker pulsar contribution, our calculation from appendix A.5 would result in a weaker condition on distance and age. This is not part of this study, as we were consequent in our choice of the model BG in order to, in coherence with chapter 3, discuss the impact of the Local Bubble later on.

4.3. Pulsar candidates for energetic $e^{\pm}$ contributions

The *Second Fermi-LAT Catalog of Gamma-ray Pulsars* from 2013 [158] contains 117 gamma-ray pulsars, discovered in three years of data taking by the Fermi-LAT telescope. Besides the whole set of known pulsars from the ATNF catalog [159], it is likely that pulsars with magnetic field strong enough for significant $e^{\pm}$ production are also visible in gamma rays. From these, [160] estimate the local contributions expected to most contribute to the local $e^{\pm}$ flux. For each of the cataloged pulsars, this estimation is dependent on its *total energy output* W_0, *age* t_{age} and *distance d*. The total energy output is not a directly measurable quantity, but is derived from the currently observed *spin-down luminosity* $\dot{\mathcal{E}}$, assuming a simple model of magnetic dipole radiation from a rotating magnetized sphere [41]. The following considerations refer to the Fermi $e^{\pm}$ sum flux measurement, but similarly hold for the single e^-, e^+ fluxes, too.

In [160], the authors also conclude that no considerable $e^{\pm}$ contribution from γ-ray quiet pulsars is expected. There is, however, a remaining possibility that there could be other γ-ray pulsars overlooked by the blind search performed by Fermi. We disregard any such contribution, as it could hardly be constrained in $\dot{\mathcal{E}}$, t_{age}, d and thus would be highly artificial.

---

[1] We can here use the e^+/p values, as there is no proton contribution from the pulsar.

The local flux expectation of any pulsar is commonly calculated using a simple transport scenario, comprising of basic terms of diffusion and energy loss only, and treating the source function as burst-like, $\left[\, Q(E,\vec{r},t) = Q_{\mathrm{inj}}(E)\delta(\vec{r}-\vec{d})\delta(t-t_{\mathrm{age}}) \,\right]$. The analytical solution for such a scenario was given in (2.116) in section 2, and carries an unknown pulsar injection spectrum $Q_{\mathrm{inj}}[\Gamma, E_{\mathrm{cut}}](E)$, parametrized by the *slope Γ* and *cut-off energy E_{cut}*. In Fig. 2.11, the effect of varying pulsar parameters on the local flux prediction was shown.

In contrast, publications based on more general propagation models employing GAL-PROP/DRAGON use a different source setup, $\delta(\vec{r}-\vec{d})$ replaced by a thin Gaussian width (for numerical reasons), and considering the source injection to be homogeneous over time. This leads to differing predictions in spectrum and especially in anisotropy, which we will explicitly emphasize at the end of our study.

By help of the analytical transport equation solution $N(E,\vec{r},t)$, it is then possible to constrain t_{age}, d and $\dot{\mathcal{E}}$. While age and distance directly enter the analytical solution, the spin-down luminosity is used as a measure for the total energy output W_0 of the pulsar, equating it with the overall source normalization Q_0. This bears a certain uncertainty from the details of the particular pulsar spin-down process, as is described now. With $\tau = 1..10\,\mathrm{kyr}$ the characteristic spin-down decay time scale, the source normalization condition is [41]

$$\int dE\, Q_{\mathrm{inj}}(E)E \overset{!}{=} \eta W_0 \approx \eta\dot{\mathcal{E}}\tau\left(1+\frac{t_{\mathrm{age}}}{\tau}\right)^{\frac{k+1}{k-1}} \approx \eta\frac{\dot{\mathcal{E}}t_{\mathrm{age}}^{\,2}}{\tau}\,, \qquad (4.9)$$

with the $e^{\pm}$-production efficiency η and the *braking index k*. The last approximation follows from the simple magnetic dipole radiation model usually assumed for pulsars, in which $k = 3$. k is defined over angular velocity Ω and angular spin-down $\dot{\Omega}$, generally taken as

$$\dot{\Omega} \propto -\Omega^k \quad \text{and therefore} \quad k = -\frac{\Omega\ddot{\Omega}}{\dot{\Omega}^2}\,. \qquad (4.10)$$

A general pulsar model, as the magnetic dipole radiation model predicting $k = 3$, has to be assumed for most pulsars because the pulsar age t_{age} and the decay time τ are not known independently [41]. One famous counterexample is the Crab pulsar, observed in 1054 and thus $t_{\mathrm{age}} = 962\,\mathrm{yr}$. From the ATNF Catalog [159], $\ddot{\Omega}$ can then be taken and reveals a braking index $k \approx 2.5$ and decay time $\tau \approx 0.7\,\mathrm{kyr}$. This is not universal and the measurement of pulsar braking indices is an active field itself [161]. It is thus common for simplicity, to use the approximation $k = 3$ [160], but this means deviations in (4.9), dependent on pulsar age, are easily possible to an order of magnitude or more. We choose to follow the choice $k = 3$, and account for the flatter by assuming an uncertainty of source strength of a factor 10 up or down, to parametrize this missing knowledge.

In section 2.5.1, the *propagation length* was discussed. Energy losses during the diffusion of cosmic rays then limit the parameters of interesting pulsars, i.e. [160],

- if it is too old, Synchrotron radiation and Inverse Compton emissions will have made the $e^{\pm}$ component too weak in the $E > 100\,\text{GeV}$ range. An estimation of the maximum age a pulsar can have in order to contribute at an energy E is stated as

$$t_{\text{age}} \lesssim 2.3\,\text{Myr} \left(\frac{100\,\text{GeV}}{E} \right) . \tag{4.11}$$

- if it is too young, however, this component would not have reached us yet, due to the diffusion radius for $t_{\text{age}} \lesssim 0.1\,\text{Myr}$ of the energetic component is only approximately 0.5 kpc, from

$$R_{\text{diff}} \simeq 0.5\,\text{kpc} \sqrt{ \frac{D_0}{3.6 \cdot 10^{28}\text{cm}^2\text{s}^{-1}} \cdot \frac{t_{\text{age}}}{0.1\,\text{Myr}} \cdot \left(\frac{100\,\text{GeV}}{E} \right)^{\delta} } . \tag{4.12}$$

Also, for very young pulsars like e.g. Vela X, it is assumed that most particles are still trapped inside the pulsar magnetosphere [162]).

- the further away the source is, of course, the stronger it must be visible in current spin-down luminosity, else its total $e^{\pm}$ output is not enough to match the measurement − as the spatial distribution follows the Gaussian shape

$$N(\vec{r}) \propto \dot{\mathcal{E}} \times \exp\left(-\left(\frac{\vec{r} - \vec{d}}{R_{\text{diff}}} \right)^2 \right) . \tag{4.13}$$

Fig. 4.5, as taken from [160], shows the authors' restriction of parameters $\dot{\mathcal{E}}$ and t_{age} for two exemplary distances $d \approx 0.4\,\text{kpc}$ (left) and $d \approx 0.8\,\text{kpc}$ (right). The yellow marked area identifies the aforementioned range of restriction, and pulsars from the Fermi (black) as well as the ATNF (blue) catalogs are shown. The vertical line marks the $\dot{\mathcal{E}}$-weakest pulsar that was recorded in the Fermi catalog (i.e. sufficiently visible by its gamma ray emission). The 10 close-by pulsars most expected to amount for the local $e^{\pm}$ flux are listed in Tab. 4.1, from [160]. Foremost, it is to be remarked that the stated pulsar distances (as e.g. these in Fig. 4.5) are raw *estimates* only. The lower and upper limits are given after the Fermi Catalog [158]. This makes the quest for positron sources very intriguing because altogether, uncertainties now include

- the actual distance d of relevant sources and their number,

- the injection spectrum parameters, usually taken $\Gamma \in [1, 2]$, $E_{\text{cut}} \in [100\,GeV, 10\,\text{TeV}]$,

- the total energy output $W_0(\dot{\mathcal{E}}, t_{\text{age}}, k)$ and therefore $e^{\pm}$ output ηW_0

- the galactic transport model and local transport model.

The uncertainties on the local flux by varying distance and injection spectrum were showed in Fig. 2.11. We restrict the study to 5 pulsars, abbreviated "PS1" (J0633+1746/Geminga), "PS2" (J1836+5925), "PS3" (J2021+4026), "PS4" (J1057−5226), "PS5" (J0659+1414/Monogem).

These are (PS1, PS2, PS3, PS5) the four pulsars lying in the yellow, allowed region of Fig. 4.5 (left) and (PS4) the most luminous pulsar from Fig. 4.5 (right). Due to the missing knowledge about their injection spectrum, these can not be ordered in their importance of contribution, but are generally likely to contribute.
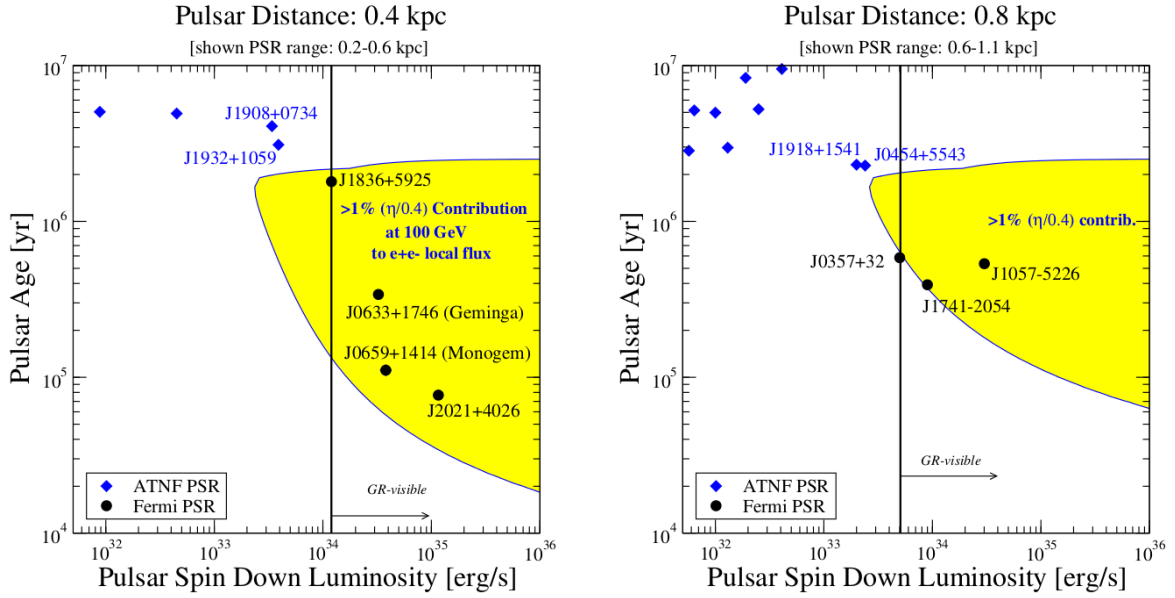
Figure 4.5. Parameter constraints for pulsar age and spin-down luminosity. In the **left** panel the parameter space is shown for a pulsar distance of ca. 400 pc, in the **right** panel for a distance of ca. 800pc. The yellow regions mark the range of pulsars expected to contribute to the $e^{\pm}$ flux at Earth. Taken from [160]. Pulsar distances are put as determined by the authors thereof. The blue-dotted pulsars to the left of each plot are not visible in γ rays and thus not in the Second Fermi Catalog [158]. For our study, we select the four γ-ray pulsars in the yellow region for 400 pc (left), and the highest-luminosity γ-ray pulsar J1057-5226 from the yellow region for 800 pc (right).

4.3.1. Pulsar contributions to e^+ flux and e^+/p dipole anisotropy

A visual representation of the allowed pulsar locations (from Tab. 4.1) is given in Fig. 4.6. Employing a MINUIT optimization algorithm, we try to find suitable source scenarios in which the pulsar contribution to the positron flux, added to the BG secondary positron background, matches the AMS-02 measurement. Please note that the description of Synchrotron and Inverse Compton energy losses by the common parametrization $\dot{E} = b_0 E^2$, $b_0 = 1.4 \cdot 10^{16} \, \text{GeV}^{-1}\text{s}^{-1}$ is in good agreement with the DRAGON model (confirmed below, Fig. 4.16). While in [160], diffusion properties are taken as customary ($D_0 = 3.6 \cdot 10^{28} \text{cm}^2 \, \text{s}^{-1}$, $\delta = 0.33$), our investigation is based on the previously defined BG model ($D_0 = 2.29 \cdot 10^{28} \text{cm}^2 \, \text{s}^{-1}$, $\delta = 0.576$).

The fitting routine for each pulsar PSi was then set up to optimize each pulsar distance d_i within the given interval, injection spectrum parameter ($\Gamma_i, E_{\text{cut},i}$) and an uncertainty $f_i \in [0.1, 10]$ of one order in the overall energy output $W_0(t_{\text{age}_i}, \dot{\mathcal{E}}_i)$. The fit was only performed to match χ^2 at the *signal region $E \geq 10$ GeV*. Solar modulation was then made

Pulsar name	l (°)	b (°)	distance / limits (kpc)	t_{age} (kyr)	$\dot{\mathcal{E}}$ $(10^{34}\frac{\mathrm{erg}}{\mathrm{s}})$
J0633+1746[1] ≡ PS1	-164.87	4.27	0.28 (0.18 - 0.47)	341.9	3.3
J1836+5925 ≡ PS2	88.88	25.00	0.44 (0.04 - 0.84)	1800	1.1
J2021+4026 ≡ PS3	78.23	2.09	0.44 (0.38 - 1.95)	76.8	11.4
J1057−5226 ≡ PS4	-75.00	6.65	1.02 (0.10 - 1.22)	535	3.0
J0659+1414[2] ≡ PS5	-158.89	8.26	1.39 (0.25 - 1.56)	110	3.8
J0357−32	162.76	-16.00	0.82 (0.66 - 0.98)	585	0.6
J1732−31	-3.69	1.01	1.52 (1.21 - 1.83)	120	14.6
J1741−2054	6.43	4.91	1.11 (0.27 - 1.43)	392.1	0.9
J1809−2332	7.39	-1.99	1.45 (0.70 - 2.70)	67	43.0
J2043+2740	70.61	-9.15	3.35 (1.26 - 4.12)	1200	5.5

commonly called [1] Geminga and [2] Monogem.

Table 4.1. Physical parameters of the 10 nearby pulsars expected to contribute topmost to the local $e^{\pm}$ flux. This is *not* a ranking in importance, because of the uncertainty on the physical reality. PS1..PS5 are the abbreviations given to the five pulsars selected for this study. A color code is introduced which is kept throughout this chapter to identify the particular pulsars.

to be fit in order to approximately describe the low energy range. This usually resulted in a minor deviation from the measured data in the intermediate range $E \approx 2..8\,\mathrm{GeV}$ that can actually described within the uncertainty of conventional background models, as is shown in Fig. 4.1. Also, as shown by [56], the uncertainty on the positron production rate in this energy range can amount to a factor of 1.2 to 1.3, depending on the cross section calculation.

Overall, with the parameter freedoms given it is not at all complicated to find suitable pulsar-including models that describe the energetic positron component well. Due to their different source configurations $(d_i, \Gamma_i, E_{\mathrm{cut},i})$ the resulting prediction of anisotropy differs between different setups. Considering that the proton background is not affected by the extra leptons, we choose the e^+/p dipole anisotropy $delta_{e^+/p}$ as a good quantity for measure.

As seen in the previous chapter, our BG model shows $\delta_{e^+/p}(E = 16..350\,\mathrm{GeV}) = 1.39 \cdot 10^{-4}$. It is directed exactly away from the galactic center, which is expected due to the symmetry in the GALPROP SNR distribution model and the isotropy of transport processes. An extra e^+ contribution from a point source (PS) would increase this value, in the cumulative energy interval $E = 16..350\,\mathrm{GeV}$ as:

$$\delta_{e^+/p} = |9.3\% \, \vec{\delta}_{e^+}^{\mathrm{BG}} + 90.7\% \, \vec{\delta}_{e^+}^{\mathrm{PS}} - \vec{\delta}_p^{\mathrm{BG}}| = |1.39 \cdot 10^{-4} \vec{e}_X + 90.7\% \, \vec{\delta}_{e^+}^{\mathrm{PS}}| \, , \qquad (4.14)$$

the unlikely case of anisotropy reduction by this contribution alone would only be possible if all pulsars would lie farther away from the center to cancel this X contribution, and if their Y and Z contribution would also be small (note that all 5 of the chosen PSi lie *above* the galactic plane).

We now propose to define five different setup $G1..G5$, via the following characteristica.

G1 takes only the two pulsars PS3, PS4 lying towards the galactic center ($|l| < 90°$). This should then enhance the BG anisotropy. They are preferably taken to be close, but over 200 pc away.

G2 places PS3, PS4 at least $d_i \geq 400$ pc away and allows the other three in a range $d_i \in [150, 300]$ pc.

G3 places all pulsars in a range $d_i \in [150, 400]$ pc.

G4 takes for every pulsar the distance measurement of [160] (also given in Tab. 4.1).

G5 places PS3 at $d_3 = 700$ pc (far enough so it does not dominate the highest energies), and the others anywhere $d_i > 150$ pc.

The condition $d > 150$ pc that exists in any scenario was imposed voluntarily, in order not to run into numerical computation problems later, when we switch to using DRAGON with local diffusion inhomogeneities. For example, a scenario similar to G1 was found with $d_4 = 100$ pc, but it could have raised the problem of the source distribution overlapping the wall regions, requiring specific numerical treatment (e.g. grid refinement). We have studied this case for G1 with PS4 inside the Local Bubble, and found that it did not change the outcome overall.

We define a way of visualization for the pulsar source locations in Fig. 4.6. Only the pulsar distance and its galactic longitude are shown, as pulsars generally lie within the Galactic Disc. In Figs. 4.7 to 4.11, we show the pulsar distribution and positron spectrum for each of the scenarios, subsequently. As is seen, the freedom in pulsar parameters allows for good AMS-02 positron description, $\chi^2 \lesssim 1$ in all cases. In the visualization, the size of the marker represents the overall energy output $f_i \cdot W_0(t_{\mathrm{age}_i}, \dot{\mathcal{E}}_i)$ (which is not varying much). The color codification (PS1, PS2, PS3, PS4, PS5) is applied, cf. Tab. 4.1.

From the analytical solution and the background flux from BG, we calculate the expectation of dipole anisotropy in $e^\pm$ and e^+/p. These are all compatible with Fermi-LAT [125] and AMS-02 [99] upper limits, although G2 and G5 are not far from the Fermi-LAT UL on $e^\pm$ anisotropy. The values are given in Tab. 4.2.
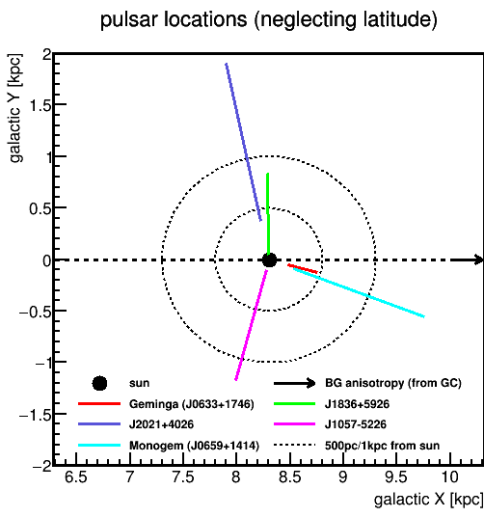
Figure 4.6. Visualization of the allowed locations for PS1..PS5. This schematic shows the pulsars galactic longitude l and allowed range of distance from the sun, according to Tab. 4.1. The galactic latitude b is not represented, as all pulsars lie in the Galactic Disc (most above is PS2 with $b = 25°$. $l = 0°$ is pointing towards the galactic center, to the left. Due to the source distribution, the anisotropy of the background model is directed away from the GC (noted by the black arrow).
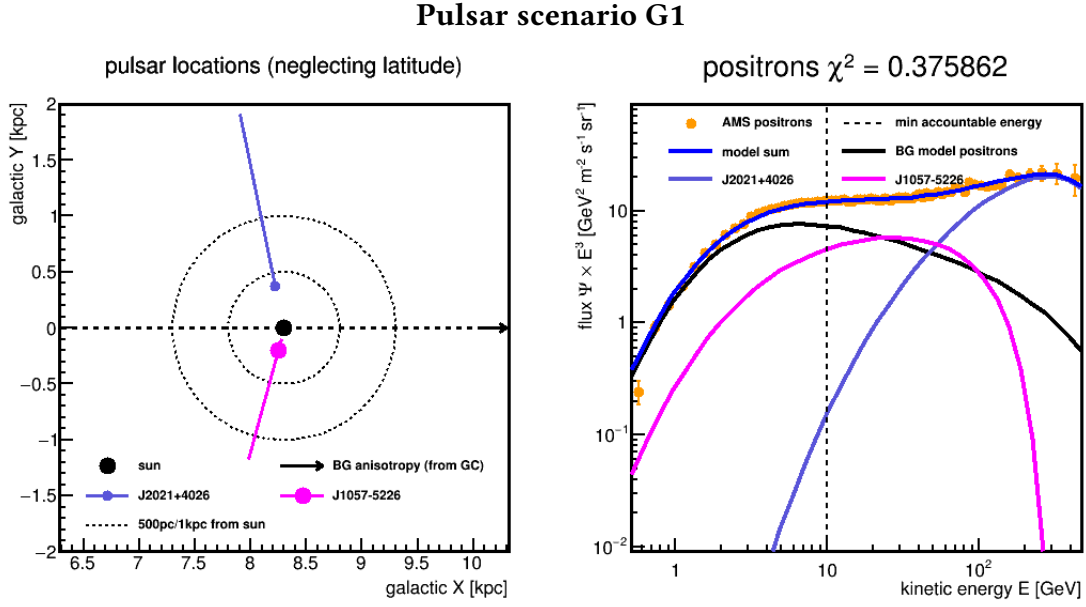
Pulsar scenario G1

Figure 4.7. In scenario G1, we take only PS3 and PS4. From our pulsar selection, these are the only two lying towards the Galactic Center (galactic longitude $|l| < 90°$), i.e. in coarse alignment with the background anisotropy. Their distance was chosen as close as possible, but at least 200 pc away. The **left** panel shows the top view visualization of pulsar source localization after Fig. 4.6 (neglecting their galactic latitude). The **right** panel shows the local e^+ energy spectrum (scaled with E^3), in agreement with the AMS-02 [103] e^+ measurement, with background component calculated from BG.
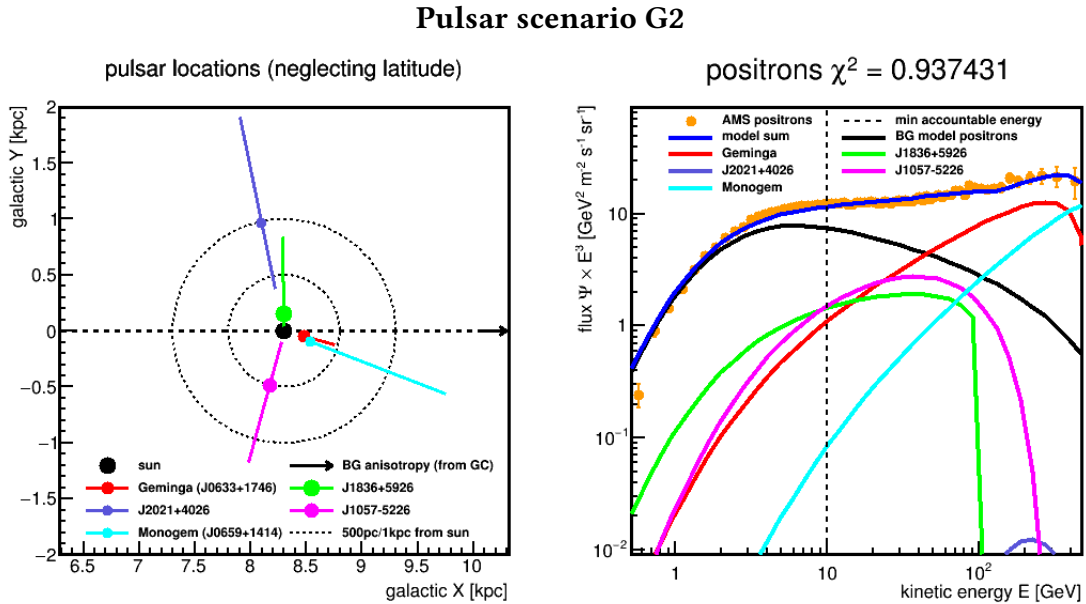
Pulsar scenario G2

Figure 4.8. In scenario G2, we place PS3 and PS4 at least 400 pc away, as contrast to G1 (above). PS1, PS2 and PS5 are allowed in a range $[150, 300]$ pc. The **left** panel shows the top view visualization of pulsar source localization after Fig. 4.6 (neglecting their galactic latitude). The **right** panel shows the local e^+ energy spectrum (scaled with E^3), in agreement with the AMS-02 [103] e^+ measurement, with background component calculated from BG.

Pulsar scenario G3
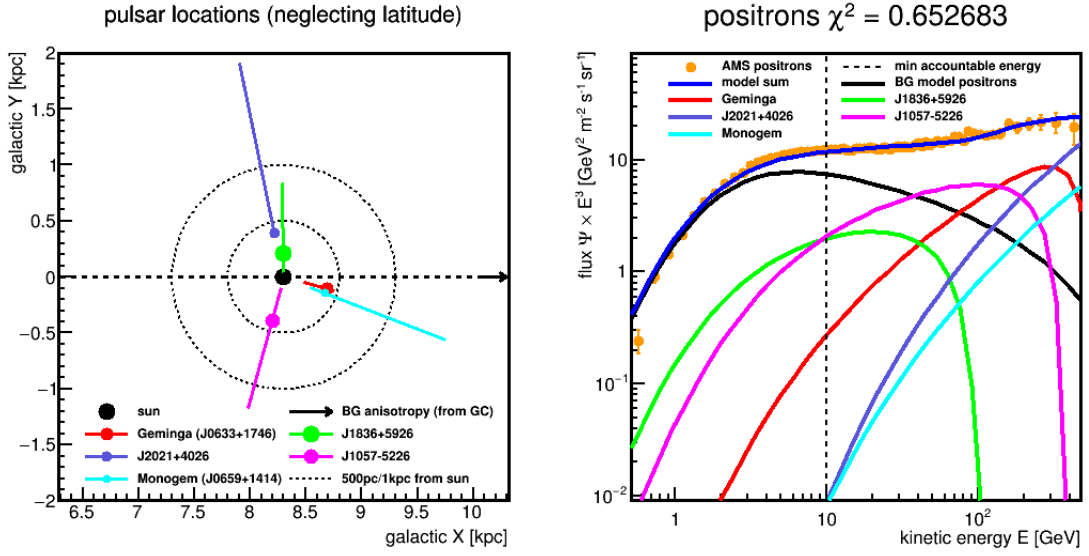
Figure 4.9. In scenario G3, we allow all five PS1..PS5 within a range $[150, 400]$ pc. The **left** panel shows the top view visualization of pulsar source localization after Fig. 4.6 (neglecting their galactic latitude). The **right** panel shows the local e^+ energy spectrum (scaled with E^3), in agreement with the AMS-02 [103] e^+ measurement, with background component calculated from BG.

Pulsar scenario G4
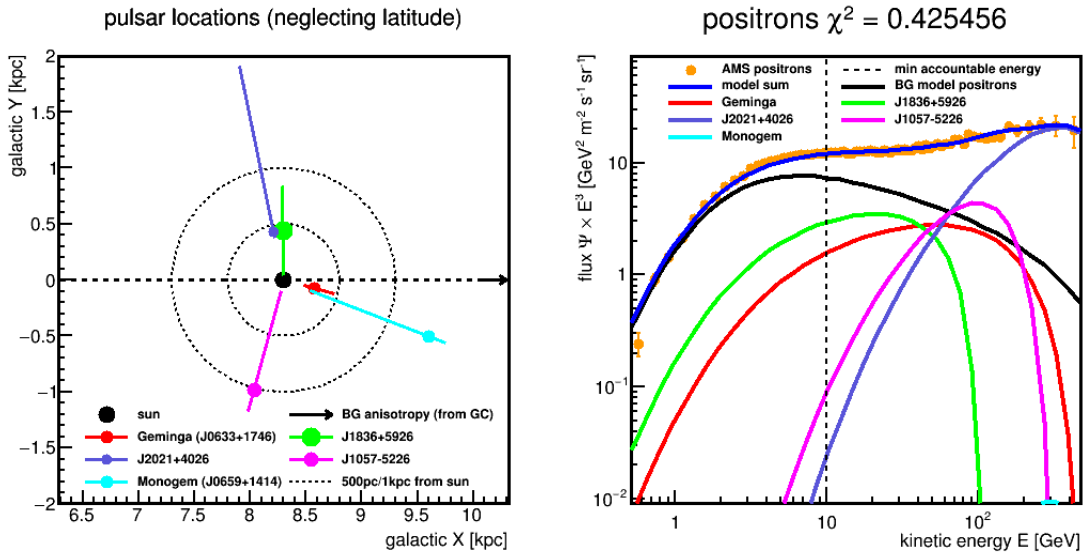
Figure 4.10. In scenario G4, we fix the pulsar distance to the value inferred by [160] (cf. Tab. 4.1). The **left** panel shows the top view visualization of pulsar source localization after Fig. 4.6 (neglecting their galactic latitude). The **right** panel shows the local e^+ energy spectrum (scaled with E^3), in agreement with the AMS-02 [103] e^+ measurement, with background component calculated from BG.

Pulsar scenario G5
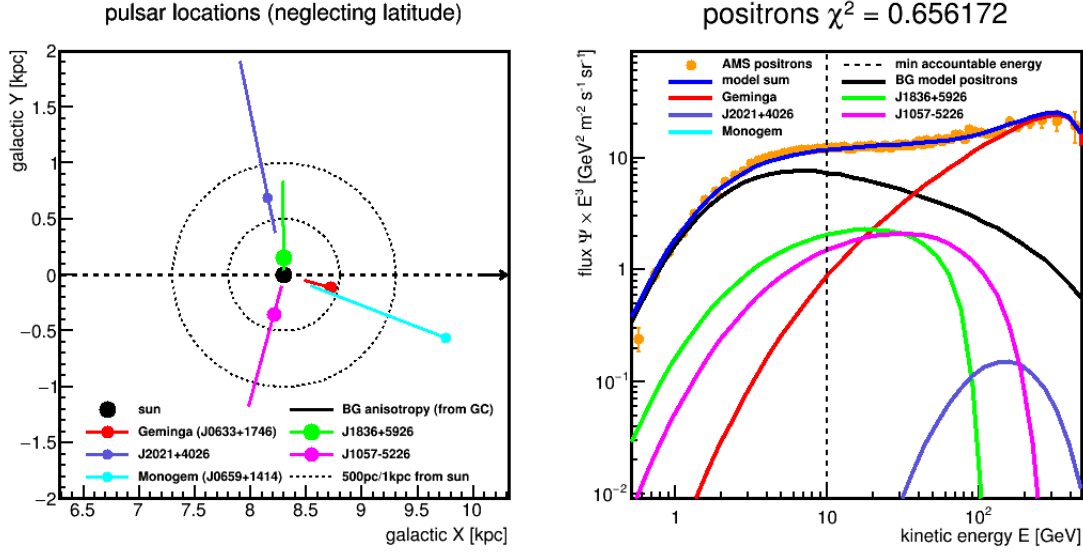
places PS3 at $d_3 = 700\,$pc (far enough so it does not dominate the highest energies), and the others anywhere $d_i > 150\,$pc.

Figure 4.11. In scenario G5, we place PS3 at 700 pc and the other four at least 150 pc away. The distance of PS3 was chosen far so that it would not dominate the fit to the highest positron data energies. The **left** panel shows the top view visualization of pulsar source localization after Fig. 4.6 (neglecting their galactic latitude). The **right** panel shows the local e^+ energy spectrum (scaled with E^3), in agreement with the AMS-02 [103] e^+ measurement, with background component calculated from BG.

Model	$\delta_{e^\pm}(E \in [60, 480\,\mathrm{GeV}])$	$\delta_{e^+/p}(E \in [16, 350\,\mathrm{GeV}])$
G1	$0.86 \cdot 10^{-3}$	$2.49 \cdot 10^{-3}$
G2	$4.17 \cdot 10^{-3}$	$1.33 \cdot 10^{-3}$
G3	$0.47 \cdot 10^{-3}$	$0.82 \cdot 10^{-3}$
G4	$0.13 \cdot 10^{-3}$	$1.20 \cdot 10^{-3}$
G5	$3.33 \cdot 10^{-3}$	$1.68 \cdot 10^{-3}$
UL	$5.28 \cdot 10^{-3}$	$1.99 \cdot 10^{-2}$
	Fermi-LAT [125]	AMS-02 [99]

Table 4.2. From the five pulsars PS1..PS5 and background contribution BG, we constructed five scenarios G1..G5 with each of the pulsar parameters adjusted within realistic values. Here we show the resulting dipole anisotropy in $e^\pm$ for $E \in [60, 480]\,$GeV and e^+/p for $E \in [16, 350]\,$GeV, compared to recent experimental limits.

Before we turn on reproduction of these scenarios as numerical solutions - which will allows us greater flexibility, as foremost the presented Local Bubble implementation - we want to discuss the presence of a quadrupole anisotropy or higher multipoles.

4.3.2. Negligibility of quadrupole anisotropy

Judging from the amount of possibilities (see Fig. 4.6 again) in which the $e^{\pm}$ point sources can be distributed around the Sun, it appears justified to pose the question of anisotropies beyond the dipole anisotropy. These could be further observables for testing the pulsar hypothesis (DM annihilation from the smooth DM halo would appear very isotropic). As an illustration, a quadrupole contribution could stem from the fact that all potential astrophysical source candidates were likely positioned near the Galactic Disc (as pulsars do). if we were surrounded by an even, ring-like distribution in the galactic disc like (as indicated by Fig. 4.12), with the equator showing where sources could lie.
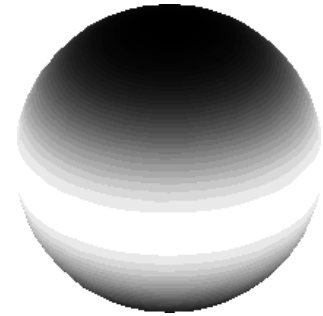
Figure 4.12. In principle, the flux from several sources holds higher multipole orders. As an illustration, a homogeneous distribution throughout the Galactic Disc contributes a small Y_{20} component, seen here. We will show that any such contribution is negligible.

Using the established propagation framework, however, this question can not be treated. Not only would the discrete representation of such a distribution require a local grid resolution considerably higher than we already took as requirement for the Local Bubble studies, but more fundamentally, the transport equation does not describe propagation in terms of directed fluxes - it is derived using statistical averages over the pitch-angle information of CR distribution (see section 2.1.1), leaving us with an equation for isotropic phase space density only: They hold no directional information of velocity anymore. This is the reason why in section 2.3, the dipole anisotropy is purely given by Fick's first law, i.e. defined by the diffusion flux balancing any gradient in density N, linking $\delta \sim |\vec{\nabla} N|/N$.

We suggest a method to estimate the *maximum quadrupole anisotropy* that could be deduced in the isotropic diffusion picture: A space-born detector like AMS-02 would, in a galactic coordinate system, orbit through the small fluctuations of density distribution $N(\vec{r})$ on a sphere of a given height h. This is illustrated in Fig. 4.13 by the light circle around the Earth (the black circles are pulsars and the background gradients depict the particle density). The measured flux, then, is the isotropic flux $I_0 = \frac{4\pi}{v} N$. Pointwise taken, this results in a local mapping of the density distribution, which can be tested for multipole components.

The representation in Fig. 4.13 is, of course, heavily exaggerated. In reality the "light circle" equals the ISS orbit over the Earth radius:

$$R_{\text{ISS}} = R_{\oplus} + h_{\text{ISS}} = 6371\,\text{km} + 400\,\text{km} = 2.194 \cdot 10^{-10}\,\text{pc}\,,$$

a very tiny fraction of any pulsar distance. Yet, we test this method in order to verify the dipole anisotropy and the relative magnitude of higher orders. This calculation is only possible using an analytically given shape of the pulsar-given $e^{\pm}$ component, such as the one already presented.
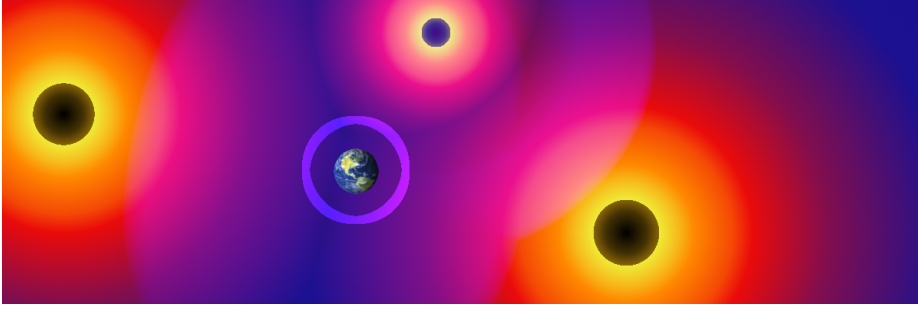
Figure 4.13. The transport equation of cosmic rays does not provide directional information of the particle momenta, as these were averaged out in its derivation. To estimate the amount of higher-order multipole information a space-based detector would measure, we suggest to evaluate the isotropic density N over the surface of the orbit (light circle around the Earth). This produces a skymap $N(\theta, \phi)$ which we can expand into multipole orders. The distances here are heavily exaggerated as the detector orbit is below the nanoparsec scale, 12 orders of magnitude smaller than the typical scale of pulsar distances.

For each position on this orbit, the value of $N = \sum_i N_{\mathrm{PS}i} + N_{\mathrm{BG}}$. Because of the above-mentioned restriction of the transport equation, the background can only hold a dipole gradient, so the numerical solution for BG will be interpolated to each point accordingly. The surface of the R_{ISS}-sphere is partitioned into equal-area divisions using HEALPIX "sky map"s. This also has the advantage that the HEALPIX facility *anafast* for expanding each sky map into spherical harmonics $Y_{lm}(\theta, \phi) = Y_{lm}(\pi/2 - b, l)$. It follows from the Taylor[2] and spherical expansion of CR density around the Sun (with $N_0 = N(\vec{r}_\odot)$ the local value):

$$N(\vec{r}_\odot + \Delta\vec{r}) = N_0 + \Delta\vec{r} \cdot \vec{\nabla}N + \frac{1}{2}\Delta\vec{r}^T H_N \Delta\vec{r} + \dots \tag{4.15}$$

$$= N_0 \cdot \left(1 + \frac{3c}{D}\vec{\delta} \cdot \Delta\vec{r} + \dots\right) \tag{4.16}$$

$$N(R, \theta, \phi) = \sum_{l=0}^{\infty}\sum_{m=-l}^{l} a_{lm}Y_{lm} = N_0\left(1 + (\vec{\delta} \cdot \vec{e}_r) + \dots\right) \tag{4.17}$$

with the spherical expansion coefficients a_{lm} similar to (2.77), and defining the multipole powers C_l,

$$a_{lm} = \int d\Omega\, N(\theta, \phi)Y_{lm}^*(\theta, \phi) \tag{4.18}$$

$$C_l = \frac{1}{2l+1}\sum_{m=-l}^{l}|a_{lm}^2| = \frac{1}{2l+1}\left(|a_{l0}|^2 + 2\sum_{m=1}^{l}|a_{lm}|^2\right). \tag{4.19}$$

---

[2]The second term introduces the Hessian matrix $(H_N)_{ij} = \left(\partial^2 N/\partial x_i \partial x_j\right)$ and would describe the quadrupole contribution, but is mentioned only for completeness. We do not need H_N later on.

It follows then from (4.17) straightforward that, with $|\Delta \vec{r}| = R_{\text{ISS}}$,

$$C_0 = 4\pi N_0^2 \tag{4.20}$$

$$C_1 = \left(\frac{4\pi}{3} \cdot \frac{c}{3D} \cdot |\vec{\delta}| \cdot R_{\text{ISS}} \right)^2 \tag{4.21}$$

$$\Rightarrow \quad |\vec{\delta}| = \frac{9D}{c \cdot R_{\text{ISS}}} \sqrt{\frac{C_1}{C_0}} \, . \tag{4.22}$$

We can then search for higher terms in 4.17 by evaluating the density $N(R_{\text{ISS}}, \theta, \phi)$ a detector would see on an orbit as sketched in Fig. 4.13. We can represent this density on a sky map $N(\theta, \phi)$, as introduced in section 2.3.1. Multipole expansion of $N(\theta, \phi)$ equals the decomposition into a pure monopole (average value), pure dipole maps (from Y_{1m}), pure quadrupole maps (from Y_{2m}) and so on. Examples of such of a pure multipole skymaps were given before in Fig. 2.5.

Analysis. The analysis was done using the publicly available HEALpix facility *anafast*, which provides a numerical implementation of (4.18), after writing a piece of code to evaluate $N(\theta, \phi)$ on the orbital sphere in HEALpix format. Using these tools, caution is required because of the large difference in multitude of the monopole (N_0), dipole and every subsequent order, as this difference in precision could exceed the capacity of the 8 Byte *double* structure. A workaround is found by excluding the monopole contribution numerically before filling the $N(\theta, \phi)$ sky map, as C_0 is reconstructable by ((4.20)) anyway. The result of such a numerical evaluation can be seen, for our set of 5 models, in Fig. 4.15.

This evaluation is done for one energy bin, taken at $E = [91..131]\,\text{GeV}$. This can be directly computed by *anafast*. The cumulation of several energy bins could in principle be done similarly, but is more tedious in implementation, and we do not consider it more informative: Towards higher energies, diffusion coefficient rises and CR density distributions are spread out further, so they could contribute less in the quadrupole. A finer structure in e^+ flux is more likely seen at lower energies, but energy has to be large enough so that the pulsar contribution is not too small overall. We analyze the absolute e^+ anisotropy here, because a relative flux as e^+/p holds small *fake* quadrupole anisotropy information from the contamination from the dipole anisotropy in the p flux, as we have calculated in section 2.3.1.

The skymaps for CR distribution $N(\theta, \phi)$ in this energy interval are seen in Fig. 4.14 for every pulsar scenario G1..G5, after the average value was subtracted. The average values and minima/maxima (which define the color scale from blue to red in each skymap representation) are given to illustrate the difference in order of the monopole to the dipole. We see that the skymaps appear very dipole-like in every case, that means the quadrupole order is is already visibly small.

Figure 4.14. After defining the skymaps $N(\theta, \phi)$ for $E \in [91, 131]$ GeV via the method shown in Fig. 4.13, we subtract the monopole (average value) for numerical reasons. Representation in skymaps is in galactic $b = \pi/2 - \theta, l = \phi$ coordinates, with the GC centered. For each skymap, the blue minimum and red maximum are given to the right. From **(top)** G1 to **(bottom)** G5.

(G1)

$E \in [91, 131]$ GeV

average (subtracted)	$2.198 \cdot 10^{-5}$ GeV^{-1}kpc^{-3}
minimum	$-1.342 \cdot 10^{-17}$ GeV^{-1}kpc^{-3}
maximum	$+1.833 \cdot 10^{-17}$ GeV^{-1}kpc^{-3}

(G2)

$E \in [91, 131]$ GeV

average (subtracted)	$2.122 \cdot 10^{-5}$ GeV^{-1}kpc^{-3}
minimum	$-1.880 \cdot 10^{-18}$ GeV^{-1}kpc^{-3}
maximum	$+3.569 \cdot 10^{-18}$ GeV^{-1}kpc^{-3}

(G3)

$E \in [91, 131]$ GeV

average (subtracted)	$2.076 \cdot 10^{-5}$ GeV^{-1}kpc^{-3}
minimum	$-1.735 \cdot 10^{-18}$ GeV^{-1}kpc^{-3}
maximum	$+7.606 \cdot 10^{-19}$ GeV^{-1}kpc^{-3}

(G4)

$E \in [91, 131]$ GeV

average (subtracted)	$2.206 \cdot 10^{-5}$ GeV^{-1}kpc^{-3}
minimum	$-9.287 \cdot 10^{-18}$ GeV^{-1}kpc^{-3}
maximum	$+9.287 \cdot 10^{-18}$ GeV^{-1}kpc^{-3}

(G5)

$E \in [91, 131]$ GeV

average (subtracted)	$2.111 \cdot 10^{-5}$ GeV^{-1}kpc^{-3}
minimum	$-1.338 \cdot 10^{-18}$ GeV^{-1}kpc^{-3}
maximum	$+6.777 \cdot 10^{-18}$ GeV^{-1}kpc^{-3}

multipole amplitudes (relative to monopole)

$E \in [91, 131]\,\mathrm{GeV}$

Setup	$|\vec{\delta}|$	$\sqrt{C_1/C_0}$	$\sqrt{C_2/C_1}$
BG	$1.593 \cdot 10^{-3}$	$2.60 \cdot 10^{-14}$	0
G1	$1.476 \cdot 10^{-2}$	$2.41 \cdot 10^{-13}$	$7.3 \cdot 10^{-6}$
G2	$2.614 \cdot 10^{-3}$	$4.26 \cdot 10^{-14}$	$7.4 \cdot 10^{-6}$
G3	$1.224 \cdot 10^{-3}$	$2.00 \cdot 10^{-14}$	$2.5 \cdot 10^{-5}$
G4	$8.597 \cdot 10^{-3}$	$1.40 \cdot 10^{-13}$	$1.3 \cdot 10^{-5}$
G5	$3.914 \cdot 10^{-3}$	$6.38 \cdot 10^{-14}$	$1.6 \cdot 10^{-5}$

Figure 4.15. The numerical expansion gives us the multipole powers C_l of expected e^+ density distribution $N(\theta, \phi)$ as shown in Fig.4.14). We evaluate each map using the HEALPix facility *anafast*. The fluctuating behavior of higher orders is not physical, but resembles algorithmic artifacts, some of them are HEALpix-resolution dependent... At this energy, (4.22) equals $\delta = 6.31 \cdot 10^{10} \sqrt{C_1/C_0}$.

As the ISS orbit is only $2.194 \cdot 10^{-10}$ pc, and the diffusive propagation of the cosmic rays from heavily blurs out the point-like character of the source. The resulting quadrupole contributions, as seen in Fig. 4.15, are expected 5-6 orders below the dipole anisotropy. We suggest that this is a level which is inaccessible at the precision of measurement. Regarding further, that the particle flux modulation by the heliospheric field should actually be described by a anisotropic diffusion scenario, given by the spatial shape of the Sun's magnetic field (*Parker spiral*), which should overshadow any higher multipole prediction available from the local interstellar transport processes. At the current time, no calculations are known in which this additional effect is taken into account - the solar field is usually only accounted for by the simplistic force-field approximation. Therefore, future calculations beyond the force-field approach are required to discuss higher-order multipoles in this field.

As a conclusion: So far, we showed that the modeling of nearby pulsars (in analytical solutions of burst-like point sources) easily allows to match the positron spectrum. We defined 5 distinct distribution setups, chosen arbitrarily by our Minuit routine, and in no way the only five scenarios deemed realistic. As there is no known way in constraining the pulsar injection spectrum, there is certain ambiguity in the dipole anisotropy prediction. Moreover, any higher multipoles resulting from a multi-pulsar setup are not to be described within the framework of the isotropic transport equation, therefore, experimental detection of a quadrupole shape or similar would require a completely different understanding of the heliospheric propagation.

4.4. Evaluation of numerical pulsar models

We now leave the analytical framework, in order to address the inclusion of the Local Bubble. For the local transport models presented previously, there is no description of an

analytical solution. We therefore implement a point-like source with pulsar properties in numerical codes, compare the outcome, and can then use DRAGON with our local diffusion setups as in chapter 3. Considering the discreteness of spatial spacing and time steps during the propagation, the source distribution has to be adjusted, in which we chose the following finite functions:

$$\delta(\vec{r} - \vec{d})\delta(t - t_{\text{age}}) \longrightarrow G_{50\,\text{pc}}(\vec{r} - \vec{d})\Theta(1\,\text{kyr} - t) \tag{4.23}$$

$$G_w(\vec{r}) = \exp\left(-\ln 16 \cdot \left(\frac{\vec{r}}{w}\right)^2\right) \tag{4.24}$$

$$\Theta(1\,\text{kyr} - t) = 1 \text{ for } t \leq 1\,\text{kyr, 0 afterwards.} \tag{4.25}$$

and evaluated the solution after a total propagation time of $t = t_{\text{age}}$ has passed. The Gaussian *source width* $w = 50\,\text{pc}$ was chosen as the range around the source, in which the injection strength has dropped to a relative level of $\frac{1}{16}$ "≈ 0". The injection energy spectrum $Q_{\text{inj}} = Q_0 (E/1\,\text{GeV})^{-\Gamma} \exp(-E/E_{\text{cut}})$ was used as implemented. Normalization of the source strength, Q_0 has then been chosen in such a fashion that the analytical pulsar solution, for same d, t_{age} and injection spectrum $Q_{\text{inj}}(E)$ was best met. Hereof, two remarks are to be made:

1. our choice $w = 50\,\text{pc}$ does slightly exceed the size usually assigned to the PWN of a few parsecs surrounding each pulsars, these are as extensive as their wind pressure surmounts the ambient pressure. E.g, the Crab SNR including the Crab PWN, Figs. 1.12 and 1.13, spans about 2 pc in total. It is necessary, though, as the numerical algorithm can not handle extreme source gradients between neighboring spatial grid bins (this leads to artificial oscillations, as described in appendix A.2), and it would be very resource expensive to refine the grid at every possible pulsar location.

2. The time dependence $\Theta(1\,\text{kyr} - t)$ was a specific modification of the DRAGON code on our own. There has been published investigations of pulsar-injected leptons in GALPROP and DRAGON before, treating the additional source constant in time (e.g. [163, 56]) and assuming that the steady state is actually reached. While the latter can be considered true for the galactic background distribution, the local source and propagation properties are, for cosmic leptons, so prone to fluctuations that we do not consider it true. Implications thereof will be compared below, in subsection 4.4.4.

Already stated above, the analytical pulsar expression was evaluated for diffusion properties set to those of our BG model ($D_0 = 2.29 \cdot 10^{28}\,\text{cm}^2\,\text{s}^{-1}, \delta = 0.576$). As an act of providence, we already dismissed convection or reacceleration effects in this DRAGON model, as these are also not included in the simplified propagation model giving equation (2.116). Because of our treatment of the Θ-like temporal source injection and rejection of the steady-state condition, no influence is supposed to be caused from the boundary conditions at $Z = \pm 2.8\,\text{kpc}$ height. For cutting short computing time, the grid was also cut at $\pm 4\,kpc$ from the Sun in X and Y directions.

4.4.1. Agreement numerical vs. analytical solution

As a first test of agreement, we evaluated a single, Geminga-like pulsar, with sample parameters ($d = 280\,\text{pc}, \Gamma = 1.7, E_{\text{cut}} = 1\,\text{TeV}$) as used in [160]. This is seen in Fig. 4.16 as the black line. We used a customary DRAGON algorithm configuration, with the maximum timestep adjusted to match the pulsar age

- energy resolution factor $\Delta \log E = \log 1.2 \approx 0.08$

- number of repetitions $N_{\text{rept}} = 30$

- minimum timestep $\Delta t_{\text{min}} = 1\,\text{yr}$

- timestep reduction factor $f_{\Delta t} = \frac{1}{4}$

- maximum timestep[3] $\Delta t_{\text{max}} = 8.57\,\text{kyr}$

Source normalization Q_0 was fixed using the condition

$$Q_0 \int_0^\infty dE\, Q_{\text{inj}}(E)E \int dV\, G_w(\vec{r}) \int dt\, \Theta(1\,\text{kyr} - t) \overset{!}{=} \eta W_0(t_{\text{age}}, \dot{\mathcal{E}}) \frac{c}{4\pi}\,, \qquad (4.26)$$

with $\frac{c}{4\pi} = \frac{\psi}{N}$ the conversion factor between particle density and particle flux. As will be shown below, a considerable deviation emerged in the absolute deviation, which will be addressed in the following. The Gaussian volume integral is actually readily given as $(\pi w^2 / \ln 16w)^{3/2}$, but was nevertheless evaluated by summing the source function over the discrete grid bin contents inside DRAGON, because deviations from this value became visible for pulsars more distant, were grid spacing became larger. The energy integral was also numerically evaluated; another correction was applied to resolve the fact that 1 kyr is already $\frac{1}{8.57}$ of the very first time step. Conversion factors from the internal DRAGON units ($\text{Myr} \to \text{s}, \text{kpc} \to \text{m}$) have also been taken care of.
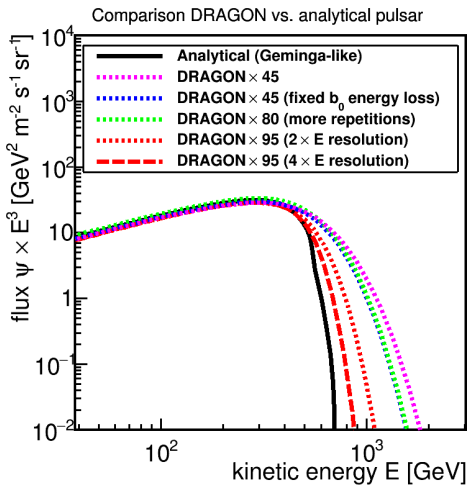
Figure 4.16. For one Geminga-like pulsar example, the comparison between the analytical solution (black) and numerical DRAGON is shown with varying algorithm settings. The overall normalization had to be adjusted by a certain factor (discussed in the text) **(pink)** our standard algorithm setting shows a widened cooling break, **(blue)** the approximation of energy losses with a homogeneous b_0 is not showing a large difference in shape, **(green)** increasing the number of algorithm repetitions N_{rept} is also not showing large differences in shape, **(red)** by increasing the energy grid resolution, we increase the accordance with the numerical solution.

---

[3]From the geometric series, it follows that the total time elapsed during DRAGON propagation equals $t_{\text{age}} = \Delta t_{\text{max}} N_{\text{rept}} (1 - f_{\Delta t})^{-1}$

Still, for some reasons unknown, the local flux prediction differed by a medium scale factor of ca. 45 from the analytic solution, which is seen in Fig. 4.16 as the pink line. For comparison, we replaced the Dragon energy loss functions internally by the parametrization $\dot{E} = b_0 \cdot E^2$ the analytical expression uses. This is the blue line, scaled with the same factor 45. Also, we compared the effect of increasing $N_{\mathrm{rept}} \longrightarrow 70$ (reducing the maximum time step to keep the total propagation time fixed at the pulsar age), seen as green line. This solution required a scale factor of ca. 80. Increasing the energy grid (dotted red line) required a factor 95, which did not rise further with an even finer energy grid resolution (dashed red line). Not shown are adjustments of the timestep resolution, which were shaped like the blue and green line, but required a factor of 95 for $\Delta t_{\mathrm{min}} \longrightarrow 1\,\mathrm{myr}$ and even 140 for $f_{\Delta t} \longrightarrow \frac{1}{2}$ (with t_{age} fixed).

This defect in overall normalization varied for different pulsars. It is somewhat dependent of the internal timesteps and could probably be due to being unable to resolve the very first years of propagation, where timesteps Δt_{max} are initially large (but chosen differently for different pulsars, see above). The energy grid has an *open* lower boundary, i.e. particles affected by low-energy losses at the beginning of propagation are at all removed from the system. Unconcernedly about the exact reasons, we decided to use a Minuit fitting routine to minimize, for scaling factor C, by defining a χ^2_{DRAGON} as:

$$\chi^2_{\mathrm{DRAGON}} = \sum_{E_i = E_{\mathrm{min}}}^{E_{\mathrm{max}}} \frac{\psi_{\mathrm{analytical}}(E_i) - C \times \psi_{\mathrm{DRAGON}}(E_i)}{\psi_{\mathrm{analytical}}(E_i)} \tag{4.27}$$

The correction factor C was found *not* to be changing under variation of the injection spectrum – as expected as the integral $\int Q_{\mathrm{inj}}(E)E dE$ is treated correctly in (4.26). If calculated for one scenario, each pulsar's C can then be applied in any scenario in which the spatial source distributions and algorithm settings are kept constant.

The other difference in Fig. 4.16 is the heavy softening of the the cooling break at $E_{\mathrm{max}} = (b_0 t_{\mathrm{age}})^{-1} \approx 665\,\mathrm{GeV}$. It is visible that this is also present when the Dragon model uses the b_0 approximation (comparison of the blue line), which actually appears to come close to the more realistic Dragon model (this might, however, cease to be valid for farther source distances). Increasing the resolution of the energy grid $\Delta \log E \longrightarrow \frac{\log 1.2}{2}, \frac{\log 1.2}{4}$ increases the steepness of the break. Further adjustment, as the increase of N_{rept} did not change this, as variations of Δt_{min} and $f_{\Delta t}$ also did not (described above, but not shown).

We consider this likely to be an artifact of the Dragon propagation, due to the timestep-reduction scheme that treats fast energy losses like Synchrotron & Inverse Compton processes only when the smaller time steps are reached. With the energy grid too coarse, the slower diffusive transport operator, that is computed first, can propagate particles inside one energy bin to places where they would actually not be propagated to if their energy losses (which are very fast, so computed after diffusion is finished) could be resolved at an earlier time. Double or quadruple resolution in energy resolution involve double or quadruple CPU memory requirement and computation time, respectively. We thus choose the doubled resolution, $\Delta \log E = \frac{1}{2} \log 1.2 = 0.04$ to be sufficient.
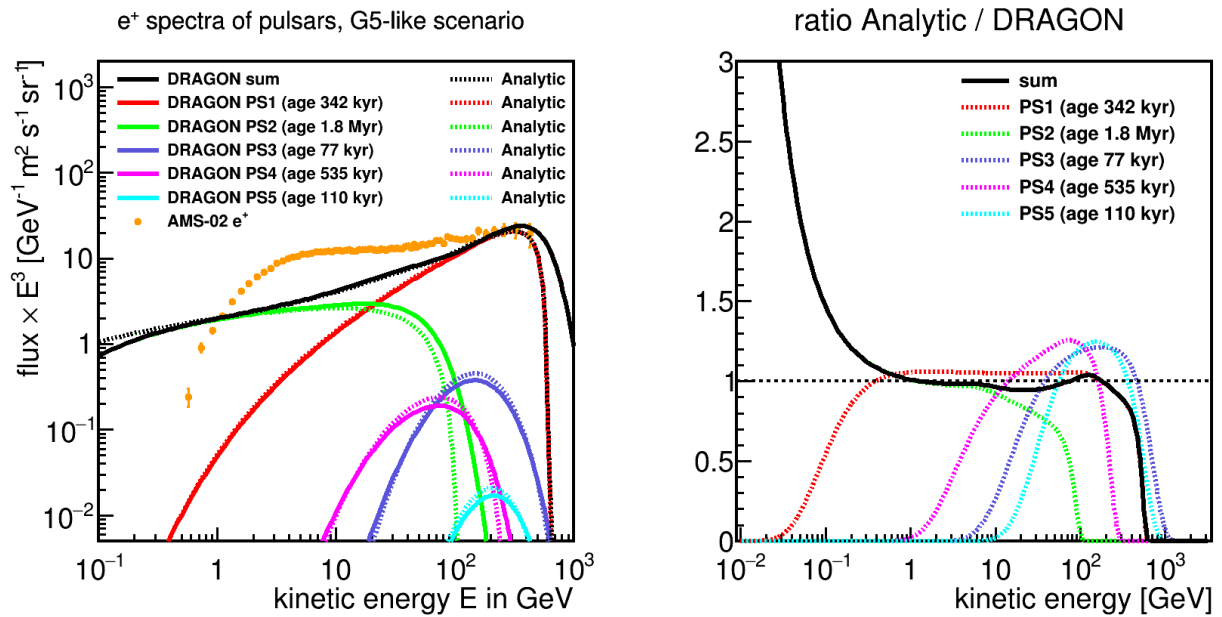
Figure 4.17. Agreement is shown between the analytical and the numerical treatment of one five-pulsar scenario, taken to be G5-like in this example. This especially is a test, whether the small deviations near the cooling break of single pulsars, or deviations from the normalization scheme we proposed, appear as significant trouble. This is not the case. The **left** panel shows the energy spectrum (scaled by E^3) of each pulsar contribution, each computed analytically and numerically. The green lines of PS2 show some deviation due to its old age. The AMS-02 positron spectrum [103] is described in the high-energy (background was left away). The **right** panel shows the ratio of the analytical to the numerical solution of the sum (black) and single pulsar contributions (colored).

Proof of concept is shown in Fig. 4.17, in a "G5-like" scenario (pulsars are placed as in G5, but the injection spectra were adjusted in order to test the analytical-DRAGON agreement more thoroughly, i.e. PS1 and PS2 were made to show distinct cooling breaks). For each pulsar PSi, the correction factor C_i was determined by numerically minimizing (4.27). It is shown, then (Fig.4.17 left), that the e^+ signal region $E = 1..400$ GeV is described in agreement with the analytical prediction. Single pulsar shapes do show some differences, especially PS2 which is by far the very oldest one, but these deviations blend into the overall solution. We can thus consider our algorithm settings to be adequate for further investigations.

Scenario replication with DRAGON

Hence, we can proceed in reconstruction of the 5 pulsar distributions G1..G5 within the numerical framework. In the last chapter, we showed for one example setup (similar to G5), that the DRAGON pulsar prediction is in approximate agreement to the analytical solution of the simplified transport setup. Given that the single pulsars showed slight deviations we allowed another small freedom in normalization, implementing another MINUIT routine to find the best AMS-02 data description. This allowed each single pulsars normalization to vary a factor $f_N = \frac{1}{2}..2$, except in case of G5, where $f_N = \frac{1}{3}..3$ was necessary to match the data. The results are summarized in Tab. 4.3.

The outcome for leptonic spectra and anisotropies can be seen in Figs. 4.18 and 4.19. Fig. 4.20 shows the density distribution of e^+ for $E = 200\,\text{GeV}$ around the Sun ($\vec{r}_\odot = (8.3, 0, 0)$ kpc) in the Galactic plane: Depending on scenario, the local flux in leptons can appear steeper (G1 and G4) or flatter (G2, G3, G5). This is especially interesting for the observable anisotropy in $e^\pm$ flux, because the scenarios (G2, G3, G5) show a reduction of anisotropy compared to the background electron anisotropy.

Scenario	Pulsar	d_i	Γ_i	$E_{\text{cut},i}$	analytical χ^2	DRAGON $f_{N,i}$	DRAGON χ^2
G1	**PS3**	380 pc	1.387	322 GeV	0.376	1.024	0.381
	PS4	203 pc	1.978	105 GeV		1.073	
G2	PS1	180 pc	1.404	922 GeV	0.937	0.5	0.840
	PS2	150 pc	1.992	931 GeV		2	
	PS3	990 pc	1.993	100 GeV		2	
	PS4	500 pc	1.956	102 GeV		0.556	
	PS5	250 pc	1.067	1.21 TeV		1.394	
G3	**PS1**	400 pc	1.273	775 GeV	0.653	1.513	0.688
	PS2	207 pc	1.949	100 GeV		1.314	
	PS3	400 pc	1.152	2.25 TeV		0.5	
	PS4	400 pc	1.843	511 GeV		0.804	
	PS5	400 pc	1.098	2.23 TeV		0.5	
G4	PS1	280 pc	1.957	199 GeV	0.425	1.063	0.445
	PS2	440 pc	1.991	100 GeV		1.104	
	PS3	440 pc	1.131	312 GeV		1.007	
	PS4	1020 pc	1.242	103 GeV		0.765	
	PS5	1390 pc	1.976	137 GeV		0.507	
G5	**PS1**	432 pc	1.407	1.18 TeV	0.656	0.351	0.636
	PS2	150 pc	1.989	102 GeV		0.335	
	PS3	700 pc	2	100 GeV		3	
	PS4	360 pc	2	100 GeV		2.109	
	PS5	1560 pc	2	100 GeV		2.176	

Table 4.3. The physical parameters (distance d_i, injection slope Γ_i and injection cutoff $E_{\text{cut},i}$) in each scenario definition G1..G5 is given. For the corresponding analytical and numerical DRAGON solutions and assuming the background contribution from model BG, the χ^2 values above 10 GeV to the AMS-02 e^+ measurement [103] are good. The uncertainty in pulsar lepton output was taken in the numerical description as a parameter $f_{N,i}$ for each pulsar, adjusted for best data description. **bold PS** are marked those dominating the high-energy population, grayed out PS are generally insignificant in this scenario.
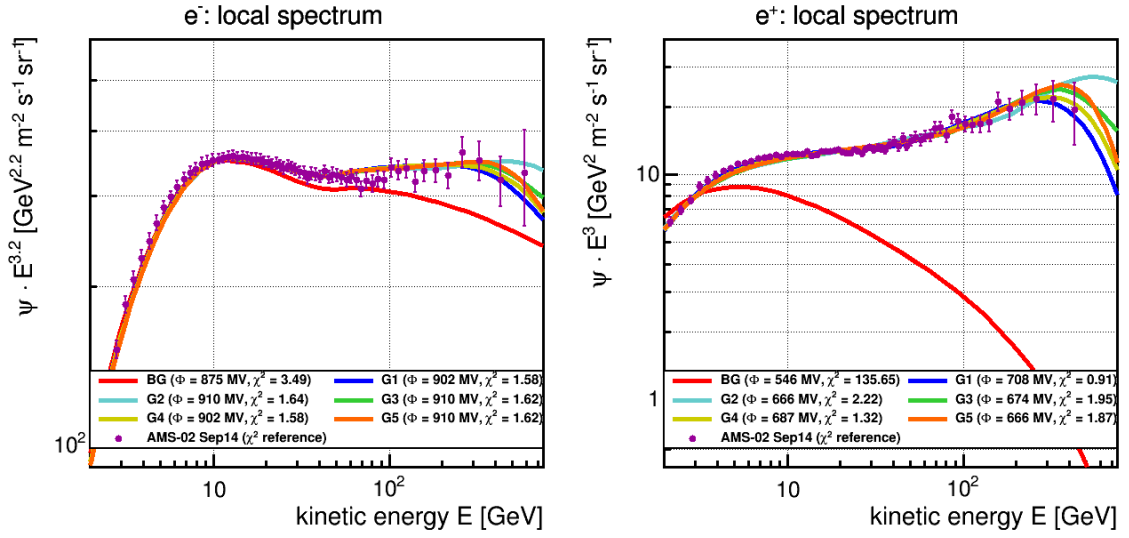
Figure 4.18. Left panel: The local e^- energy spectrum (scaled by $E^{3.2}$) is seen for the BG model (red), and the sum of BG plus the pulsar contributions in the five scenarios G1..G5. The high end of the AMS-02 e^- data [103] is well described, the overall χ^2 is given in the legend. This value depends on the assumption of primary electron injection in BG, which was not retuned in this case. Solar modulation is set to best fit. **Right panel:** The local e^+ energy spectrum (scaled by E^3) is seen for the BG model (red), and the sum of BG plus the pulsar contributions in the five scenarios G1..G5. The high end of the AMS-02 e^+ data [103] is well described, the overall χ^2 is given in the legend. Solar modulation is set to best fit.
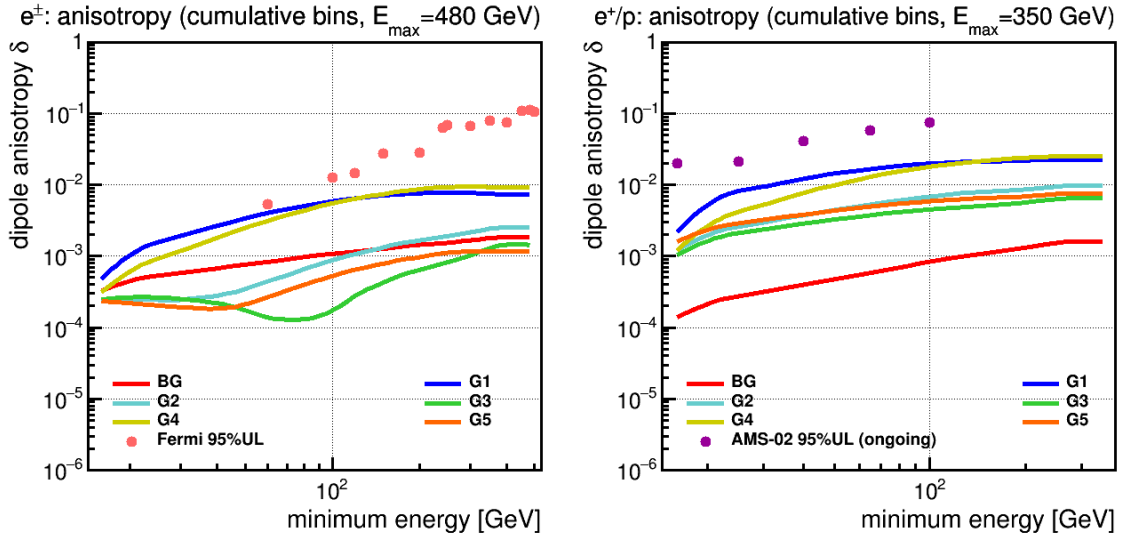
Figure 4.19. Predicted dipole anisotropy in the pulsar scenarios G1..G5, in the **left** panel for $e^\pm$ compared with Fermi-LAT upper limits, and in the **right** panel for e^+/p compared with AMS-02 upper limits. It is shown that all five pulsars are agreeing with the current limits, but G1 and G4 are generally more anisotropic than G2, G3 or G5. It is seen that for $e^\pm$, the pulsar addition does not lead to an overall increase in anisotropy description for G2, G3 and G5, as these are counteracting the anisotropy present in BG (stronger for electrons, thus not as visible in the e^+/p prediction).
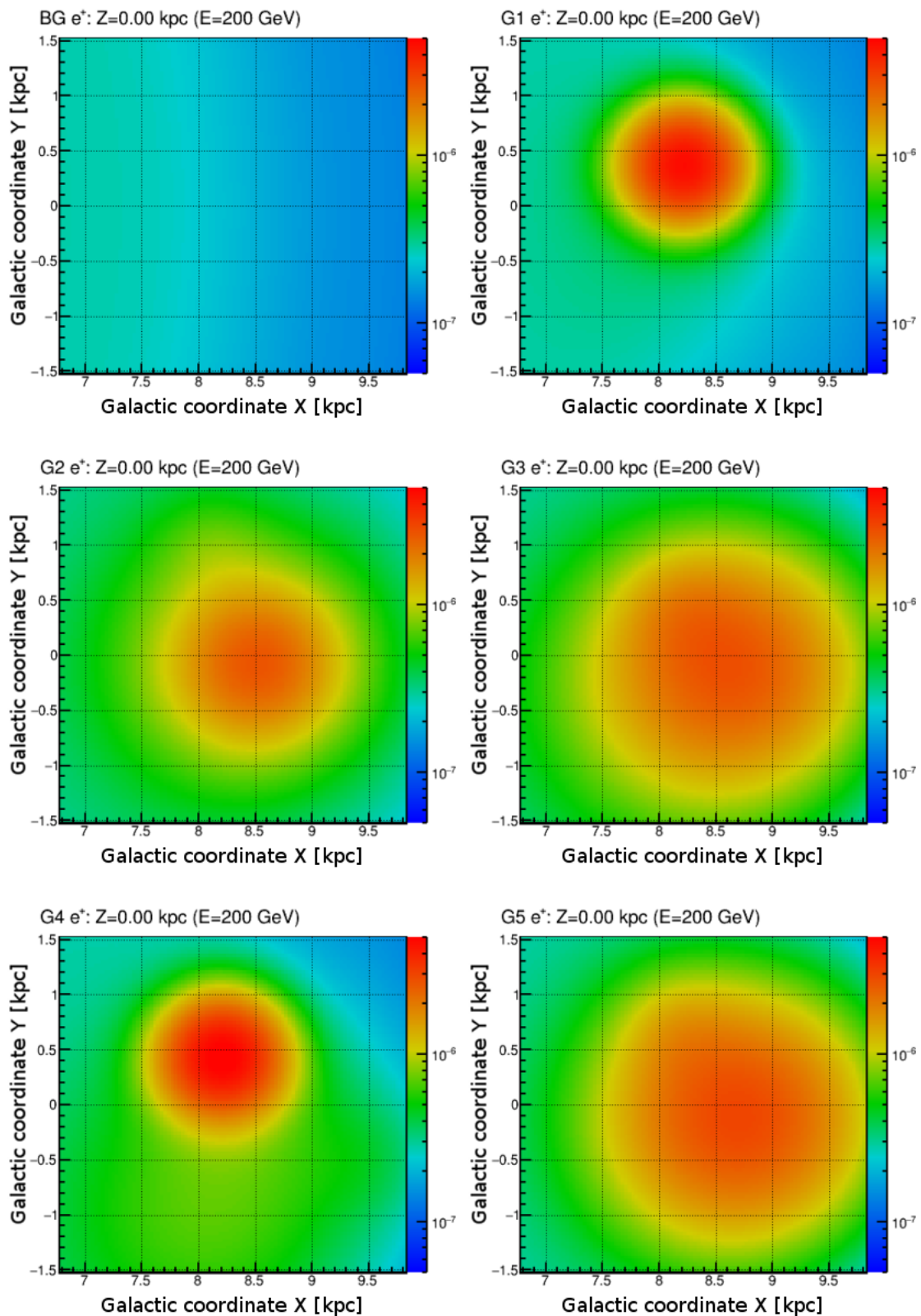
Figure 4.20. Density distributions of e^+ at $E = 200\,\text{GeV}$ in the galactic plane ($z = 0$). The background scenario is shown top left, then the G1..G5 scenarios follow in subsequent order. The models with a more stretched-out distribution, G2, G3 and G5, were showing a decrease in $e^\pm$ anisotropy in Fig. 4.19.

4.4.2. Pulsar scenarios in locally inhomogeneous transport models

Starting from Tab. 3.4, there are a few Local Bubble models compatible with the hadronic observable data, of which we choose the few, which cover a range of local environments. The study was performed on nearly all of these models, but to compactify the discussion, we pick one of each of the more basic setups, either with modified interior or modified wall properties, and none of the mixed A*,B* scenarios:

- **Interior scenarios:** C10g and c10g, the basic environments decreasing the local gas density, and in- or decreasing local diffusion coefficient, respectively. We add model C100, which leaves gas unchanged, but increases local diffusion by a factor 100 (this comes with a strong reduction in dipole anisotropy)

- **Wall scenarios:** d10 and D10, these do not leave much choice because most models are red, thus we will study the implications with these two scenarios which leave the gas density unchanged and modify the diffusion coefficient by a factor 10 down and up.

The summary of these models, from Tab. 3.4, is listed again in Tab. 4.4 below.

	Model	χ^2_p	$\chi^2_{\bar{p}/p}$	$\chi^2_{^{10}Be/^9Be}$	$\chi^2_{B/C}$	rel. $\delta_{p/p_{[40,80]}}$	rel. $\delta_{e^\pm}$	rel. $\delta_{e^+/p}$
	BG	**0.83**	**1.58**	**0.23**	**0.27**	**100%**	**100%**	**100%**
S.I.	c10g	0.78	0.97	0.13	0.32	16%	16%	23%
F.I.	C10g	0.81	1.34	0.14	0.25	300%	301%	272%
	C100	0.83	1.56	0.19	0.27	344%	345%	289%
S.W.	d10	0.85	1.75	0.90	0.39	64%	63%	70%
F.W.	D10	0.83	1.56	0.18	0.27	59%	59%	55%

Table 4.4. A revision of Tab. 3.4, this shows the five transport models we investigated for their impact on the pulsar scenarios. These models were in agreement with the hadronic observables, i.e. could be used without adjusting transport parameters. They already show large differences in predicted dipole anisotropies.

As the pulsar scenarios were constructed for the basic transport model with a flat diffusion coefficient, the same source scenario will not be expected to describe the local AMS-02 e^- or e^+ observation, when the local diffusion fluctuations are just "switched on" in these models. For the example of G1, Fig. 4.21 shows how the five chosen local modifications affect the two pulsars alone, spectra (left) and distributions (in Y direction at $E = 200\,\text{GeV}$, right). Significant changes in the spectra can be seen. The shapes of the Y profiles are similar to the effect each local setup showed on the primary particles (the presence of gas in C10g, c10g does not influence these high-energy particles notably, as we found out in chapter 3). The total effect of adding these local fluctuation models is then seen in the next Fig. 4.22, added on the corresponding background e^- (left) and e^+ (right).

As the pulsar contribution is relatively small for e^-, these local changes to not affect the overall data description in terms of χ^2 (to AMS-02 data). However, in this description the low-energy contribution of the electrons might have negative effects on χ^2 because

the error bars of the data are small there. This could always be improved by adjusting the primary injection spectrum in the background model, which we did not perform.
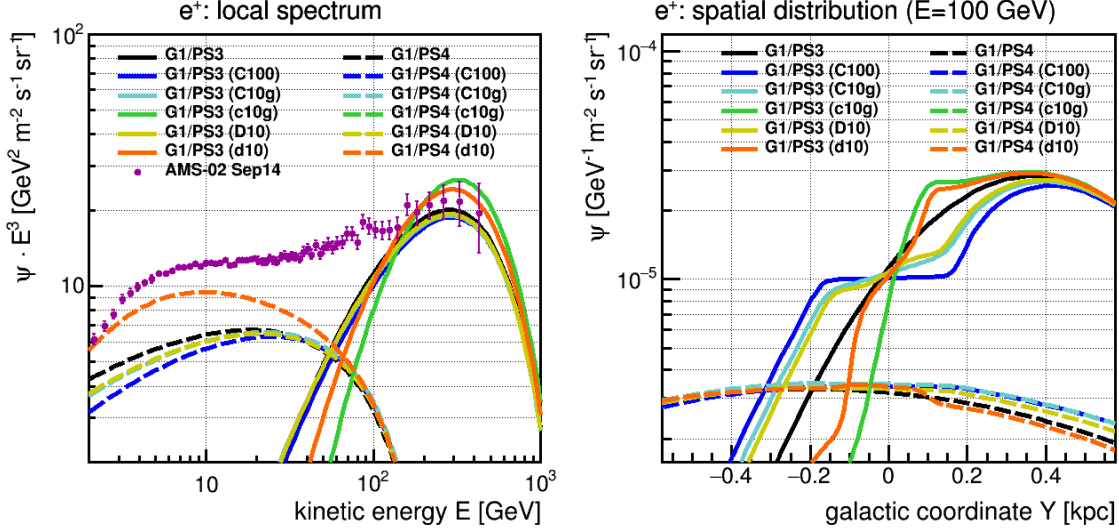
Figure 4.21. If the pulsar parameters are kept unchanged for a local transport model, the single pulsar spectra become affected differently. The **left** panel shows the energy spectra in e^+ (scaled with E^3) and the **right** panel shows the flux of e^+ at $E = 100\,\text{GeV}$ in y direction from the Sun. Solid lines refer to PS3, dashed lines refer to PS4. Black lines refer to the original scenario, the different colors refer to the five local bubble scenarios applied (see legend). This makes the case for pulsar retuning, which is described in the text.
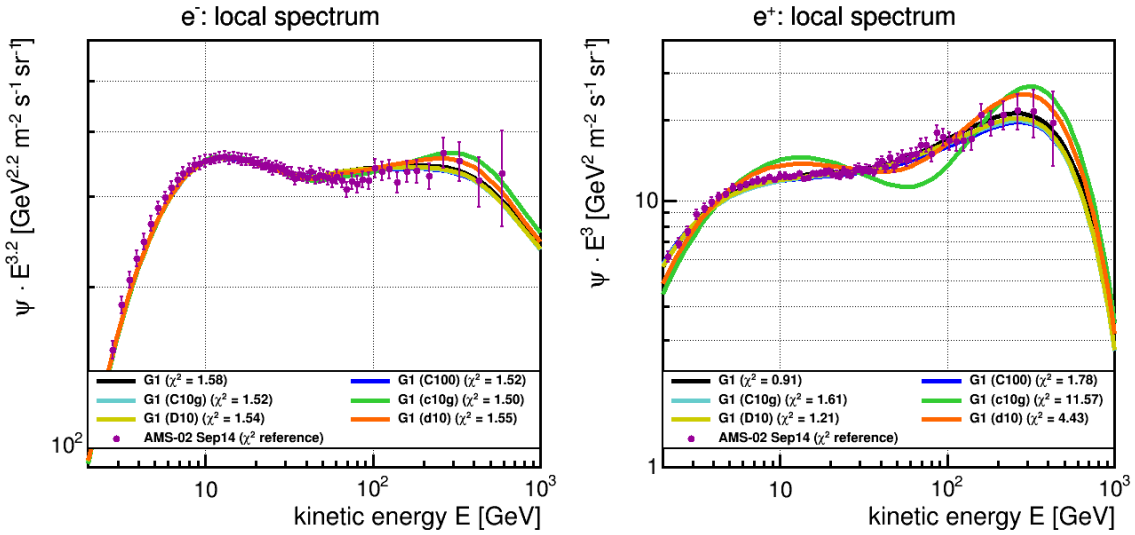
Figure 4.22. Similar to Fig. 4.21, but with the background added. AMS-02 data [103] is not well described anymore. The **left** panel shows the energy spectra in e^- (scaled with $E^{3.2}$) and the **right** panel shows the energy spectra in e^+ (scaled with E^3), for the reference model scenario (black) and the five local transport scenarios selected in Tab. 4.4.

The modification of transport properties re-shapes the local spectrum, as this lepton population now arrives at a sooner, or at a later, time, at Earth, having experienced less,

or more, interactions, emitting Synchrotron radiating and Inverse Compton. It is noted here that It is noted that the local variation of gas distribution is not relevant in this context, as our high-energy population does not see the gas, i.e. its energy loss is given by the magnetic field and photonic radiation alone, as described before). The difference in leptonic spectra by local gas modifications is thus only the difference in background leptons via the varied secondary production.

Now, it is suggestive to adjust the $(\Gamma_i, E_{\mathrm{cut}i})$ injection parameters in order to see whether the change in amount of energy loss can be compensated for. This involves large computation expenses, as for every choice of injection slope Γ_i and cutoff energy $E_{\mathrm{cut}i}$, and for every pulsar PSi involved, a DRAGON calculation has to be made. On our local machines, this means a runtime of ~ 2.5 h each with the algorithm settings required as explained above. In contrast with the quick optimization possible implementing the analytical approximation by our MINUIT optimization, this application would then make a slow-going scan through the parameter space necessary. This makes it necessary to seek more efficient ways of retuning, than a simple, e.g. randomized, parameter scan.

By virtue of the analytical expression (2.116), if a pulsar is sufficiently young $E \ll E_{\mathrm{max}} = (b_0 t_{\mathrm{age}})^{-1}$,

$$N(E, \vec{r}, t) = \frac{Q_0}{(\sqrt{\pi} R_{\mathrm{diff}})^3} \, (1 - E b_0 t)^{\Gamma - 2} \left(\frac{E}{1 \, \mathrm{GeV}} \right)^{-\Gamma} \cdot \exp\left(-\frac{E}{E_{\mathrm{cut}}} \frac{1}{1 - E b_0 t} \right) \cdot \exp\left(-\left(\frac{\vec{r} - \vec{d}}{R_{\mathrm{diff}}} \right)^2 \right)$$

$$(2.116)$$

$$\approx \frac{Q_0}{(\sqrt{\pi} R_{\mathrm{diff}})^3} \underbrace{\left(\frac{E}{1 \, \mathrm{GeV}} \right)^{-\Gamma} \cdot \exp\left(-\frac{E}{E_{\mathrm{cut}}} \right)}_{Q_{\mathrm{inj}}[\Gamma, E_{\mathrm{cut}}](E)} \cdot \exp\left(-\left(\frac{\vec{r} - \vec{d}}{R_{\mathrm{diff}}} \right)^2 \right) , \qquad (4.28)$$

so the injection spectrum does, to a certain degree, *factorize* out the propagated spectrum (R_{diff} is a function of energy, but not of injection parameters). In fact, this is sometimes (e.g. [Hooper 2008]) held as a generality. In our case, we see (Tab. 4.5) that it should hold for PS1, PS3, PS5 in our signal region, for PS4 with borderline value. For comparison, the highest energy bins by the AMS-02 measurement are, for e^+, 370-500 GeV (mean 426 ± 13 GeV) and, for e^-, 500-700 GeV (mean 589 ± 22 GeV).

Pulsar	PS3	PS5	PS1	PS4	PS2
age t_{age}	77 kyr	110 kyr	342 kyr	535 kyr	1.8 Myr
cooling break E_{max}	2945 GeV	2061 GeV	663 GeV	424 GeV	126 GeV

Table 4.5. The cooling break E_{max} is the maximum energy an infinitely energetic particle can have after a time t_{age}, due to Synchrotron and Inverse Compton energy losses. We compare these values for the different ages of our 5 selected pulsars.

Within validity thereof, the ratio between two *propagated* solutions, "NUM" and "DEN", comes close to the ratio between the *injection* spectra on their own, which takes the form

of a injection spectrum expression itself:

$$\frac{\text{NUM}[\Gamma_1, E_{\text{cut},1}]}{\text{DEN}[\Gamma_2, E_{\text{cut},2}]}(E) \approx \left(\frac{E}{1\,\text{GeV}}\right)^{-\Delta\Gamma} \cdot \exp\left(-\frac{E}{\tilde{E}_{\text{cut}}}\right) = Q_{\text{inj}}[\Delta\Gamma, \tilde{E}_{\text{cut}}](E) \tag{4.29}$$

with

$$\Delta\Gamma = \Gamma_1 - \Gamma_2 \tag{4.30}$$

$$\frac{1}{\tilde{E}_{\text{cut}}} = \frac{1}{E_{\text{cut},1}} - \frac{1}{E_{\text{cut},2}} \quad \Rightarrow \quad \tilde{E}_{\text{cut}} = \frac{E_{\text{cut},1}E_{\text{cut},2}}{E_{\text{cut},2} - E_{\text{cut},1}} \tag{4.31}$$

If (4.29) also holds for models with locally modified diffusion parameters - that is, the shape shift from the local diffusion setup does, for a given pulsar, not significantly depend on (Γ, E_{cut}) injection parameters. For this purpose, we demonstrate our technique in Fig. 4.23: we selected one of the most extreme bubble setups investigated in the last chapter, A100, and compared two exemplary runs - one test with the second oldest pulsar of our set, PS4, another with the oldest pulsar PS2, by directly evaluating their ratio. A χ^2-like variable was defined as in (4.32), i.e. a pure spectral shape $Q_{\text{inj}}[\Delta\Gamma, \tilde{E}_{\text{cut}}](E)$ with two free parameters was fitted to the ratio.
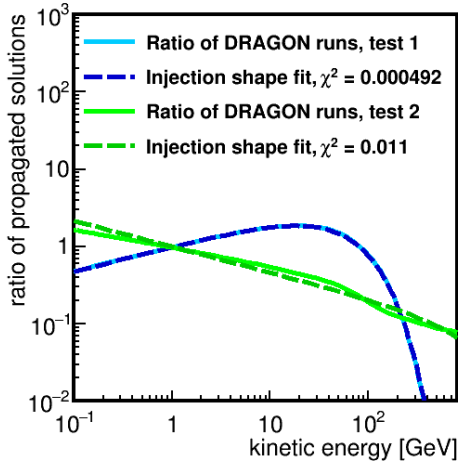
$$\chi^2 = \frac{1}{\#\text{E.bins}} \sum_{E_i} \frac{\frac{\text{NUM}}{\text{DEN}}(E_i) - Q_{\text{inj}}[\Delta\Gamma, \tilde{E}_{\text{cut}}](E_i)}{\frac{\text{NUM}}{\text{DEN}}(E_i)} \tag{4.32}$$

A100 model tests		definition		expectation		fit results		
		Γ_{inj}	$E_{\text{cut, inj}}$	$\Delta\Gamma$	$\tilde{E}_{\text{cut}}$	$\Delta\Gamma$	$\tilde{E}_{\text{cut}}$	χ^2
test 1 (G1 PS4)	NUM	2.00	300 GeV	0.32	60.0 GeV	0.3227	57.0 GeV	$4.92 \cdot 10^{-4}$
	DEN	1.68	50 GeV					
test 2 (G2 PS2)	NUM	1.758	9.98 TeV	-0.242	309.3 GeV	-0.3341	1688.4 GeV	$1.15 \cdot 10^{-2}$
	DEN	2.00	300 GeV					

Figure 4.23. We present the method suggested to perform pulsar injection retuning efficiently, i.e. without having to call the numerical DRAGON code for every assumption of Γ, E_{cut}. The method is described in the text and only needs one DRAGON evaluation. It works especially well for younger pulsars (blue in the example figure), but is also applicable for older ones (green in the example figure)

To conclude, this fit went astonishingly well. The second test did not perform as smoothly, which was supposable considering its low cooling break $E_{\text{max}} = 126\,\text{GeV}$. This is acceptable, as PS2 (see Figs. 4.7-4.11 and Tab. 4.3) always a kind of auxiliary contribution for the medium energy population. It overlaps with the solar modulation region and can, due to its age, never contribute to the rising positron population at higher energies.

Tests with the other, younger sources showed good agreement with the test 1. It is then possible, for a given Local Bubble scenario and given G1..G5 pulsar distribution, to reduce computation time to one sample propagation in DRAGON. The result can then, with a set of free parameters $(\Delta\Gamma_i, \tilde{E}_{\text{cut},i})$ for each pulsar, legitimately re-shaped to optimize data description. Therefore we implemented a new MINUIT optimization routine. In order to keep the total source power of each pulsar constant, the normalization factor C is then, in every case, rescaled according to the retuned injection spectra

$$C \longrightarrow C \times \frac{\int dE\, E \cdot Q_{\text{inj}}(E)\Big|_{\text{original scenario}}}{\int dE\, E \cdot Q_{\text{inj}}(E)\Big|_{\text{retuned scenario}}} \tag{4.33}$$

As a crosscheck, another DRAGON model was then computed, using the injection spectrum determined this way. For reasons of reproducibility, it might be noted that the MINUIT optimization for the E_{cut} parameter performed much better if the fitting routine is not directly set up to adjust E_{cut} inside $[E_{\text{cut}}^{\text{min}}, E_{\text{cut}}^{\text{max}}]$, starting with original value $E_{\text{cut}}^{\text{orig}}$. Instead, it is passed $\kappa \in [0, 1]$ with

$$E_{\text{cut}} = \left(\frac{1}{E_{\text{cut}}^{\text{min}}} \left(\frac{E_{\text{cut}}^{\text{max}}}{E_{\text{cut}}^{\text{min}}} \right)^{-\kappa} - \frac{1}{E_{\text{cut}}^{\text{orig}}} \right)^{-1} . \tag{4.34}$$

this is due to the nonlinear behavior of the $\exp\left(-E/E_{\text{cut}}\right)$ behavior and the innately decreased performance of MINUIT at interval borders.

Model evaluation

The results of applying this routine to the models C10g, C100, c10g, D10, d10 is given in the next section. The goal of the optimization was the model description of the AMS-02 e^+ flux. These were models in which our routine worked very well. As in the previous chapter, we will now demonstrate it for one model, and refer to appendix A.6 for the full details.

As the BG was designed this way, the e^- measurement of AMS-02 could be described similarly well to the e^+ flux. To recall: At the beginning of our study, we tuned the primary e^- injection for the BG model in such a way, that it describes the AMS-02 e^- data *minus* the e^+ signal component. While in principal, this might lead to slight deviations in models of increased secondary production - because the *pi* and K decays are not entirely charge-symmetric - this is expected to be negligible compared to the the total e^- flux. The primary pulsar injections themselves are taken equal in in e^- and e^+. The overall e^- description thus gives not an independent description or constraint, it is only shown for reference.

Below, we then compare the impact of the five chosen local transport models on the model prediction of $\delta_{e^\pm}(60..480\,\text{GeV})$ and $\delta_{e^+/p}(16..350\,\text{GeV})$, relative to the unmodified G1..G5 pulsar scenarios.

For demonstration, we choose the model C100. The corresponding modification curve for diffusion coefficient is shown in Fig. 4.24 (it is a drop $D \to \frac{1}{100}D$ spherically symmetric around the Sun and the gas distribution is unchanged).

For this model, the total retuned electron and positron spectra are plotted in Fig. 4.26, together with the C100 background prediction (no pulsars, black line). χ^2 values in the legend refer to the full, solar-modulated spectrum each. For comparison with the original injection spectra on the no-bubble BG model, Tab. 4.6 gives both $\chi^2_{>10\,\text{GeV}}$ for each scenario. The left part of this table is replication of Tab. 4.3, while the retuned injection parameter are visible to the right. While in many cases only minor changes occur, there are occasions in which a pulsar assumes a very different shape. This is especially remarkable in **bold-faced** pulsars (second column), which are these pulsars that played a dominant role in the high-

Figure 4.24. The functional shape of Local Bubble model C100. Interior diffusion is fastened by a factor 100, the gas density is unchanged. The Walls are not accounted for. The y-axis shows the factor applied to diffusion (blue) and to gas (orange), the x-axis the distance to the Sun in pc. This model bubble is spherically symmetric.

energy component. The signal decomposition into signle pulsar signals is demonstrated in Fig. 4.25, both before and after the C100 modification was applied. Note that this is a composite effect from the effect of C100 on the background e^+ component and its effect on the single pulsar spectra.

Ultimately, this showcases the flexibility in choosing a pulsar explanation for the energetic positron contribution. Unless injection parameters were further restricted by observation or astrophysical, theoretical arguments, a great number of pulsar combinations can be found, resulting in low-χ^2 electron and positron description. These are shown (Tab. 4.6, rightmost column) to be below 0.6 in every pulsar scenario, for this local diffusion setup. It is remarked that in extreme scenarios like c100g, it did not work for every scenario to achieve a good description over the whole $E = 10..500\,\text{GeV}$ range. It could then be showed, that a loosening of retuning restriction $\Gamma \in [1,2] \to [0.5; 2.5]$ could, again, result in well described e^+ data.

Scenario	Pulsar	d	original Γ_i	$E_{\text{cut},i}$	$\chi^2_{\geq 10\,\text{GeV}}$	retuned Γ_i	$E_{\text{cut},i}$	$\chi^2_{>10\,\text{GeV}}$
G1	**PS3**	380 pc	1.387	322 GeV	0.381	1.370	313 GeV	0.390
	PS4	203 pc	1.978	105 GeV		2	100 GeV	
G2	PS1	180 pc	1.404	922 GeV		1.021	339 GeV	
	PS2	150 pc	1.992	931 GeV		2	106 GeV	
	PS3	990 pc	1.993	100 GeV	0.840	1.916	112 GeV	0.571
	PS4	500 pc	1.956	102 GeV		2	4.95 TeV	
	PS5	250 pc	1.067	1.21 TeV		2	107 GeV	
G3	**PS1**	400 pc	1.273	775 GeV		1	4.24 TeV	
	PS2	207 pc	1.949	100 GeV		2	100 GeV	
	PS3	400 pc	1.152	2.25 TeV	0.688	1	240 GeV	0.400
	PS4	400 pc	1.843	511 GeV		2	100 GeV	
	PS5	400 pc	1.098	2.23 TeV		1	102 GeV	
G4	PS1	280 pc	1.957	199 GeV		2	100 GeV	
	PS2	440 pc	1.991	100 GeV		2	5.0 TeV	
	PS3	440 pc	1.131	312 GeV	0.445	1	218 GeV	0.427
	PS4	1020 pc	1.242	103 GeV		2	9.5 TeV	
	PS5	1390 pc	1.976	137 GeV		1.996	140 GeV	
G5	**PS1**	432 pc	1.407	1.18 TeV		1.650	7.92 TeV	
	PS2	150 pc	1.989	102 GeV		1.998	8.47 TeV	
	PS3	700 pc	2	100 GeV	0.636	1.446	170 GeV	0.405
	PS4	360 pc	2	100 GeV		2	100 GeV	
	PS5	1560 pc	2	100 GeV		1	373 GeV	

Table 4.6. Injection spectrum retuning is necessary between the galactic transport model BG and local models with modified transport conditions. We show the original No-Local-Bubble values from Tab. 4.3 again (left), and in the C100 model the adjusted parameters (right), using the routine described in the text. This shows that description of the AMS-02 positron measurement [103] is also possible in local transport models within the usual uncertainties of pulsar scenarios. Each χ^2 value is given for $E > 10\,\text{GeV}$. Marked as **bold PS** are those that dominate the high-energy population in the reference model, grayed out PS the generally insignificant ones, for each scenario. By spectral shape or overall normalization, these can gain or lose importance when the local diffusion model is considered.

Due to the enhancement of local diffusion coefficient by a factor 100, the different pulsars contributions in this scenario play a distinctive role for the compatibility of dipole anisotropy with the present measurements. It is seen in Fig. 4.27 that for C100 the scenarios G1, G4 and G5 are in conflict at least with one of the Fermi-LAT ($e^{\pm}$) and AMS-02 (e^+/p) anisotropy 95% CL upper limits. It is remarkable that this rise in anisotropy δ is indeed merely given from the local value of the diffusion coefficient, or mean free path length, and not due to a large local gradient in CR density distribution - as seen in Fig. 4.4.3, where the local positron distributions, at $E = 200\,\text{GeV}$, in X and Y directions around the sun, are shown to be remarkably flat. As will be demonstrated below, the models with locally reduced D_0 (i.e. "opposite" assumption) do show large gradients in density but result in a

considerably smaller dipole anisotropy. This reinforces that, somewhat counterintuitively, the large-scale CR density gradient is not decisive in determining the local anisotropy.
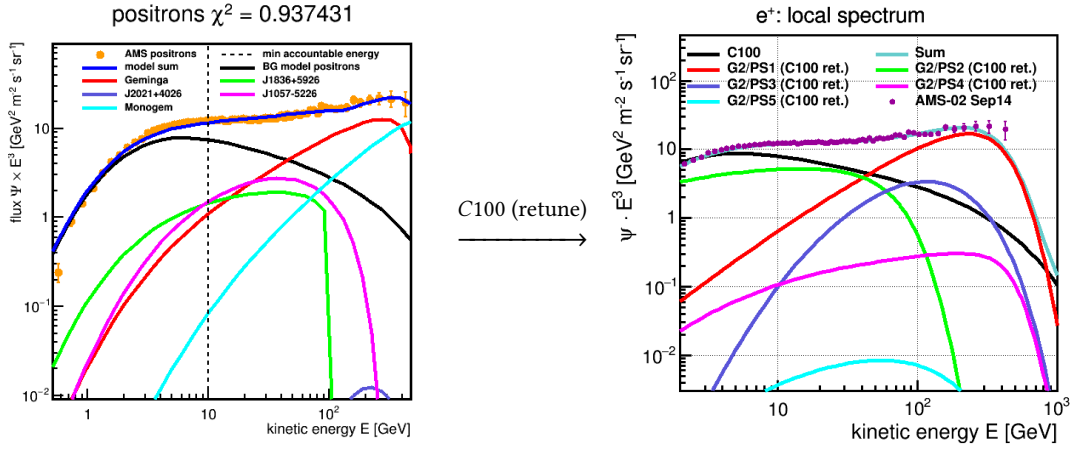
Figure 4.25. Pulsar retuning when a local diffusion model is considered (here for the case of the G2 scenario and the C100 local diffusion model). Positron energy spectra (scaled with E^3) are shown for G2 in the **left** panel for the reference BG model (without Local Bubble assumptions), and in the **right** panel with the C100 local diffusion assumptions. The injection parameters are then changed in order to achieve best description of the AMS-02 positron data [103], and their choice can heavily differ between the particular pulsar contributions. For example, PS5 (Monogem) is very present in the high-energy range in the reference setup (left), but not after retuning (right).
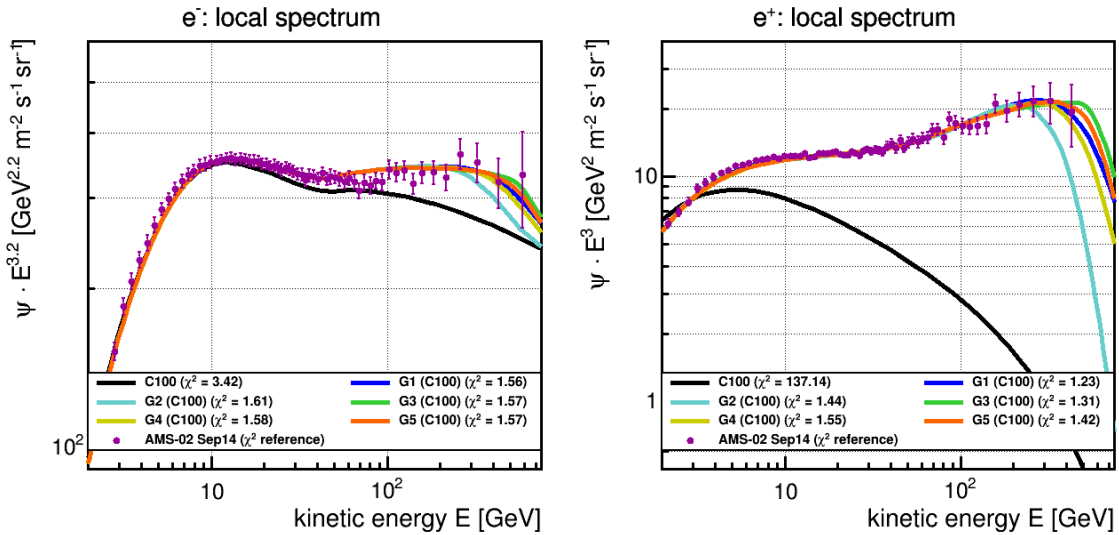
Figure 4.26. After retuning pulsar injection parameters, the C100 model shows good agreement with the AMS-02 measurements [103] again: The **left** panel shows the e^- energy spectrum (scaled with $E^{3.2}$) and the **right** panel shows the e^+ energy spectrum (scaled with E^3). It shows the background contribution (black), and the five different pulsar scenarios G1..G5 (colored lines).
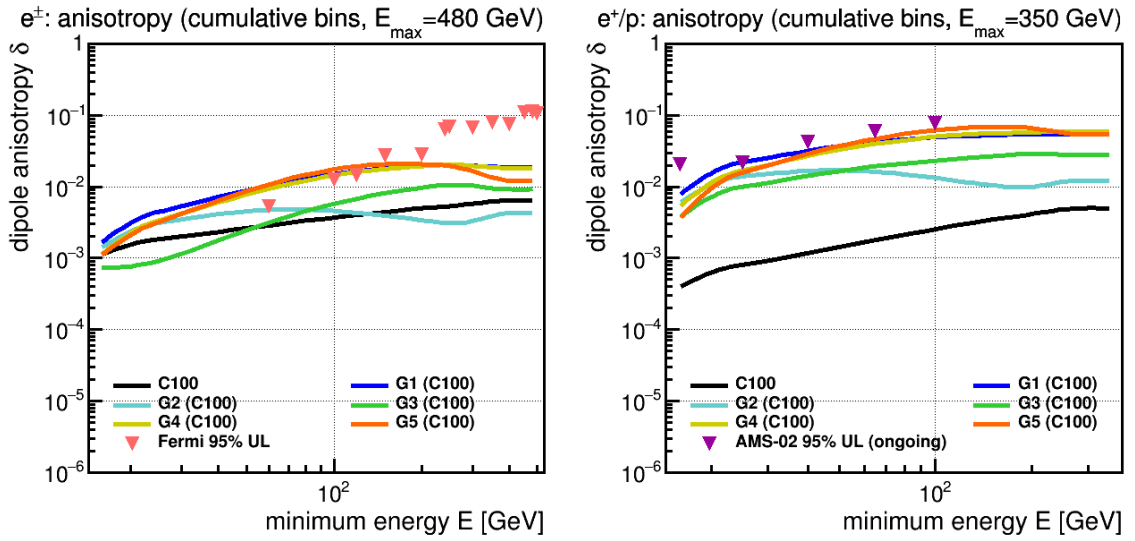
Figure 4.27. As Fig. 4.26; Showing, after pulsar injection retuning, the predicted dipole anisotropy in the **left** panel for $e^{\pm}$ in agreement with Fermi-LAT [125] limits, and in the **right** panel for e^+/p in agreement with AMS-02 [99] limits.
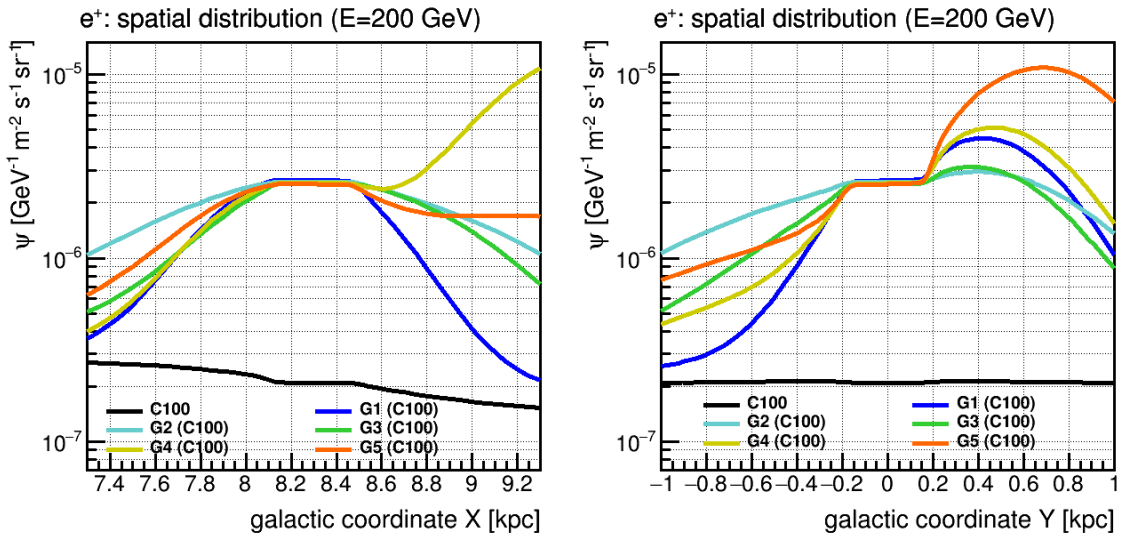
Figure 4.28. As Fig. 4.26; Showing, after pulsar injection retuning, the predicted e^+ distribution at $E = 200$ GeV, in the **left** panel in x and in the **right** panel in y (right) direction through the solar position at $(8.3, 0, 0)$ kpc.

In general, a rather good description of the AMS-02 e^- and e^+ measurements is possible in the less extreme diffusion setups. Details of the models c10g, C10g, D10, d10 are found in appendix A.6.

4.4.3. Impact on leptonic dipole anisotropies

Quantitatively, we summarize the effect of our local diffusion models on both of the considered leptonic dipole anisotropies, $\delta_{e^{\pm}}(60..480\,\text{GeV})$ (Tab. and $\delta_{e^{+}/p}(25..350\,\text{GeV})$, cumulated over the energy range corresponding to the most constraining intervals from the $e^{\pm}$ Fermi-LAT measurement and the current e^{+}/p AMS-02 analysis, respectively. We display each value as relative change, compared to the corresponding reference model, i.e. the model without any local diffusion assumptions).

This evaluation allows three conclusions:

1. Raising the very local diffusion coefficient endangers compatibility with the experimental limits (marked as red in Tab. 4.7). The Fermi-LAT upper limits on $\delta_{e^{\pm}}(60..480\,\text{GeV})$ are in disagreement with every pulsar scenario in the C10g case. Generally, the local rise in anisotropy due to a local enhancement of diffusion coefficient seems critical. However, increasing the diffusion coefficient *somewhere else*, as in D10, is not indicative for the anisotropy prediction in whether to rise (as for G3) or to drop (other scenarios).

2. Due to the (non-pulsar) background, the electron component gets affected differently than the positron component. The predictions for $\delta_{e^{\pm}}(60..480\,\text{GeV})$ and $\delta_{e^{+}/p}(25..350\,\text{GeV})$ do not show the same behavior in every case. For example, the G3 scenario with c10g diffusion model leads to a local rise of 250% in $\delta_{e^{\pm}}(60..480\,\text{GeV})$, but a local drop to 26% in $\delta_{e^{+}/p}(25..350\,\text{GeV})$. The difference, i.e. the electron distribution that only influences $\delta_{e^{\pm}}$, was not investigated yet but emphasizes the point that the local electron distribution needs to be understood *independently* from the local positron distribution.

3. Generally, no correlation can actually be made between the properties of the local diffusion setup (characterized by the value in the BG column) and the source scenario of local point sources (characterized by the G1..G5 columns). Without any understanding of the local diffusion coefficient, the anisotropic component in CR flux can, under reasonable assumptions, be predicted almost arbitrarily. This is in contrast to the common assumption that the correlation $\delta \propto |\nabla N|/N$ allows for model constraining.

	$\delta_{e^\pm}$ (60..480 GeV)					
	no pulsars	G1	G2	G3	G4	G5
C100	345 %	261 %	1013 %	2568 %	298 %	4053 %
C10g	301 %	252 %	1231 %	6209 %	319 %	6334 %
c10g	16 %	4 %	71 %	415 %	39 %	250 %
D10	59 %	52 %	45 %	1394 %	47 %	619 %
d10	63 %	91 %	220 %	2066 %	94 %	923 %

	$\delta_{e^+/p}$ (25..350 GeV)					
	no pulsars	G1	G2	G3	G4	G5
C100	296 %	279 %	530 %	475 %	408 %	530 %
C10g	298 %	263 %	451 %	784 %	407 %	876 %
c10g	22 %	1 %	45 %	64 %	67 %	26 %
D10	56 %	57 %	62 %	144 %	62 %	79 %
d10	68 %	123 %	161 %	271 %	140 %	100 %

Table 4.7. Summary: Relative change on the background ("no pulsars" column) alone and impact of the local diffusion models on the dipole anisotropy prediction of the five chosen pulsar scenarios (G1..G5 columns). Values are shown relative to the reference diffusion scenario with no local modification. Red marked are models in conflict with the experimental upper limit, from Fermi-LAT for $e^\pm$ and from AMS-02 for e^+/p.

To further show that a strong gradient in density does not necessarily mean a large anisotropy, we illustrate models c10g more closely, see density distribution at $E = 200$ GeV in Fig. 4.29. Due to the Slow-Interior diffusion $D_0 \rightarrow \frac{1}{10}D_0$ as well as Interior gas density reduced by a factor $n_H \rightarrow \frac{1}{10}n_H$ (which causes stronger secondary production more asymmetrical around the sun), in contrast to the very flat structure for C100 (Fig.). The dipole anisotropy predictions are shown in Fig. 4.30) and are all in agreement with the current experimental upper limits. Again, this stresses the point that the knowledge of the diffusion coefficient in our local environment is more crucial to understanding the low dipole anisotropy in cosmic ray flux than then knowledge of the source distribution.

One of the natural next steps could be, to investigate a range of difference background reference models in this context. This has not yet be done, and also would only be one approach in order to fully investigate the role of the Local Bubble in the observation of a cosmic ray dipole anisotropy. To conclude, we see that the uncertainties about the background distribution (given by the choice of reference model), the local diffusion model (C100, C10g, c10g, D10, d10) and CR source scenario (G1,G2,G3,G4,G5) allow for a very broad range of anisotropy predictions. The assumptions entering this study in every step come to play together and demonstrate, how little could actually be inferred from an observation of a CR dipole anisotropy in this energy range.
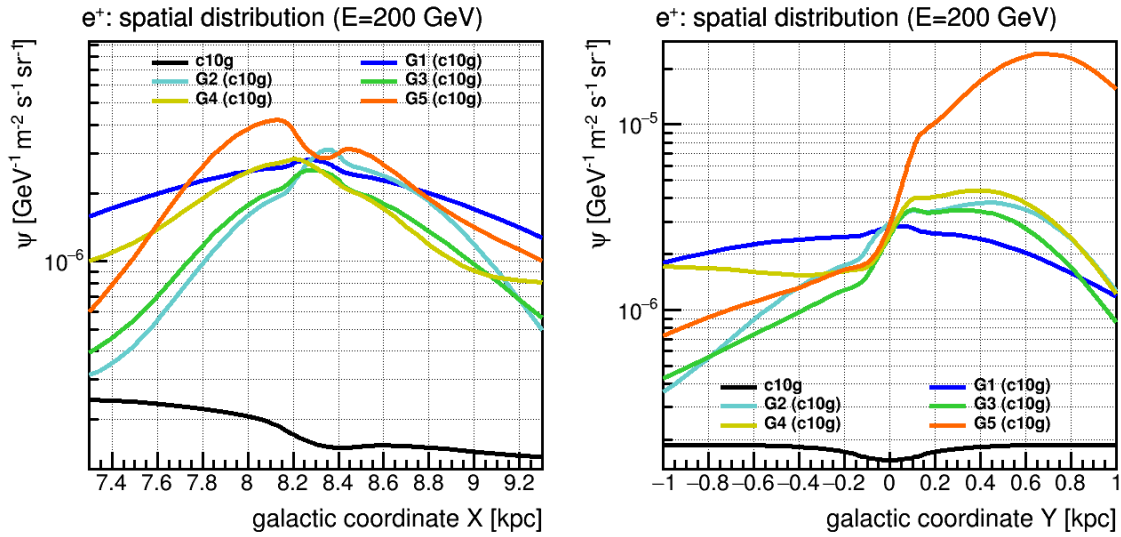
Figure 4.29. For LB model c10g: The distribution of e^+ at $E = 200$ GeV shows the reason of the data conflicting predictions in Fig. 4.27. As shown in the **left** panel for the x and in the **right** panel for the y direction through the solar position, this model assumption are producing large density gradients.
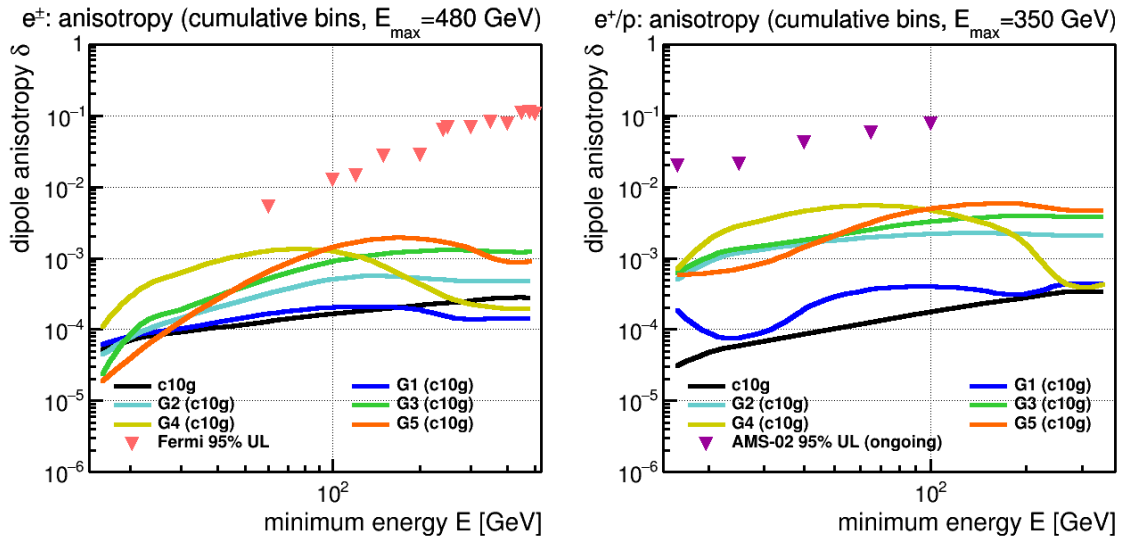
Figure 4.30. For LB model c10g: The predicted dipole anisotropy in the **left** panel for $e^\pm$ and in the **right** panel for e^+/p. They are in agreement with the respective Fermi-LAT and AMS-02 [99] limits.

Finally, one comparison with the current AMS-02 measurement can be done in order to demonstrate the total uncertainty within these assumptions. From the pulsar model estimation of [148] (see Fig. 4.3), a dipole anisotropy in e^+/e^-, *positrons over electrons*, is inferred at $\delta_{e^+/e^-}(16..350\,\mathrm{GeV}) \approx 1\%$. This can be compared with the projected dipole measurement by the AMS collaboration, which estimates[4] until 2022, this value of δ_{e^+/e^-} will lie inside the 1σ (68.3% CL) limit of an isotropic e^+/e^- measurement. A pulsar as the Geminga-like one in [148] (see Fig. 4.3) is not to be measured or excluded before. We can compare this with the δ_{e^+/e^-} values that result from our five pulsar scenarios, in our five chosen local transport models, and the reference model BG. Tab. 4.8 states these *absolute* $\delta_{e^+/e^-}(16..350\,\mathrm{GeV})$ values for direct contrast, which are in every case well below the 1% limit. The e^+/e^- dipole anisotropy therefore does not pose a strong constraint for further model exclusion (it is, in fact, for our models weaker than the Fermi-LAT $e^\pm$ limits or the AMS-02 e^+/p limit from [99].)

| | $\delta_{e^+/e^-}(16..350\,\mathrm{GeV})$ | | | | |
	G1	G2	G3	G4	G5
BG	0.209%	0.096%	0.081%	0.105%	0.135%
C100	0.747%	0.573%	0.294%	0.489%	0.336%
C10g	0.656%	0.327%	0.466%	0.467%	0.579%
c10g	0.018%	0.046%	0.055%	0.068%	0.052%
D10	0.148%	0.066%	0.069%	0.069%	0.078%
d10	0.275%	0.180%	0.149%	0.145%	0.134%

Table 4.8. Absolute values for the predicted e^+/e^- anisotropy in our five pulsar scenarios, in the five chosen local transport models and the reference BG model.

---

[4]Private communication with I. Gebauer.

4.4.4. Temporal evolution of dipole anisotropy from a pulsar-like source

We finish this topic with a further remark, how the anisotropy prediction changes with time. This happens over kiloyear scales and is therefore not expected to be observable soon. An important distinction has to be made in this case, as it is not universally accounted for in the literature that the pulsar source injection is *burst-like*, with a $\delta(t)$ time dependence, rather than being constant in time and solved in the stationary-state solution.

In our current understanding, for SNRs and PWNe [41] alike the diffusive shock acceleration process is likely to be efficient in particular when the CR particles are trapped inside the shocked region until the whole structure dissolves. For hadronic CR particles primarily injected in SNRs, this distinction is not necessary. With a typical SNR lifetime of $\sim 100\,\mathrm{kyr}$ and galactic SN frequency of $\sim \frac{1..3}{100\,\mathrm{yr}}$, the injection happens at a rate way faster than e.g. the CR residence time $\tau_\mathrm{esc} \sim 10\,\mathrm{Myr}$ inferred from $^{10}Be/^9Be$ observation. Then, it is likely not required to precisely resolve the single remnants in propagation models. The solution of the transport equation in *steady-state* is well justified for this scenario, while it cannot be applied for a burst-like source behavior $\sim \delta(t)$ (which would gradually reduce to zero in steady-state, due to the free escape boundary conditions), or generally when the temporal evolution between the injection bursts is significant.

For our pulsar studies, we specifically disabled the source injection after a characteristic decay time $\tau = 1\,\mathrm{kyr}$, and then chose the number of time step repetitions in the solver algorithm of DRAGON to exactly match the assumed pulsar age (described above). As this was our own modification, caution has to be made when comparing different publications, i.e. whether this is distinctly accounted for or neglected.

The importance of a correct temporal source description arises for leptons, whose strong energy losses between two primary injection bursts, be it by SNR, PWN or otherwise, might violate the steady-state assumption in general. For our pulsar scenarios, this makes the correct estimation of the injection time, i.e. the pulsar age, crucial.

We shed light on this issue by direct comparison of one point source that we evaluate in certain time steps after their injection. This will be done for one burst-like, $\delta(t)$, source, and one source constant in time. Fig. 4.31 shows the time evolution of e^+ density from a PS3-like source, centered at $\vec{r} = (8.222, 0.372, 0.014)\,\mathrm{kpc}$, in galactic y direction for $x = 8.222\,\mathrm{kpc}$, $z = 0.014\,\mathrm{kpc}$ (i.e. in y distance from the source point. The sun position is then close to $Y = 0$ in this graph, the actual age of this pulsar is $t_\mathrm{age} = 77\,\mathrm{kyr}$, the bright red line in each plot. While the solution from a constant injection always has a rather steep local gradient, due to the permanent afterflow from the source, the more realistic burst-like solution flattens out over time. A very close pulsar is therefore not necessarily strongly isotropic in positron flow, if the diffusion process since their injection already smeared. This direct contrast has to be heavily emphasized in making predictions for leptonic dipole anisotropies $\delta \propto |\vec{\nabla}N|/N$.

The constant-t solution is, for each time step, the temporal integral over $\delta(t)$ bursts in every time step before (as these are nearly Green's functions to the transport equation.) This is also clear from the spectra, Fig. 4.32: Older constant-time solutions do not show the cooling breaks as they are mixed with particle populations injected more recently,
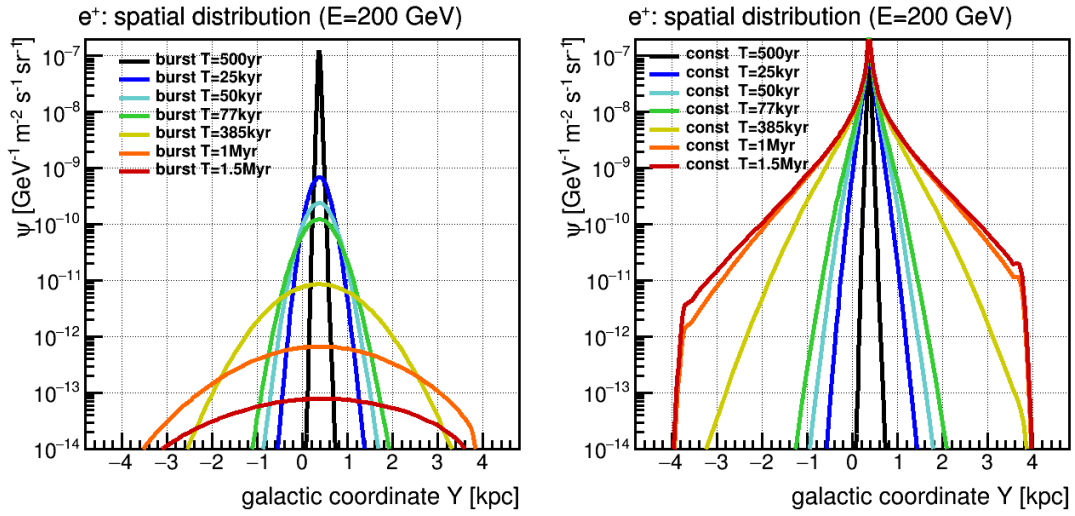
Figure 4.31. The correct burst-like time dependence has to be regarded for numeric pulsar scenario predictions. This is hereby illuminated as important, because as opposed to a source injection constant in time, the burst-like solution is much flatter locally. For a single PS3-like source, the **left** panel shows the y distribution (through the source) for burst-like $\delta(t)$ injection and the **right** panel shows the y distribution (through the source) for time-constant injection. The local dipole anisotropy is correlated to the relative density gradient $\vec{\nabla}N/N$ or flux gradient $\vec{\nabla}\psi/\psi$ at $y = 0$. Especially for old pulsars, the difference in gradient is significant.

yielding a local spectrum much broader in energy range. It can be recalled, again, that the energetic positron population does show a smooth structure, so it is unlikely to consist of multiple contributions of old (burst-like) sources.
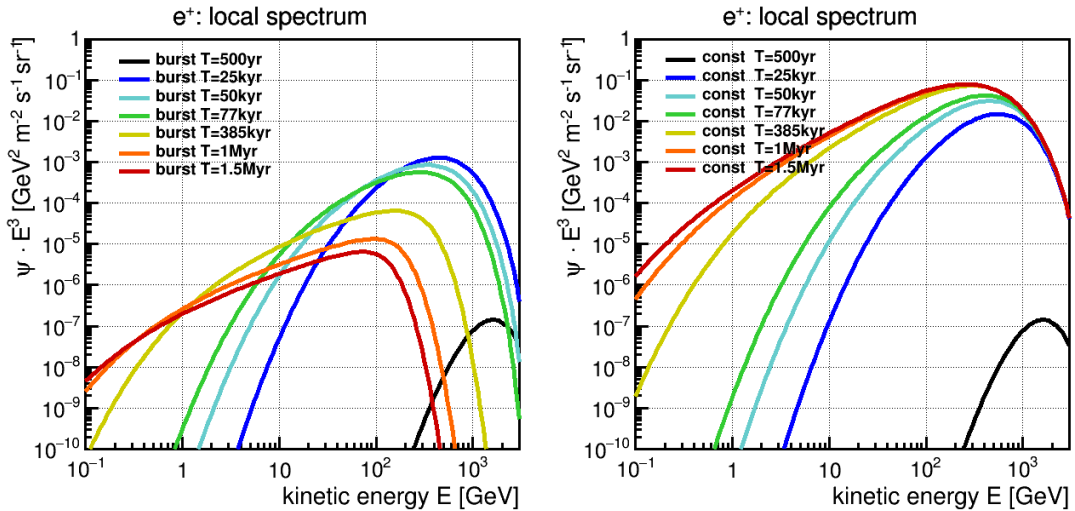
Figure 4.32. The correct burst-like time dependence has to be regarded for numeric pulsar scenario predictions, cf. Fig. 4.31. Shown here are the local spectra (scaled with E^3) of positrons, for a PS3-like source, in the **left** panel for burst-like and in the **right** panel for time-constant source injection. The overall normalization is arbitrary here. This illuminates the difference in spectral shapes. It is an important aspect to account for when comparing different literature, because numerical codes do not treat the $\delta(t)$ burst-like time injection of a pulsar automatically.

4.5. Conclusion

In a in-depth study, we found that the current *pulsar hypothesis* can explain the positron excess in AMS-02 data [103]. We show that it is very easy to construct a scenario with realistic assumptions of five surrounding pulsars. that are treated as burst-like point sources. As currently the realistic assumptions allow for a very wide range of possibilities, such models can not be constrained very tightly. We construct five scenarios that are all viable explanations for the observed positron fluxes, and by the method described, many more such scenarios could be produced.

It has been claimed that the detection of a electron or positron anisotropy could lead to the confirmation or exclusion of the pulsar hypothesis. We conclude that this *does not have to be true.* For one reason, the pulsar addition in some scenarios could be seen to counteract the background anisotropy. We regard such a scenario as coincidental. For the other reason, the impact of the Local Bubble on the transport processes of cosmic rays is not understood.

As seen in chapter 3, this allows for large ambiguity in predictions of dipole anisotropy. We show that in models of locally modified transport parameters, it is still possible to describe the observed positron fluxes. We see that in our exemplary local transport models, the predicted anisotropy in leptonic sum flux can vary between a factor 0.04 and 25.68, without violation of the current upper limits. In some local models, the anisotropy prediction is in conflict with the data, for at least some source scenarios.
This is neither an exclusion for these model assumptions, nor an exclusion for these source assumptions. It shows how closely linked the uncertainties in both local diffusion and leptonic sources are.

The uncertainty of the Local Bubble transport is not only interesting in a way that specific assumptions could account for the reduction of an otherwise large gradient in CR density (isotropization). We also find, that under other assumptions the local CR densities show increased gradients over an otherwise smooth distribution. This contradicts the assumption, that a DM annihilation origin of the positron excess would be in conflict with any observable anisotropy.

Before the local propagation of cosmic rays in the solar neighborhood is understood more closely, their arrival directions can not be used as a tool to discriminate between different source scenarios alone. In particular, the magnitude of the very local mean free path length is important.

As a remark to currently available studies in the literature, it is emphasized how the correct time-dependence of a point source has to be accounted in pulsar models.

5.Conclusion and Outlook

By the time this thesis is written, cosmic rays have been known to exist for 104 years. They have lead to a number of important discoveries in the field of particle physics and have increased our understanding of the Milky Way in numerous ways. Now, the high-precision measurement accessible with detectors like AMS-02 has initiated a shift in modeling cosmic ray transport.

Throughout the 20th century, models of cosmic ray propagation used to describe the Galaxy in a very general way. For the first time, the few-percent level of observational accuracy exceeds the accuracy of available galactic transport models. At the same time, complex packages are developed to include a wealth of realistic conditions in the calculation of such models. Models of cosmic ray transport can now move on to give consistent predictions for multiple observables at once.

Currently there exists no single transport model able to coherently explain the AMS-02 measurements. The Galaxy can not be treated anymore as a simple box, in which cosmic rays propagate from their sources through a homogeneous gas. The highly topical, precise measurement of the positron fraction $e^+/e^\pm$ and the electron e^- and positron e^+ fluxes demonstrates inevitably, that the previous state-of-the-art models are now forced to *decrease the level of reductionism.* In particular, they need to account for the characteristics of transport phenomena in the neighborhood of the Sun, the so-called Local Bubble, which is shown to exert crucial influence on local cosmic ray observations.

In this thesis, we, for the first time, demonstrate that the spatial distribution of cosmic ray sources is not the decisive factor determining the local amplitude of the anisotropic component.

- Overall, it is shown that the dipole anisotropy model prediction heavily depends on the magnitude of the local diffusion coefficient. For cosmic ray leptons, it was shown that this influence exceeds the impact of varying the spatial distribution of the sources. As the interstellar medium is known to be very heterogeneous, the common assumption of a widely homogeneous diffusion coefficient may not hold and structures as small as the Local Bubble have to be resolved in order to interpret the predicted anisotropy in cosmic ray transport models.

- In particular, this study rectifies the currently prevalent notion that from the current observation of low dipole anisotropy in positron flux, reinforced by highly topical AMS-02 measurements, a clear distinction criterion for the nature of positron source can be applied. The high-energy positron component can successfully be modeled as originating from nearby pulsars without necessarily implying a measureable dipole anisotropy.

The study presented here yields a first glimpse into the future of cosmic ray transport modeling. For the first time, an attempt is made to coherently model the impact of the

Local Bubble on the observed cosmic ray fluxes. For this, a number of simplified scenarios were chosen and implemented in the publicly available DRAGON code. We implemented the Local Bubble in either spherical or cylindrical shape as a region surrounding the Sun, in which gas densities, diffusion coefficients, the interstellar radiation field and magnetic field strengths can deviate from the surrounding regions. This code had to be advanced significantly on a technical level, to allow for the spatial accuracy this study required, of ten parsecs order. Currently, the behaviour of the turbulent magnetic field inside the Local Bubble is not understood. We therefore suggest a range of diffusion models to best represent these uncertainties, allowing the diffusion coefficient to locally increase or decrease by a factor of hundred at most.

Based on 34 different scenarios, we have found that, compared to a galactic transport reference model (see Tab. 3.4 in chapter 3.4.3),

- the local fluxes of protons remain largely unchanged in all considered scenarios, but the galactic proton density might deviate from the predictions by previous models by up to 30%. Such deviations are also suggested to explain the fluxes of diffuse galactic γ-ray emission by pion decay;

- in a total of 17 models the combined data description of the local proton flux, the secondary-to-primary ratios of antiprotons over protons ($\bar{p}/p$) and boron over carbon (B/C) as well as the "cosmic clock" ($^{10}Be/^9Be$) was matched equally well while introducing no further conflict in the measurement of electrons and positrons;

- that the level of expected anisotropy in protons of $E \in [80\,\text{GeV}, 1.8\,\text{TeV}]$ relative to protons of $E \in [40, 80]\,\text{GeV}$ showed differences ranging from 0.3% to 344% considering all 34 models relative to our reference model (whereas the strongest increase is already at the value of the experimental AMS-02 upper limit);

- in general, local models of increased or decreased diffusion coefficient lead also to an increase or decrease in dipole anisotropy, despite the fact that the former leads to an *flattening* in cosmic ray density and the latter to *steeper* gradients;

- an increase of secondary production rates, either by a decrease of the diffusion coefficient or an increase of the gas density, would lead to a worse model description of $\bar{p}/p$, B/C or $^{10}Be/^9Be$ measurements. It is recalled that the reference model was chosen in a way as to describe the available observational data well. It is up to further research to show whether these models can in principle be adjusted in galactic transport parameters so as to restore the description of the $\bar{p}/p$, B/C and $^{10}Be/^9Be$ ratios.

For the leptonic components of cosmic rays, we found that

- similarly to protons, the local e^- fluxes remain largely unaffected, but their galactic density might deviate from previous predictions by up to 50%. This can account for differences in model predictions of the diffuse γ-ray Bremsstrahlung and Inverse Compton emissions;

- the local e^+ fluxes, which is known to show a deficit in the *energetic population* ($E > 10\,\mathrm{GeV}$), as in 30 models described equally well or better in the intermediate, few GeV region. This is attributed to enhanced positron production in the denser Local Bubble Walls. In 2 models, this effect lead to an over-prediction, exceeding the data; In 2 models, the deficit widened due to decreased positron production in the Bubble Interior;

- considering all 34 models, the level of expected anisotropy in the leptonic sum flux showed differences ranging from 0.4% to 345% relative to our reference model;

- considering all 34 models, the level of expected anisotropy in positrons relative to protons showed differences ranging from 0.6% to 325% relative to our reference model.

- the aforementioned extreme values all appear in models that also are in agreement with $\bar{p}/p$, B/C, $^{10}Be/^9Be$ observations;

An increase of the dipole anisotropy was usually accompanied by strongly enhanced density gradients in the surrounding cosmic ray distribution, so that the specific position of the Sun would be relevant. In models of "true" isotropization, which is achieved by local increase of diffusion coefficient, the exact position of the Sun inside the local bubble is not of importance.

It is to be stressed that the above numerical values carry little information by themselves as they depend on the various assumptions made about the details of the local transport processes, and on the reference model. Given the large uncertainties in our understanding of these processes, the range of the numbers given above serves as an *illustration of the expected level of corrections* that need to be attributed to local transport. Now that models are confronted with the AMS-02 data at few-percent accuracy, these numbers illustrate that the study of local transport phenomena has gained crucial importance. In general, the relative changes in dipole anisotropy were comparable for proton and positron measurements, indicating that as the proton anisotropy is further determined by measurements, conclusions can then be made about the (an)isotropizing effect on the local positron flux, as well.

We showed that the AMS-02 "positron excess" measurement is easily described within the pulsar hypothesis. We demonstrated this by the inclusion of 5 nearby pulsars, from which we constructed 5 completely different realistic source scenarios. This is possible due to the large uncertainty in the pulsar distance and injection spectrum parameters. The predicted anisotropy from these scenarios is consistent with the currently most constraining experimental upper limits, the limits given for $e^\pm$ by Fermi-LAT and for e^+/p by currently ongoing AMS-02 analysis (to be released this year), at 95% confidence level. The study was first performed using a minimization routine employing an analytical solution to a simplified diffusion equation. In a second step, the time-dependent pulsar source terms were implemented in the advanced numerical DRAGON package. It was shown that the numerical solution is in agreement with the analytical solution in the respective simplifying limits.

It was then shown, that model description of the AMS-02 e^+ observation is still possible when considering Local Bubble transport models. It was found that the assumptions on pulsar injection parameters have to be chosen differently, but are possible within realistic boundaries. It was further checked that higher multipoles, in particular the quadrupole order which is in principle observationally accessible, are subdominant for pulsar sources, by at least four orders of magnitude compared to the dipole anisotropy. This is seen not as a specific feature of these pulsar scenarios, but seems to hold in a general fashion.

Based on 5 local transport models defined by the previous study in agreement with the combined $p, \bar{p}/p, B/C, {}^{10}Be/{}^9Be$ measurements and also in agreement with the measured AMS-02 e^- and e^+ fluxes, we showed that (see Tabs. 4.7 and **??** in chapter 4.4.3)

- in 3 models, all 5 pulsar scenarios showed agreement with the upper limits on Fermi-LAT $e^\pm$ and AMS-02 e^+/p dipole anisotropy;

- in 1 model, 2 pulsar scenarios showed agreement with the upper limits on Fermi-LAT $e^\pm$ and AMS-02 e^+/p dipole anisotropy, and 3 scenarios were in conflict;

- in 1 model, all 5 pulsar scenarios where in conflict with said upper limits;

- over all models within the observed $e^\pm$ and e^+/p limits, predicted dipole anisotropy was seen to change by up to nearly two orders (factors appeared from 4% to 2600%) compared to the galactic transport model

- every transport model with every pulsar scenario was compatible with the e^+/e^- 68% CL isotropy measurement of AMS-02, projected until the end of the mission in 2024.

Even though a variety of models found that is in agreement with the current experimental upper limits on the dipole strength, the question of the impact of our local environment is of relevance:
The local transport parameters heavily influence the local electron and positron spectra and anisotropy. Taking different, realistic assumptions about the Local Bubble into account, the dipole anisotropies predicted in our realistic scenarios can only in a few cases be excluded by the experimental upper limits. And in general, the large variations of over a factor 30-40 up or down are contradictory to the assumption, that between the pulsar hypothesis and the Dark Matter hypothesis, *model discrimination can actually be done on the argument of positron anisotropy alone.* We show several pulsar scenarios that are also in agreement with the observational limits if the local transport model leads to an enhancement of anisotropy. This means that future model discrimination needs to take into account further observables to find the true nature of the positron excess, for instance the rising precision in antiproton measurements, the determination of higher-energy proton anisotropies, or entirely different observables like the γ-ray flux from the known point sources, which might shed some light on the source distribution.

This thesis is the continuation of three proceedings [164, 165, 166] published during the years of my dissertation. In an upcoming publication, the readjustment of galactic transport parameters will be addressed, that was mentioned in the discussion, but could not be investigated yet.

To our knowledge, the study presented here provides the first estimate of the possible impact of the Local Bubble on the spectra and arrival directions of cosmic rays. We believe this to be extremely timely: On the one hand, because the accuracy of highly topical leptonic observations clearly asks to pay more attention to local transport, and on the other hand, because the computational expenses, particularly required for high-resolution models of our local galactic environment, finally became accessible in recent years.

Bibliography

[1] Y. Xu et al. "Rings and Radial Waves in the Disk of the Milky Way". In: *ApJ* 801, 105 (Mar. 2015), p. 105. DOI: `10.1088/0004-637X/801/2/105`. arXiv: `1503.00257`.

[2] Katia M. Ferriere. "The interstellar environment of our galaxy". In: *Rev. Mod. Phys.* 73 (2001), pp. 1031–1066. DOI: `10.1103/RevModPhys.73.1031`. arXiv: `astro-ph/0106359 [astro-ph]`.

[3] M.-Y. Lee et al. "The CO-to-H_2 Conversion Factor across the Perseus Molecular Cloud". In: *ApJ* 784, 80 (Mar. 2014), p. 80. DOI: `10.1088/0004-637X/784/1/80`. arXiv: `1401.5117`.

[4] R. Schlickeiser. *Cosmic Ray Astrophysics.* 2002.

[5] "Savage, B. D., Jenkins, E. B., 1972. Astrophys. J., 172, 491." In: ().

[6] Donald P Cox and Ronald J Reynolds. "The local interstellar medium". In: *Annual review of astronomy and astrophysics* 25 (1987), pp. 303–344.

[7] "Ionization in the solar chromosphere. Philosophical Magazine Series 6, 40 (1920), Nr. 238, S. 472-488". In: ().

[8] Kryvdyk, V. "Formation of the cosmic-ray spectrum due to its propagation in the Galaxy". In: *A&A* 400.1 (2003), pp. 1–7. DOI: `10.1051/0004-6361:20021860`. URL: `http://dx.doi.org/10.1051/0004-6361:20021860`.

[9] L. Spitzer Jr. "On a Possible Interstellar Galactic Corona." In: *ApJ* 124 (July 1956), p. 20. DOI: `10.1086/146200`.

[10] C. F. McKee and J. P. Ostriker. "A theory of the interstellar medium - Three components regulated by supernova explosions in an inhomogeneous substrate". In: *ApJ* 218 (Nov. 1977), pp. 148–169. DOI: `10.1086/155667`.

[11] NASA/ESA/Hubble Heritage Team (STScI/AURA)/J. Hester, P. Scowen (Arizona State U.)

[12] A. Lazarian, E.M. de Gouveia Dal Pino, and C. Melioli. *Magnetic Fields in Diffuse Media.* Astrophysics and Space Science Library. Springer Berlin Heidelberg, 2014. ISBN: 9783662446256. URL: `https://books.google.de/books?id=ZjlpBQAAQBAJ`.

[13] R. Beck and R. Wielebinski. "Magnetic Fields in Galaxies". In: *Planets, Stars and Stellar Systems. Volume 5: Galactic Structure and Stellar Populations.* Ed. by T. D. Oswalt and G. Gilmore. 2013, p. 641. DOI: `10.1007/978-94-007-5612-0_13`.

[14] P. C. Cortes et al. "Interferometric Mapping of Magnetic Fields: The ALMA View of the Massive Star-forming Clump W43-MM1". In: *ApJ* 825, L15 (July 2016), p. L15. DOI: `10.3847/2041-8205/825/1/L15`. arXiv: `1605.08037`.

[15] E. G. Blackman. "On deriving flux freezing in magnetohydrodynamics by direct differentiation". In: *European Journal of Physics* 34 (Mar. 2013), p. 489. DOI: `10.1088/0143-0807/34/2/489`. arXiv: `1301.3562 [physics.plasm-ph]`.

[16]   H. Alfvén. "Existence of Electromagnetic-Hydrodynamic Waves". In: *Nature* 150 (Oct. 1942), pp. 405–406. DOI: 10.1038/150405d0.

[17]   A. Brandenburg, D. Sokoloff, and K. Subramanian. "Current Status of Turbulent Dynamo Theory. From Large-Scale to Small-Scale Dynamos". In: *Space Sci. Rev.* 169 (Sept. 2012), pp. 123–157. DOI: 10.1007/s11214-012-9909-x. arXiv: 1203.6195 [astro-ph.SR].

[18]   C. Heiles. "The interstellar magnetic field". In: *ARA&A* 14 (1976), pp. 1–22. DOI: 10.1146/annurev.aa.14.090176.000245.

[19]   J. C. Brown. "The Magnetic Field of the Milky Way Galaxy". In: *The Dynamic Interstellar Medium: A Celebration of the Canadian Galactic Plane Survey*. Ed. by R. Kothes, T. L. Landecker, and A. G. Willis. Vol. 438. Astronomical Society of the Pacific Conference Series. Dec. 2010, p. 216. arXiv: 1012.2932 [astro-ph.GA].

[20]   ESA / Planck collaboration.

[21]   A. W. Strong. "Recent extensions to GALPROP". In: *ArXiv e-prints* (July 2015). arXiv: 1507.05020 [astro-ph.HE].

[22]   Alexandra Dobrynina, Alexander Kartavtsev, and Georg Raffelt. "Photon-photon dispersion of TeV gamma rays and its role for photon-ALP conversion". In: *Phys. Rev.* D91 (2015), p. 083003. DOI: 10.1103/PhysRevD.91.083003. arXiv: 1412.4777 [astro-ph.HE].

[23]   Pasquale Blasi. "Recent results in cosmic ray physics and their interpretation". In: *Braz. J. Phys.* 44 (2014). [,1291(2013)], pp. 426–440. DOI: 10.1007/s13538-014-0223-9. arXiv: 1312.1590 [astro-ph.HE].

[24]   W. R. Binns et al. "Cosmic-Ray Neon, Wolf-Rayet Stars, and the Superbubble Origin of Galactic Cosmic Rays". In: *ApJ* 634 (Nov. 2005), pp. 351–364. DOI: 10.1086/496959. eprint: astro-ph/0508398.

[25]   K. Lodders, H. Palme, and H.-P. Gail. "Abundances of the Elements in the Solar System". In: *Landolt Börnstein* (2009). DOI: 10.1007/978-3-540-88055-4_34. arXiv: 0901.1149 [astro-ph.EP].

[26]   from P.Blasi.

[27]   ENRICO Fermi. "On the Origin of the Cosmic Radiation". In: *Phys. Rev.* 75 (8 Apr. 1949), pp. 1169–1174. DOI: 10.1103/PhysRev.75.1169. URL: http://link.aps.org/doi/10.1103/PhysRev.75.1169.

[28]   D. A. Green. "The distribution of SNRs with galactocentric radius". In: *American Institute of Physics Conference Series*. Ed. by F. A. Aharonian, W. Hofmann, and F. M. Rieger. Vol. 1505. American Institute of Physics Conference Series. Dec. 2012, pp. 5–12. DOI: 10.1063/1.4772214. arXiv: 1208.3107.

[29]   D. A. Green. "A catalogue of 294 Galactic supernova remnants". In: *Bulletin of the Astronomical Society of India* 42 (June 2014), pp. 47–58. arXiv: 1409.0637 [astro-ph.HE].

[30] W. Tian and D. Leahy. "Distance measurements to radio supernova remnants". In: *Antenna Technology and Applied Electromagnetics and the Canadian Radio Science Meeting, 2009. ANTEM/URSI 2009. 13th International Symposium on.* Feb. 2009, pp. 1–4. DOI: `10.1109/ANTEMURSI.2009.4805122`.

[31] D. R. Lorimer et al. "The Parkes Multibeam Pulsar Survey - VI. Discovery and timing of 142 pulsars and a Galactic population analysis". In: *MNRAS* 372 (Oct. 2006), pp. 777–800. DOI: `10.1111/j.1365-2966.2006.10887.x`. eprint: `astro-ph/0607640`.

[32] Q. Yuan, S. Liu, and X. Bi. "An Attempt at a Unified Model for the Gamma-Ray Emission of Supernova Remnants". In: *ApJ* 761, 133 (Dec. 2012), p. 133. DOI: `10.1088/0004-637X/761/2/133`. arXiv: `1203.0085 [astro-ph.HE]`.

[33] C.-A. Faucher-Giguère and V. M. Kaspi. "Birth and Evolution of Isolated Radio Pulsars". In: *ApJ* 643 (May 2006), pp. 332–355. DOI: `10.1086/501516`. eprint: `astro-ph/0512585`.

[34] A. W. Strong and J. R. Mattox. "Gradient model analysis of EGRET diffuse Galactic γ-ray emission." In: *A&A* 308 (Apr. 1996), pp. L21–L24.

[35] W. Becker and B. Aschenbach. "ROSAT HRI Observations of the Crab Pulsar: an Improved Temperature Upper Limit for PSR 0531+21". In: *NATO Advanced Science Institutes (ASI) Series C.* Ed. by M. A. Alpar, U. Kiziloglu, and J. van Paradijs. Vol. 450. NATO Advanced Science Institutes (ASI) Series C. 1995, p. 47. eprint: `astro-ph/9503012`.

[36] J. Hester NASA ESA and A. Loll (Arizona State University).

[37] NASA and Chandra Science Center.

[38] P. Blasi and E. Amato. "Positrons from pulsar winds". In: *Astrophysics and Space Science Proceedings* 21 (2011), p. 624. arXiv: `1007.4745 [astro-ph.HE]`.

[39] S. Della Torre et al. "Pulsar Wind Nebulae as a source of the observed electron and positron excess at high energy: The case of Vela-X". In: *Journal of High Energy Astrophysics* 8 (Dec. 2015), pp. 27–34. DOI: `10.1016/j.jheap.2015.08.001`. arXiv: `1508.01457 [astro-ph.HE]`.

[40] R. Schlickeiser. "Cosmic-ray transport and acceleration". In: *ApJS* 90 (Feb. 1994), pp. 929–936. DOI: `10.1086/191927`.

[41] Dmitry Malyshev, Ilias Cholis, and Joseph Gelfand. "Pulsars versus dark matter interpretation of ATIC/PAMELA". In: *Phys. Rev. D* 80 (6 Sept. 2009), p. 063005. DOI: `10.1103/PhysRevD.80.063005`. URL: `http://link.aps.org/doi/10.1103/PhysRevD.80.063005`.

[42] D. R. Lorimer and M. Kramer. *Handbook of Pulsar Astronomy.* Dec. 2004.

[43] HESS Collaboration. "Acceleration of petaelectronvolt protons in the Galactic Centre". In: *Nature* 531 (Mar. 2016), pp. 476, 0028–0836. DOI: `10.1038/nature17147`. eprint: 479 (2016/03/24/print).

[44] *from Wikipedia www.wikipedia.org, October 11th 2016.*

[45]   Iris Gebauer. "An Anisotropic Model for Galactic Cosmic Ray Transport and its Implications for Indirect Dark Matter Searches". PhD thesis. KIT, 2010.

[46]   Daniele Gaggero, P. D. Serpico, and V. Bonnivard. "Impact of annihilation and triplet pair production on secon dary cosmic ray positrons". In: *Proceedings, 33rd International Cosmic Ray Conference (ICRC2013): Rio de Janeiro, Brazil, July 2-9, 2013*, p. 0361. URL: http://www.cbpf.br/%7Eicrc2013/papers/icrc2013-0361.pdf.

[47]   P. Lipari. "The lifetime of cosmic rays in the Milky Way". In: *ArXiv e-prints* (July 2014). arXiv: 1407.5223 [astro-ph.HE].

[48]   D. E. Greiner et al. "Momentum Distributions of Isotopes Produced by Fragmentation of Relativistic ^{12}C and ^{16}O Projectiles". In: *Phys. Rev. Lett.* 35 (3 July 1975), pp. 152–155. DOI: 10.1103/PhysRevLett.35.152. URL: http://link.aps.org/doi/10.1103/PhysRevLett.35.152.

[49]   S. P. Swordy et al. "Relative abundances of secondary and primary cosmic rays at high energies". In: *ApJ* 349 (Feb. 1990), pp. 625–633. DOI: 10.1086/168349.

[50]   G. D. Badhwar et al. "Cosmic ray antiproton and positron production in the interstellar medium". In: *Astrophysics and Space Science* 37.2 (1975), pp. 283–300. ISSN: 1572-946X. DOI: 10.1007/BF00640354. URL: http://dx.doi.org/10.1007/BF00640354.

[51]   I. V. Moskalenko and A. W. Strong. "Production and Propagation of Cosmic-Ray Positrons and Electrons". In: *ApJ* 493 (Jan. 1998), pp. 694–707. DOI: 10.1086/305152. eprint: astro-ph/9710124.

[52]   M. Kachelriess, I. V. Moskalenko, and S. S. Ostapchenko. "New Calculation of Antiproton Production by Cosmic Ray Protons and Nuclei". In: *ApJ* 803, 54 (Apr. 2015), p. 54. DOI: 10.1088/0004-637X/803/2/54. arXiv: 1502.04158 [astro-ph.HE].

[53]   C. Evoli, D. Grasso, and L. Maccione. "Diffuse neutrino and gamma-ray emissions of the galaxy above the TeV". In: *J. Cosmology Astropart. Phys.* 6, 003 (June 2007), p. 003. DOI: 10.1088/1475-7516/2007/06/003. eprint: astro-ph/0701856.

[54]   M. Garcia-Munoz, G. M. Mason, and J. A. Simpson. "The age of the galactic cosmic rays derived from the abundance of Be-10". In: *ApJ* 217 (Nov. 1977), pp. 859–877. DOI: 10.1086/155632.

[55]   Andreas Obermeier et al. "Galactic propagation of cosmic rays and the B/C ratio". In: *International Cosmic Ray Conference.* Vol. 6. 2011, p. 39.

[56]   Simon Kunz. "Constraints on Transport Models for Galactic Cosmic Rays and their Implications for the Anomalous Positron Abundance". PhD thesis. KIT, 2014.

[57]   V. Dogiel and D. Breitschwerdt. "Cosmic Rays in the Disk and Halo of Galaxies". In: *ArXiv e-prints* (May 2009). arXiv: 0905.3071 [astro-ph.HE].

[58]   D. Breitschwerdt, J. F. McKenzie, and H. J. Voelk. "Galactic winds. I - Cosmic ray and wave-driven winds from the Galaxy". In: *A&A* 245 (May 1991), pp. 79–98.

[59]   N. Henbest and H. Couper. "Die Milchstraße ". In: *original title "A Guide to the Galaxy"*. Ed. by Birkhäuser Verlag. 1996.

[60] L. Zaninetti. "On the Shape of Superbubbles Evolving in the Galactic Plane". In: *PASJ* 56 (Dec. 2004), pp. 1067–1082. DOI: 10.1093/pasj/56.6.1067. eprint: astro-ph/0510558.

[61] D. McCammon and W. T. Sanders. "The soft X-ray background and its origins". In: *ARA&A* 28 (1990), pp. 657–688. DOI: 10.1146/annurev.aa.28.090190.003301.

[62] Randall K. Smith and Donald P. Cox. "Multiple Supernova Remnant Models of the Local Bubble and the Soft X-Ray Background". In: *The Astrophysical Journal Supplement Series* 134.2 (2001), p. 283. URL: http://stacks.iop.org/0067-0049/134/i=2/a=283.

[63] B. Fuchs et al. "The search for the origin of the Local Bubble redivivus". In: *MNRAS* 373 (Dec. 2006), pp. 993–1003. DOI: 10.1111/j.1365-2966.2006.11044.x. eprint: astro-ph/0609227.

[64] D. Breitschwerdt et al. "The locations of recent supernovae near the Sun from modelling 60Fe transport". In: *Nature* 532.7597 (Apr. 2016). Letter, pp. 73–76. ISSN: 0028-0836. URL: http://dx.doi.org/10.1038/nature17424.

[65] B. Y. Welsh and R. L. Shelton. "The trouble with the Local Bubble". In: *Ap&SS* 323 (Sept. 2009), pp. 1–16. DOI: 10.1007/s10509-009-0053-3. arXiv: 0906.2827 [astro-ph.GA].

[66] R. Lallement et al. "3D mapping of the dense interstellar gas around the Local Bubble". In: *A&A* 411 (Dec. 2003), pp. 447–464. DOI: 10.1051/0004-6361:20031214.

[67] R. Lallement et al. "3D maps of the local ISM from inversion of individual color excess measurements". In: *A&A* 561, A91 (Jan. 2014), A91. DOI: 10.1051/0004-6361/201322032. arXiv: 1309.6100.

[68] L. Puspitarini et al. "Local ISM 3D distribution and soft X-ray background. Inferences on nearby hot gas and the North Polar Spur". In: *A&A* 566, A13 (June 2014), A13. DOI: 10.1051/0004-6361/201322942. "arXiv": 1401.6899.

[69] R. E. Streitmatter et al. "Cosmic ray propagation in the local superbubble". In: *A&A* 143 (Feb. 1985), pp. 249–255.

[70] R. E. Streitmatter and F. C. Jones. "Superbubbles and Local Cosmic Rays". In: *International Cosmic Ray Conference* 3 (2005), p. 157.

[71] Lallement, R. et al. "3D maps of the local ISM from inversion of individual color excess measurements". In: *A&A* 561 (2014), A91. DOI: 10.1051/0004-6361/201322032. URL: http://dx.doi.org/10.1051/0004-6361/201322032.

[72] Cristina Consolandi, on Behalf of the AMS Collaboration. "Proceedings, 34th International Cosmic Ray Conference (ICRC 2015)". In: vol. ICRC2015. 2015. URL: http://pos.sissa.it/cgi-bin/reader/conf.cgi?confid=236.

[73] S.I. Syrovatskii V. L Ginzburg. *The Origin of Cosmic Rays.*

[74] J. R. Jokipii. "Cosmic-Ray Propagation. I. Charged Particles in a Random Magnetic Field". In: *ApJ* 146 (Nov. 1966), p. 480. DOI: 10.1086/148912.

[75] V. S. Berezinskii et al. *Astrophysics of cosmic rays.* 1990.

[76] A. A. Vlasov. "Reviews of Topical Problems: the Vibrational Properties of AN Electron Gas". In: *Soviet Physics Uspekhi* 10 (June 1968), pp. 721–733. DOI: 10.1070/PU1968v010n06ABEH003709.

[77] C. F. Kennel and F. Engelmann. "Velocity Space Diffusion from Weak Plasma Turbulence in a Magnetic Field". In: *Physics of Fluids* 9.12 (1966), pp. 2377–2388. DOI: http://dx.doi.org/10.1063/1.1761629. URL: http://scitation.aip.org/content/aip/journal/pof1/9/12/10.1063/1.1761629.

[78] J. R. Jokipii. "Cosmic-Ray Propagation. Ii. Diffusion in the Interplanetary Magnetic Field". In: *ApJ* 149 (Aug. 1967), p. 405. DOI: 10.1086/149265.

[79] I. N. Toptygin. *Cosmic rays in interplanetary magnetic fields*. 1983.

[80] R. Bruno and V. Carbone. "The Solar Wind as a Turbulence Laboratory". In: *Living Rev. Solar Phys.* 10 (2013).

[81] A. N. Kolmogorov. "The local structure of turbulence in incompressible viscous fluid for very large Reynolds numbers". In: *Proceedings of the Royal Society of London Series A* 434 (July 1991), pp. 9–13. DOI: 10.1098/rspa.1991.0075.

[82] D. Shaikh, P. K. Shukla, and L. Stenflo. "Spectral properties of acoustic gravity wave turbulence". In: *Journal of Geophysical Research (Atmospheres)* 113, D06108 (Mar. 2008), p. D06108. DOI: 10.1029/2007JD009305. arXiv: 0803.3264 [physics.ao-ph].

[83] J. W. Armstrong, B. J. Rickett, and S. R. Spangler. "Electron density power spectrum in the local interstellar medium". In: *ApJ* 443 (Apr. 1995), pp. 209–221. DOI: 10.1086/175515.

[84] Kraichnan, Robert H. "Inertial-Range Spectrum of Hydromagnetic Turbulence". In: *Physics of Fluids* 8.7 (1965), 1385–1387. DOI: {http://dx.doi.org/10.1063/1.1761412}. URL: %7Bhttp://scitation.aip.org/content/aip/journal/pof1/8/7/10.1063/1.1761412%7D.

[85] P. S. Iroshnikov. "Turbulence of a Conducting Fluid in a Strong Magnetic Field". In: *Soviet Ast.* 7 (Feb. 1964), p. 566.

[86] D. Gaggero et al. "Three dimensional modeling of CR propagation". In: *ArXiv e-prints* (June 2013). arXiv: 1306.6850 [astro-ph.HE].

[87] R. Kulsrud and W. P. Pearce. "The Effect of Wave-Particle Interactions on the Propagation of Cosmic Rays". In: *ApJ* 156 (May 1969), p. 445. DOI: 10.1086/149981.

[88] J. L. Han, K. Ferriere, and R. N. Manchester. "The Spatial Energy Spectrum of Magnetic Fields in Our Galaxy". In: *ApJ* 610 (Aug. 2004), pp. 820–826. DOI: 10.1086/421760. eprint: astro-ph/0404221.

[89] E. S. Seo and V. S. Ptuskin. "Stochastic reacceleration of cosmic rays in the interstellar medium". In: *ApJ* 431 (Aug. 1994), pp. 705–714. DOI: 10.1086/174520.

[90] A. W. Strong, I. V. Moskalenko, and O. Reimer. "Diffuse Continuum Gamma Rays from the Galaxy". In: *ApJ* 537 (July 2000), pp. 763–784. DOI: 10.1086/309038. eprint: astro-ph/9811296.

[91] Luis Batalha. "Solar Modulation effects on Cosmic Rays - Modelization with Force Field approximation, 1D and 2D numerical approaches and characterization with AMS-02 proton fluxes". PhD thesis. University of Lisbon, 2012.

[92] E. N. Parker. "The effect of adiabatic deceleration on the cosmic ray spectrum in the solar system". In: *Planet. Space Sci.* 14 (Apr. 1966), pp. 371–380. DOI: `10.1016/0032-0633(66)90074-2`.

[93] L. J. Gleeson and W. I. Axford. "Solar Modulation of Galactic Cosmic Rays". In: *ApJ* 154 (Dec. 1968), p. 1011. DOI: `10.1086/149822`.

[94] S. Della Torre et al. "Cosmic Rays Propagation with HelMod: Difference between forward-in-time and backward-in-time approaches". In: *ArXiv e-prints* (Aug. 2015). arXiv: `1511.00541 [physics.space-ph]`.

[95] C. Evoli et al. "Cosmic-ray propagation with DRAGON2: I. numerical solver and astrophysical ingredients". In: *ArXiv e-prints* (July 2016). arXiv: `1607.07886 [astro-ph.HE]`.

[96] F. Effenberger et al. "A Generalized Diffusion Tensor for Fully Anisotropic Diffusion of Energetic Particles in the Heliospheric Magnetic Field". In: *ApJ* 750, 108 (May 2012), p. 108. DOI: `10.1088/0004-637X/750/2/108`. arXiv: `1202.6319 [physics.space-ph]`.

[97] M. Kachelriess. "Lecture notes on high energy cosmic rays". In: *ArXiv e-prints* (Jan. 2008). arXiv: `0801.4376`.

[98] Jorge Casaus and the Ams Collaboration. "First Results of the AMS-02 Experiment on the ISS". In: *Journal of Physics: Conference Series* 531.1 (2014), p. 012007. URL: `http://stacks.iop.org/1742-6596/531/i=1/a=012007`.

[99] Stefan Zeißler. "PhD thesis (ongoing AMS-02 dipole anisotropy analysis)". PhD thesis. KIT, 2014.

[100] William H. Press et al. *Numerical Recipes in C (2Nd Ed.): The Art of Scientific Computing.* New York, NY, USA: Cambridge University Press, 1992. ISBN: 0-521-43108-5.

[101] J. Crank and P. Nicolson. "A practical method for numerical evaluation of solutions of partial differential equations of the heat-conduction type". In: *Advances in Computational Mathematics* 6.1 (1996), pp. 207–226. ISSN: 1572-9044. DOI: `10.1007/BF02127704`. URL: `http://dx.doi.org/10.1007/BF02127704`.

[102] L. H. Thomas. *Elliptic Problems in Linear Differential Equations over a Network.* Tech. rep. New York: Columbia University, 1949.

[103] M. Aguilar et al. "Electron and Positron Fluxes in Primary Cosmic Rays Measured with the Alpha Magnetic Spectrometer on the International Space Station". In: *Phys. Rev. Lett.* 113 (12 Sept. 2014), p. 121102. DOI: `10.1103/PhysRevLett.113.121102`. URL: `http://link.aps.org/doi/10.1103/PhysRevLett.113.121102`.

[104] D. A. Green. "A revised Galactic supernova remnant catalogue". In: *Bulletin of the Astronomical Society of India* 37 (Mar. 2009), pp. 45–61. arXiv: `0905.3699 [astro-ph.HE]`.

[105] D. Grasso et al. "On possible interpretations of the high energy electron-positron spectrum measured by the Fermi Large Area Telescope". In: *Astroparticle Physics* 32 (Sept. 2009), pp. 140–151. DOI: 10.1016/j.astropartphys.2009.07.003. arXiv: 0905.0636 [astro-ph.HE].

[106] R. Kissmann, O. Reimer, and A. W. Strong. "Galactic cosmic ray propagation models using Picard". In: *ArXiv e-prints* (Oct. 2015). arXiv: 1510.02580 [astro-ph.HE].

[107] O. Adriani et al. "An anomalous positron abundance in cosmic rays with energies 1.5-100GeV". In: *Nature* 458 (Apr. 2009), pp. 607–609. DOI: 10.1038/nature07942. arXiv: 0810.4995.

[108] M. Ackermann et al. "Measurement of Separate Cosmic-Ray Electron and Positron Spectra with the Fermi Large Area Telescope". In: *Physical Review Letters* 108.1, 011103 (Jan. 2012), p. 011103. DOI: 10.1103/PhysRevLett.108.011103. arXiv: 1109.0521 [astro-ph.HE].

[109] L. Accardo et al. "High Statistics Measurement of the Positron Fraction in Primary Cosmic Rays of 0.5–500 GeV with the Alpha Magnetic Spectrometer on the International Space Station". In: *Phys. Rev. Lett.* 113 (2014), p. 121101. DOI: 10.1103/PhysRevLett.113.121101.

[110] O. Adriani et al. "New Measurement of the Antiproton-to-Proton Flux Ratio up to 100 GeV in the Cosmic Radiation". In: *Physical Review Letters* 102.5, 051101 (Feb. 2009), p. 051101. DOI: 10.1103/PhysRevLett.102.051101. arXiv: 0810.4994.

[111] G. Giesen et al. "AMS-02 antiprotons, at last! Secondary astrophysical component and immediate implications for Dark Matter". In: *J. Cosmology Astropart. Phys.* 9, 023 (Sept. 2015), p. 023. DOI: 10.1088/1475-7516/2015/09/023. arXiv: 1504.04276 [astro-ph.HE].

[112] M. Aguilar et al. "Precision Measurement of the Proton Flux in Primary Cosmic Rays from Rigidity 1 GV to 1.8 TV with the Alpha Magnetic Spectrometer on the International Space Station". In: *Phys. Rev. Lett.* 114 (17 Apr. 2015), p. 171103. DOI: 10.1103/PhysRevLett.114.171103. URL: http://link.aps.org/doi/10.1103/PhysRevLett.114.171103.

[113] Rolf Kappl, Annika Reinert, and Martin Wolfgang Winkler. "AMS-02 Antiprotons Reloaded". In: *JCAP* 1510.10 (2015), p. 034. DOI: 10.1088/1475-7516/2015/10/034. arXiv: 1506.04145 [astro-ph.HE].

[114] M. Aguilar et al. "Precision Measurement of the Helium Flux in Primary Cosmic Rays of Rigidities 1.9 GV to 3 TV with the Alpha Magnetic Spectrometer on the International Space Station". In: *Phys. Rev. Lett.* 115 (21 Nov. 2015), p. 211101. DOI: 10.1103/PhysRevLett.115.211101. URL: http://link.aps.org/doi/10.1103/PhysRevLett.115.211101.

[115] Y. S. Yoon et al. "Cosmic-ray Proton and Helium Spectra from the First CREAM Flight". In: *ApJ* 728, 122 (Feb. 2011), p. 122. DOI: 10.1088/0004-637X/728/2/122. arXiv: 1102.2575 [astro-ph.HE].

[116] Yutaka Ohira, Norita Kawanaka, and Kunihito Ioka. "Cosmic-ray hardenings in light of AMS-02 data". In: *Phys. Rev.* D93.8 (2016), p. 083001. DOI: 10.1103/PhysRevD.93.083001. arXiv: 1506.01196 [astro-ph.HE].

[117] W. de Boer et al. "Evidence for a hadronic origin of the Fermi Bubbles and the Galactic Excess". In: *ArXiv e-prints* (Sept. 2015). arXiv: 1509.05310 [astro-ph.HE].

[118] D. Maurin, F. Melot, and R. Taillet. "A database of charged cosmic rays". In: *A&A* 569, A32 (Sept. 2014), A32. DOI: 10.1051/0004-6361/201321344. arXiv: 1302.5525 [astro-ph.HE].

[119] O. Adriani et al. "PAMELA Measurements of Cosmic-Ray Proton and Helium Spectra". In: *Science* 332 (Apr. 2011), p. 69. DOI: 10.1126/science.1199172. arXiv: 1103.4055 [astro-ph.HE].

[120] O. Adriani et al. "Measurement of the flux of primary cosmic ray antiprotons with energies of 60 MeV to 350 GeV in the PAMELA experiment". In: *Soviet Journal of Experimental and Theoretical Physics Letters* 96 (Jan. 2013), pp. 621–627. DOI: 10.1134/S002136401222002X.

[121] N. E. Yanasak et al. "Measurement of the Secondary Radionuclides ^{10}Be, ^{26}Al, ^{36}Cl, ^{54}Mn, and ^{14}C and Implications for the Galactic Cosmic-Ray Age". In: *ApJ* 563 (Dec. 2001), pp. 768–792. DOI: 10.1086/323842.

[122] T. Hams et al. "Measurement of the Abundance of Radioactive ^{10}Be and Other Light Isotopes in Cosmic Radiation up to 2 GeV Nucleon^{-1} with the Balloon-borne Instrument ISOMAX". In: *ApJ* 611 (Aug. 2004), pp. 892–905. DOI: 10.1086/422384.

[123] O. Adriani et al. "Measurement of Boron and Carbon Fluxes in Cosmic Rays with the PAMELA Experiment". In: *ApJ* 791, 93 (Aug. 2014), p. 93. DOI: 10.1088/0004-637X/791/2/93. arXiv: 1407.1657 [astro-ph.HE].

[124] O. Adriani et al. "Cosmic-Ray Electron Flux Measured by the PAMELA Experiment between 1 and 625 GeV". In: *Physical Review Letters* 106.20, 201101 (May 2011), p. 201101. DOI: 10.1103/PhysRevLett.106.201101. arXiv: 1103.2880 [astro-ph.HE].

[125] M. Ackermann et al. "Searches for cosmic-ray electron anisotropies with the Fermi Large Area Telescope". In: *Phys. Rev. D* 82.9, 092003 (Nov. 2010), p. 092003. DOI: 10.1103/PhysRevD.82.092003. arXiv: 1008.5119 [astro-ph.HE].

[126] R. McCray. "Supernovae and the interstellar medium". In: *NATO ASIC Proc. 210: Physical Processes in Interstellar Clouds*. Ed. by G. E. Morfill and M. Scholer. 1987, pp. 95–104.

[127] S. R. Spangler. "Plasma Turbulence in the Local Bubble". In: *Space Sci. Rev.* 143 (Mar. 2009), pp. 277–290. DOI: 10.1007/s11214-008-9391-7. arXiv: 0802.2260.

[128] L. Landau. "On the vibration of the electronic plasma." In: *J. Phys. USSR 10* 25 (1946).

[129] Steven R. Spangler. "Two-dimensional Magnetohydrodynamics and Interstellar Plasma Turbulence". In: *The Astrophysical Journal* 522.2 (1999), p. 879. URL: http://stacks.iop.org/0004-637X/522/i=2/a=879.

[130] H.R. Griem and R.H. Lovberg. *Plasma Physics*. Methods in Experimental Physics. Elsevier Science, 1971. ISBN: 9780080859866. URL: https://books.google.de/books?id=Tb-Sc1M1h60C.

[131] I. Lerche and R. Schlickeiser. "Linear Landau damping and wave energy dissipation in the interstellar medium". In: *A&A* 366 (Feb. 2001), pp. 1008–1015. DOI: 10.1051/0004-6361:20000242.

[132] K. Kifonidis et al. "Non-spherical core collapse supernovae. I. Neutrino-driven convection, Rayleigh-Taylor instabilities, and the formation and propagation of metal clumps". In: *A&A* 408 (Sept. 2003), pp. 621–649. DOI: 10.1051/0004-6361:20030863. eprint: astro-ph/0302239.

[133] G. L. Eyink and H. Aluie. "The breakdown of Alfvén's theorem in ideal plasma flows: Necessary conditions and physical conjectures". In: *Physica D Nonlinear Phenomena* 223 (Nov. 2006), pp. 82–92. DOI: 10.1016/j.physd.2006.08.009. eprint: physics/0607073.

[134] A. R. Bell and S. G. Lucek. "Cosmic ray acceleration to very high energy through the non-linear amplification by cosmic rays of the seed magnetic field". In: *MNRAS* 321 (Mar. 2001), pp. 433–438. DOI: 10.1046/j.1365-8711.2001.04063.x.

[135] A. R. Bell. "Turbulent amplification of magnetic field and diffusive shock acceleration of cosmic rays". In: *MNRAS* 353 (Sept. 2004), pp. 550–558. DOI: 10.1111/j.1365-2966.2004.08097.x.

[136] B. G. Elmegreen and J. Scalo. "Interstellar Turbulence I: Observations and Processes". In: *ARA&A* 42 (Sept. 2004), pp. 211–273. DOI: 10.1146/annurev.astro.41.011802.094859. eprint: astro-ph/0404451.

[137] R. Kulsrud and W. P. Pearce. "The Effect of Wave-Particle Interactions on the Propagation of Cosmic Rays". In: *ApJ* 156 (May 1969), p. 445. DOI: 10.1086/149981.

[138] S. R. Spangler, A. H. Savage, and S. Redfield. "Ion-Neutral Collisions in the Interstellar Medium: Wave Damping and Elimination of Collisionless Processes". In: *American Institute of Physics Conference Series*. Ed. by V. Florinski et al. Vol. 1366. American Institute of Physics Conference Series. Sept. 2011, pp. 97–106. DOI: 10.1063/1.3625594. arXiv: 1012.4121.

[139] T.W. Hartquist, J.E. Dyson, and D.P. Ruffle. *Blowing Bubbles in the Cosmos: Astronomical Winds, Jets, and Explosions*. Oxford University Press, 2004. ISBN: 9780195351439. URL: https://books.google.de/books?id=NAMTDAAAQBAJ.

[140] A. Balogh et al. *Microphysics of Cosmic Plasmas*. Space Sciences Series of ISSI. Springer US, 2014. ISBN: 9781489974136. URL: https://books.google.de/books?id=0zfABAAAQBAJ.

[141] A. J. Farmer and P. Goldreich. "Wave Damping by Magnetohydrodynamic Turbulence and Its Effect on Cosmic-Ray Propagation in the Interstellar Medium". In: *ApJ* 604 (Apr. 2004), pp. 671–674. DOI: 10.1086/382040. eprint: astro-ph/0311400.

[142]   R. I. Klein, C. F. McKee, and P. Colella. "On the hydrodynamic interaction of shock waves with interstellar clouds. 1: Nonradiative shocks in small clouds". In: *ApJ* 420 (Jan. 1994), pp. 213–236. DOI: 10.1086/173554.

[143]   F. Nakamura et al. "On the Hydrodynamic Interaction of Shock Waves with Interstellar Clouds. II. The Effect of Smooth Cloud Boundaries on Cloud Destruction and Cloud Turbulence". In: *ApJS* 164 (June 2006), pp. 477–505. DOI: 10.1086/501530. eprint: astro-ph/0511016.

[144]   I. V. Moskalenko and A. W. Strong. "Production and Propagation of Cosmic-Ray Positrons and Electrons". In: *ApJ* 493 (Jan. 1998), pp. 694–707. DOI: 10.1086/305152. eprint: astro-ph/9710124.

[145]   I. V. Moskalenko et al. "Secondary Antiprotons and Propagation of Cosmic Rays in the Galaxy and Heliosphere". In: *ApJ* 565 (Jan. 2002), pp. 280–296. DOI: 10.1086/324402. eprint: astro-ph/0106567.

[146]   M. J. Rees and J. E. Gunn. "The origin of the magnetic field and relativistic particles in the Crab Nebula". In: *MNRAS* 167 (Apr. 1974), pp. 1–12. DOI: 10.1093/mnras/167.1.1.

[147]   B. M. Gaensler and P. O. Slane. "The Evolution and Structure of Pulsar Wind Nebulae". In: *ARA&A* 44 (Sept. 2006), pp. 17–47. DOI: 10.1146/annurev.astro.44.051905.092528. eprint: astro-ph/0601081.

[148]   D. Hooper, P. Blasi, and P. Dario Serpico. "Pulsars as the sources of high energy cosmic ray positrons". In: *J. Cosmology Astropart. Phys.* 1, 025 (Jan. 2009), p. 025. DOI: 10.1088/1475-7516/2009/01/025. arXiv: 0810.1527.

[149]   T. Linden and S. Profumo. "Probing the Pulsar Origin of the Anomalous Positron Fraction with AMS-02 and Atmospheric Cherenkov Telescopes". In: *ApJ* 772, 18 (July 2013), p. 18. DOI: 10.1088/0004-637X/772/1/18. arXiv: 1304.1791 [astro-ph.HE].

[150]   J. Diemand et al. "Clumps and streams in the local dark matter distribution". In: *Nature* 454.7205 (Aug. 2008), pp. 735–738. ISSN: 0028-0836. DOI: 10.1038/nature07153. URL: http://dx.doi.org/10.1038/nature07153.

[151]   Timur Delahaye et al. "Astrophysical boost factor and dark matter indirect detection". In: *Journal of Physics: Conference Series* 203.1 (2010), p. 012050. URL: http://stacks.iop.org/1742-6596/203/i=1/a=012050.

[152]   Andi Hektor et al. "The cosmic-ray positron excess from a local Dark Matter over-density". In: *Physics Letters B* 728 (2014), pp. 58–62. ISSN: 0370-2693. DOI: http://dx.doi.org/10.1016/j.physletb.2013.11.017. URL: http://www.sciencedirect.com/science/article/pii/S0370269313009209.

[153]   M. Cirelli et al. "Model-independent implications of the e^+, e^-, $\bar{p}$ cosmic ray spectra on properties of Dark Matter". In: *Nuclear Physics B* 813 (May 2009), pp. 1–21. DOI: 10.1016/j.nuclphysb.2008.11.031. arXiv: 0809.2409 [hep-ph].

[154]   P. D. Serpico. "Possible causes of a rise with energy of the cosmic ray positron fraction". In: *Phys. Rev. D* 79.2, 021302 (Jan. 2009), p. 021302. DOI: 10.1103/PhysRevD. 79.021302. arXiv: 0810.4846 [hep-ph].

[155]   Kfir Blum, Boaz Katz, and Eli Waxman. "AMS-02 Results Support the Secondary Origin of Cosmic Ray Positrons". In: *Phys. Rev. Lett.* 111 (21 Nov. 2013), p. 211101. DOI: 10.1103/PhysRevLett.111.211101. URL: http://link.aps.org/doi/10. 1103/PhysRevLett.111.211101.

[156]   Martin H. Israel. "An Alternative Approach to Understanding the Observed Positron Fraction". In: *Brazilian Journal of Physics* 44.5 (2014), pp. 530–533. ISSN: 1678-4448. DOI: 10.1007/s13538-014-0235-5. URL: http://dx.doi.org/10.1007/s13538- 014-0235-5.

[157]   Ł. Stawarz, V. Petrosian, and R. D. Blandford. "On the Energy Spectra of GeV/TeV Cosmic Ray Leptons". In: *ApJ* 710 (Feb. 2010), pp. 236–247. DOI: 10.1088/0004- 637X/710/1/236. arXiv: 0908.1094.

[158]   A. A. Abdo et al. "The Second Fermi Large Area Telescope Catalog of Gamma-Ray Pulsars". In: *ApJS* 208, 17 (Oct. 2013), p. 17. DOI: 10.1088/0067-0049/208/2/17. arXiv: 1305.4385 [astro-ph.HE].

[159]   G. Hobbs et al. "The ATNF Pulsar Catalog". In: *Young Neutron Stars and Their Environments*. Ed. by F. Camilo and B. M. Gaensler. Vol. 218. IAU Symposium. 2004, p. 139. eprint: astro-ph/0309219.

[160]   Leo Gendelev, Stefano Profumo, and Michael Dormody. "The contribution of Fermi gamma-ray pulsars to the local flux of cosmic-ray electrons and positrons". In: *Journal of Cosmology and Astroparticle Physics* 2010.02 (2010), p. 016. URL: http: //stacks.iop.org/1475-7516/2010/i=02/a=016.

[161]   S.-N. Zhang and Y. Xie. "Why Do the Braking Indices of Pulsars Span a Range of More Than 100 Millions?" In: *ApJ* 761, 102 (Dec. 2012), p. 102. DOI: 10.1088/0004- 637X/761/2/102. arXiv: 1209.2478 [astro-ph.HE].

[162]   Hasan Yüksel, Matthew D. Kistler, and Todor Stanev. "TeV Gamma Rays from Geminga and the Origin of the GeV Positron Excess". In: *Phys. Rev. Lett.* 103 (5 July 2009), p. 051101. DOI: 10.1103/PhysRevLett.103.051101. URL: http: //link.aps.org/doi/10.1103/PhysRevLett.103.051101.

[163]   Daniele Gaggero et al. "PAMELA and AMS-02 e^+ and e^- spectra are reproduced by three-dimensional cosmic-ray modeling". In: *Phys. Rev. D* 89 (8 Apr. 2014), p. 083007. DOI: 10.1103/PhysRevD.89.083007. URL: http://link.aps.org/doi/10.1103/ PhysRevD.89.083007.

[164]   I. Gebauer, S. Kunz, M. Weinreuter. "The impact of cosmic ray transport scenarios on the local positron fraction". In: (Rio de Janeiro). 33rd ICRC. International Cosmic Ray Conference, 2013.

[165]   I. Gebauer, M. Weinreuter, S. Kunz, D. Gaggero. "On the impact of the Local Bubble on cosmic ray electron and positron spectra and anisotropy". In: (The Hague). 34th ICRC. International Cosmic Ray Conference, 2015.

[166] I. Gebauer, M. Weinreuter, S. Kunz, D. Gaggero. "The Local Bubble as a cosmic-ray isotropizer". In: ASTRA, 2015. DOI: doi:10.5194/ape-2-1-2015.

[167] M. Ackermann et al. "A Cocoon of Freshly Accelerated Cosmic Rays Detected by Fermi in the Cygnus Superbubble". In: *Science* 334.6059 (2011), pp. 1103–1107. ISSN: 0036-8075. DOI: 10.1126/science.1210311. eprint: http://science.sciencemag.org/content/334/6059/1103.full.pdf. URL: http://science.sciencemag.org/content/334/6059/1103.

[168] R. Weaver et al. "Interstellar bubbles. II - Structure and evolution". In: *ApJ* 218 (Dec. 1977), pp. 377–395. DOI: 10.1086/155692.

[169] C. C. Lin and F. H. Shu. "On the Spiral Structure of Disk Galaxies." In: *ApJ* 140 (Aug. 1964), p. 646. DOI: 10.1086/147955.

[170] R. McCray and M. Kafatos. "Supershells and propagating star formation". In: *ApJ* 317 (June 1987), pp. 190–196. DOI: 10.1086/165267.

[171] M Sasai Y. Kaneda and H. Kawamura. "Numerical experimentation : A third way to study Nature". In: *Frontiers of Computational Science* Springer (2007), pp. 15–28.

[172] B. Rossi and S. Olbert. *Introduction to the physics of space.* 1970.

[173] Jih Kwin Chao and Stanislaw Olbert. "Observation of slow shocks in interplanetary space". In: *Journal of Geophysical Research* 75.31 (1970), pp. 6394–6397. ISSN: 2156-2202. DOI: 10.1029/JA075i031p06394. URL: http://dx.doi.org/10.1029/JA075i031p06394.

[174] Y. Lithwick and P. Goldreich. "Imbalanced Weak Magnetohydrodynamic Turbulence". In: *ApJ* 582 (Jan. 2003), pp. 1220–1240. DOI: 10.1086/344676. eprint: astro-ph/0208046.

[175] Huirong Yan and A. Lazarian. "Cosmic-Ray Propagation: Nonlinear Diffusion Parallel and Perpendicular to Mean Magnetic Field". In: *The Astrophysical Journal* 673.2 (2008), p. 942. URL: http://stacks.iop.org/0004-637X/673/i=2/a=942.

[176] A. Lazarian and H. Yan. "Superdiffusion of Cosmic Rays: Implications for Cosmic Ray Acceleration". In: *ApJ* 784, 38 (Mar. 2014), p. 38. DOI: 10.1088/0004-637X/784/1/38. arXiv: 1308.3244 [astro-ph.HE].

A.Appendix

A.1. Formation of SNR and Superbubbles

As in this thesis we discuss several astrophysical aspects of the Local Bubble, we want to give a brief outline of how it is currently thought to have formed. The formation of superbubbles is a very active field of research and itself, which contributes to the uncertainty that are currently immanent in discussing the impact of the Local Bubble environment on CR propagation. Besides the Local Bubble, superbubbles are theorized to be important for CR propagation, as they can grow significantly larger than SNR and the maximum energy, cf. (1.2) of shock acceleration scales linearly with the radius R of the shock structure. This also is a very current idea from Fermi-LAT measurements in the Cygnus superbubble, only published in 2011 in Science [167].

The maximum R of a typical SNR is of a few parsecs order, both dependent on the mass of the progenitor star mass and the pressure of the ambient ISM. To understand their physical environment, their theory of development is of interest. This is commonly divided into three phases:

1. $R(t) \propto t$ – **Free expansion** ("bursting phase") for about $100-300$ years:
   At first, the inner pressure is highly exceeding the ambience, so the supernova ejecta consume as much space as is available – this constitutes a *supersonic shock wave*, constant in velocity. The ambient material is steamrolled, compressed and heated, aspiring pressure equilibrium. This causes a reverse shock wave into the inner ejecta, reheating these. The boundary between the (expanded, so less dense) ejecta and the accumulated material is called the *contact discontinuity*. Free expansion comes to a halt when the accumulations are about the same mass as the ejecta themselves.

2. $R(t) \propto t^{2/5}$ – **Adiabatic expansion ("Sedov-Taylor phase")** of the blast wave, enduring about $1-3 \cdot 10^4$ yr:
   The reverse shock has reached the center, pressure equilibrium is reached, and the temperature is $T \gg 10^6$ K. During this phase, total energy is nearly conserved, as the matter inside the SNR stays completely ionized and so no radiative transitions (e,g electron capture) occur. Adiabatic expansion implies adiabatic cooling, until such transitions can occur.

3. $R(t) \propto t^{1/4}$ **Radiative ("Snow-Plow") phase** (lasting about $10^5 - 10^6$ yr) Below $T \lesssim 10^6$ K, electron capture is possible, and radiative losses by the outer layers get significant. By this, energy is lost rapidly in this phase and the shock cools down. The SNR ceases to accumulate ambient material, so total momentum is now conserved. The whole system now aspires pressure equilibrium, it will expand as long as the internal pressure exceeds the ambient one, but the ambient is not heated anymore. The inner, hot gas however may persist for longer than 1 Myr, whereas the remnant stops being visible in optical and radio waves after about $1 - 5 \cdot 10^4$ yr. Before this phase, the SNR expansion is dominant in energy and thus relatively

indifferent of the surrounding. *Young* SNRs like the one detected by Tycho Brahe in 1572 have a nearly spherical form. Late in the radiative phase, the shock wave turns into a sound wave: the shape likely becomes asymmetric because of the ISM non-uniformity. This leads to the pile-up of *dense, cold clouds* around the SNR, and at other places, to the shell ripping open where the shock pressure has already sufficiently declined.

SNRs are now widely believed to be main constituents not only as CR accelerators, but also as generator for shock waves that drives the whole dynamic of the ISM (e.g. triggering star formation), and as source for the uncertain, but certainly large presence of coronal gas.

Another, and surprisingly similar mechanism was given by [168], who find that equivalent topologies appear in so-called *bubbles* around the heaviest (early-type) stars. Even before their imminent supernova, their strong *stellar winds* release a large deposit of energy continuously into their surrounding. Integrated over such a star lifetime, this can account up to $\sim 10^{43}$ J and be of comparable significance to SNRs. As well, the bubble structures show the three stages described for supernovae above, and provide shocked wind regions suitable for CR shock acceleration, plus they fill the ISM with coronal gas.

It is the omnipresence of these structures that makes it possible to think of the interstellar space to be continuously stirred up by random shock waves. This picture becomes a bit more complicated due to turbulent interactions, but is valid nonetheless. As will turn out in chapter 2, this is of essential importance for the question of cosmic ray propagation. However, what is not clear is how the path of a CR particle, once accelerated and propagating, is affected by the presence of a varying large fraction (volume filling factor) of coronal gas.

Especially, the question about the local interstellar environment is raised: The Local Bubble consists of largely coronal gas extending to at least 50 pc in every direction. By that, it is a structure even larger than supernova remnants and stellar bubbles; it is a **superbubble**, a merger of multiple SNR and/or wind-driven bubbles.

Fig. A.1 shows an actual example of a superbubble forming, in a region called "LHa115-N19" located in the Small Magellanic Cloud. The feint-blue highlighted regions are three remnants called J0047.5-7308, J0047.2-7308, J0046.6-7308 (from left to right), from massive stars that roughly core-collapsed at short times apart and are now all in their snow-plow phase.

Figure A.1. The superbubble Henize 70 (N70) in the Large Magellanic Cloud [HST].

Generally, it is believed that most superbubbles form even earlier, when a group of the heaviest stars - O and B stars in a so called *OB association* - sequentially turn into supernovae. It is actually not uncommon, because the stars in an OB associations tend to be of similar age: They themselves are spawned upon the gravitational collapse of one single, giant molecular cloud (of $\sim 10^5 \, M_\odot$). These carry several tens to hundreds dense cores. A likely mechanism to trigger this instability [169] is the shock compression associated with such a cloud moving through a galactic spiral arm region, which means that many neighboring cores start nuclear fusion at a similar time. After that, the lifetime of these stars is a function of their mass only: It is only a few Myr for the heaviest ones, i.e. stars in OB associations are still young (in comparison, the Sun has an age of 4.6 Gyr with a lifetime of about 10 Gyr) not enough time for their separation to increase.

This spatial and temporal correlation of massive O & B stars allows for the extreme conditions of a superbubble. For the first few Myr, the stellar winds blow smaller bubbles around themselves, whose cumulative power significantly rises when they overlap [2]. When the first supernovae start to explode, the environment is already hot and rarefied so that the free expansion mode lasts significantly longer. Further SN then feature an approximately steady injection of energy [170], rather than producing isolated remnants, lasting up to ~ 40 Myr.

The research on superbubbles is a very active field nowadays. Their role in CR acceleration is not clear, especially whether their increased dimensions make them suitable galactic PeVatrons, and so there is speculation whether we, given the Local Bubble, actually live inside a giant particle accelerator.

A.2. **Numerical oscillations in Crank-Nicolson schemes**

In chapter 2, the concept of *truncation error η* was introduced as the deviation of a finite differencing schemes to the actual mathematical differential operator, estimated by Taylor expansion. The *order of accuracy n* of a numerical scheme is the order of grid spacing Δt, Δx, ... in the truncation error, i.e. a scheme of

$$\eta \propto \Delta t^2 \tag{A.1}$$

is a scheme second-order in time. This is the case for the Crank-Nicolson scheme. It is known, that

> "Typically, for first-order schemes the truncation error has a diffusive effect on the solutions, which thus smooth the gradients. For second-order schemes the truncation error does have, conversely, a dispersive effect that is characterized by the appearance and spreading of spurious oscillations in high gradient regions (e.g. shocks, fronts)." [171]

Because of the appearance of such spurious oscillations in bad nonuniform grid choices, I have concerned myself with this topic for this thesis and include it here for the inclined reader.

The *stability* of any discretization scheme for a given partial differential equation (PDE) can be evaluated using so-called *von Neumann analysis*, which returns a limit on exponential growing solutions for a choice of discrete step size. For PDEs containing only time and spatial derivatives, all dimensions decoupled from the others, this is based on the notion that the spatial solution is somehow Fourier-decomposable, that is, the exponentials e^{ikx} form a set of eigenfunctions on any operator $\partial^n/\partial x^n$ ($n \in \mathbb{N}$, analogous for other spatial dimensions). Inserting these into the PDE gives a condition on the wave number k linked with the step sizes Δt, Δx: If it is possible by any choice of steps to allow k in the negative imaginary half space, the scheme supports exponential growth of these Fourier modes.

Not to be demonstrated here, the Crank-Nicolson scheme is known for any diffusive-advective equation to be *unconditionally stable* because it relies on the choice of central differencing for spatial derivatives. This is useful in comparison to other schemes which place hard limits on the magnitude of time steps, making computation on high spatial resolutions inefficient[1] However, this choice is also known to stabilize high-frequency modes oscillations ($|e^{ikx}| \approx 1$ for small k) and this can be a problem in the presence of *sharp edges*, a.k.a. steep 2nd derivatives. This is most extreme in the case of a square wave package, which, by Fourier decomposition, contain the highest frequencies representable in any grid (see the left ridge in A.2). This circumstance then appear as the "spurious oscillations" and are typical of schemes like Crank-Nicolson.

---

[1]For example, the "Forward Euler" scheme on a simple diffusion equation $\partial\psi/\partial t = D\,\partial^2\psi/\partial x^2$ demands a choice $\Delta t < \Delta x^2/(2D)$ in order not to show these exponential growing modes.

This effect is avoided by choosing a grid that suppresses hard gradients between neighboring grid points. In DRAGON, it appeared still as an issue when the source distribution of a point source was chosen too narrow. In such cases, the oscillations were propagated very fast through space, locally dominating the gradient of CR density and thus creating a spurious drop or rise in prediction of dipole anisotropy $\delta \propto \vec{\nabla} N / N$.
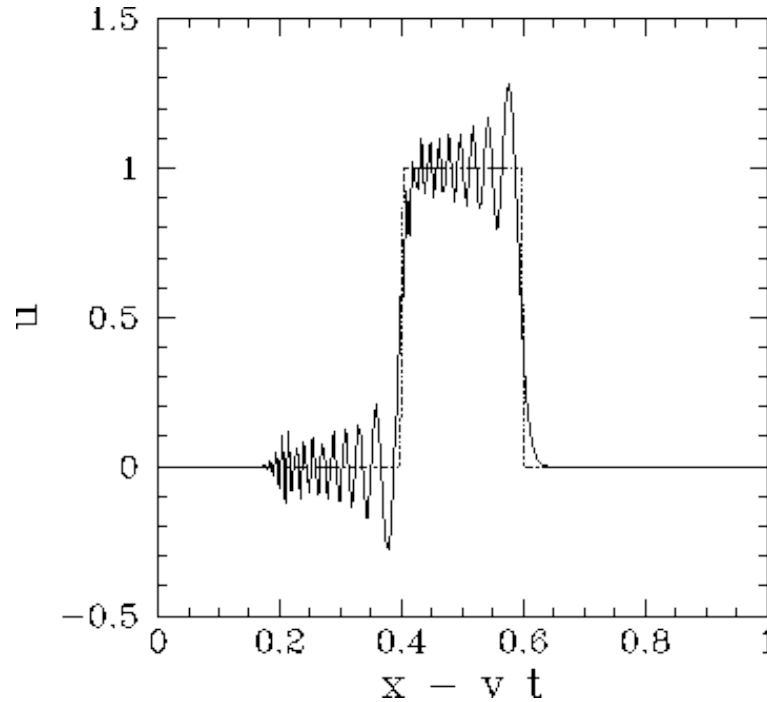
Figure A.2. The numerical values on either axis do not matter for this illustration: The rectangular function gives a sharply defined source distribution, which is then subjected to diffusive or convective propagation using a Crank-Nicolson (CN) scheme. When gradients between two grid points become too large, CN schemes can lead to the propagation of fake oscillations. The grid has to be refined if this happens, or the source function smoothened, or both.

A.3. A few basics about MHD waves

From the ansatz that derived the transport equation for cosmic rays, based on the Vlasov equation, it is also possible to derive the fluid equations for continuity, momentum, pressure and energy and Ohm's law. Generally, *warm* plasmas are considered, so the thermal pressure becomes relevant, but in some environments the *cold* approximation is justified, in which magnetic pressure dominates. The equations then allow for wave-like modes of propagation, as is known from other fields of physics. The diffusion of cosmic rays is therefore tightly linked to the plasma physics of the interstellar medium. Some standard introductions are given e.g. in [172] and [173]. Here, I want to summarize the results that are of believed to be of relevance for cosmic ray propagation from our current state of understanding. The MHD equations allow for the following wave modes: ($k_\parallel = \vec{k} \cdot \vec{B}_\mathrm{reg}/|\vec{B}_\mathrm{reg}|$ is the wave vector component parallel to the ambient magnetic field)

- **"Fast" magnetosonic waves**

  Magnetosonic (or *magnetoacoustic*) means that these waves are sound-like in that they are compressible, longitudinal oscillations. This means, they describe the propagation of fluctuations in magnetic and thermal pressure (moving in opposed phase). With the characteristic Alfvén velocity $v_A = B_\mathrm{reg}/\sqrt{4\pi\rho_\mathrm{Ions}}$ and speed of sound $v_S = \sqrt{\kappa p/\rho_\mathrm{Gas}}$, the slow mode dispersion relation is

$$\omega_F = k \sqrt{2}^{-1} \sqrt{v_A^2 + v_S^2 + \sqrt{(v_A^2 + v_S^2)^2 + 4v_A^2 v_S^2 \cos^2\theta}}$$

- **"Alfvén" Waves**

  The Alfvén mode is an incompressible one, it oscillates transversally to the ambient magnetic field and moves along its field lines (thus also called "Alfvén shear wave", Fig. A.3). This mode has a dispersion relation

$$\omega_A = v_A |k_\parallel|$$

  which is not dependent of the sound speed v_S as it thrives on the restoring force of the magnetic field alone: Electromagnetic fluctuations cause local overdensities in magnetic pressure which the ambient magnetic field seeks to compensate for. As astrophysical plasmas can be considered perfect electric conductors, movement of magnetic fields is directly coupled to movement of the material, they are "frozen in". Due to their incompressibility, Alfvén waves seem to undergo less efficient damping processes. Turbulent cascades emerge by wave-wave collisions, which are nonlinear and allow shifting energies between different wave modes.

- **"Slow" Magnetosonic Waves** Again, these are longitudinal oscillations in magnetic and thermal pressure, but as opposed to the fast mode, these oscillations proceed to be in phase. Unlike the fast mode, these can only propagate parallel to the ambient

magnetic field $\vec{B}_{\text{reg}}$, so $k = k_{\parallel}$. The dispersion relation is

$$\omega_S = k \sqrt{2}^{-1} \sqrt{v_A^2 + v_S^2 - \sqrt{(v_A^2 + v_S^2)^2 - 4v_A^2 v_S^2 \cos^2 \theta}}$$

and it is always $\omega_F \geq \omega_A \geq \omega_S$.

This wave mode is considered unimportant in directly affecting cosmic ray propagation, but, as the following mode, can play a significant role in the generation of turbulent magnetic fields.

- **"Entropy mode"**

  Often left out, there is actually a fourth solution of MHD wave equations, that some sources cite as a considerable source of MHD turbulence. This mode is actually *non-propagating*,

  $$\omega = 0$$

  thus describing fluctuations frozen into the plasma flow. This [174] is interpreted as isobaric entropy fluctuations in which density gradients are exactly opposed to temperature gradients. By being mixed with surrounding fluctuations, the spectrum of this mode can conform to a turbulent one, thus contributing a significant amount of the turbulent fluctuations (this is effect, in fact, noticeable as the cause of the twinkling of star light by turbulent density fluctuations in the Earth atmosphere).

For diffusion of cosmic rays, fast magnetosonic and Alfvén waves are considered most important. A current review on the limits of linear diffusion theories is e.g. given by Yan & Lazarian [175, 176].

Many of the microscopic details of interactions between MHD waves and CR particles are not known to this day. It is even discussed that the quasi-linear theory is not enough in describing CR diffusion, and nonlinear orders have to be taken into account [176]. Overall, it is not predictable how the cosmic ray diffusion coefficient behaves in real astrophysical scenarios. Thus one resorts to QLT theory, as given in section 2.1. One can then use parameter fitting routines to derive simple models in agreement with experimental data, as is commonly done with the Galprop and Dragon packages, e.g. [56].
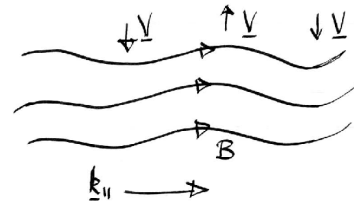
Figure A.3. Alfvén waves are transversal oscillations, propagating along the direction of the magnetic field. Their restoring force is given by the magnetic pressure.

A.4. Details of local transport models

In this appendix, details of the model evaluation in section 3.4.2 are given. In this chapter, the spectra of $\bar{p}/p$, B/C and $^{10}Be/^{9}Be$ have solar modulation applied to best fit the data, but for reasons of readability, the potential is not given. The corresponding χ^2 values are listed in Tab. 3.4.

Slow-Wall-Fast-Interior setups "A"
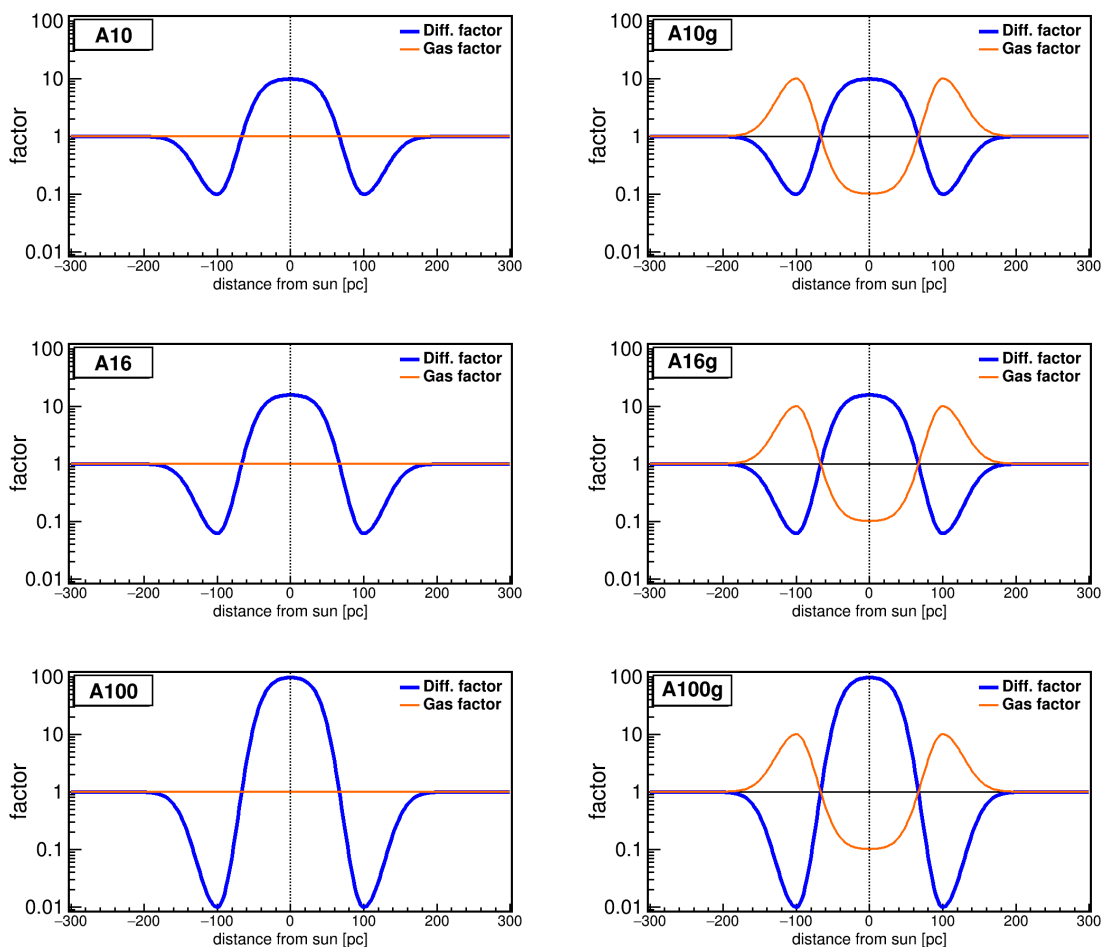
Figure A.4. The functional shape of type A models. Interior diffusion is fastened by a varying factor, Wall diffusion is slowed by the same factor. In "g" models, the gas density is increased in the Walls and decreased in the Interior. The y-axis shows the factor applied to diffusion (blue) and to gas (orange), the x-axis the distance to the Sun in pc. These model bubbles are spherically symmetric.

First, we investigate models that consider enhanced scattering in the bubble walls, and an essential cleaning of magnetic turbulences in the hot bubble interior. The model definitions A10, A10g, A16, A16g, A100 and A100g are given in Figs. A.4.

Striking about the A*g models is that the low-diffusion (thus long residence) region coincides with the thick wall gas. This allows for a strong enhancement of secondary production, visible in $e^+, \bar{p}/p, {}^{10}Be/{}^9Be$ and B/C spectra. For the intermediate E $\sim$ 1..10 GeV positrons, this allows for a better description of the measurement than the reference model BG (which is, compared with the whole K450 range, a generally e^+-weak model). However, in the case of A100g the medium-energy e^+ prediction exceeds the measurement by far: A diffusion modulation of maximum factor 100 up and down is too strong when taking the gas in the wall into account. The factor 16 scenario was included as it was found to be the "strongest" setups still in agreement with this medium-energy positron population. The steady decline in e^+ flux towards higher energies, however, remains unchanged, i.e. this modification does not allow for a description of the highly energetic positron population.

The change in prediction of anisotropy is seen in Figs. A.6, A.7 and is summarized in Tab. A.5. It appears that over a certain modification strength, these bubbles leads to a significant reduction in δ (while the anisotropy rises for A10(g), it decreases for A16(g) and even for A100(g), where the local diffusion coefficient becomes enlargened by a factor of 100!). When accounting for the gas, the anisotropy slightly decreases for $p/p_{[40,80]}$ and $e^\pm$, but the effect on e^+/p anisotropy is more complicated due to the change in positron production in the Bubble Walls.

The enhancement of secondary production is also seen in the secondary hadronic ratios. In fact, the choice of factor 10 vs. 16 is critical for B/C - the former case still compatible with the measurement, while the slighly stronger scenario suffers an overproduction of boron, i.e. the cosmic rays experience too much grammage. ${}^{10}Be/{}^9Be$ also shows an increase in residence time (but there is still a lack of precision measurement except for the few ACE-CRIS data). For the case of ${}^3He/{}^4He$, model prediction actually gets improved for $\approx$ 0.9..3GeV.

Model	p	$p/p_{[40,80]}$	e^-	e^+	$e^\pm$	e^+/p
BG	$5.35 \cdot 10^{-4}$	$5.97 \cdot 10^{-4}$	$3.20 \cdot 10^{-4}$	$6.58 \cdot 10^{-4}$	$8.58 \cdot 10^{-4}$	$1.39 \cdot 10^{-4}$
A10	$7.95 \cdot 10^{-4}$	$8.96 \cdot 10^{-4}$	$4.74 \cdot 10^{-4}$	$9.76 \cdot 10^{-4}$	$1.27 \cdot 10^{-3}$	$2.21 \cdot 10^{-4}$
A10g	$6.33 \cdot 10^{-4}$	$7.10 \cdot 10^{-4}$	$3.76 \cdot 10^{-4}$	$7.76 \cdot 10^{-4}$	$1.03 \cdot 10^{-3}$	$2.23 \cdot 10^{-4}$
A16	$4.19 \cdot 10^{-4}$	$4.72 \cdot 10^{-4}$	$2.50 \cdot 10^{-4}$	$5.08 \cdot 10^{-4}$	$6.71 \cdot 10^{-4}$	$1.15 \cdot 10^{-4}$
A16	$4.19 \cdot 10^{-4}$	$4.72 \cdot 10^{-4}$	$2.48 \cdot 10^{-4}$	$5.14 \cdot 10^{-4}$	$6.82 \cdot 10^{-4}$	$1.66 \cdot 10^{-4}$
A100	$7.15 \cdot 10^{-5}$	$8.96 \cdot 10^{-5}$	$4.28 \cdot 10^{-5}$	$7.90 \cdot 10^{-5}$	$1.22 \cdot 10^{-4}$	$3.74 \cdot 10^{-5}$
A100g	$5.99 \cdot 10^{-5}$	$7.76 \cdot 10^{-5}$	$3.55 \cdot 10^{-5}$	$8.23 \cdot 10^{-5}$	$1.15 \cdot 10^{-4}$	$4.90 \cdot 10^{-5}$
upper limit		$3 \cdot 10^{-3}$	$6 \cdot 10^{-3}$		$5.28 \cdot 10^{-3}$	$2 \cdot 10^{-2}$
		AMS-02*	AMS-02*		Fermi-LAT	AMS-02*
min. cumul. E	16 GeV	80 GeV	16 GeV	16 GeV	60 GeV	16 GeV
max. cumul. E	1.8 TeV	1.8 TeV	350 GeV	350 GeV	480 GeV	350 GeV

Figure A.5. Dipole anisotropy in cumulative energy bins, for "A" bubbles
* ongoing work [99]).
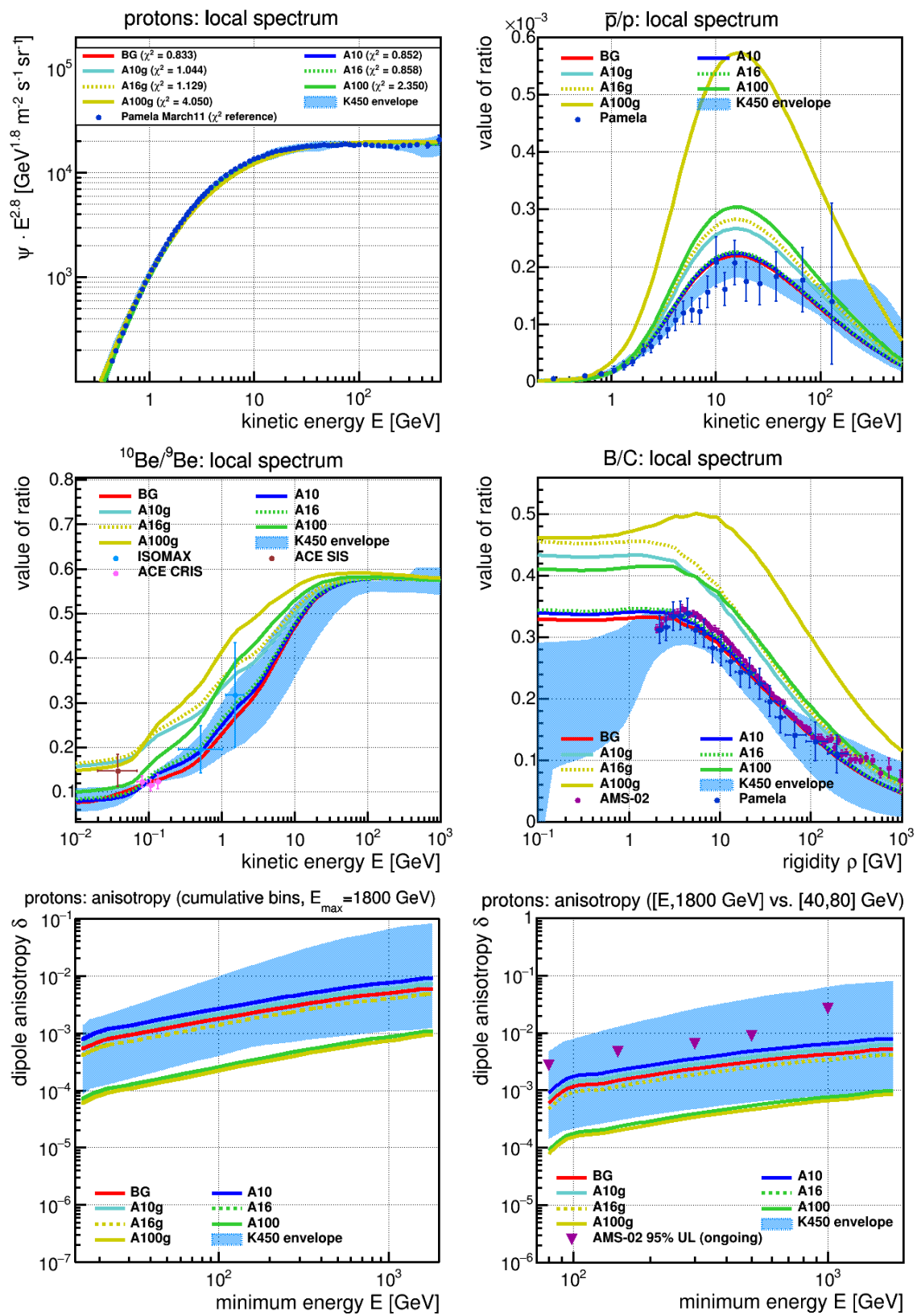
Figure A.6. Hadronic observables in type A bubbles. In this order: Proton spectrum (scaled with $E^{2.8}$), $\bar{p}/p$, $^{10}Be/^{9}Be$, B/C and dipole anisotropy of protons and protons relative in energy.
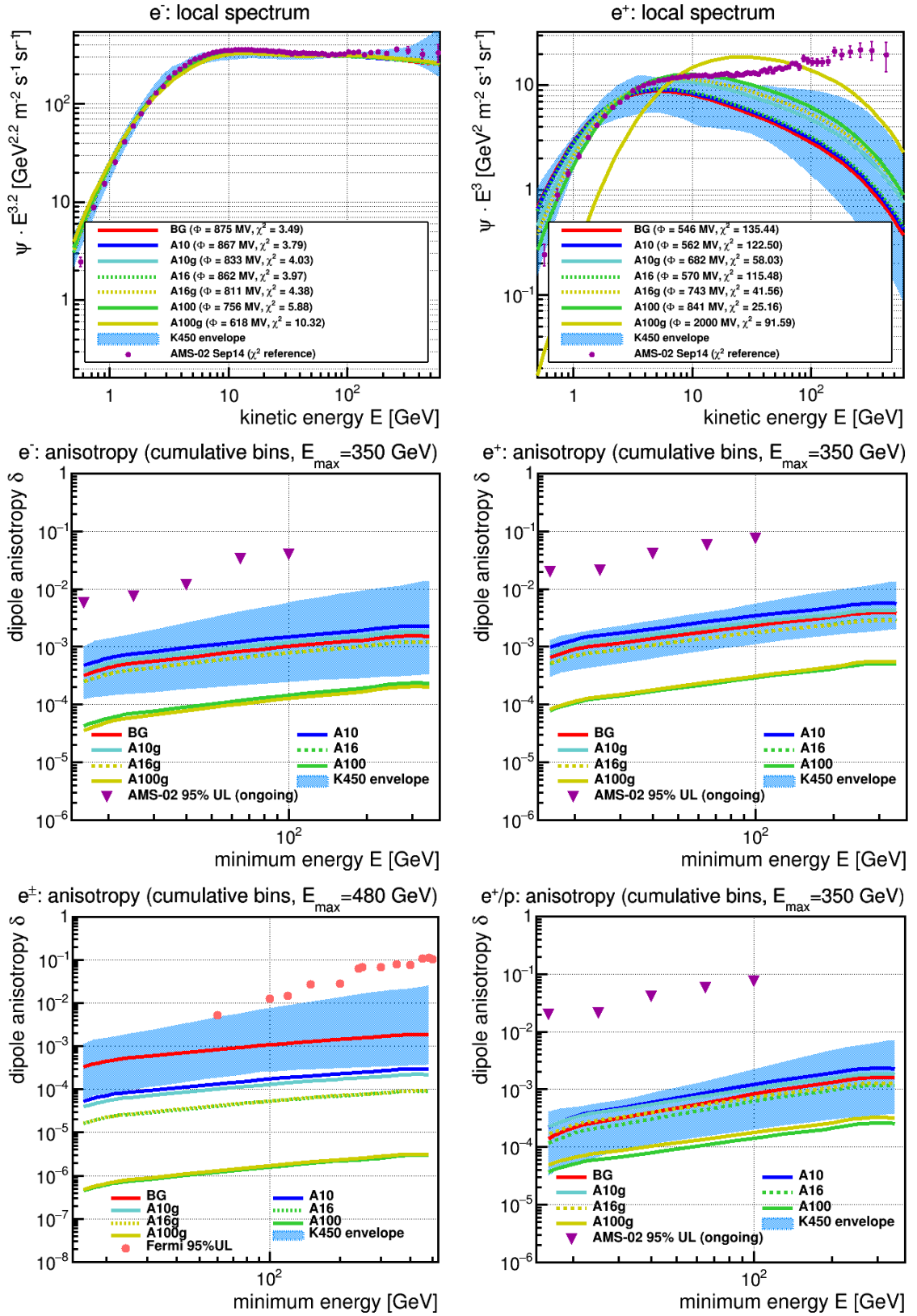
Figure A.7. Leptonic observables in type A bubbles. In this order: Electron spectrum (scaled with $E^{3.2}$), positron spectrum (scaled with E^3) and dipole anisotropy of electrons, protons, lepton sum and positrons relative to protons.

Fast-Wall-Slow-Interior setups "B"
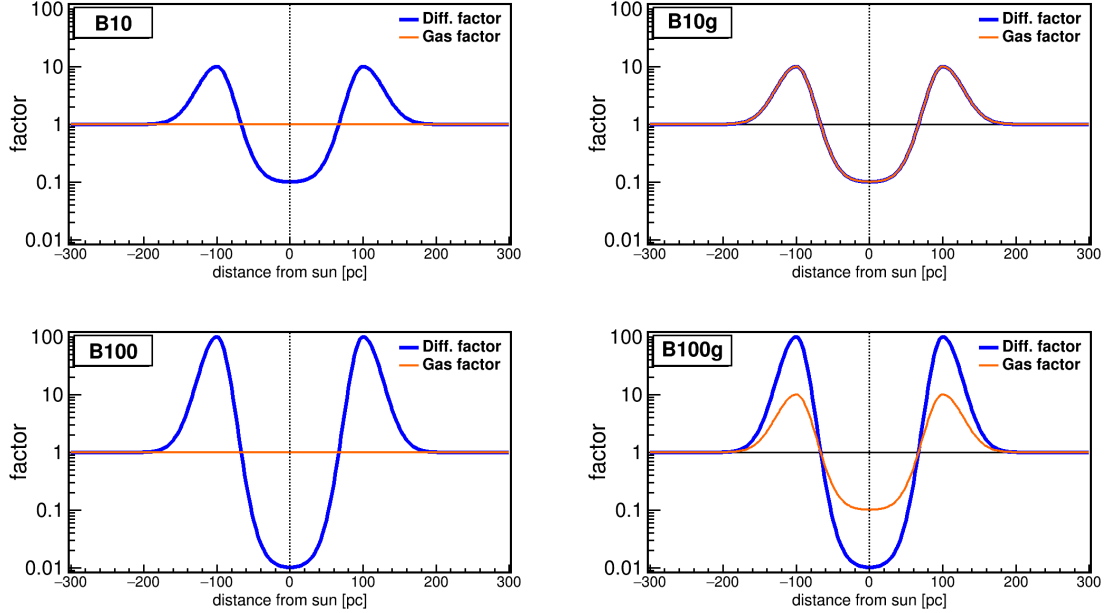
Figure A.8. The functional shape of type B models. Interior diffusion is slowed by a varying factor, Wall diffusion is fastened by the same factor. In "g" models, the gas density is increased in the Walls and decreased in the Interior. The y-axis shows the factor applied to diffusion (blue) and to gas (orange), the x-axis the distance to the Sun in pc. These model bubbles are spherically symmetric.

In the "opposite" picture, it would be actually easier for cosmic rays to enter the bubble wall, due to turbulence damping by ion-neutral friction. Then, towards the interior of the bubble, relics of the bubble expansion could have left behind strong chaotic magnetic fields, increasing the scattering. In this case, the denser gas would be passed more quickly and the amount of extra secondary production is little (and no threat is posed in outmatching medium-energy positrons). Also therefore, the Bxg setups do not differ too greatly from the Bx ones, in any of the particle spectra. An exception are the $p, e^+, e^+/p$ anisotropies, this will be highlighted below.

Model	p	$p/p_{[40,80]}$	e^-	e^+	$e^\pm$	e^+/p
BG	$5.35 \cdot 10^{-4}$	$5.97 \cdot 10^{-4}$	$3.20 \cdot 10^{-4}$	$6.58 \cdot 10^{-4}$	$8.58 \cdot 10^{-4}$	$1.39 \cdot 10^{-4}$
B10	$5.34 \cdot 10^{-5}$	$5.97 \cdot 10^{-5}$	$3.22 \cdot 10^{-5}$	$6.51 \cdot 10^{-5}$	$8.64 \cdot 10^{-5}$	$1.35 \cdot 10^{-5}$
B10g	$5.35 \cdot 10^{-5}$	$5.97 \cdot 10^{-5}$	$3.22 \cdot 10^{-5}$	$6.07 \cdot 10^{-5}$	$8.64 \cdot 10^{-5}$	$1.05 \cdot 10^{-5}$
B100	$1.62 \cdot 10^{-6}$	$1.79 \cdot 10^{-6}$	$1.06 \cdot 10^{-6}$	$2.20 \cdot 10^{-6}$	$2.93 \cdot 10^{-6}$	$8.23 \cdot 10^{-7}$
B100g	$1.63 \cdot 10^{-6}$	$1.79 \cdot 10^{-6}$	$1.07 \cdot 10^{-6}$	$1.70 \cdot 10^{-6}$	$2.91 \cdot 10^{-6}$	$2.99 \cdot 10^{-7}$
upper limit		$\mathbf{3 \cdot 10^{-3}}$	$\mathbf{6 \cdot 10^{-3}}$		$\mathbf{5.28 \cdot 10^{-3}}$	$\mathbf{2 \cdot 10^{-2}}$
		AMS-02*	AMS-02*		Fermi-LAT	AMS-02*
min. cumul. E	16 GeV	80 GeV	16 GeV	16 GeV	60 GeV	16 GeV
max. cumul. E	1.8 TeV	1.8 TeV	350 GeV	350 GeV	480 GeV	350 GeV

Figure A.9. Dipole anisotropy in cumulative energy bins, for "B" bubbles
* ongoing work [99]).
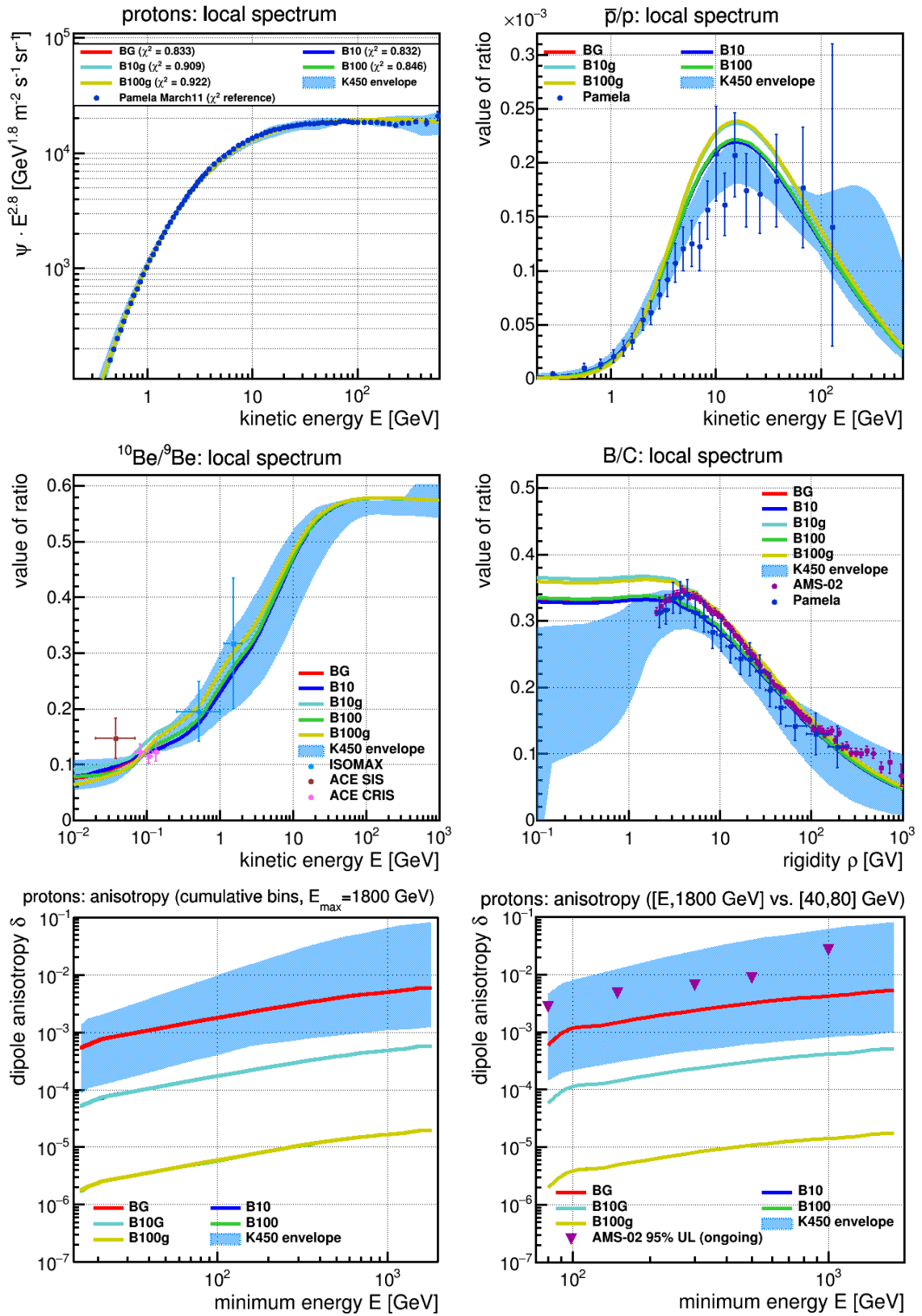
Figure A.10. Hadronic observables in type B bubbles. In this order: Proton spectrum (scaled with $E^{2.8}$), $\bar{p}/p$, $^{10}Be/^{9}Be$, B/C and dipole anisotropy of protons and protons relative in energy.
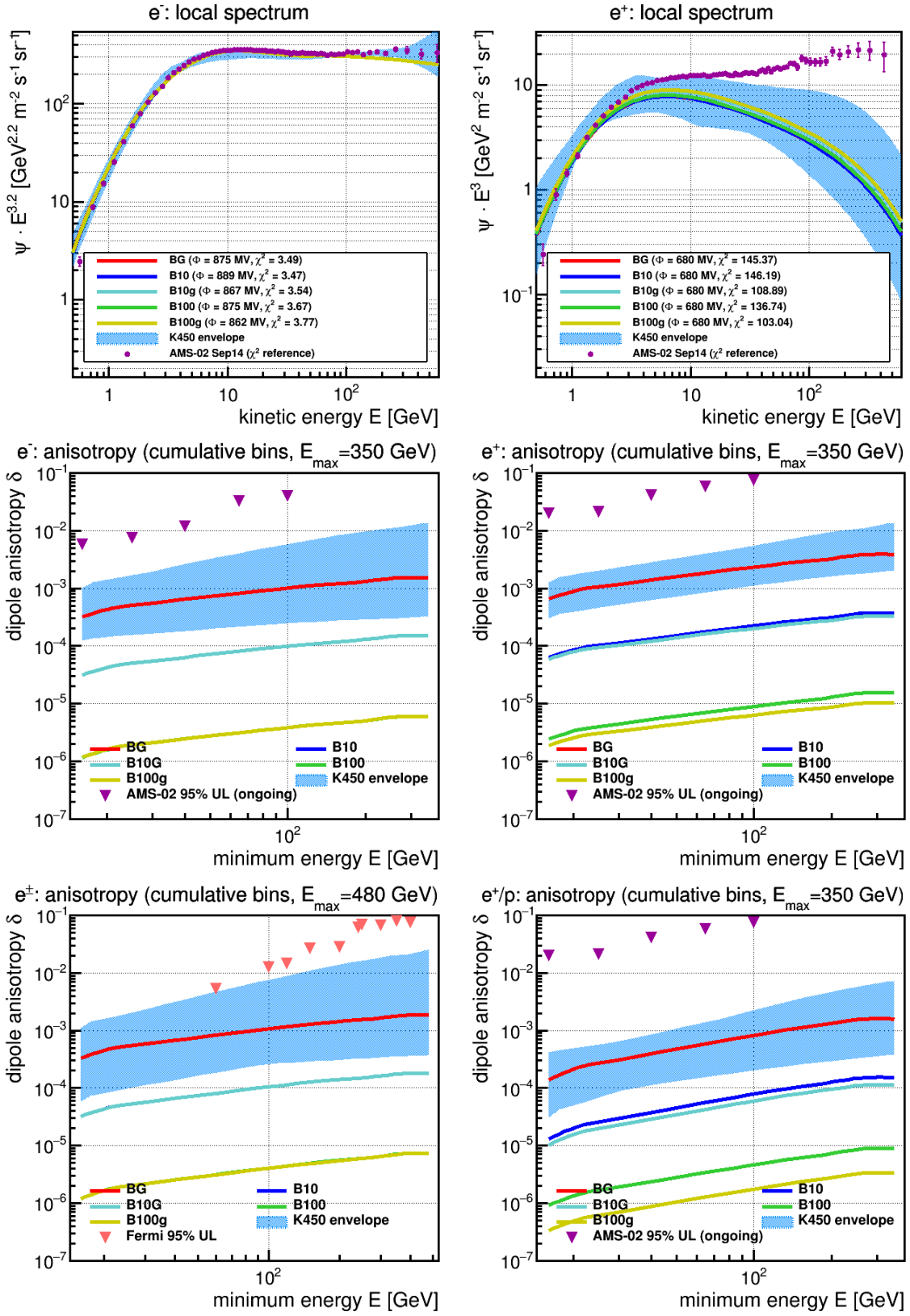
Figure A.11. Leptonic observables in type B bubbles. In this order: Electron spectrum (scaled with $E^{3.2}$), positron spectrum (scaled with E^3) and dipole anisotropy of electrons, protons, lepton sum and positrons relative to protons.

Interestingly, both of the mutually-inverse "A" and "B" scenarios presented so far show a drop in the expected dipole anisotropy of protons and leptons (if the modification is strong enough, so excluding A10(g)), but the drop in the "B" scenarios is somewhat more pronounced (of all models considered, the most extreme example is B100 that e.g. for the proton anisotropy shows a drop in $|\delta N|/N$ of $\sim /frac13$, which together with the actual factor $\frac{1}{100}$ in D results in a drop of $\sim 0.3\%$. To illuminate this further, we turn to the local density distribution $N(\vec{r})$ of the species (Fig. A.12 for p, A.13 for e^+). We focus on the X and Z directions through the sun, as the distribution is very flat in the local Y direction and no further insight is gained thereof. The sun is at $\vec{r}_\odot = (8.3, 0, 0)$ kpc, the "bubble wall peak" in each of the models at ± 0.1 kpc for any direction. The BG distribution is drawn for comparison (red). For the A10 bubble (black), the wall regions are "crowded" from each side: particles near the wall tend to stay longer in the wall region. This also applies for particles touching the wall *for the inside*. As a consequence, the inner distribution is flattened out (over an extension of about 50 pc in each direction from the sun). In the B10 case (blue), the wall regions serve as a kind of "tunnel transportation": From every side, particles can reach any other wall region more easily, thus leading to a shell of particles locally more evenly distributed as the outside region, and from this shell the inwards propagation is leading to a small bump at the place of the earth (best seen in Z directions).

This is qualitatively different. In the B scenarios, the local flattening is due to the symmetry of the choice of our model: If the sun is moved a minor amount in any direction, the local gradient would follow the bumpiness of the density distribution, possibly increasing $\vec{\nabla}N/N$. In contrast, in a A-like scenario the exact position of the center would not be relevant.
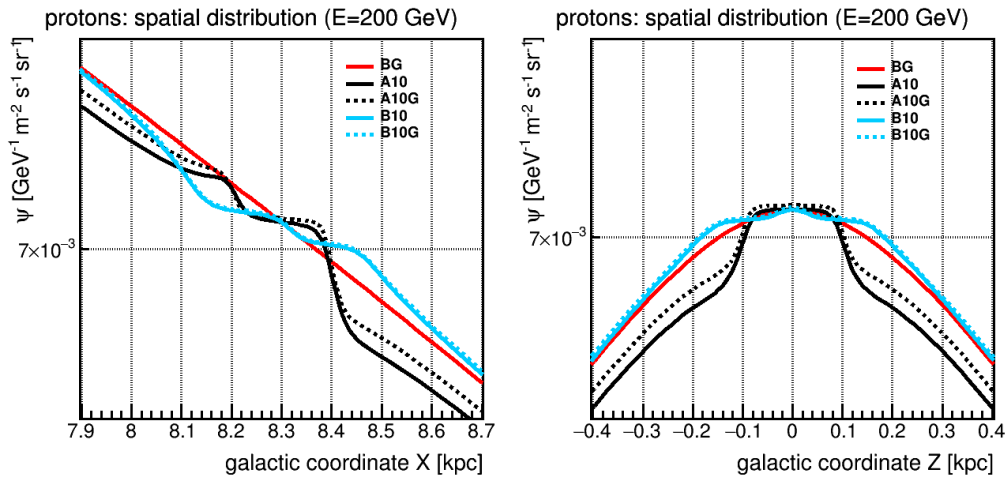
Figure A.12. Spatial distribution of protons at $E = 200\,\text{GeV}$ around the Sun, in the **left** panel for the x direction and in the **right** panel for the z direction.

For positrons, this argument holds in the cases where gas is not affected (solid lines). The A10 model leads to a flat plateau, which is raised above the no-bubble BG distribution because these $E = 200\,\text{GeV}$ leptons are produced directly in place, and the B10 model shows the familiar bump, coincidentally leading to a local flattening. For the A10g bubble, then, the

effect is slightly enhanced due to more secondary production in the wall regions. Now, for the B10g bubble, this overproduction is relatively smaller, because less primary cosmic rays reside in the wall, but at the same time, these are much more evenly distributed throughout the whole wall. This conceals the background anisotropy: The "extra isotropization" in case of the B10g vs. B10 scenario, or B100g vs. B100, is due to an extra component of secondary positrons, created from an evened-out primary distribution inside the denser walls.
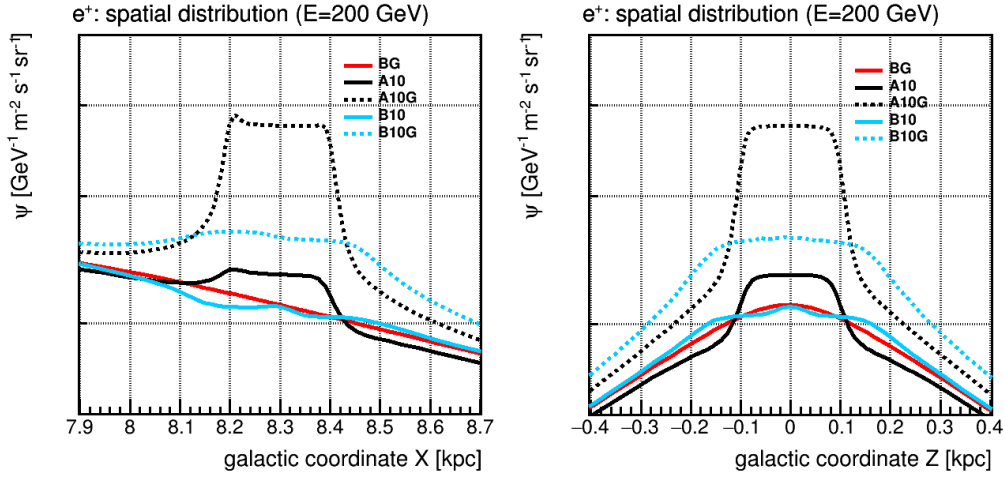
Figure A.13. Spatial distribution of positrons at $E = 200\,\text{GeV}$ around the Sun, in the **left** panel for the x direction and in the **right** panel for the z direction.

In order to support this explanation by secondary production, we can turn to the B/C distribution through the bubbles. If the e^+ distribution is indeed isotropized as an effect of secondary production, we expect the save behavior in this secondary-to-primary ratio. If it were instead a peculiarity of leptonic CRs, e.g. attributable to energy losses, B/C would not show it. As seen, in Fig. A.14 for the X coordinate, our assumption is confirmed.
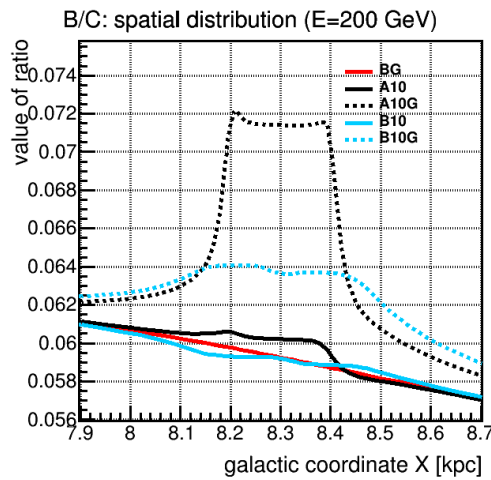
Figure A.14. Comparison of spatial distribution of B/C ($E = 200\,\text{GeV}$) for type A and type B

Slow-Interior setups "c"

In the following set of models, we reject the idea that the bubble wall has a significant effect, or that if it has, it does not have an antithetical behavior to the interior. Thus, we first *decrease* the local diffusion coefficient, and in the next subsection, we investigate a pure increase.

In terms of secondary production, these models show an interesting flexibility, e.g. e^+ or B/C between c100 and c100g: Without modifying the gas distribution, the slowed-down propagation in the bubble interior leads to a large amount of extra secondaries, similar to what was described in the wall regions of the Slow-Fall-Fast-Interior bubbles "A". For the secondary production visible in B/C, this assumption might be excluded. However, with the local gas density dropping a factor $\frac{1}{10}$ (c100g), the production rate of both these particles drops below the referential K450 range (which, for itself, is no statement of exclusion).
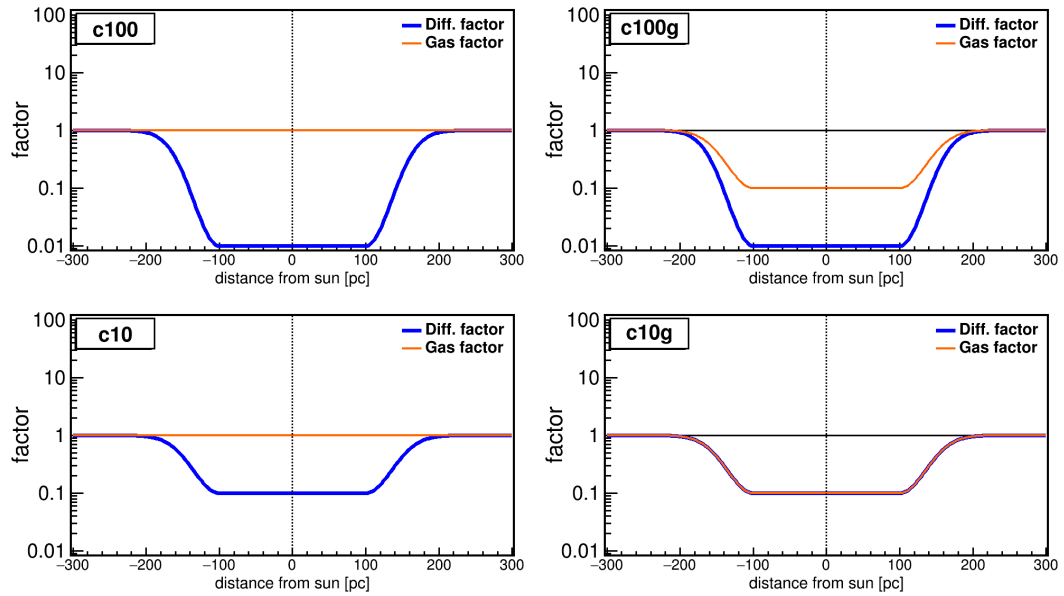
Figure A.15. The functional shape of type c models. Interior diffusion is slowed by a varying factor, the Walls are not accounted for. In "g" models, the gas density is decreased in the Interior. The y-axis shows the factor applied to diffusion (blue) and to gas (orange), the x-axis the distance to the Sun in pc. These model bubbles are spherically symmetric.

Model	p	$p/p_{[40,80]}$	e^-	e^+	$e^\pm$	e^+/p
BG	$5.35 \cdot 10^{-4}$	$5.97 \cdot 10^{-4}$	$3.20 \cdot 10^{-4}$	$6.58 \cdot 10^{-4}$	$8.58 \cdot 10^{-4}$	$1.39 \cdot 10^{-4}$
c10	$8.52 \cdot 10^{-5}$	$9.55 \cdot 10^{-5}$	$5.02 \cdot 10^{-5}$	$1.07 \cdot 10^{-4}$	$1.35 \cdot 10^{-4}$	$2.66 \cdot 10^{-5}$
c10g	$8.53 \cdot 10^{-5}$	$9.55 \cdot 10^{-5}$	$5.04 \cdot 10^{-5}$	$1.10 \cdot 10^{-4}$	$1.34 \cdot 10^{-4}$	$2.65 \cdot 10^{-5}$
c100	$1.05 \cdot 10^{-5}$	$1.19 \cdot 10^{-5}$	$5.89 \cdot 10^{-6}$	$1.44 \cdot 10^{-5}$	$1.59 \cdot 10^{-5}$	$5.96 \cdot 10^{-6}$
c100g	$1.06 \cdot 10^{-5}$	$1.19 \cdot 10^{-5}$	$5.95 \cdot 10^{-6}$	$1.61 \cdot 10^{-5}$	$1.53 \cdot 10^{-5}$	$5.89 \cdot 10^{-6}$
upper limit		$\mathbf{3 \cdot 10^{-3}}$	$\mathbf{6 \cdot 10^{-3}}$		$\mathbf{5.28 \cdot 10^{-3}}$	$\mathbf{2 \cdot 10^{-2}}$
		AMS-02*	AMS-02*		Fermi-LAT	AMS-02*
min. cumul. E	16 GeV	80 GeV	16 GeV	16 GeV	60 GeV	16 GeV
max. cumul. E	1.8 TeV	1.8 TeV	350 GeV	350 GeV	480 GeV	350 GeV

Figure A.16. Dipole anisotropy in cumulative energy bins, for "c" bubbles
* ongoing work [99]).
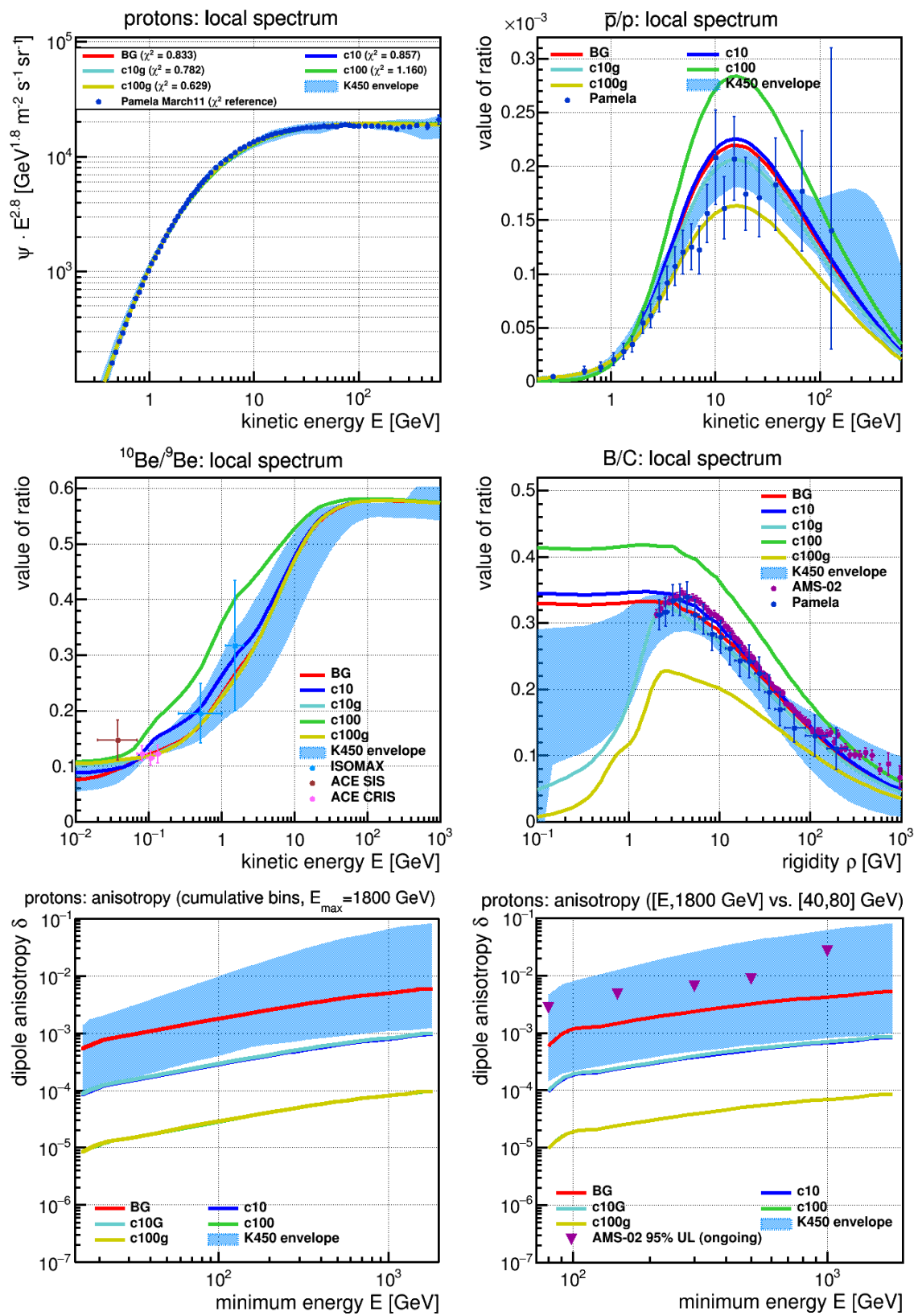
Figure A.17. Hadronic observables in type c bubbles. In this order: Proton spectrum (scaled with $E^{2.8}$), $\bar{p}/p$, $^{10}Be/^9Be$, B/C and dipole anisotropy of protons and protons relative in energy.
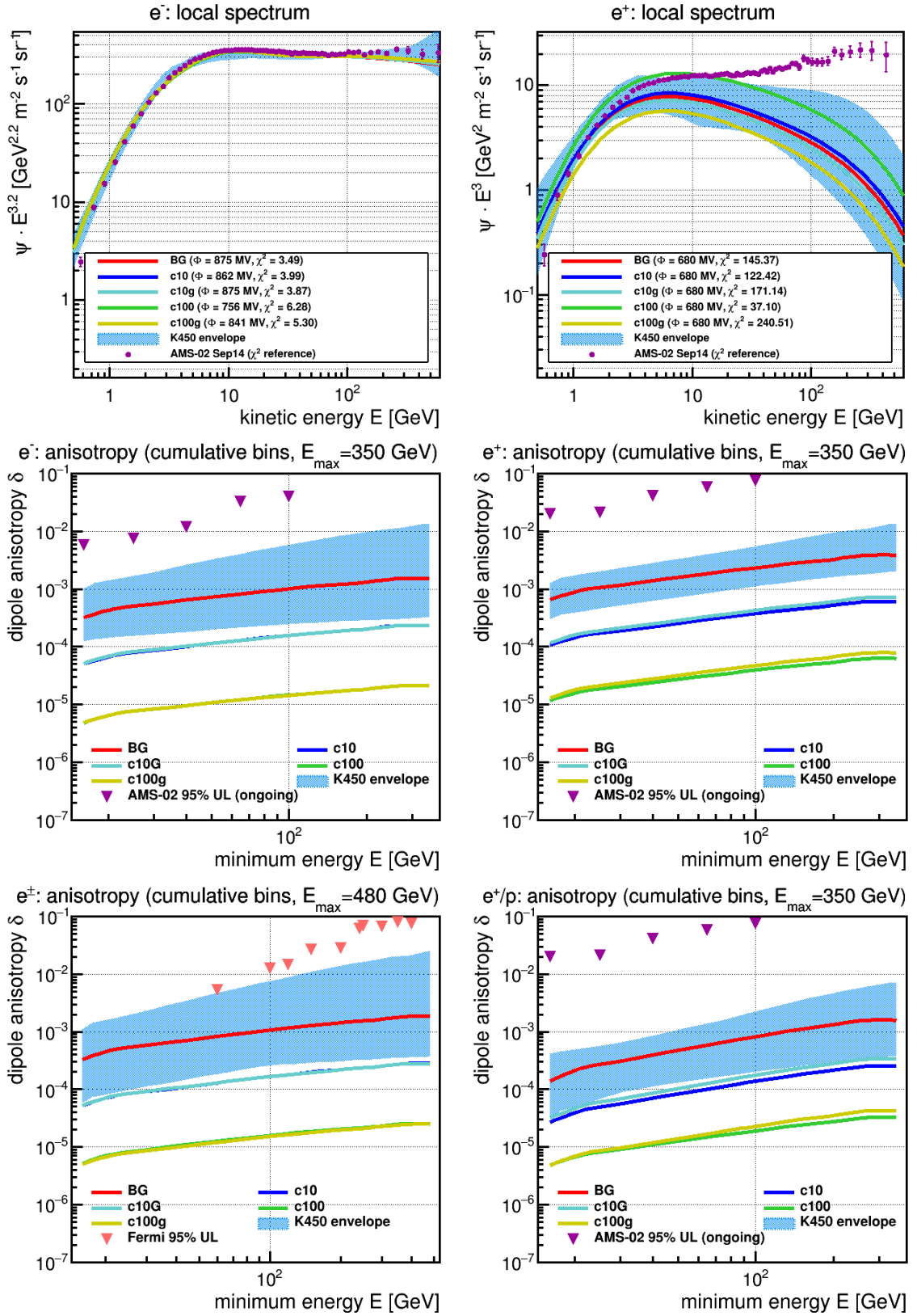
Figure A.18. Leptonic observables in type c bubbles. In this order: Electron spectrum (scaled with $E^{3.2}$), positron spectrum (scaled with E^3) and dipole anisotropy of electrons, protons, lepton sum and positrons relative to protons.

As explained in the introductory sections, the secondary-to-primary observables, $\bar{p}/p$ and B/C are an indicator for the grammage, the total interstellar material a CR particle passed through. The cosmic clock $^{10}Be/^9Be$ further is a measure for their average time of residence in the Galaxy. It is not distinguishable whether this residence was largely inside the local environment or the outer parts of the Milky Way. The reference scenario BG was tuned so that the combination of diffusion coefficient and propagation box height were in agreement with these observables. With local assumptions, the galactic parameters might need to be retuned.

Regions of locally decreased D tend to accumulate more CR density compared to the outside region, in which large gradients can occur (here, by coincidence, the Sun is located nearly exactly at the local CR density maxima. Was the position of the sun shifted, the local gradient could lead to an increase of dipole anisotropy compared with the reference scenario. Note that the factor D entering $\vec{\delta}$ in (2.69) is mostly responsible for the resulting value, as a pure increase in D is expected to lead to a increase in $|\vec{\delta}|$, as shown in the next case of Fast-Interior models. There, also density distributions of the Slow-Interior models are shown.

Fast-Interior setups "C"
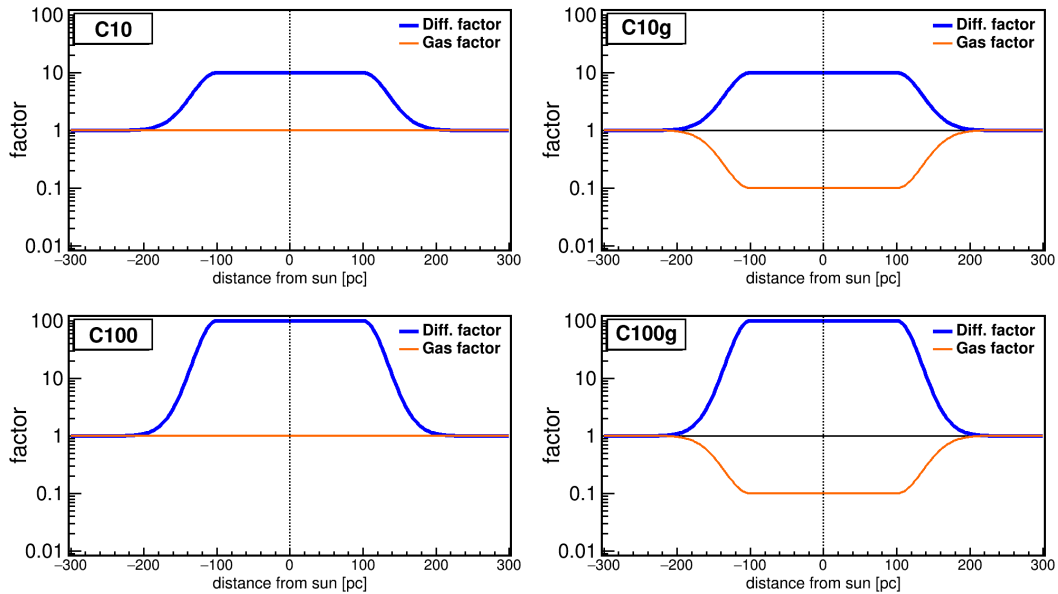
Figure A.19. The functional shape of type c models. Interior diffusion is fastened by a varying factor, the Walls are not accounted for. In "g" models, the gas density is decreased in the Interior. The y-axis shows the factor applied to diffusion (blue) and to gas (orange), the x-axis the distance to the Sun in pc. These model bubbles are spherically symmetric.

In order to address the question, how a Slow-Interior diffusion setup leads to a rise in any dipole anisotropy while a Fast-Interior scenario doesn't, we show - in Fig.A.23 - the local density distribution $N(\vec{r})$ of positrons and protons at high energies (E = 200 GeV). We

compare the most extreme diffusion settings, applying to D a factor 100 (yellow lines) and 0.01 (green), respectively. Dashed lines are considering the local gas density n_H drop to $\frac{n_H}{10}$ in the affected region.

The Fast-Interior setups are the ones under investigation that significantly lead to an *increase* of the local dipole anisotropy, of about a factor of 3. In proton anisotropy, these are actually in conflict, or nearly in conflict with the AMS-02 measurement. It is interesting that the prediction in the models with a factor 100 is similar to the models of factor 10, which means that in the case of stronger modification the $|\nabla N|/N$ term decreases about another factor of 10.

The high-diffusion setups (C100, C100G) allow for a strongly increased inflow of cosmic rays into the bubble, symmetrically from any direction. The steady-state solution is a locally-flattened solution, that, for large distances, reduces to the unmodified BG case. The relative gradient $|\vec{\nabla} N|/N$ of this distribution is then a factor $\approx 3 \cdot 10^{-4}$ smaller than in the bubble-free case, leading to an overall $\approx 3\%$ drop in δ.

Upon entering the low-diffusion setups (c100, c100G), protons experience a higher scattering rate the further they move towards the bubble interior. This leads to a locally confined concentration of every cosmic ray species. Such a scenario is, thus, very sensitive to the exact environment in the closest region around the sun. In our simple setups, the locally large gradient $|\vec{\nabla} N|/N$ exceeds the drop of $\frac{1}{100}$ in diffusion coefficient, raising the local δ.

In the case of protons, the requirement to match high-energy measurements (Pamela, in our case) implies a globally reduced cosmic ray source strength. When the local gas distribution becomes modified (dashed green line), this effect is slightly stronger. . For positrons, the reduction of gas equals a reduction of secondary production site of the same factor $\frac{1}{10}$ (cf. last subsection). In the unmodified gas distribution, the slower diffusion scenario and its local concentration of CR lead to a significant increase in secondary production, which, similar to the scenario A16G, is just in agreement with the e^+ spectrum at intermediate energies (an even slower diffusion coefficient would, in this case, exceed the measured e^+ flux at energies 1..20 GeV.

Model	p	$p/p_{[40,80]}$	e^-	e^+	$e^\pm$	e^+/p
BG	$5.35 \cdot 10^{-4}$	$5.97 \cdot 10^{-4}$	$3.20 \cdot 10^{-4}$	$6.58 \cdot 10^{-4}$	$8.58 \cdot 10^{-4}$	$1.39 \cdot 10^{-4}$
C10	$1.61 \cdot 10^{-3}$	$1.79 \cdot 10^{-3}$	$9.67 \cdot 10^{-4}$	$1.94 \cdot 10^{-3}$	$2.59 \cdot 10^{-3}$	$3.79 \cdot 10^{-4}$
C10g	$1.61 \cdot 10^{-3}$	$1.79 \cdot 10^{-3}$	$9.67 \cdot 10^{-4}$	$1.98 \cdot 10^{-3}$	$2.59 \cdot 10^{-3}$	$4.08 \cdot 10^{-4}$
C100	$1.83 \cdot 10^{-3}$	$2.05 \cdot 10^{-3}$	$1.11 \cdot 10^{-3}$	$2.18 \cdot 10^{-3}$	$2.96 \cdot 10^{-3}$	$4.01 \cdot 10^{-4}$
C100g	$1.83 \cdot 10^{-3}$	$2.05 \cdot 10^{-3}$	$1.11 \cdot 10^{-3}$	$2.24 \cdot 10^{-3}$	$2.96 \cdot 10^{-3}$	$4.52 \cdot 10^{-4}$
upper limit		$3 \cdot 10^{-3}$	$6 \cdot 10^{-3}$		$5.28 \cdot 10^{-3}$	$2 \cdot 10^{-2}$
		AMS-02*	AMS-02*		Fermi-LAT	AMS-02*
min. cumul. E	16 GeV	80 GeV	16 GeV	16 GeV	60 GeV	16 GeV
max. cumul. E	1.8 TeV	1.8 TeV	350 GeV	350 GeV	480 GeV	350 GeV

Figure A.20. Dipole anisotropy in cumulative energy bins, for "C" bubbles
* ongoing work [99]).
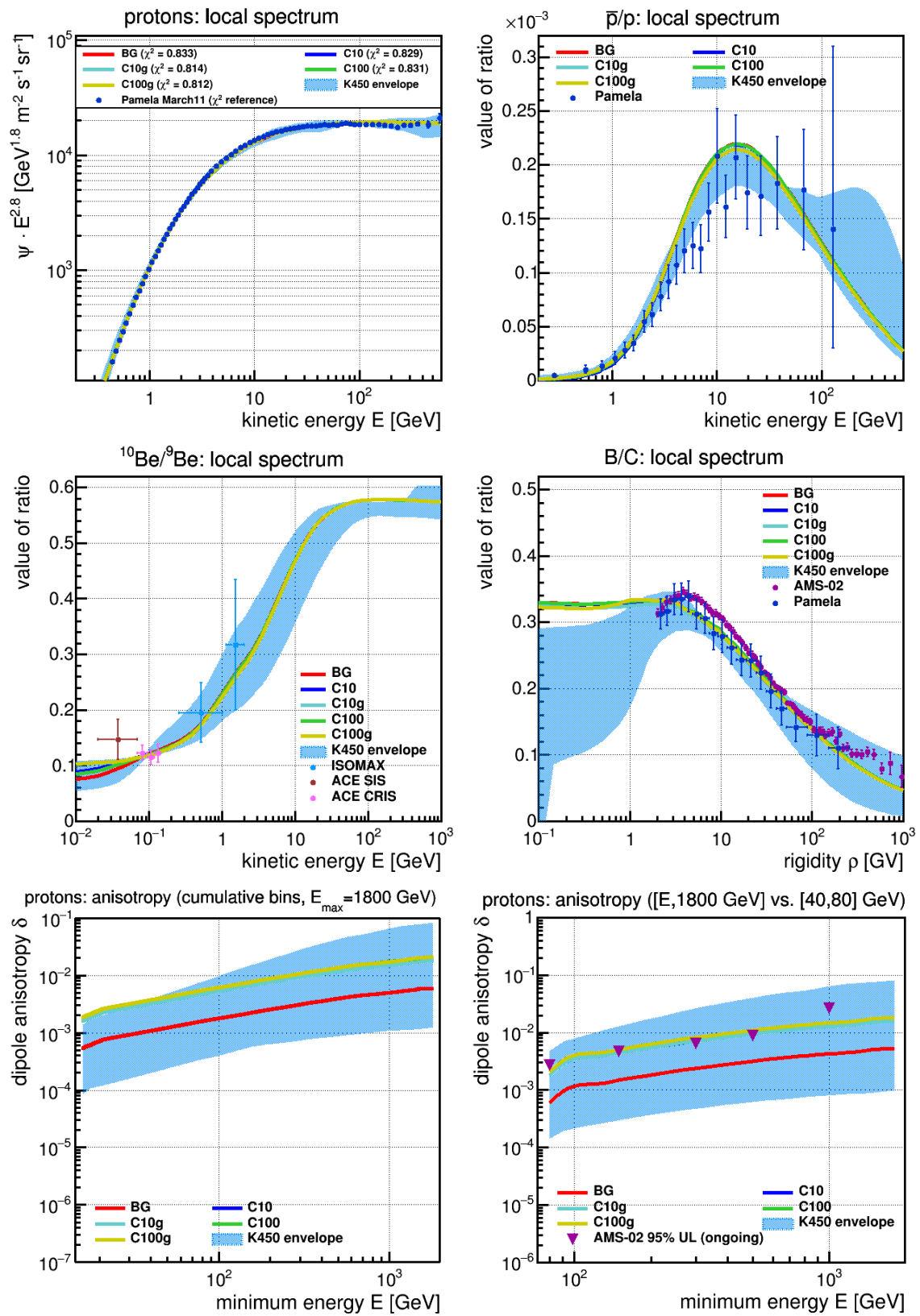
Figure A.21. Hadronic observables in type C bubbles. In this order: Proton spectrum (scaled with $E^{2.8}$), $\bar{p}/p$, $^{10}Be/^{9}Be$, B/C and dipole anisotropy of protons and protons relative in energy.
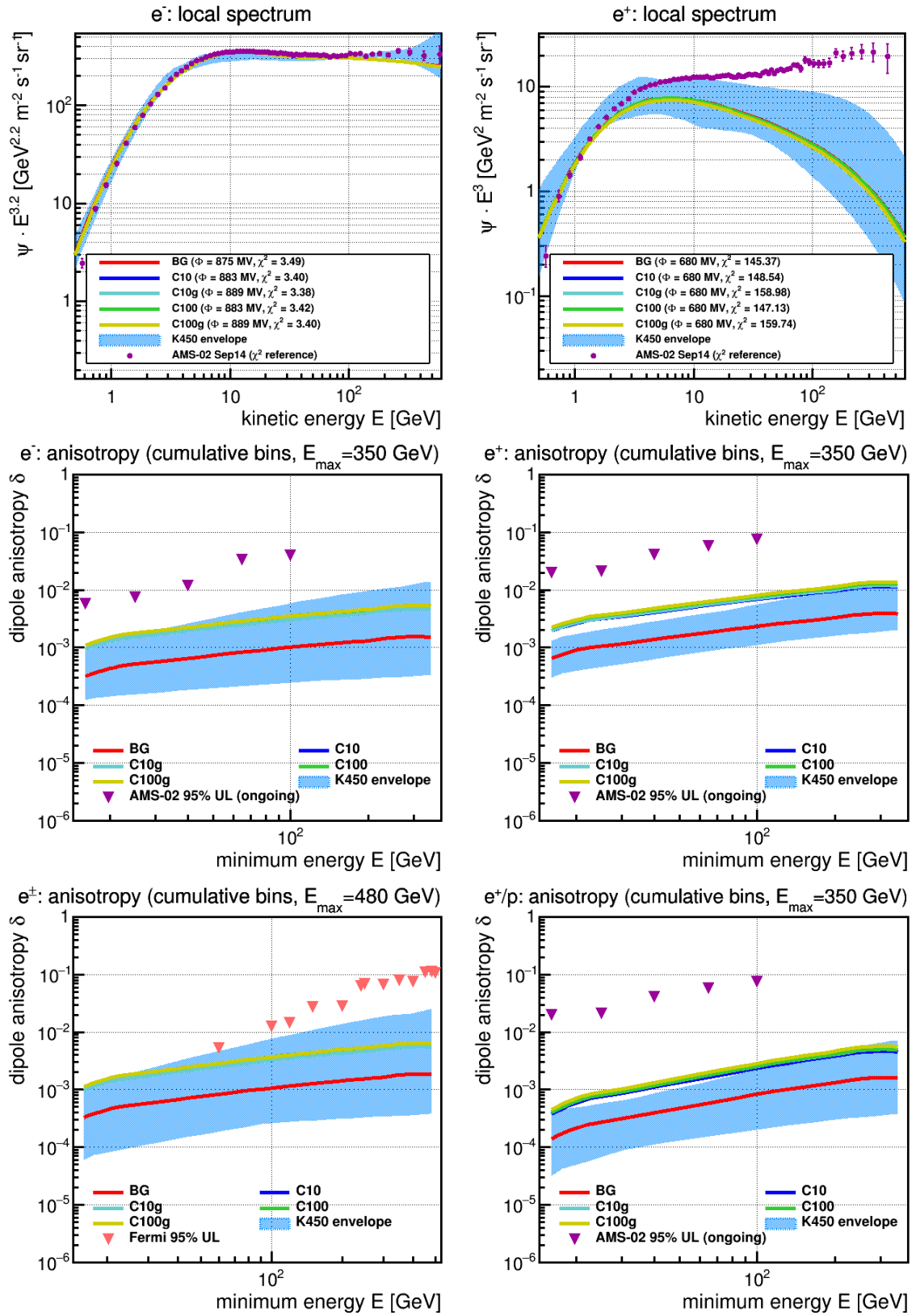
Figure A.22. Leptonic observables in type C bubbles. In this order: Electron spectrum (scaled with $E^{3.2}$), positron spectrum (scaled with E^3) and dipole anisotropy of electrons, protons, lepton sum and positrons relative to protons.

In Fig. A.23, the x distributions of p and e^+ in the Slow-Interior bubbles c100(g) and the Fast-Interior bubbles C100(g) are shown, and their e^+/p anisotropy juxtaposed.
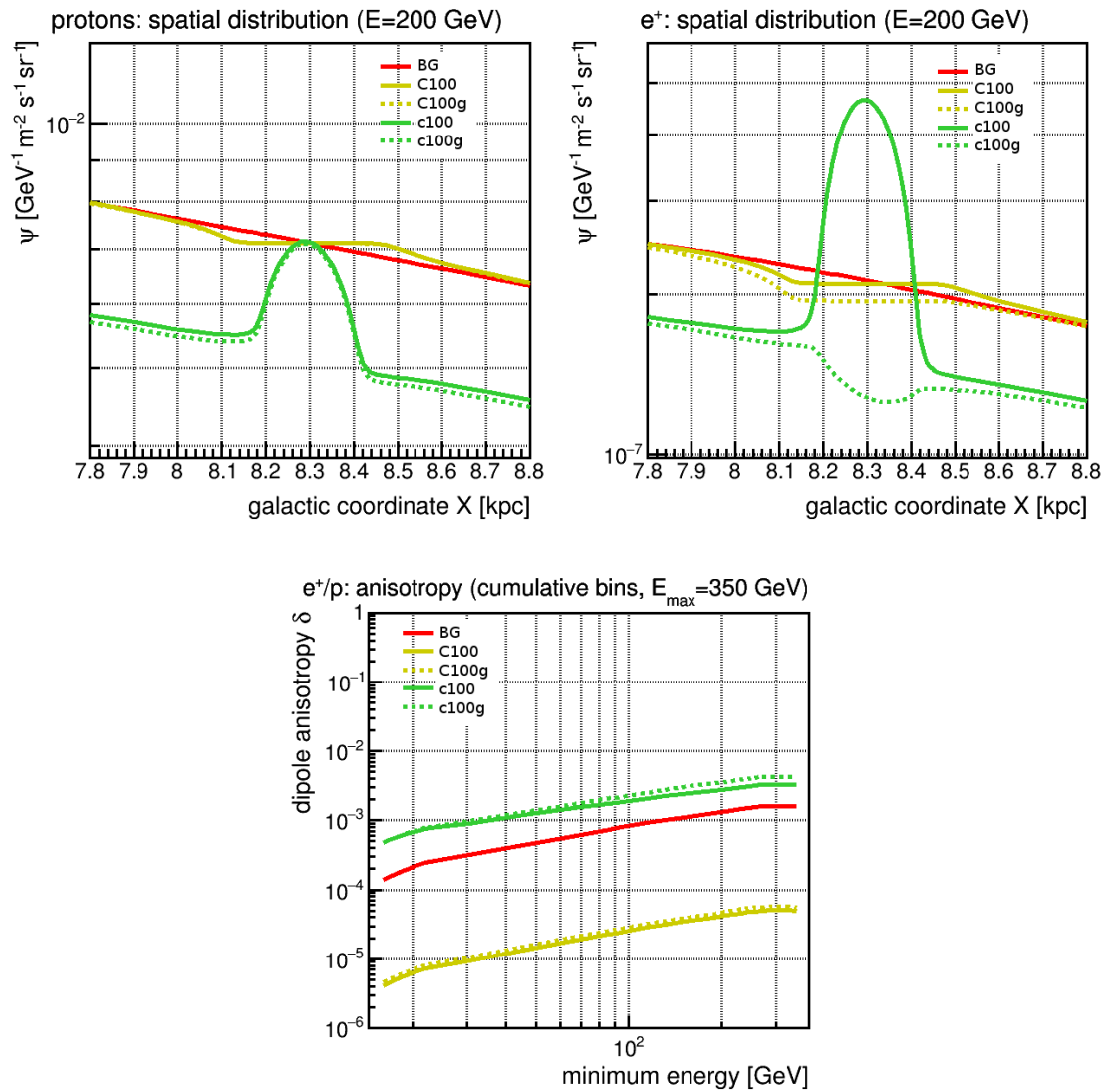
Figure A.23. Comparing types C and c: Density distribution of p (left) and e^+ (middle) at $E = 200$ GeV each. e^+/p anisotropy (right) shown for comparison.

Slow-Wall setups "d"

It might also be the case that the diffusion coefficient in the inner volume is actually described adequately by the galactic average value, but the bubble walls alone cause either a rise or a drop in D_0, depending on the magnetic turbulence in the wall regions. These setups, the *Slow-Wall scenarios* d10, d10g, d100, d100g, resemble a variation of the *Slow-Wall-Fast-Interior* cases "A", in which the center D is not enhanced over the outside value. Therefore, we expect the impact on each observable to be similar, in principle, and can focus on the comparison between the aforementioned models.
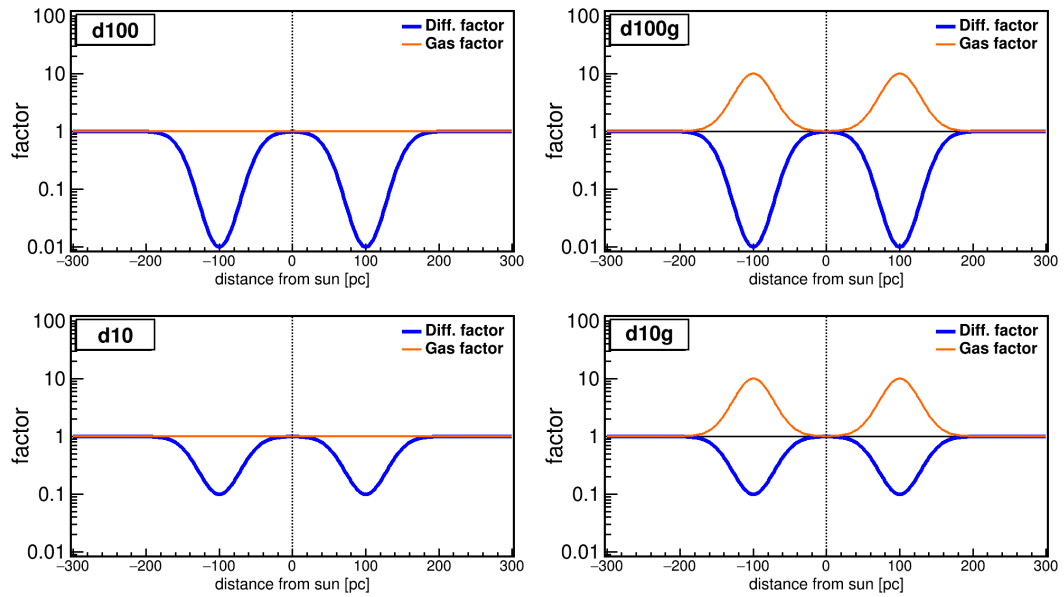
Figure A.24. The functional shape of type d models. Wall diffusion is slowed by a varying factor, the Interior is not accounted for. In "g" models, the gas density is increased in the Walls. The y-axis shows the factor applied to diffusion (blue) and to gas (orange), the x-axis the distance to the Sun in pc. These model bubbles are spherically symmetric.

Model	p	$p/p_{[40,80]}$	e^-	e^+	$e^\pm$	e^+/p
BG	$5.35 \cdot 10^{-4}$	$5.97 \cdot 10^{-4}$	$3.20 \cdot 10^{-4}$	$6.58 \cdot 10^{-4}$	$8.58 \cdot 10^{-4}$	$1.39 \cdot 10^{-4}$
d10	$3.42 \cdot 10^{-4}$	$3.82 \cdot 10^{-4}$	$2.04 \cdot 10^{-4}$	$4.25 \cdot 10^{-4}$	$5.47 \cdot 10^{-4}$	$9.77 \cdot 10^{-5}$
d10g	$3.40 \cdot 10^{-4}$	$3.82 \cdot 10^{-4}$	$2.02 \cdot 10^{-4}$	$4.24 \cdot 10^{-4}$	$5.54 \cdot 10^{-4}$	$1.31 \cdot 10^{-4}$
d100	$8.00 \cdot 10^{-5}$	$8.96 \cdot 10^{-5}$	$4.77 \cdot 10^{-5}$	$9.75 \cdot 10^{-5}$	$1.29 \cdot 10^{-4}$	$3.39 \cdot 10^{-5}$
d100g	$7.83 \cdot 10^{-5}$	$8.96 \cdot 10^{-5}$	$4.63 \cdot 10^{-5}$	$1.03 \cdot 10^{-4}$	$1.38 \cdot 10^{-4}$	$5.49 \cdot 10^{-5}$
upper limit		$\mathbf{3 \cdot 10^{-3}}$	$\mathbf{6 \cdot 10^{-3}}$		$\mathbf{5.28 \cdot 10^{-3}}$	$\mathbf{2 \cdot 10^{-2}}$
		AMS-02*	AMS-02*		Fermi-LAT	AMS-02*
min. cumul. E	16 GeV	80 GeV	16 GeV	16 GeV	60 GeV	16 GeV
max. cumul. E	1.8 TeV	1.8 TeV	350 GeV	350 GeV	480 GeV	350 GeV

Figure A.25. Dipole anisotropy in cumulative energy bins, for "d" bubbles
* ongoing work [99]).
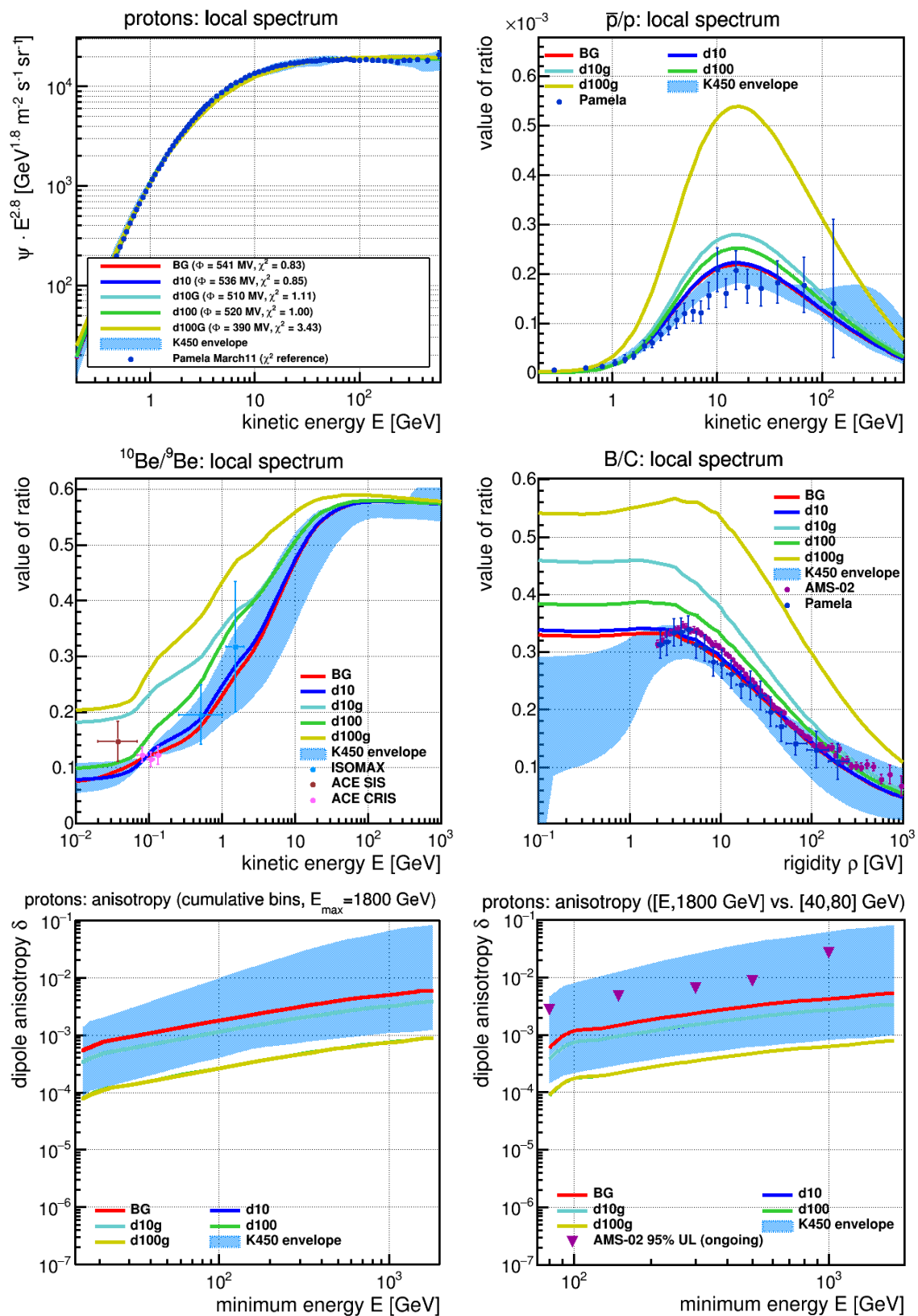
Figure A.26. Hadronic observables in type d bubbles. In this order: Proton spectrum (scaled with $E^{2.8}$), $\bar{p}/p$, $^{10}Be/^9Be$, B/C and dipole anisotropy of protons and protons relative in energy.
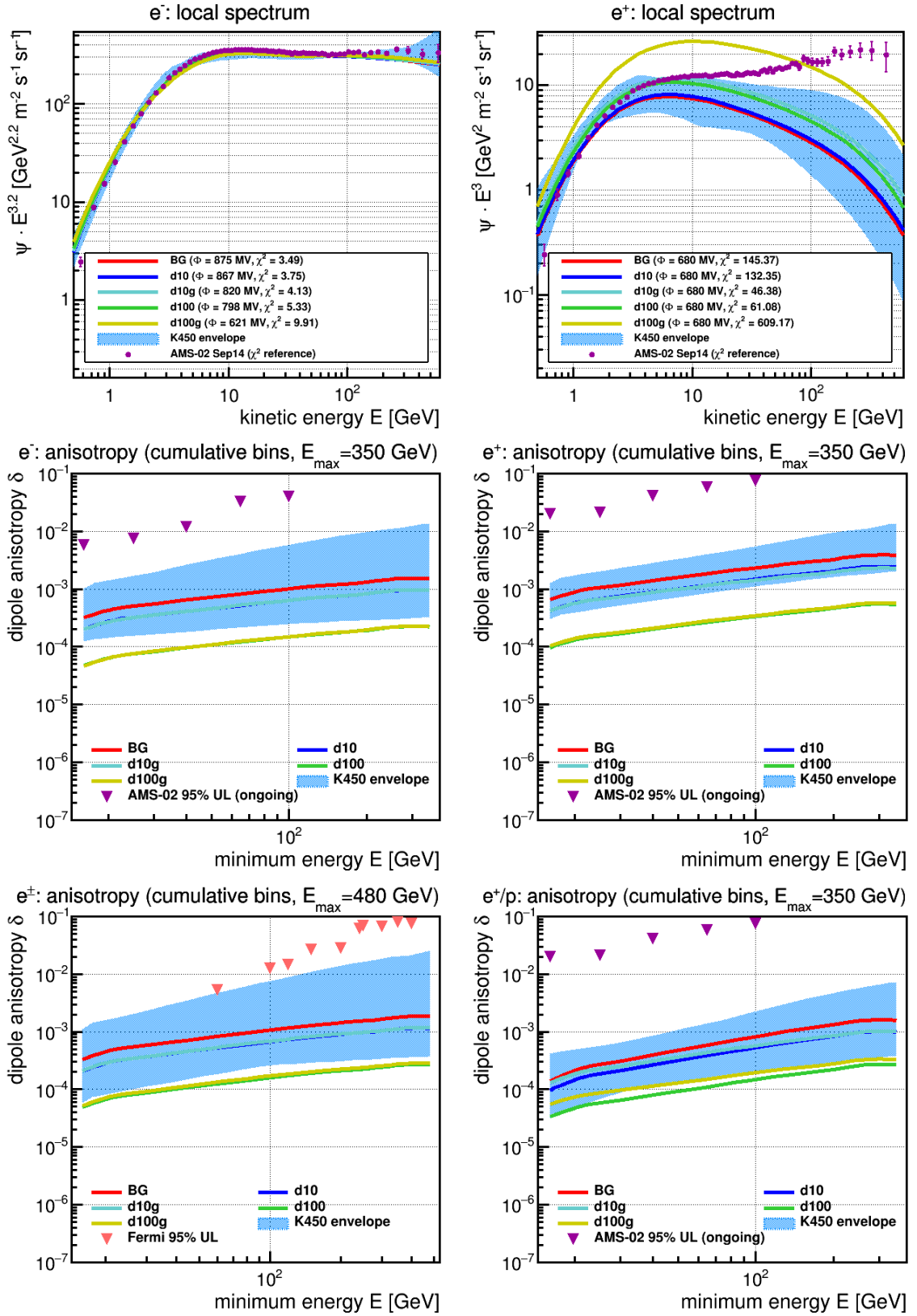
Figure A.27. Leptonic observables in type d bubbles. In this order: Electron spectrum (scaled with $E^{3.2}$), positron spectrum (scaled with E^3) and dipole anisotropy of electrons, protons, lepton sum and positrons relative to protons.

Fast-Wall setups "D"
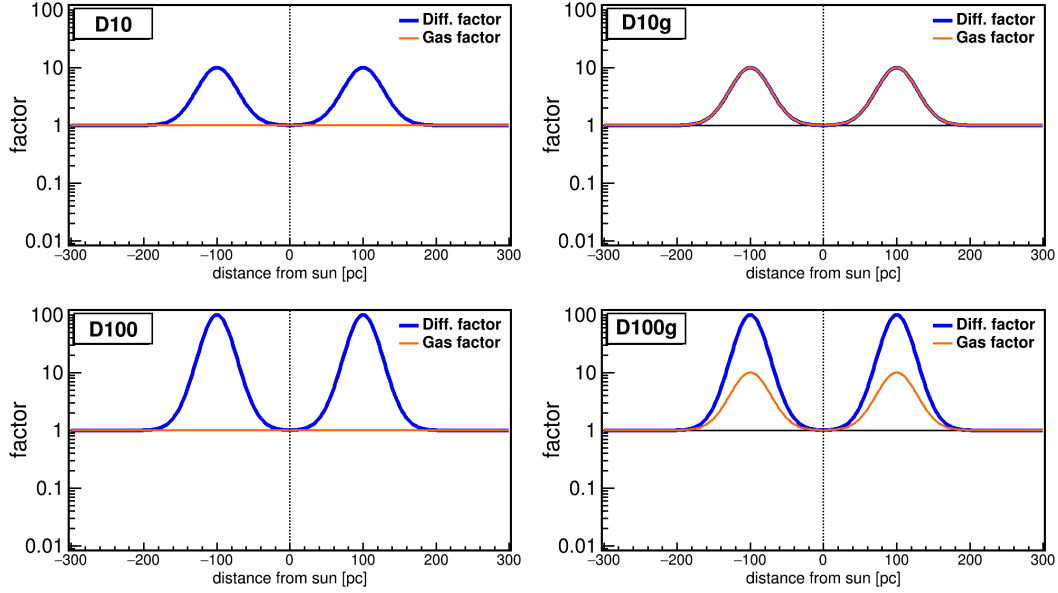
Figure A.28. The functional shape of type D models. Wall diffusion is fastened by a varying factor, the Interior is not accounted for. In "g" models, the gas density is increased in the Walls. The y-axis shows the factor applied to diffusion (blue) and to gas (orange), the x-axis the distance to the Sun in pc. These model bubbles are spherically symmetric.

Similarly, Fast-Wall scenarios are variations of Fast-Wall-Slow-Interior scenarios in which the interior diffusion coefficient is thought to be equal to the outside value. The drop in δ is *less pronounced* than in the B bubbles. The weak scenarios show an extra drop of about $\frac{1}{6}$ each, the strong scenarios a factor $\frac{1}{30}$. $^{10}Be/^{9}Be$ and B/C are slightly enhanced vs. B bubbles, but as for these, the weak setups are very similar to BG.

Model	p	$p/p_{[40,80]}$	e^-	e^+	$e^\pm$	e^+/p
BG	$5.35 \cdot 10^{-4}$	$5.97 \cdot 10^{-4}$	$3.20 \cdot 10^{-4}$	$6.58 \cdot 10^{-4}$	$8.58 \cdot 10^{-4}$	$1.39 \cdot 10^{-4}$
D10	$3.16 \cdot 10^{-4}$	$3.52 \cdot 10^{-4}$	$1.90 \cdot 10^{-4}$	$3.83 \cdot 10^{-4}$	$5.09 \cdot 10^{-4}$	$7.70 \cdot 10^{-5}$
D10g	$3.15 \cdot 10^{-4}$	$3.52 \cdot 10^{-4}$	$1.90 \cdot 10^{-4}$	$3.58 \cdot 10^{-4}$	$5.08 \cdot 10^{-4}$	$6.26 \cdot 10^{-5}$
D100	$5.34 \cdot 10^{-5}$	$5.97 \cdot 10^{-5}$	$3.23 \cdot 10^{-5}$	$6.44 \cdot 10^{-5}$	$8.73 \cdot 10^{-5}$	$1.31 \cdot 10^{-5}$
D100g	$5.36 \cdot 10^{-5}$	$5.97 \cdot 10^{-5}$	$3.24 \cdot 10^{-5}$	$5.76 \cdot 10^{-5}$	$8.70 \cdot 10^{-5}$	$1.04 \cdot 10^{-5}$
upper limit		$\mathbf{3 \cdot 10^{-3}}$	$\mathbf{6 \cdot 10^{-3}}$		$\mathbf{5.28 \cdot 10^{-3}}$	$\mathbf{2 \cdot 10^{-2}}$
		AMS-02*	AMS-02*		Fermi-LAT	AMS-02*
min. cumul. E	16 GeV	80 GeV	16 GeV	16 GeV	60 GeV	16 GeV
max. cumul. E	1.8 TeV	1.8 TeV	350 GeV	350 GeV	480 GeV	350 GeV

Figure A.29. Dipole anisotropy in cumulative energy bins, for "D" bubbles
* ongoing work [99]).
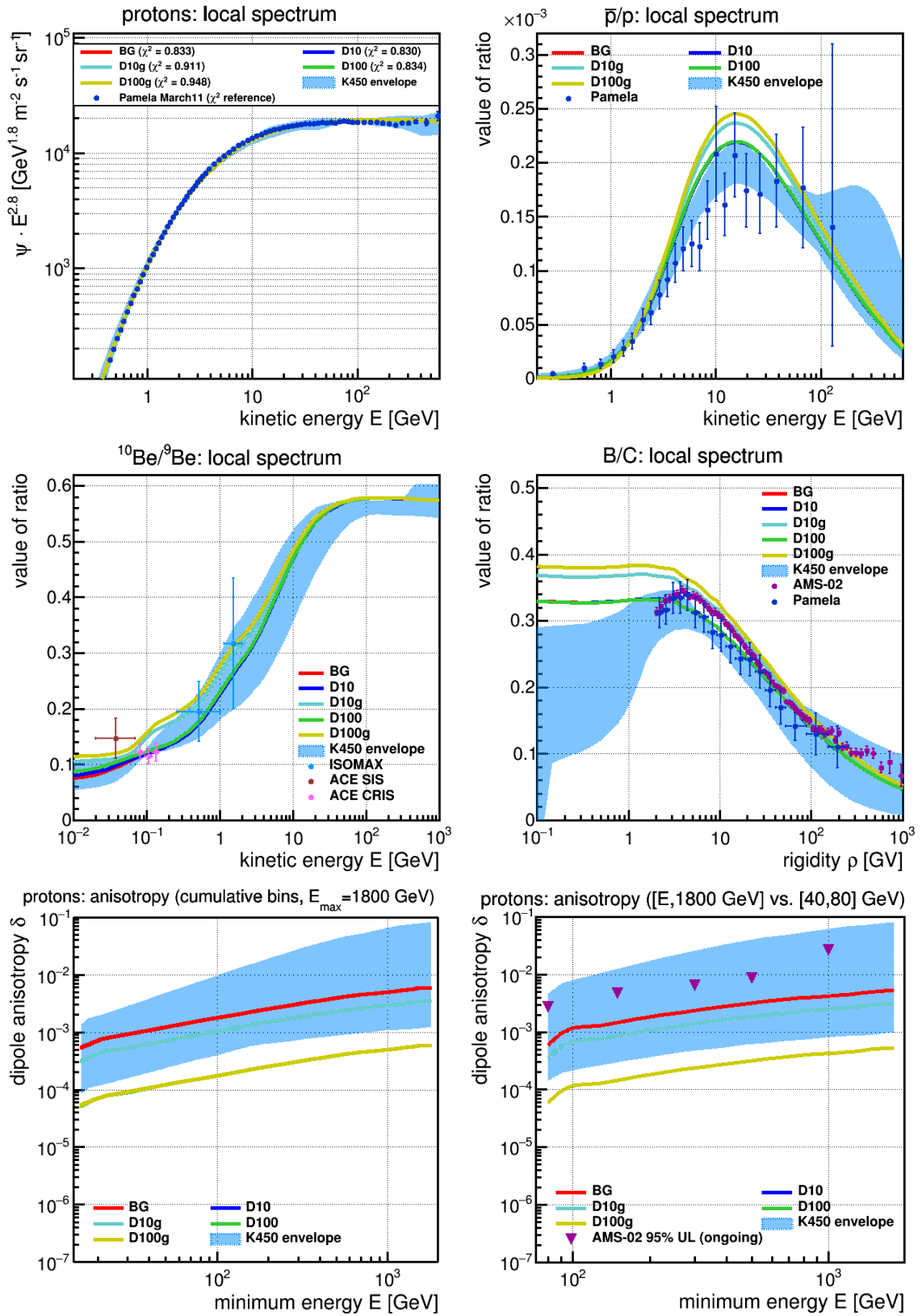
Figure A.30. Hadronic observables in type D bubbles. In this order: Proton spectrum (scaled with $E^{2.8}$), $\bar{p}/p$, $^{10}Be/^{9}Be$, B/C and dipole anisotropy of protons and protons relative in energy.
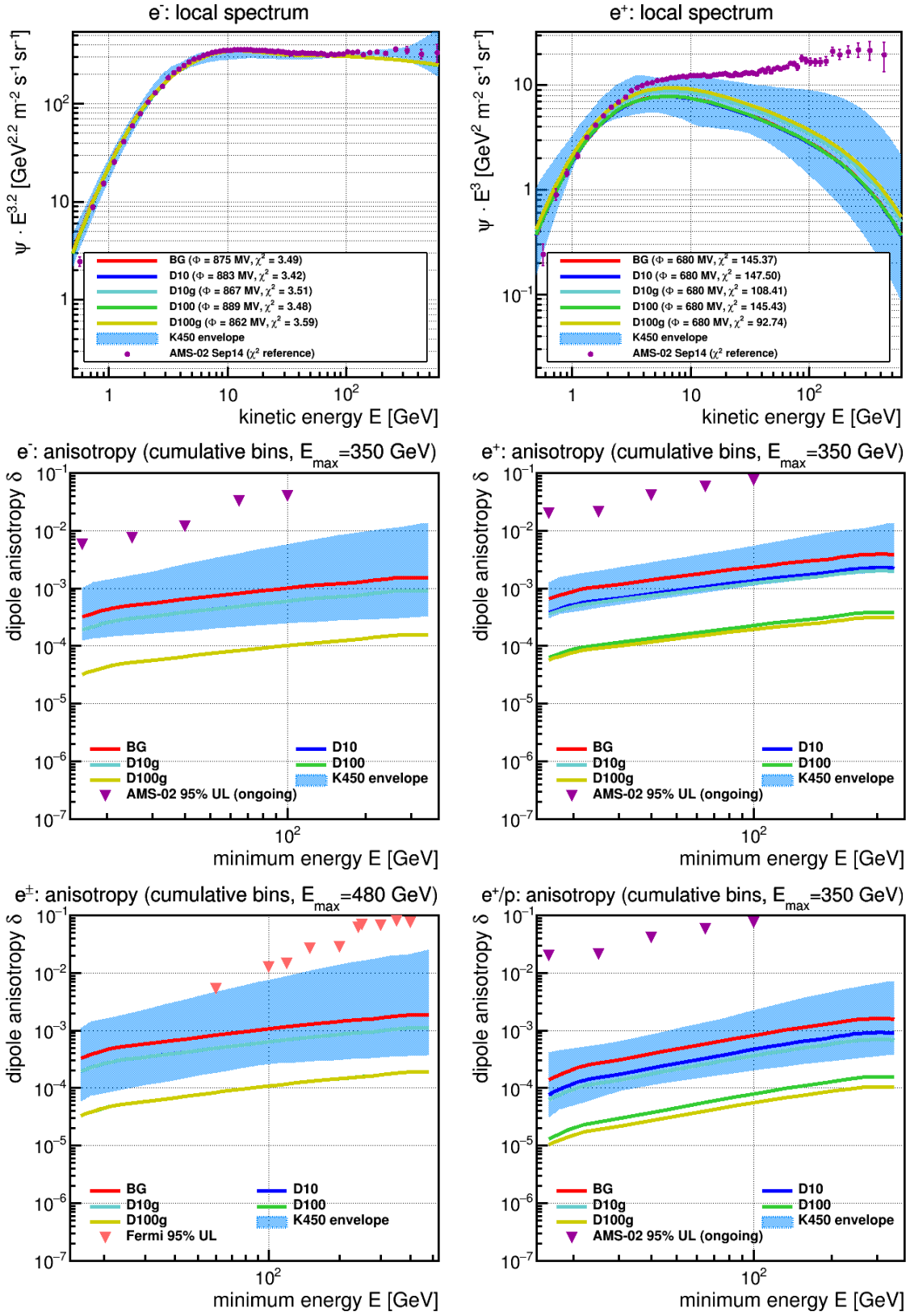
Figure A.31. Leptonic observables in type D bubbles. In this order: Electron spectrum (scaled with $E^{3.2}$), positron spectrum (scaled with E^3) and dipole anisotropy of electrons, protons, lepton sum and positrons relative to protons.

Direct comparison between types d/A and D/B

As the related A10 scenario, the spectra of d10 stay relatively close to the reference model. In secondary production, d100g and d100g are even more efficient than their A*g equivalents, as they both, in the interior, have relative more gas and a longer time of residence (especially visible in the low-energy end of $^{10}Be/^9Be$ and B/C (modulated)). Thus, the d100g is also greatly exaggerating positrons prediction in the medium-energy range and is too unrealistic. In reduction of dipole anisotropy, the Slow-Wall models are comparable, if the modification is applied strong enough (for A10, the local increase in diffusion coefficient leads to a rise in anisotropy which is not there for d10, but for A100/d100 the values of the average anisotropy are very similar in $\delta_p, \delta_{p/p}, \delta_{e^-}, \delta_{e^+}, \delta_{e^\pm}$ and $\delta_{e^+/p}$. Fig. A.32 shows the difference in density distribution, for the four weaker scenarios d10, d10g, A10, A10g, in protons (left) and positrons (right). The change in height between the wall regions and the interior, compared to the reference, is more exposed in the A bubbles. The higher diffusion inside then leads to a more even distribution, while the D bubbles more closely the BG distribution. In positrons, this effect becomes again superimposed by the extra production of secondaries in the wall, in a symmetrical fashion.
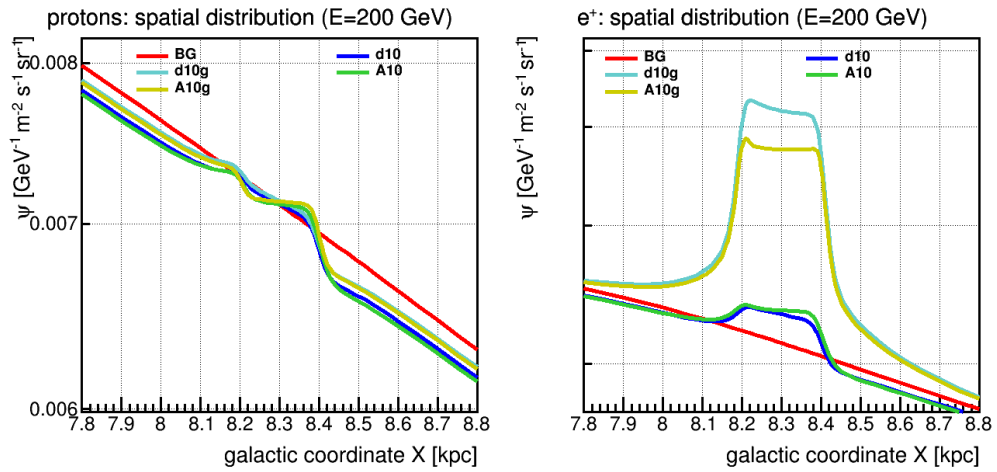
Figure A.32. Comparing Slow-Wall (d) and Slow-Wall-Fast-Interior bubbles (A). (left) Protons at $E = 200\,\text{GeV}$, (right) positrons at $E = 200\,\text{GeV}$.
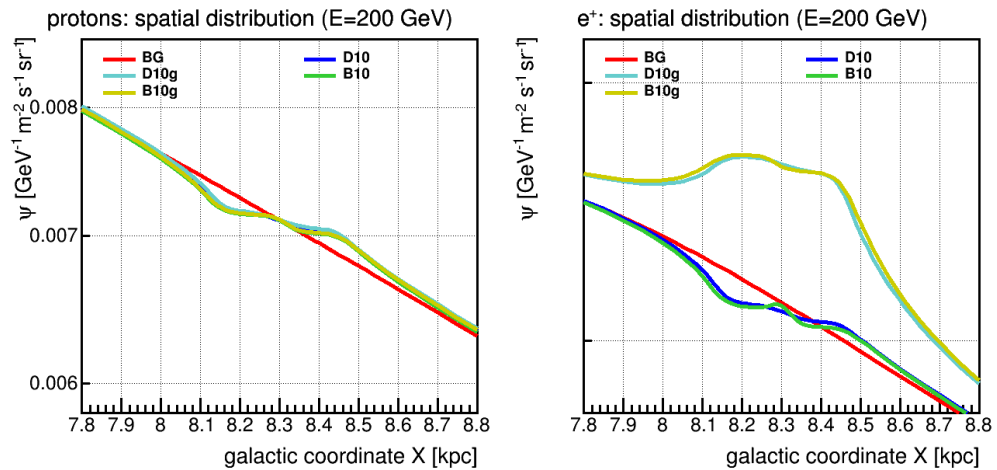
Figure A.33. Comparing Fast-Wall (D) and Fast-Wall-Slow-Interior bubbles (B). (left) Protons at $E = 200\,\text{GeV}$, (right) positrons at $E = 200\,\text{GeV}$.

213

In comparison of the *x* distribution, the "bumpy" structure of B is not as visible. As the diffusion coefficient in these D setups is relatively higher in the interior than in the B cases and at the galactic-average level, the local shape more closely resembles the BG shape.

Chimney "e/E" (cavity-like, elongated in Z direction)
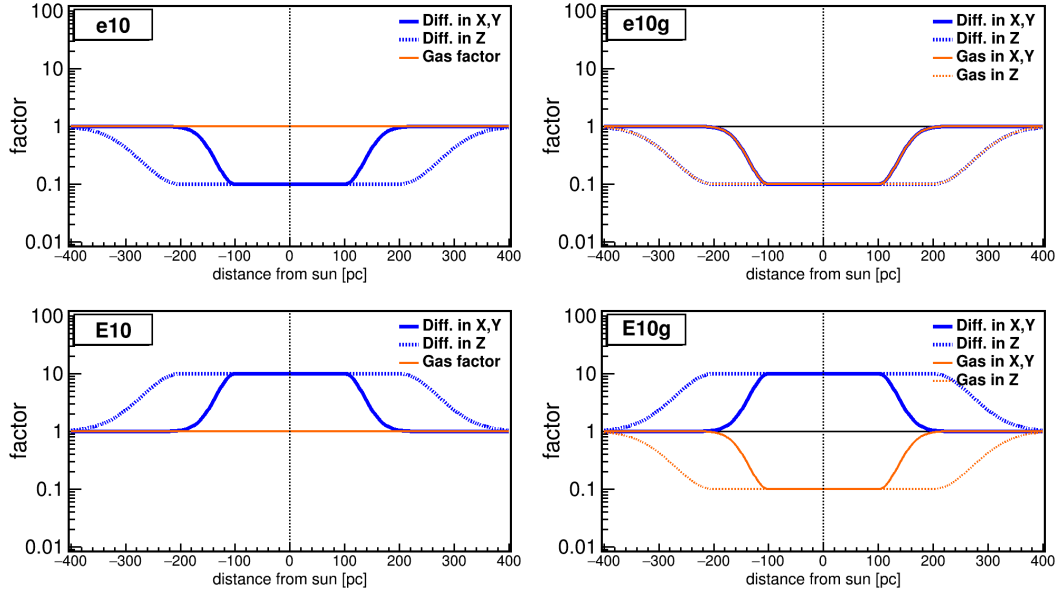
Figure A.34. The functional shape of type e or E models. These are based on the corresponding c or C model, but cylindrically symmetric, with elongation in *z* direction.

Model	p	$p/p_{[40,80]}$	e^-	e^+	$e^\pm$	e^+/p
BG	$5.35 \cdot 10^{-4}$	$5.97 \cdot 10^{-4}$	$3.20 \cdot 10^{-4}$	$6.58 \cdot 10^{-4}$	$8.58 \cdot 10^{-4}$	$1.39 \cdot 10^{-4}$
E10	$1.11 \cdot 10^{-3}$	$1.24 \cdot 10^{-3}$	$6.83 \cdot 10^{-4}$	$1.39 \cdot 10^{-3}$	$1.85 \cdot 10^{-3}$	$3.28 \cdot 10^{-4}$
E10g	$1.11 \cdot 10^{-3}$	$1.24 \cdot 10^{-3}$	$6.83 \cdot 10^{-4}$	$1.41 \cdot 10^{-3}$	$1.85 \cdot 10^{-3}$	$3.33 \cdot 10^{-4}$
e10	$1.02 \cdot 10^{-4}$	$1.13 \cdot 10^{-4}$	$5.85 \cdot 10^{-5}$	$1.26 \cdot 10^{-4}$	$1.55 \cdot 10^{-4}$	$2.93 \cdot 10^{-5}$
e10g	$1.01 \cdot 10^{-4}$	$1.13 \cdot 10^{-4}$	$5.85 \cdot 10^{-5}$	$1.32 \cdot 10^{-4}$	$1.55 \cdot 10^{-4}$	$3.29 \cdot 10^{-5}$
upper limit		$\mathbf{3 \cdot 10^{-3}}$	$\mathbf{6 \cdot 10^{-3}}$		$\mathbf{5.28 \cdot 10^{-3}}$	$\mathbf{2 \cdot 10^{-2}}$
		AMS-02*	AMS-02*		Fermi-LAT	AMS-02*
min. cumul. *E*	16 GeV	80 GeV	16 GeV	16 GeV	60 GeV	16 GeV
max. cumul. *E*	1.8 TeV	1.8 TeV	350 GeV	350 GeV	480 GeV	350 GeV

Figure A.35. Dipole anisotropy in cumulative energy bins, for "e/E" bubbles
* ongoing work [99]).
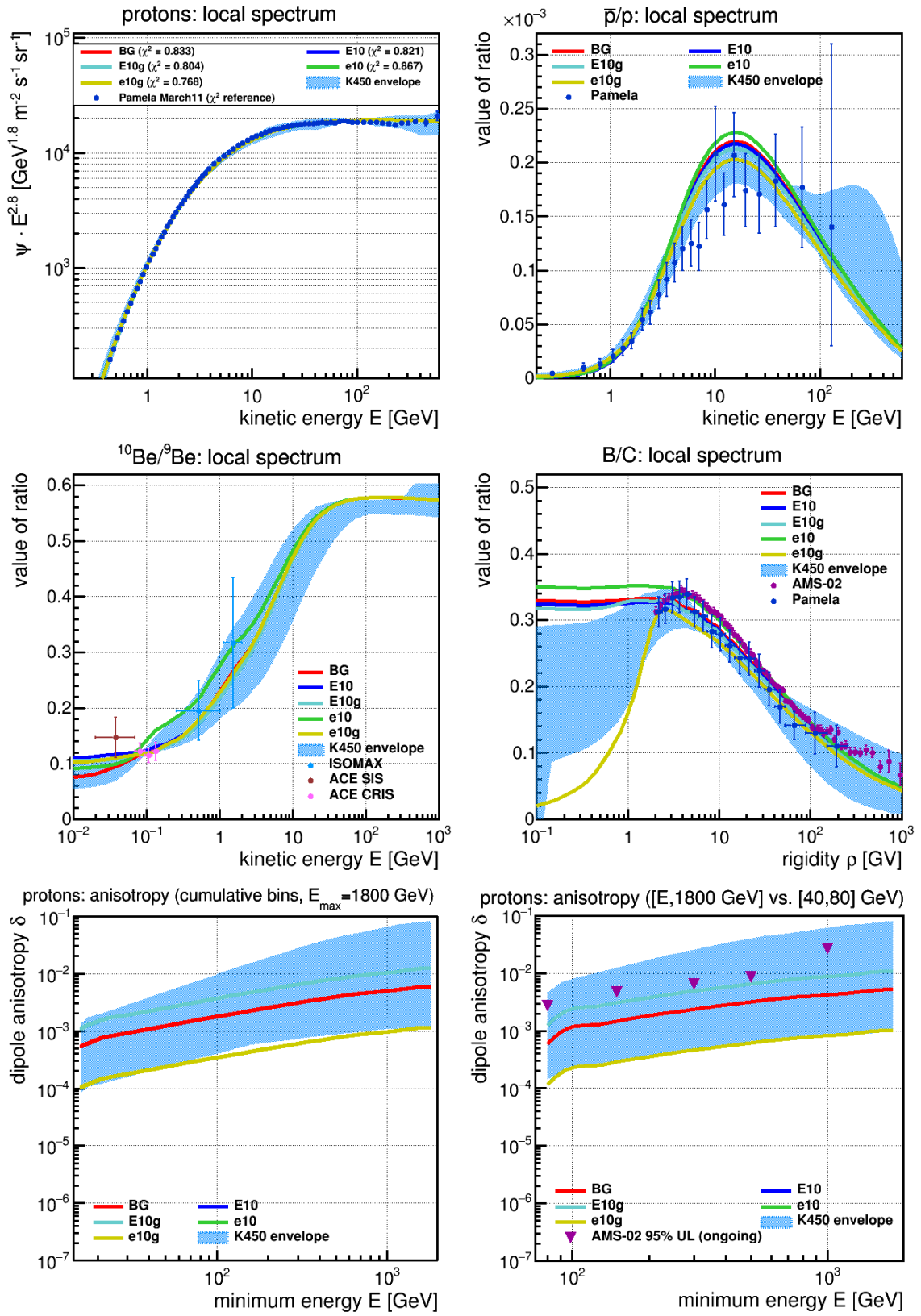
Figure A.36. Hadronic observables in type e/E bubbles. In this order: Proton spectrum (scaled with $E^{2.8}$), $\bar{p}/p$, $^{10}Be/^{9}Be$, B/C and dipole anisotropy of protons and protons relative in energy.

215
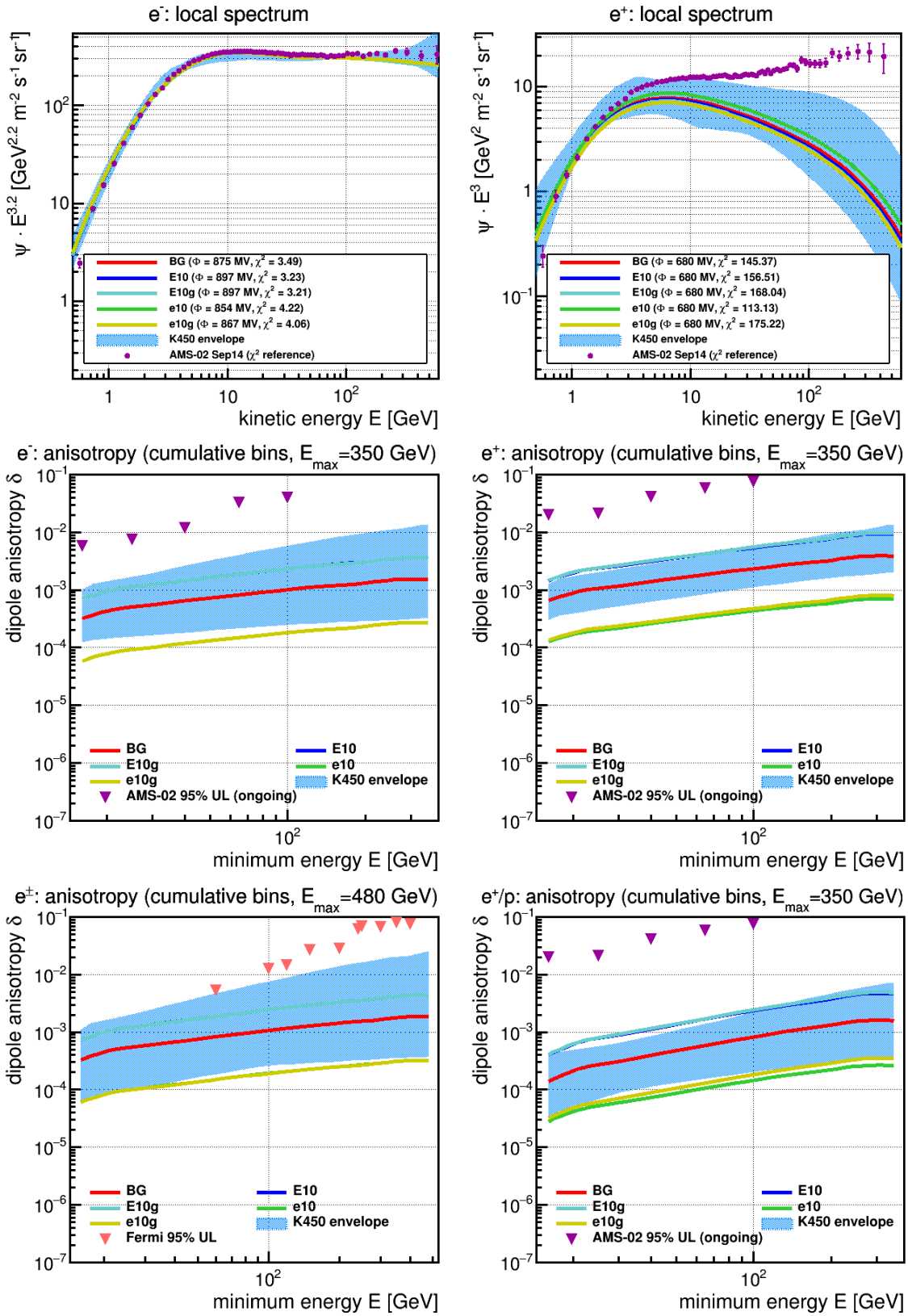
Figure A.37. Leptonic observables in type e/E bubbles. In this order: Electron spectrum (scaled with $E^{3.2}$), positron spectrum (scaled with E^3) and dipole anisotropy of electrons, protons, lepton sum and positrons relative to protons.

For direct comparison, we view the distribution of protons and positrons along the X axis around the sun, with source injection strength held normalized so that the proton distribution far outside the bubble walls agree, Fig.A.39 (top row shows scenarios without, bottom row with gas modification). The rightmost plot shows, for, δ_p, that the elongated "E" bubble slightly enhances the effect of each corresponding symmetrical "C" bubble. We can understand this behavior as a *steady-state* effect: The absolute height of the local density is determined by the inherent continuity conditions from the outside region.
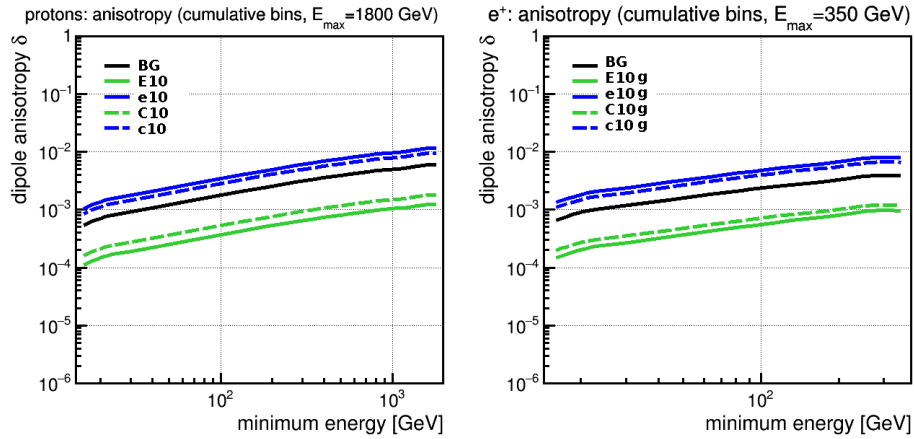
Figure A.38. Comparing "e/E" models and "eg/Eg" models, proton dipole anisotropies.
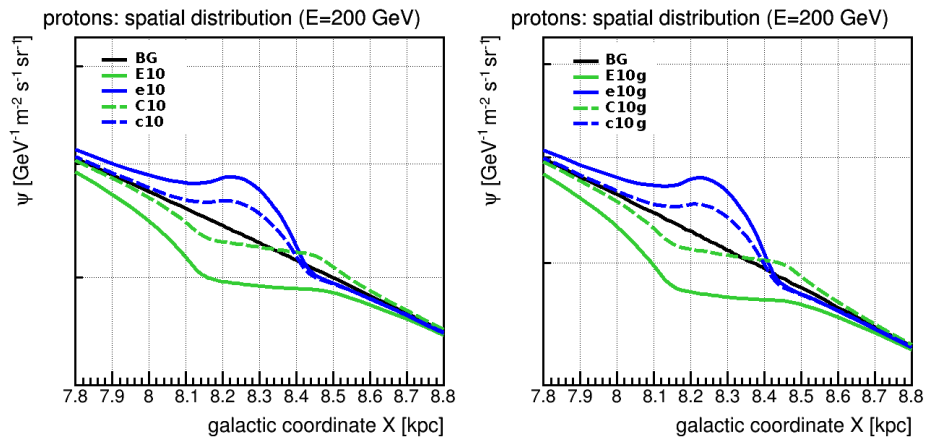
Figure A.39. Comparing "e/E" models and "eg/Eg" models, proton distribution.

217
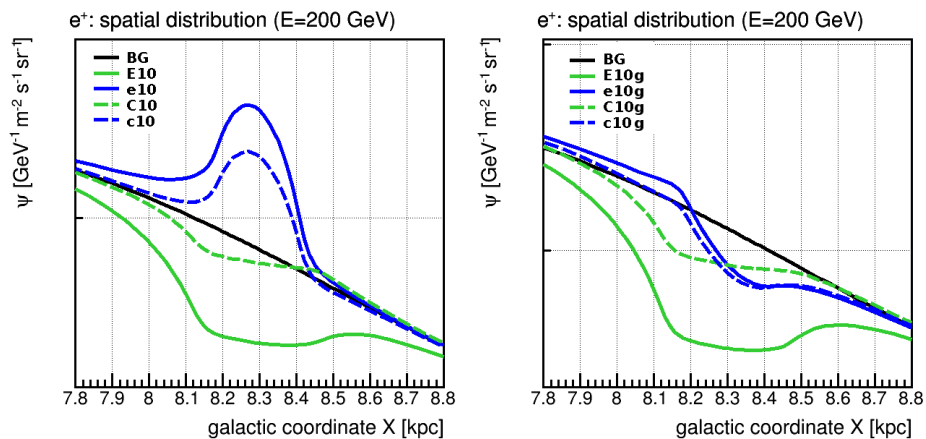
Figure A.40. Comparing "e/E" models and "eg/Eg" models, positron dipole anisotropies.

Chimney "TA/TB" (tube-like, free opening into the galactic halo)
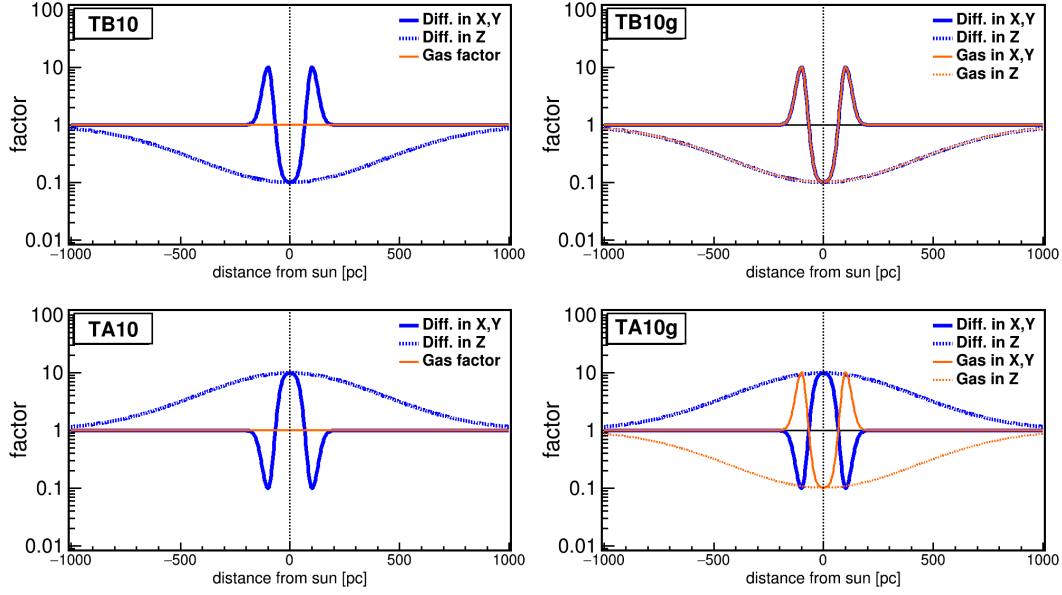
Figure A.41. The functional shape of type TA or TB models. These are based on the corresponding A or B model, but with a large elongation in z direction, of kiloparsec scale into the Galactic Halo.

Model	p	$p/p_{[40,80]}$	e^-	e^+	$e^\pm$	e^+/p
BG	$5.35 \cdot 10^{-4}$	$5.97 \cdot 10^{-4}$	$3.20 \cdot 10^{-4}$	$6.58 \cdot 10^{-4}$	$8.58 \cdot 10^{-4}$	$1.39 \cdot 10^{-4}$
TA10	$3.89 \cdot 10^{-4}$	$4.36 \cdot 10^{-4}$	$2.42 \cdot 10^{-4}$	$5.90 \cdot 10^{-4}$	$6.58 \cdot 10^{-4}$	$3.24 \cdot 10^{-4}$
TA10g	$3.85 \cdot 10^{-4}$	$4.36 \cdot 10^{-4}$	$2.38 \cdot 10^{-4}$	$7.24 \cdot 10^{-4}$	$6.67 \cdot 10^{-4}$	$5.04 \cdot 10^{-4}$
TB10	$5.88 \cdot 10^{-5}$	$6.57 \cdot 10^{-5}$	$3.60 \cdot 10^{-5}$	$7.31 \cdot 10^{-5}$	$9.71 \cdot 10^{-5}$	$1.62 \cdot 10^{-5}$
TB10g	$5.89 \cdot 10^{-5}$	$6.57 \cdot 10^{-5}$	$3.60 \cdot 10^{-5}$	$7.01 \cdot 10^{-5}$	$9.72 \cdot 10^{-5}$	$1.29 \cdot 10^{-5}$
upper limit		$3 \cdot 10^{-3}$	$6 \cdot 10^{-3}$		$5.28 \cdot 10^{-3}$	$2 \cdot 10^{-2}$
		AMS-02*	AMS-02*		Fermi-LAT	AMS-02*
min. cumul. E	16 GeV	80 GeV	16 GeV	16 GeV	60 GeV	16 GeV
max. cumul. E	1.8 TeV	1.8 TeV	350 GeV	350 GeV	480 GeV	350 GeV

Figure A.42. Dipole anisotropy in cumulative energy bins, for "T" bubbles
* ongoing work [99]).
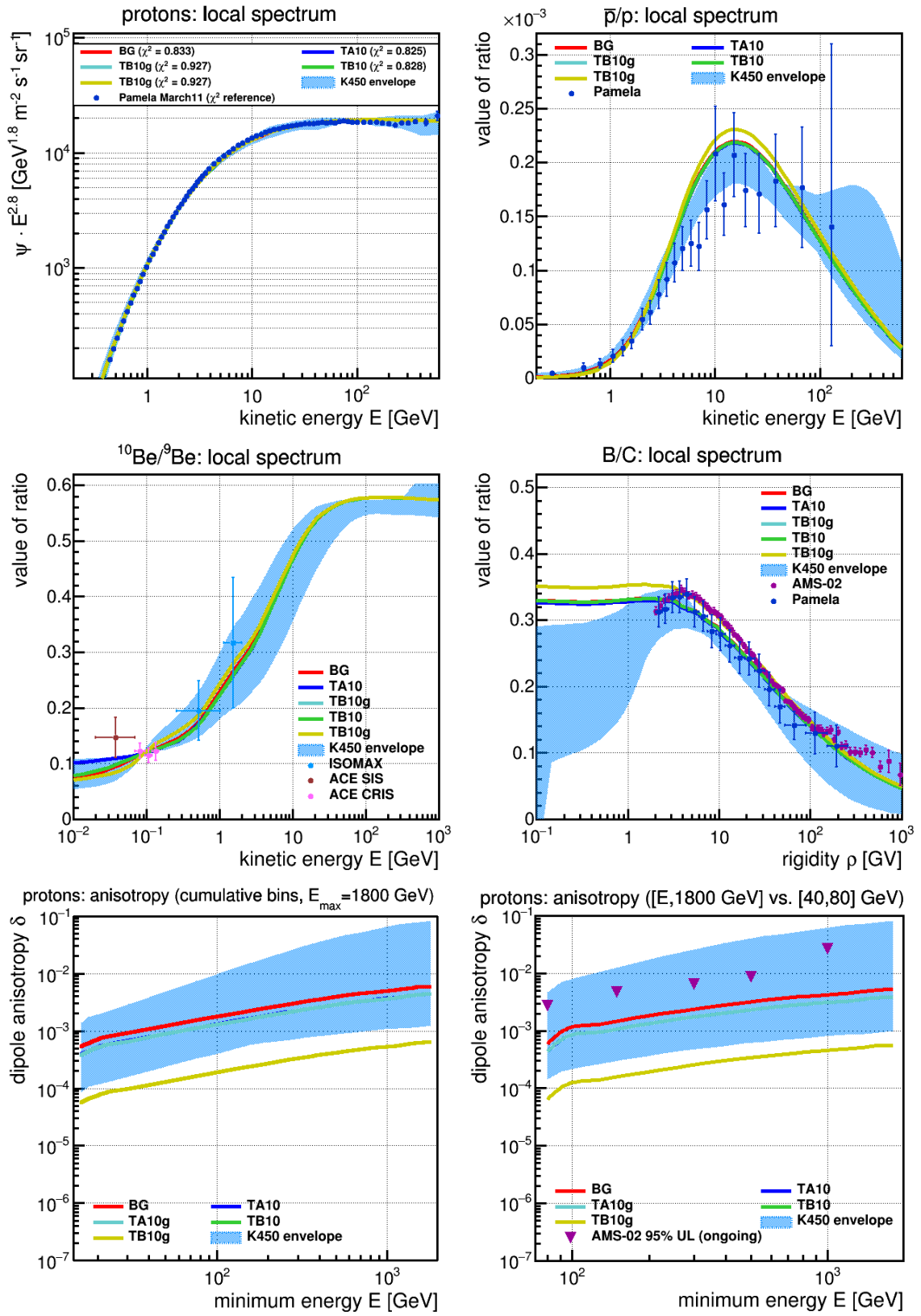
Figure A.43. Hadronic observables in type TA/TB bubbles. In this order: Proton spectrum (scaled with $E^{2.8}$), $\bar{p}/p$, $^{10}Be/^9Be$, B/C and dipole anisotropy of protons and protons relative in energy.
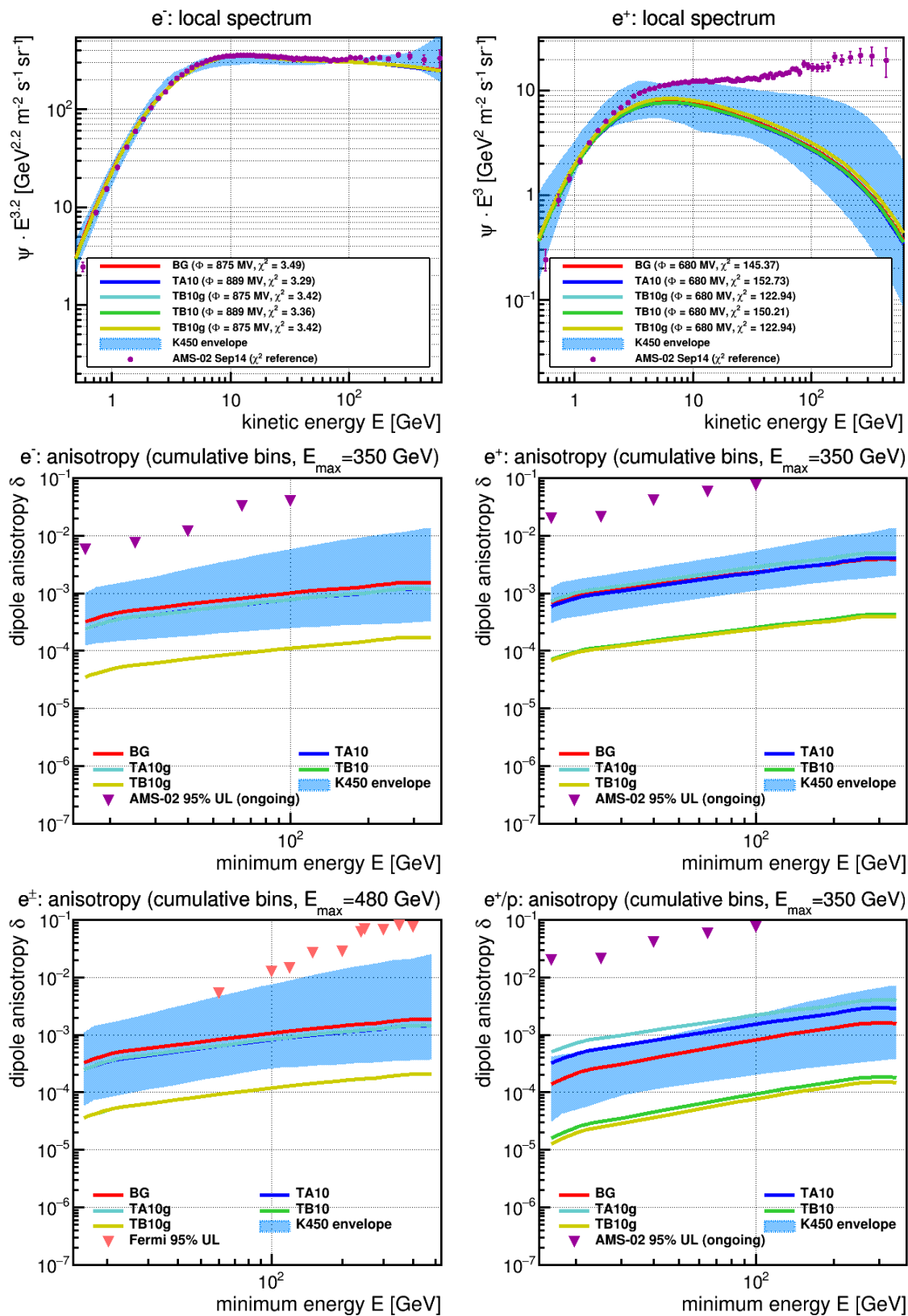
Figure A.44. Leptonic observables in type TA/TB bubbles. In this order: Electron spectrum (scaled with $E^{3.2}$), positron spectrum (scaled with E^3) and dipole anisotropy of electrons, protons, lepton sum and positrons relative to protons.

Blue lines: A-type.

The TA10 bubble intensifies the drop in anisotropy that the A10 bubble showed - it can be seen that while the A bubble show a bulge, an overdensity over the galactic surrounding. In the TA scenario, diffusion into Z direction is "preferred" by a factor of 100, which allows quick transport into the halo and out of the galaxy. Locally, in Z direction, the behavior is similar to the BG model, just decreased due to the particle loss. In diffusion equilibrium then, the gradient in X direction has completely evened out. This is a realistic scenario, as it is discussed in the literature that the hot gas in the local cavity might indeed touch the galactic halo, or other surrounding superbubbles or canals. See Fig. 1.23

Green lines: B-type

In the inverse scenario, there is nearly not a big difference in anisotropy. The local distribution in the stretched TB10 tube scenario is shifted down versus the spherical B10 scenario, because here, the quick-loss effect of particles happens inside the wall regions. The theoretical mechanism described for the B bubble is still valid, however: from the evened-out tube wall, propagation into the bubble inwards sets in evenly, with a rising scattering rate. Locally, this produces a bump in which we have placed the Sun, our place of observation, by construction.

Here, positrons have the ability to quickly escape into the halo, but the wall regions in the Galactic Disc are a steady source of production. Thus, for TA10g, the local density distribution in X direction still follows the BG X distribution, while in the A10g scenario the sources are distributed symmetrically in three dimension around the sun. The difference between TB10g and B10g does not appear interesting.
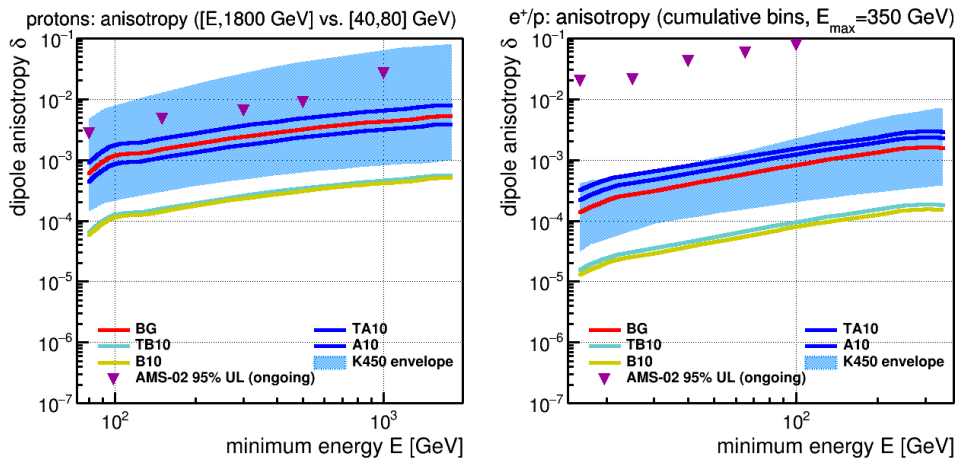
Figure A.45. Comparing elongated "TA/TB" and symmetrical "A/B" setups, dipole anisotropies.
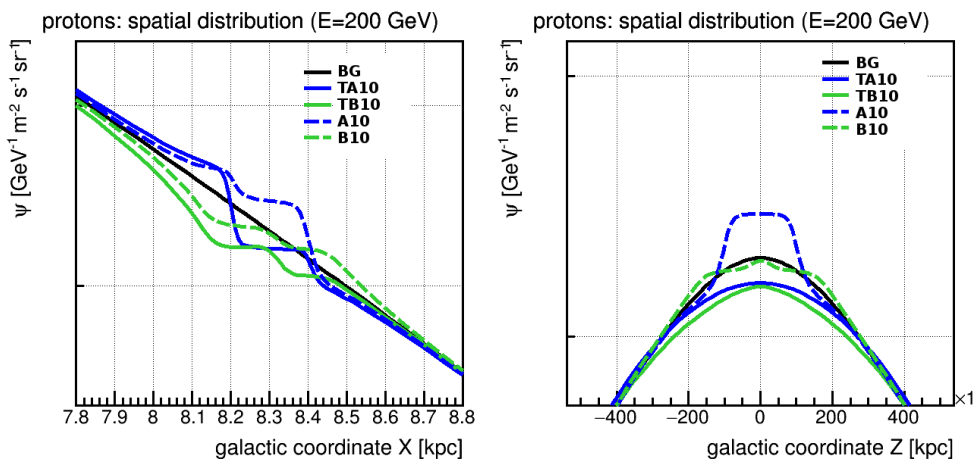
Figure A.46. Comparing elongated "TA/TB" and symmetrical "A/B" setup, proton distribution.
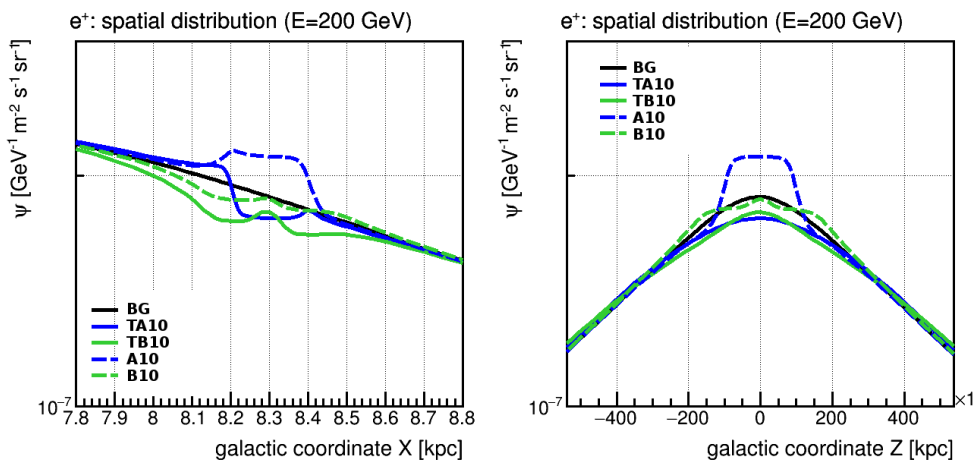
Figure A.47. Comparing elongated "TA/TB" and symmetrical "A/B" setups, positron distribution.
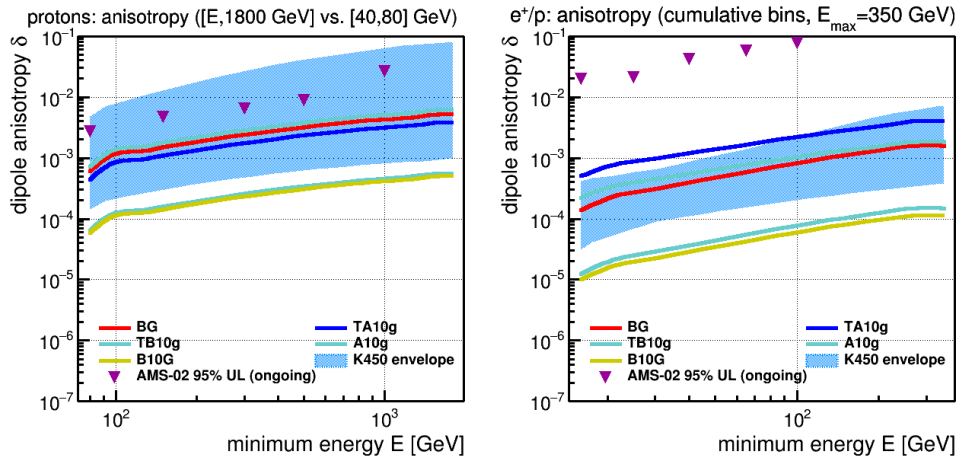
Figure A.48. Comparing elongated "TA/TB" and symmetrical "TA/TB" setups, dipole anisotropies.
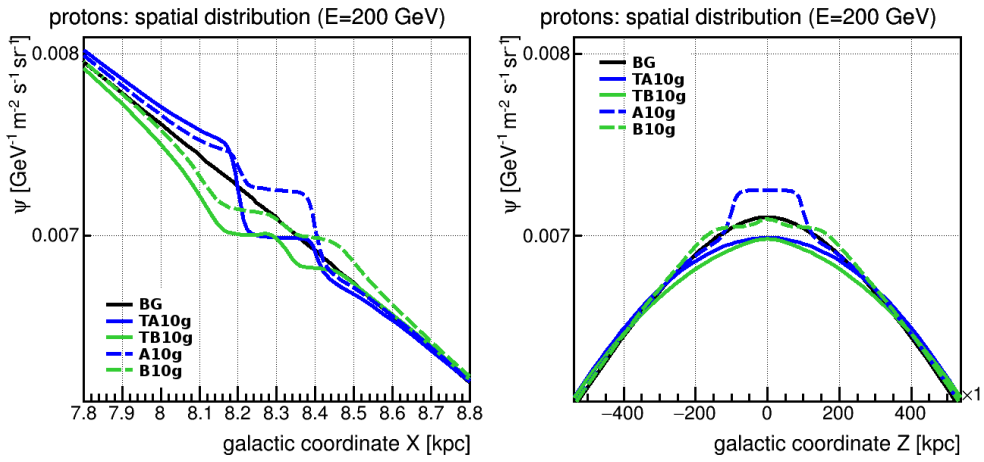
Figure A.49. Comparing elongated "TA/TB" and symmetrical "TA/TB" setups, proton distribution.
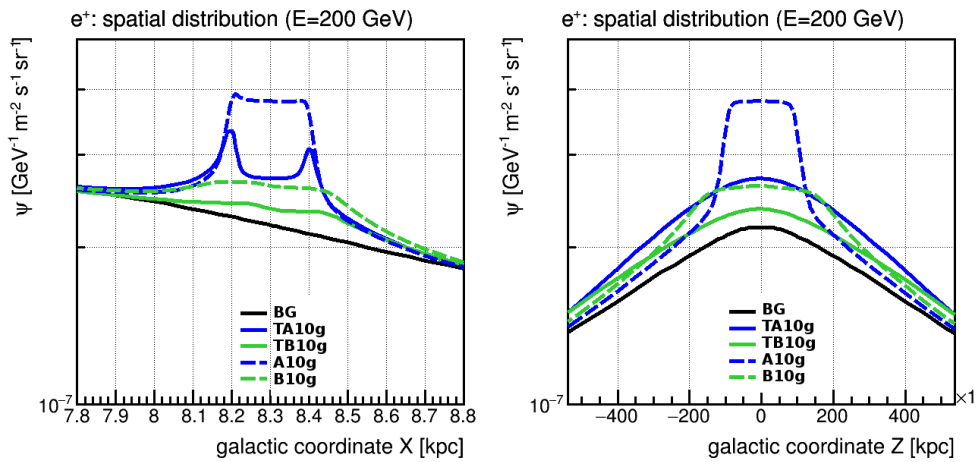
Figure A.50. Comparing elongated "TA/TB" and symmetrical "TA/TB" setups, positron distribution.

A.5. Auxiliary calculation: Anisotropy contribution from a single pulsar

This calculations addresses the details of the single pulsar exclusion argument employed in section 4.2. There, we considered the total e^+ flux I_{sum} separated into one BG contribution and a signal contribution (4.2)

$$I_{sum} = I_{BG} + I_{sig} , \tag{A.2}$$

with each component giving a contribution to the e^+ anisotropy, written as a vector in Galactic coordinates x, y, z and a unit vector $\vec{e}_r$.

$$I_{BG} = I_{0,BG}(1 + \vec{\delta}_{BG} \cdot \vec{e}_r) \tag{A.3}$$

$$I_{sig} = I_{0,sig}(1 + \vec{\delta}_{sig} \cdot \vec{e}_r) \tag{A.4}$$

$$I_{sum} = I_{0,sum}(1 + \vec{\delta}_{sum} \cdot \vec{e}_r), \tag{A.5}$$

The following calculation refers to the e^+ flux, but works with the values of the dipole anisotropy in e^+/p if no proton component is in the signal (as is the case when the signal comes from a pulsar).

From the spectral shapes of the BG secondary e^+ component and the actual observation (Fig. 4.1), it is possible to estimate the extent of which the signal, as the difference between data and background description, actually contributes to the total dipole anisotropy. This is done for the energy range $E \in [16, 350]$ GeV in which ongoing AMS-02 analyses are done.

We can convert flux intensity I to particle density N for each component as

$$I_{i,0} = \frac{4\pi}{c}N_i \tag{A.6}$$

$$\Rightarrow \quad I_{sum} = I_{sum,0}(1 + \frac{I_{BG,0}}{I_{sum,0}}\vec{\delta}_{BG}\vec{e}_r + \frac{I_{sig,0}}{I_{sum,0}}\vec{\delta}_{sig}\vec{e}_r) \tag{A.7}$$

$$= I_{sum,0}(1 + \underbrace{\left(\frac{N_{BG}}{N_{sum}}\vec{\delta}_{BG} + \left(1 - \frac{N_{BG}}{N_{sum}}\right)\vec{\delta}_{sig}\right)}_{\vec{\delta}_{sum}} \vec{e}_r) \tag{A.8}$$

Fitting a power-law function $I_{BG}(E) = I_{BG}(E_0) \cdot (E/E_0)^{-\gamma}$ to the BG over the range $E \in [10, 300]$ GeV, we obtain $\gamma_{BG} = 3.64$ (E_0 is a reference energy chosen below). For the sake of this simple estimation, we very loosely find that the AMS-02 data is described by $I_{sum}(E) = I_{sum}(E_0) \cdot (E/E_0)^{-\gamma_{sum}}$ with $\gamma_{sum} \approx 2.9$ over this energy range. This simplification is a mean value, as AMS officially sees no unique power-law [103]. They state $\gamma = 2.97 \pm 0.03$ [fit over $15.1 - 31.8$ GeV] and $\gamma = 2.75 \pm 0.05$ [fit over $49.3 - 198$ GeV] [103]. The argument hereby made stays valid if one uses the more accurate values instead of our crude approximation.

If we take E_0 at a value low enough, the equation is simplified as $I_{sum}(E_0) \approx I_{BG}(E_0)$, the signal vanishes. For our simple argument here, we therefore take $E_0 = 1\,\text{GeV}$, appearing to be valid (see Fig. 4.1). As we consider a cumulative energy bin $E = [E_{min}, E_{max}]$, this approximation gives

$$\frac{N_{BG}}{N_{sum}}\left(E_{min}..E_{max}\right) = \frac{\int\limits_{E_{min}}^{E_{max}} dE\, (E/1\,\text{GeV})^{-\gamma_{BG}}}{\int\limits_{E_{min}}^{E_{max}} dE\, (E/1\,\text{GeV})^{-\gamma_{sum}}} \tag{A.9}$$

$$\frac{N_{BG}}{N_{sum}}\left(16..350\,\text{GeV}\right) = 9.3\% \tag{A.10}$$

And therefore

$$\vec{\delta}_{sum}(16..350\,\text{GeV}) = 9.3\%\,\vec{\delta}_{BG}(16..350\,\text{GeV}) + 90.7\%\,\vec{\delta}_{sig}(16..350\,\text{GeV}) \tag{4.6}$$

this is the first result referenced to in the introductory statements in section 4.2. So far, this assumes no specific nature about the signal, it just gives the total anisotropy as a partial weighting between the two components.

Assuming a single-pulsar signal. From the derivation of dipole anisotropy $\vec{\delta}$ (2.69) in subsection 2.3, and if we assume the signal to be given by the analytical pulsar solution (2.116), we get

$$\vec{\delta} = 9.3\%\,\vec{\delta}_{BG} + 90.7\%\,\frac{3D}{c}\frac{1}{N_{sum}}\vec{\nabla}\left(N_{sig,0}\cdot\exp\left(-\left(\frac{\vec{r}-\vec{d}}{R_{diff}}\right)^2\right)\right)\Bigg|_{\vec{r}=0} \tag{A.11}$$

$$= 9.3\%\,\vec{\delta}_{BG} - 90.7\%\,\frac{6D}{c\,R_{diff}^2}\frac{N_{sig}}{N_{sum}}\cdot(d\,\vec{e}_{PS}) \tag{A.12}$$

with d the pulsar distance, $\vec{e}_{PS}$ the unit vector in direction of the pulsar, D the diffusion coefficient, c the speed of light and the diffusion radius R_{diff} given from (2.115). The latter can be approximated if assuming to be far below the cooling break, $Eb_0t \ll 1$,

$$R_{diff} = 2\sqrt{D(E)\,t\,\frac{1-(1-Eb_0t)^{1-\delta}}{(1-\delta)Eb_0t}} \tag{2.117}$$

$$\approx 0.5\,\text{kpc}\left(\frac{D_0}{3.6\cdot10^{28}\,\text{cm}^2\,\text{s}^{-1}}\frac{t}{100\,\text{kyr}}\left(\frac{E}{100\,\text{GeV}}\right)^{-\delta}\right)^{1/2} \tag{A.13}$$

$$= R_0\sqrt{D_0 t}\left(\frac{E}{1\,\text{GeV}}\right)^{-\delta/2} \quad,\text{ with } R_0 = 0.567 \tag{A.14}$$

We can then, again, use our very crude description

$$N_{\mathrm{BG}} = N(1\,\mathrm{GeV}) \cdot (E/1\,\mathrm{GeV})^{-\gamma_{\mathrm{BG}}}, \qquad \gamma_{\mathrm{BG}} = 3.64 \qquad\qquad \text{(A.15)}$$

$$N_{\mathrm{sum}} = N(1\,\mathrm{GeV}) \cdot (E/1\,\mathrm{GeV})^{-\gamma_{\mathrm{sum}}}, \qquad \gamma_{\mathrm{sum}} \approx 2.9 \qquad\qquad \text{(A.16)}$$

that we assume over the energy range $E \in [16, 350]\,\mathrm{GeV}$.

Cumulating over this range,

- the gradient ("numerator" term) reads ($\widehat{E} \equiv E/1\,\mathrm{GeV}$)

$$\int dE\, N_{\mathrm{PS}} D R_{\mathrm{diff}}^{-2} = N(1\,\mathrm{GeV}) \cdot D_0 \cdot (R_0^2 D_0 t)^{-1} \cdot 1\,\mathrm{GeV} \int_{16}^{350} d\widehat{E}\, (\widehat{E}^{-\gamma_{\mathrm{sum}}} - \widehat{E}^{-\gamma_{\mathrm{BG}}}) \cdot \widehat{E}^{2\delta}$$

$$\text{(A.17)}$$

$$= N(1\,\mathrm{GeV}) \cdot (R_0^2 t)^{-1} \cdot 1\,\mathrm{GeV} \left[\frac{\widehat{E}^{1-\gamma_{\mathrm{sum}}+2\delta}}{1 - \gamma_{\mathrm{sum}} + 2\delta} - \frac{\widehat{E}^{1-\gamma_{\mathrm{BG}}+2\delta}}{1 - \gamma_{\mathrm{BG}} + 2\delta} \right]_{16}^{350}$$

$$\text{(A.18)}$$

$$= N(1\,\mathrm{GeV}) \cdot t^{-1} \cdot 117.7\,\mathrm{MeV}\,, \qquad\qquad\qquad \text{(A.19)}$$

- the integral in the denominator still reads (note that the factor R_{diff}^2 is part of the numerator term)

$$\int dE\, N_{\mathrm{sum}} = N(1\,\mathrm{GeV}) \cdot 1\,\mathrm{GeV} \int_{16}^{350} d\widehat{E}\, \widehat{E}^{-\gamma_{\mathrm{sum}}} \qquad\qquad \text{(A.20)}$$

$$= N(1\,\mathrm{GeV}) \cdot 1\,\mathrm{GeV} \left[\frac{\widehat{E}^{1-\gamma_{\mathrm{sum}}}}{1 - \gamma_{\mathrm{sum}}} \right]_{16}^{350} \qquad\qquad \text{(A.21)}$$

$$= N(1\,\mathrm{GeV}) \cdot 0.17\,\mathrm{MeV}\,, \qquad\qquad \text{(A.22)}$$

and all in all, we have a simple estimation in terms of pulsar distance d and age t, that

$$\vec{\delta} = 9.3\%\, \vec{\delta}_{\mathrm{BG}} - 90.7\% \frac{6d}{ct} \cdot 692.4 \cdot \vec{e}_{\mathrm{PS}} \qquad\qquad \text{(A.23)}$$

$$= 9.3\%\, \vec{\delta}_{\mathrm{BG}} - 12.36 \frac{[d/\mathrm{pc}]}{[t/\mathrm{kyr}]} \vec{e}_{\mathrm{PS}} \qquad\qquad \text{(A.24)}$$

For a different choice of background model, δ and γ_{BG} have to be adjusted, accordingly.

A.6. Details of pulsar scenarios in local transport models

In this appendix, the details of the model evaluation in section 4.4.2 are given.

Fast Interior

For the *fast interior* model C100, the pulsar retuning and changes in e^-, e^+ spectra as well as $e^\pm$, e^+/p anisotropies have been given in section 4.4.2.

Here, the results are shown for model C10g, which in comparison to C100 has a weaker modification of the fast diffusion coefficient, but accounts for the lower gas density inside the Bubble Interiors. Its shape is given in Fig. A.51. Results after retuning the G1..G5 scenarios are given in the Figs. below.
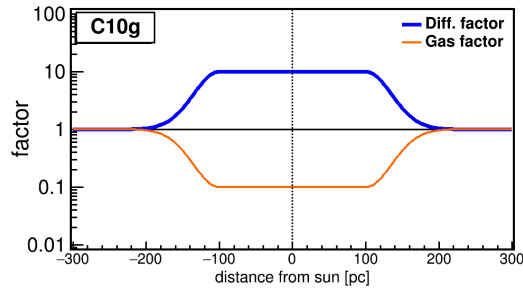
Figure A.51. The functional shape of Local Bubble model C10g. Interior diffusion is fastened by a factor 10, the gas density is decreased by a factor 10. The Walls are not accounted for. The y-axis shows the factor applied to diffusion (blue) and to gas (orange), the x-axis the distance to the Sun in pc. This model bubble is spherically symmetric.
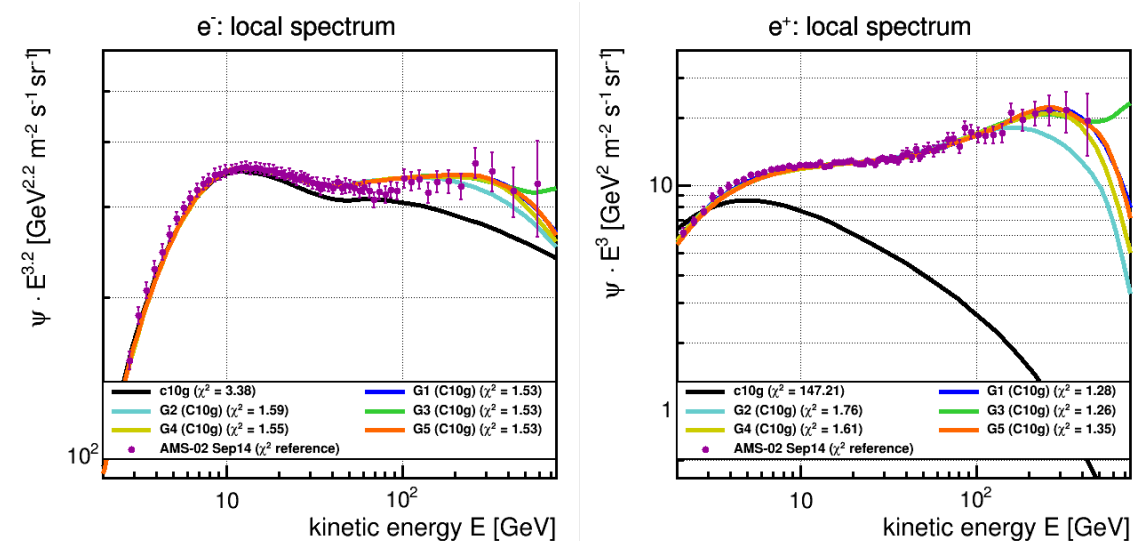
Figure A.52. The pulsar contributions of all 5 pulsar source scenarios G1..5. Pulsar injection has been retuned as described in section 4.4.2. The **left** panel shows electron flux (scaled by $E^{3.2}$). The **right** panel shows positron flux (scaled by E^3). The background (pulsar-free) scenario is shown in black, the G1..5 pulsar scenarios as colored lines.
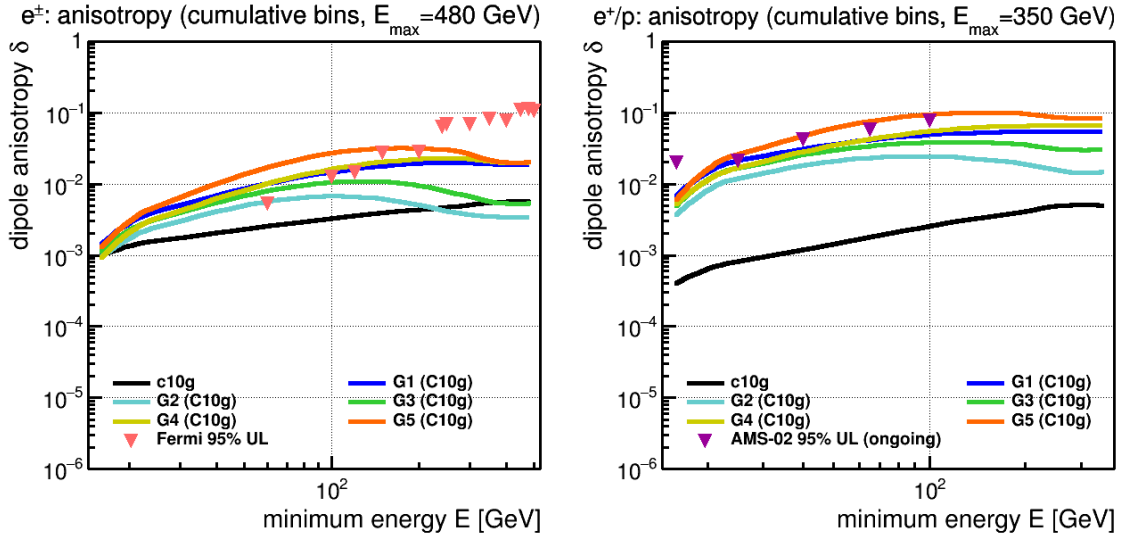
Figure A.53. The dipole anisotropy expected from pulsar scenarios G1..5 in local transport models C10g. Pulsar injection has been retuned as to describe the e^-,e^+ fluxes best (cf. Fig. A.52, as described in section 4.4.2. The **left** panel shows the leptonic sum anisotropy with the 95% UL from Fermi-LAT [125]. The **right** panel shows the relative positron to proton anisotropy with the 95% UL from AMS-02 (ongoing [99]).
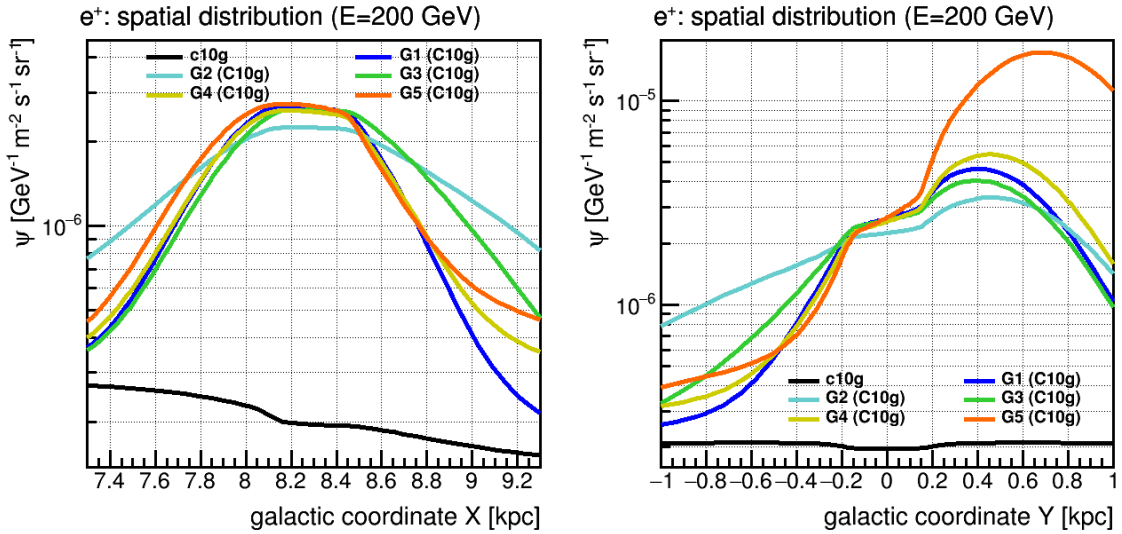
Figure A.54. The positron distribution around the sun, as expected from pule scenarios G1..5 in local transport models C10g at $E = 200$ GeV. Pulsar injection has been retuned as to describe the e^-,e^+ fluxes best (cf. Fig. A.52, as described in section 4.4.2. The **left** panel shows the x direction through the sun. The **right** panel shows the y direction through the sun. The background (pulsar-free) scenario is shown in black, the G1..5 pulsar scenarios as colored lines.

Slow Interior

As an example of a Slow-Interior model, we take c10g. Results after retuning the G1..G5 scenarios are given in the Figs. below.
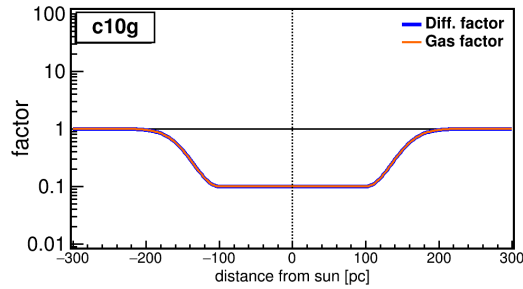
Figure A.55. The functional shape of Local Bubble model c10g. Interior diffusion is slowed by a factor 10, the gas density is decreased by a factor 10. The Walls are not accounted for. The y-axis shows the factor applied to diffusion (blue) and to gas (orange), the x-axis the distance to the Sun in pc. This model bubble is spherically symmetric.
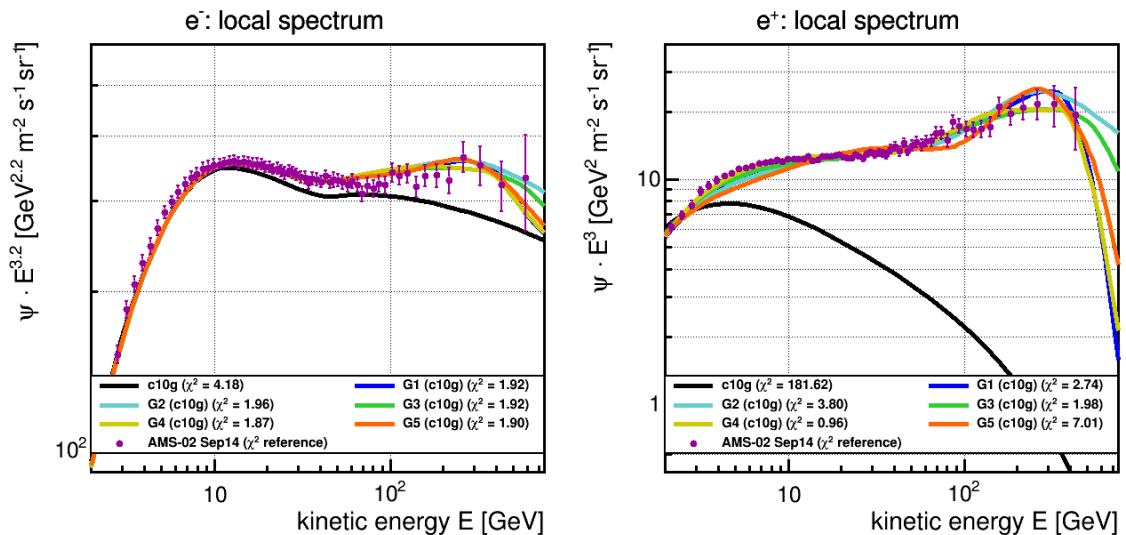
Figure A.56. The pulsar contributions of all 5 pulsar source scenarios G1..5. Pulsar injection has been retuned as described in section 4.4.2. The **left** panel shows electron flux (scaled by $E^{3.2}$). The **right** panel shows positron flux (scaled by E^3). The background (pulsar-free) scenario is shown in black, the G1..5 pulsar scenarios as colored lines.
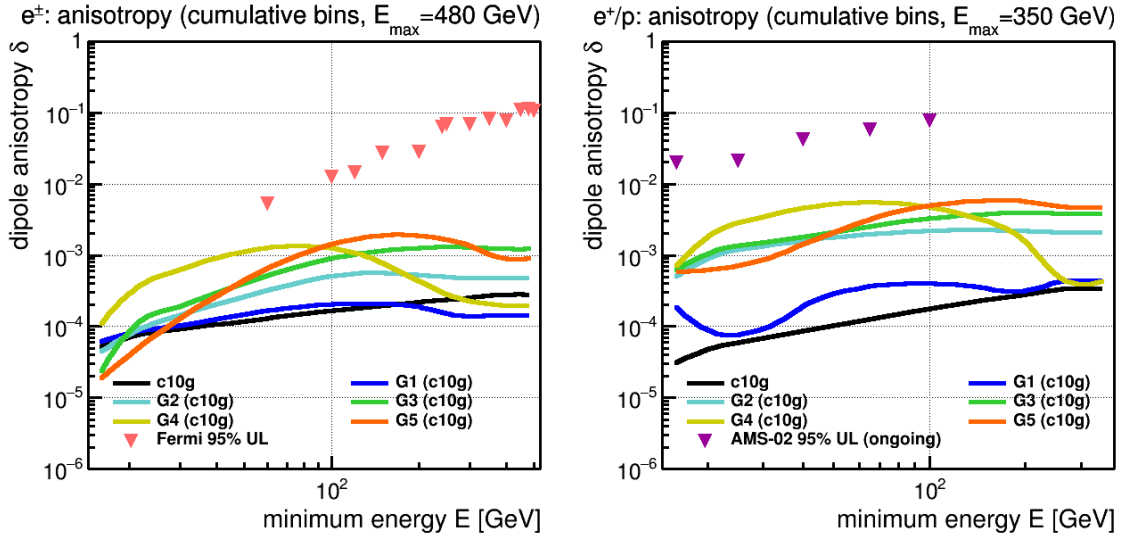
Figure A.57. The dipole anisotropy expected from pulsar scenarios G1..5 in local transport models c10g. Pulsar injection has been retuned as to describe the e^-,e^+ fluxes best (cf. Fig. A.56, as described in section 4.4.2. The **left** panel shows the leptonic sum anisotropy with the 95% UL from Fermi-LAT [125]. The **right** panel shows the relative positron to proton anisotropy with the 95% UL from AMS-02 (ongoing [99]).
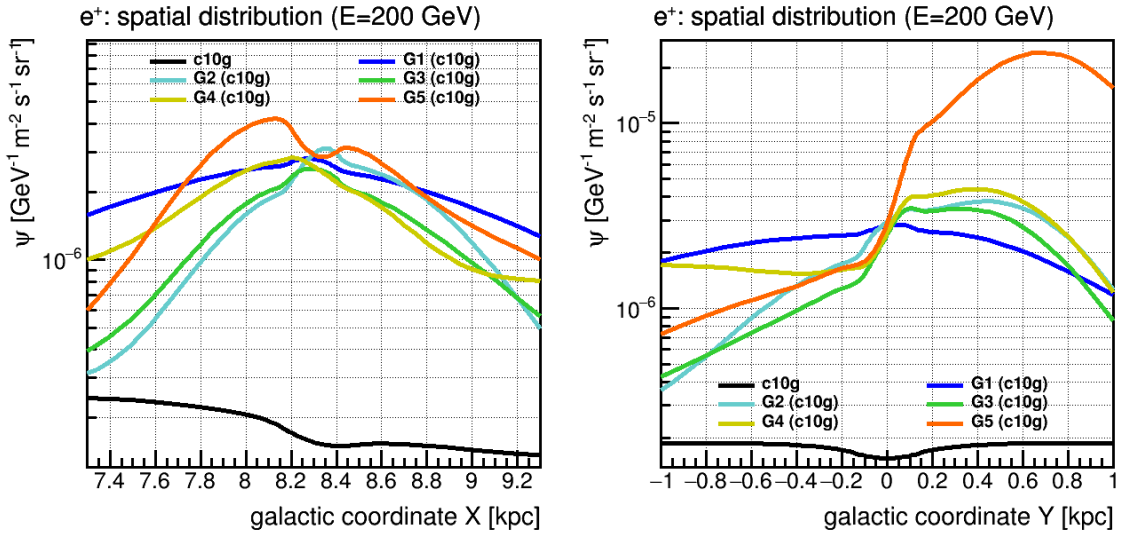
Figure A.58. The positron distribution around the sun, as expected from pulsar scenarios G1..5 in local transport models c10g at $E = 200$ GeV. Pulsar injection has been retuned as to describe the e^-,e^+ fluxes best (cf. Fig. A.56, as described in section 4.4.2. The **left** panel shows the x direction through the sun. The **right** panel shows the y direction through the sun. The background (pulsar-free) scenario is shown in black, the G1..5 pulsar scenarios as colored lines.

Fast Wall

As an example of a Fast-Wall model, we take D10. Results after retuning the G1..G5 scenarios are given in the Figs. below.
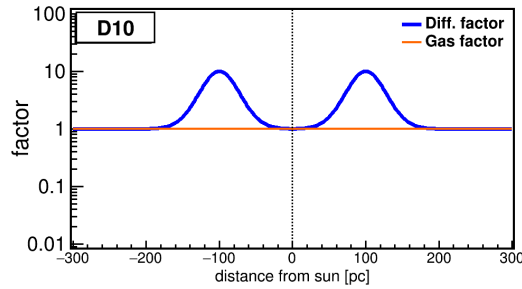
Figure A.59. The functional shape of Local Bubble model D10 Wall diffusion is fastened by a factor 10, the gas density is left untouched. The Interior is not accounted for. The y-axis shows the factor applied to diffusion (blue) and to gas (orange), the x-axis the distance to the Sun in pc. This model bubble is spherically symmetric.
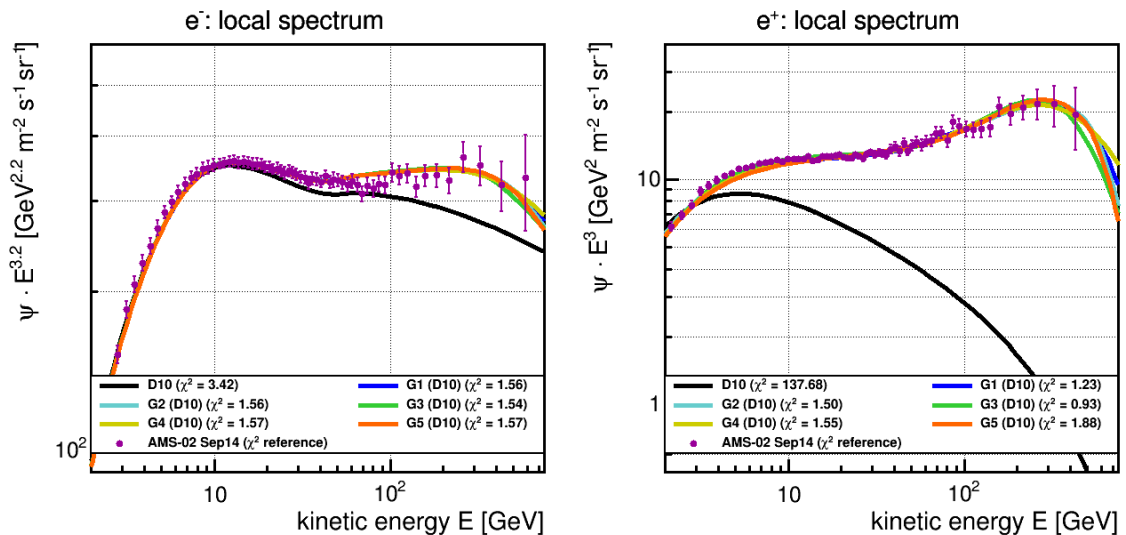
Figure A.60. The pulsar contributions of all 5 pulsar source scenarios G1..5. Pulsar injection has been retuned as described in section 4.4.2. The **left** panel shows electron flux (scaled by $E^{3.2}$). The **right** panel shows positron flux (scaled by E^3). The background (pulsar-free) scenario is shown in black, the G1..5 pulsar scenarios as colored lines.
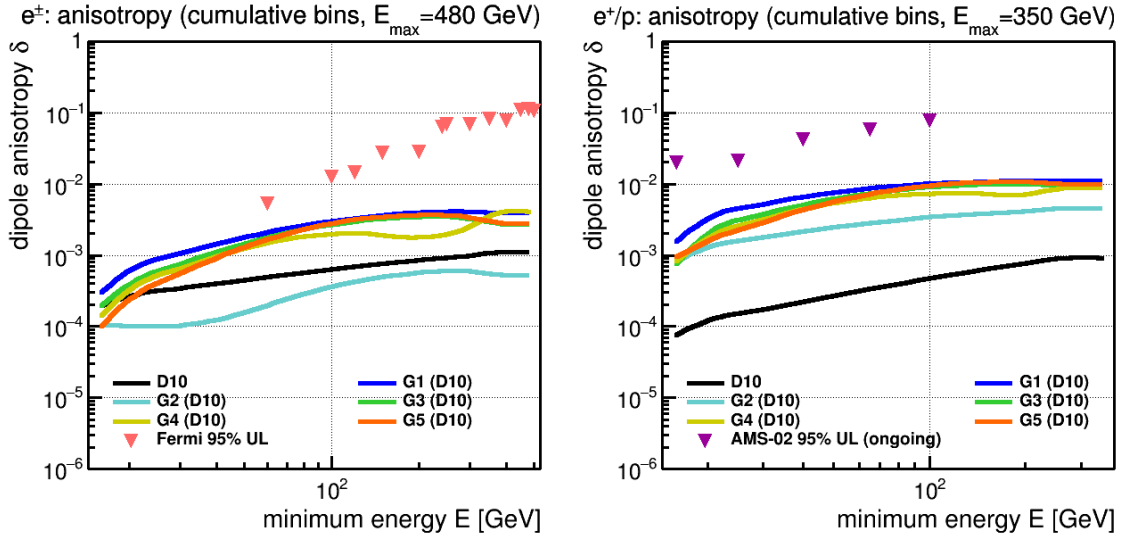
Figure A.61. The dipole anisotropy expected from pulsar scenarios G1..5 in local transport models D10. Pulsar injection has been retuned as to describe the e^-,e^+ fluxes best (cf. Fig. A.60, as described in section 4.4.2. The **left** panel shows the leptonic sum anisotropy with the 95% UL from Fermi-LAT [125]. The **right** panel shows the relative positron to proton anisotropy with the 95% UL from AMS-02 (ongoing [99]).
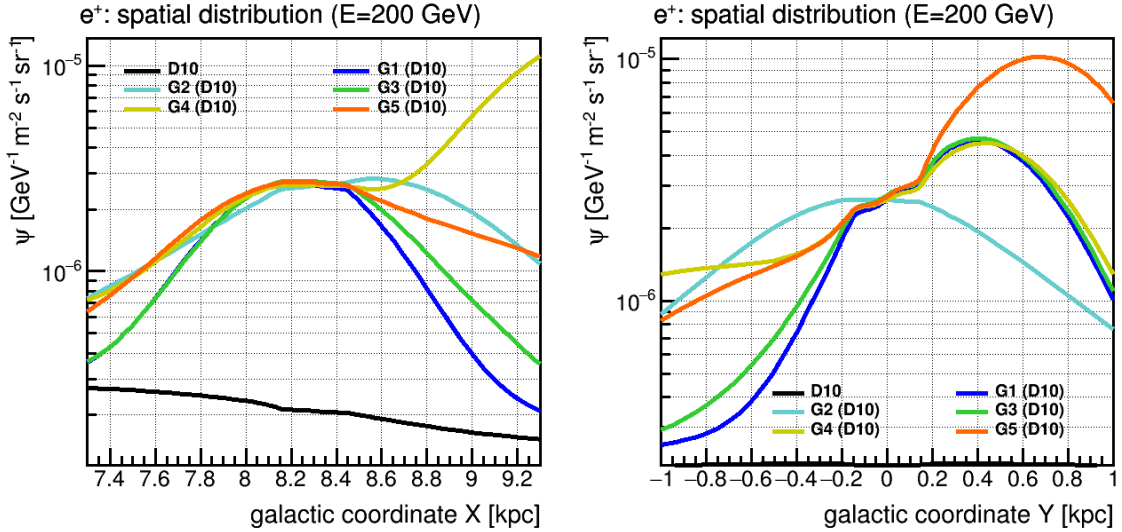
Figure A.62. The positron distribution around the sun, as expected from pulsar scenarios G1..5 in local transport models D10 at $E = 200$ GeV. Pulsar injection has been retuned as to describe the e^-,e^+ fluxes best (cf. Fig. A.60, as described in section 4.4.2. The **left** panel shows the x direction through the sun. The **right** panel shows the y direction through the sun. The background (pulsar-free) scenario is shown in black, the G1..5 pulsar scenarios as colored lines.

Slow Wall

As an example of a Slow-Wall model, we take d10. Results after retuning the G1..G5 scenarios are given in the Figs. below.
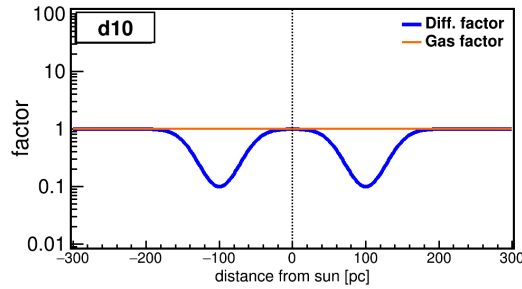
Figure A.63. The functional shape of Local Bubble model d10. Interior diffusion is slowed by a factor 10, the gas density is decreased by a factor 10. The Walls are not accounted for. The y-axis shows the factor applied to diffusion (blue) and to gas (orange), the x-axis the distance to the Sun in pc. This model bubble is spherically symmetric.
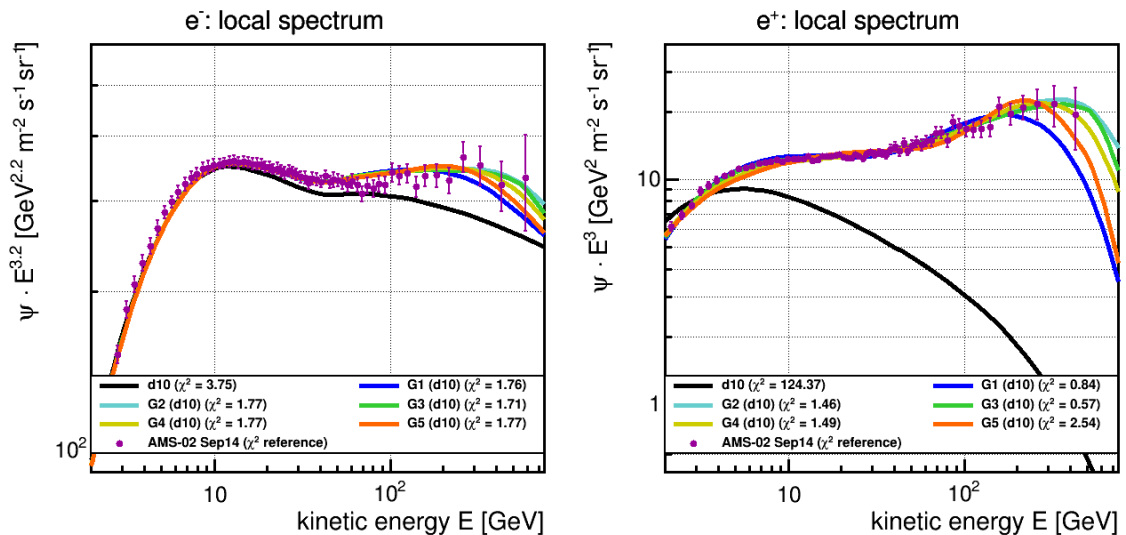
Figure A.64. The pulsar contributions of all 5 pulsar source scenarios G1..5. Pulsar injection has been retuned as described in section 4.4.2. The **left** panel shows electron flux (scaled by $E^{3.2}$). The **right** panel shows positron flux (scaled by E^3). The background (pulsar-free) scenario is shown in black, the G1..5 pulsar scenarios as colored lines.
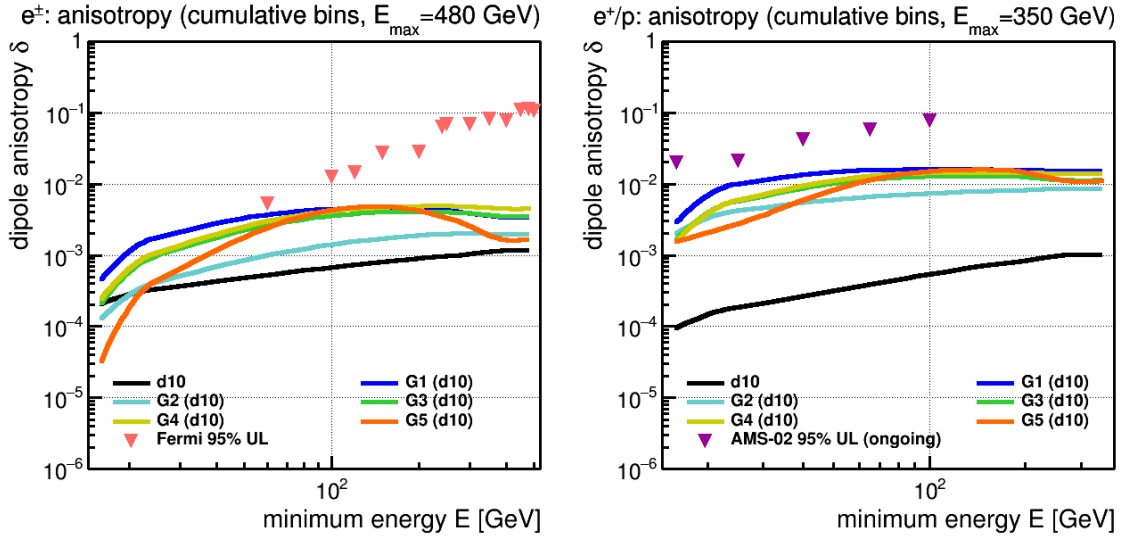
Figure A.65. The dipole anisotropy expected from pulsar scenarios G1..5 in local transport models d10. Pulsar injection has been retuned as to describe the e^-,e^+ fluxes best (cf. Fig. A.64, as described in section 4.4.2. The **left** panel shows the leptonic sum anisotropy with the 95% UL from Fermi-LAT [125]. The **right** panel shows the relative positron to proton anisotropy with the 95% UL from AMS-02 (ongoing [99]).
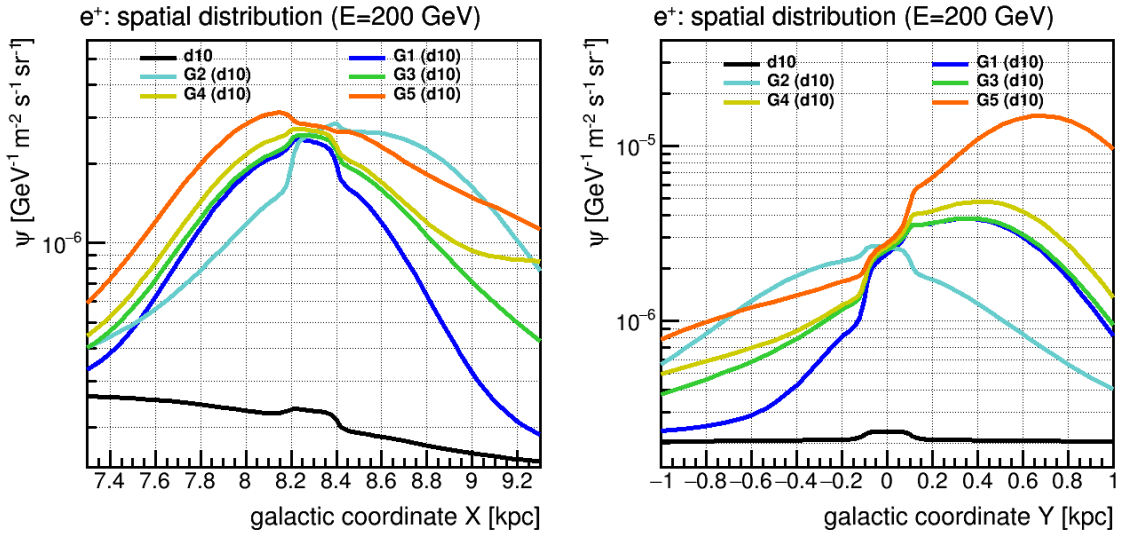
Figure A.66. The positron distribution around the sun, as expected from pulsar scenarios G1..5 in local transport models d10 at $E = 200$ GeV. Pulsar injection has been retuned as to describe the e^-,e^+ fluxes best (cf. Fig. A.64, as described in section 4.4.2. The **left** panel shows the x direction through the sun. The **right** panel shows the y direction through the sun. The background (pulsar-free) scenario is shown in black, the G1..5 pulsar scenarios as colored lines.